Abstract

Precision Measurements with the Single Electron Transistor:
Noise and Backaction in the Normal and Superconducting state

Benjamin Anthony Turek

2007

This thesis presents measurements of noise effects introduced by the Single Electron Transistor (SET) as it measures a nanoelectronic system, the single electron box/Cooper pair box. We consider the SET as a nanoscale charge amplifier, and show that the input noise of this amplifier – its "backaction" – can have a marked or even dominant effect on the system the SET measures. We report theoretical motivation and experimental results in both the normal and superconducting states.

The SET is a nanoelectronic, three-terminal, tunnel junction device, where a capacitively coupled input voltage modulates a drain-source current serving as the amplifier output. As a charge amplifier, it has been able to produce some of the fastest and most precise charge measurements currently possible. We use the SET to measure the single electron box/Cooper pair box, a nanoscale circuit where a capacitively coupled voltage modulates the tunneling of single electrons or Cooper pairs on to and off of an isolated metallic island.

Two different theoretical treatments of backaction effects motivate our experiments in the normal and superconducting states. In the normal state, backaction is modeled using a master equation for the coupled box-SET system. In the superconducting state, a density matrix treatment of the SET coupled to a qubit produces predictions about superconducting SET backaction on the Cooper pair box that are understood as quantum noise acting on a coherent two-level system.

Samples were measured in an RF-SET configuration in a dilution refrigerator. A charge-noise vetoing algorithm was implemented to permit extremely precise measurements of time-averaged box behavior. Detailed measurements of the SET/box system as the we vary the operating parameters of the SET confirm our understanding of SET backaction. Fast time-domain measurements in the

superconducting state are discussed as an additional tool to measure the SET's effects on the Cooper pair box.

Additional experiments investigate the noise effects of charged fluctuators in our box-SET samples, and the measurement of the Cooper pair box environmental impedance, whose control is important to the study of relaxation in Cooper pair box qubits.

Precision Measurements with the Single Electron Transistor: Noise and Backaction in the normal and Superconducting State

A Dissertation

Presented to the Faculty of the Graduate School

of

Yale University

in Candidacy for the Degree of

Doctor of Philosophy

by

Benjamin Anthony Turek

Dissertation Director: Professor Robert J. Schoelkopf

May, 2007

©2007 by Benjamin Anthony Turek.

All rights reserved.

Acknowledgements

This PhD could not have been completed without the love and support of innumerable colleagues, teachers, and friends. I cannot, in this space, give them each the thanks that they deserve, but I will, nevertheless, try.

My initial pursuit of physics is almost entirely due to the curiosity that my parents, Margaret and Robert, instilled in me. I have them to thank for starting me down this road, and for their support along the way.

If my parents taught me to be curious, then it was Dr. John Dell, my high school physics teacher, who focused that curiosity towards my current path. Doc Dell showed me what physics was, and taught me to love it. He has been a continuing source of inspiration, friendship, and advice during the years.

The bulk of my physics education came in the lab and under the tutelage of my advisor, Professor Rob Schoelkopf. Rob is one of the most brilliant physicists that I have ever known, and has put together a research effort that I am proud to have played a part in. Rob has been supportive and helpful, yet challenging and inspiring. I owe my development as an experimental physicist almost entirely to the guidance he has provided, and am honored to have worked in his lab.

Besides Rob, however, Yale has offered an incredible set of physicists that have been my mentors and my colleagues. First among them, Konrad Lehnert deserves thanks for bringing me into the Schoelkopf lab and for teaching me the foundations of experimental measurement. John Teufel, as well, taught me the ropes of the lab; he has also grown to be a great friend, and an incredible sounding board for my ideas. Hannes Majer deserves thanks as a companion and coworker for much of the work presented in this thesis. Andreas Wallraff and Andrew Houck deserve thanks for being "older brothers" to me when I've needed it. The theoretical work underlying this thesis was only comprehensible as a consequence of the patient explanations of Aash Clerk and Jens Koch.

Two professors at Yale deserve thanks for their roles as mentors throughout my career. First,

Professor Dan Prober has been an inspiration and a friend; he deserves full credit for making the 4th floor into what it is today. Professor Michel Devoret deserves similar thanks; I am honored to have come to know him as a physicist, an intellectual, and a friend.

In addition to those instrumental in my education, there are a great number of people who deserve thanks for keeping me sane and for helping me develop as a person during my time at Yale, before, and beyond. First among these is my best friend Sandy, who has been an endless source of sage advice and profound thought. My brother Daniel, also, has known when I've needed a real friend, and has cared for me more than a younger brother ever should. Monique and Pierre Gueydan have been like second parents to me, and I owe them thanks for their solicitude and their help (and their daughter). Sarah Bickman has kept me sane when I've needed it, and is one of the best listeners that I know. Brad Anderson has opened entire new literary worlds to me, and has helped me to know and to shape who I am. Blake and Jerry have reminded me that physics and life can, and should, be fun; their spirit will carry the Schoelkopf lab far. My identity as a physicist is also due, in small part, to the mentoring of Dr. Greg Madejski, who I am honored to call my friend. I am also grateful to all of the Soul Seekers – especially Keefer, Keith, and RJ – for giving me perspective, friendship, self-respect, and support in a way that no one at Yale was able to.

Whatever any of the above named people have been for me, none has been more of anything than my wife, Alex. She has supported me, encouraged me, and inspired me; she has brought (and continues to bring) me the best times of my life. No words can express my gratitude for her patience and her love, her quick wit and her gentle mien. As with so many other things in my life, this thesis and my work in grad school only make sense insofar as they were completed for her and with her. It is to her that this work is dedicated.

Contents

List of Figures

List of Tables

List of Symbols and Abbreviations

C_1	Capacitance between box gate lead and SET island. See figure 5.14
C_2	Capacitance between SET gate lead and box island. See figure 5.14
C_c	Coupling capacitance between SET and box islands
C_{gb}	Capacitance between box gate lead and box island. See figure 5.14
C_{ge}	Capacitance between SET ("electrometer") gate lead and SET island. See figure 5.14
$C_{\Sigma,SET}$	Total capacitance of SET island
$C_{\Sigma,box}$	Total capacitance of box island
CPB	Cooper Pair Box
CPW	Coplanar Waveguide
Δ	Superconducting gap energy
e	Charge of the electron (1.6×10^{-19}C)
$E_{C,SET}$	Single electron charging energy of SET island, calculated as $e^2/2C_{\Sigma,SET}$
$E_{C,box}$	Single electron charging energy of box island, calculated as $e^2/2C_{\Sigma,SET}$
E_{el}	Electrostatic energy
E_F	Fermi energy of a metal
E_J	Josephson coupling energy between different charge states on box island
g	Dimensionless conductance of a tunnel junction
G	Gain of an amplifier
$\Gamma_\uparrow$	Excitation rate for a quantum TLS
$\Gamma_\downarrow$	Relaxation rate for a quantum TLS
h	Planck's constant
$\hbar$	Planck's constant divided by 2π

HEMT	High Electron Mobility Transistor
k_B	Boltzmann's Constant
κ_{SET}	Fraction of an electron on the SET that is coupled as polarization charge to the box.
κ_{box}	Fraction of an electron on the box that is coupled as polarization charge to the SET.
N	Number of additional Cooper pairs on SET/Box island
n	Number of additional single electrons on SET island
n_{gb}	Total charge coupled to box island from external leads
n_{ge}	Total charge coupled to SET island from external leads
m	Number of additional electron on SET island
ϕ	Gauge-invariant phase difference across a Josephson junction.
Φ_0	Magnetic flux quantum ($h/2e$)
Φ_B	Magnetic flux
p_e	Ensemble averaged probability of finding a TLS in its excited state
p_g	Ensemble averaged probability of finding a TLS in its ground state
P	Polarization of an ensemble of two level systems
P_{SS}	Steady state polarization of an ensemble of two level systems
$\langle q \rangle$	Averaged number of excess electrons on the box from an ensemble of SET measurements.
q_{saw}	Charge on the Coupling Capacitor
R_K	Resistance quantum, $= h/2e^2$
R_{opt}	Optimum source resistance that, coupled to the input of an amplifier, gives minimum noise temperature.
R_S	Source resistance of device measured by an amplifier
RF	Radio Frequency
RF-SET	Radio Frequency Single Electron Transistor
$S_V(\omega)$	Voltage noise spectral density of an amplifier, expressed in V^2/Hz
$S_I(\omega)$	Current noise spectral density of an amplifier, expressed in A^2/Hz
SET	Single Electron Transistor

T1	Rate at which an ensemble of TLS measurements relaxes towards a steady-state polarization
T_N	Noise Temperature of an amplifier
T_N^{opt}	Optimum amplifier noise temperature, obtained by correct impedance matching to amplifier noise
TLS	Two Level System
Z_0	Characteristic impedance of a transmission line
Z_{LC}	Characteristic impedance of LC resonant circuit
ω_J	Josephson frequency, given as $2eV/\hbar$

Chapter 1

Introduction

1.1 Amplification and Nanoelectronic physics

Every experimental physicist has worked with amplifiers in some capacity, and most have paid some attention to the noise properties of these amplifiers. For macroscopic, classical measurements, however, this attention has likely been brief: there exists a well-understood framework to quantify and understand classical amplifier noise. A physicist will probably select an amplifier, perhaps based on its noise performance, and may check to see the extent to which uncertainty in his system is due to that performance – but will rarely concern him or herself with an understanding of the sources and mechanisms of that noise.

Recent developments in condensed matter physics, however, have forced a change in this thinking. In the late 1980s, the physics community became interested in the properties of mesoscopic systems(Imry, 1997), and, in the 1990s, in the fields of quantum computing and quantum measurement(Nielsen and Chuang, 2000). These fields made strict demands of the amplifiers that they used: they required unprecedented speed and accuracy in the measurements being made. However, they also cast amplifiers in a new role. As previously understood, an amplifier was a classical device, with a macroscopic voltage input, and a macroscopic voltage output to which some statistically understood noise had been added.

In these new systems, however, mesoscopic amplifiers are situated at an interface between a microscopic system (with a few degrees of freedom) and the macroscopic world on their output (see figure 1.1). Amplifiers are often the most direct route for disturbances from the environment to reach a qubit, and noise from the amplifier's input – backaction – became an important consideration that could potentially dominate the behavior of the system being measured. It is the study of this

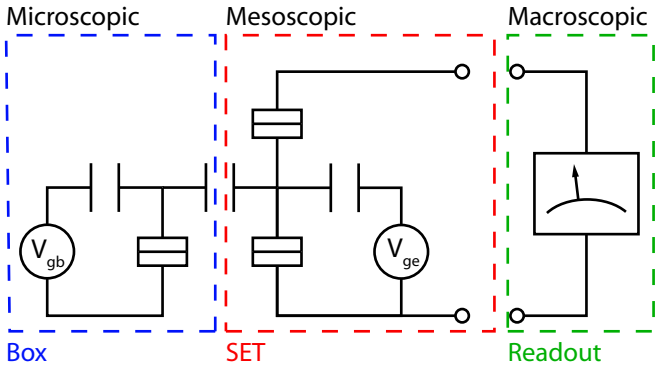

Figure 1.1: Circuit schematic of SET-box system. The SET operates as a mesoscopic charge amplifier, situated at the interface between the microscopic box and the macroscopic external world.

backaction – the effects of a mesoscopic amplifier on the microscopic system that it measures – that will be the core of this thesis.

We concern ourselves only with the backaction of a single mesoscopic amplifier, the Radio-Frequency Single Electron Transistor (RF-SET, shown schematically in figure 1.1) (Schoelkopf et al., 1998). The RF-SET is an ultrasensitive electrometer that has been proposed as a readout for qubits (Aassime et al., 2001), as well as other solid state (Kane et al., 2000) and nanomechanical (Knobel and Cleland, 2003) systems. For the experiments reported in this thesis, the SET measured the single electron/Cooper-pair box – a simple nanoelectronic system that is being investigated as a potential qubit. Because of its simplicity, and because it is in many ways a generic nanoelectronic system, the box makes an excellent demonstration of a more general understanding of SET backaction.

1.2 Noise in Classical Amplifiers

Our understanding of SET noise is based on a language that was developed to study the noise of classical amplifiers. A first grounding for this thesis, therefore, will motivate our understanding of noise in mesoscopic systems from an presentation of the well-understood noise of classical amplifiers.

In section 1.2.1, I will provide a mathematical background for the understanding of noise. In section 1.2.2 I will use this mathematical understanding of noise to describe the noise of classical amplifiers. Finally, in section 1.2.3, I will describe how these concepts extend to the amplification of signals from micro and mesoscopic systems. My treatment of these subjects will be necessarily brief; interested readers are referred to (Davenport and Root, 1958; Cerna and Harvey, 2000) for further information on the analysis of noisy signals, and to (Horowitz and Hill, 1989) for further

detail regarding the noise of amplifiers.

1.2.1 Noise Spectral Density

Amplifier noise may be most simply considered as a signal, added to an amplifier measurement, that cannot be predicted from a knowledge of the signal's history. To say that amplifier noise measurements cannot be predicted, however, does not mean that repeated measurements will be entirely uncorrelated; indeed many common classical amplifiers have noise that is confined to a range of frequencies.

We quantify the correlations in a noise signal by considering the the spectrum of the variations of that signal. This is commonly known as the noise spectral density, and usually represented by the symbol $S_V(\omega)$. The subscript usually will denote the measured quantity whose noise we are considering; the S_V in the previous sentence therefore denotes a voltage noise, although there may be noise in current, charge, frequency, phase, or any other measured quantity.

The accepted unit for a measurement of noise in a voltage is the spectral density, expressed in units of (V^2/Hz). The voltage spectral density may be intuitively understood as the mean square voltage that would be measured by a phase-insensitive detector preceded by a 1 Hz bandpass filter around a selected frequency. The noise on a signal with an arbitrary bandwidth may be found by integrating the noise spectral density across the appropriate bandwidth. Occasionally, one will find a noise spectral density expressed as in units of ($V/\sqrt{Hz}$), which is simply the square root of the usual expression.

Given a time-domain data set $V(t)$, the power spectral density of that data set is found by taking the fourier transform of its autocorrelation function [see (Davenport and Root, 1958), p.104], or:

$$S_V(\omega) = \int_{-\infty}^{+\infty} \left(\frac{1}{T} \int_0^T V(t)V(t-\tau)dt \right) e^{i\omega\tau} d\tau \tag{1.1}$$

This makes reasonable sense: the autocorrelation function, the term inside parentheses in equation (1.1), returns a nonzero signal when it finds correlated fluctuations separated by a time τ within a sampled signal. The Fourier transform then converts this into frequency space, and registers a response at frequencies corresponding to periodic correlations in the data.

We may even simplify expression somewhat: by the convolution theory of Fourier transforms, we know that equation 1.1, the fourier transform of a convolution, may be instead represented as the product of two fourier transforms; more simply, then, the power spectral density of a signal is just

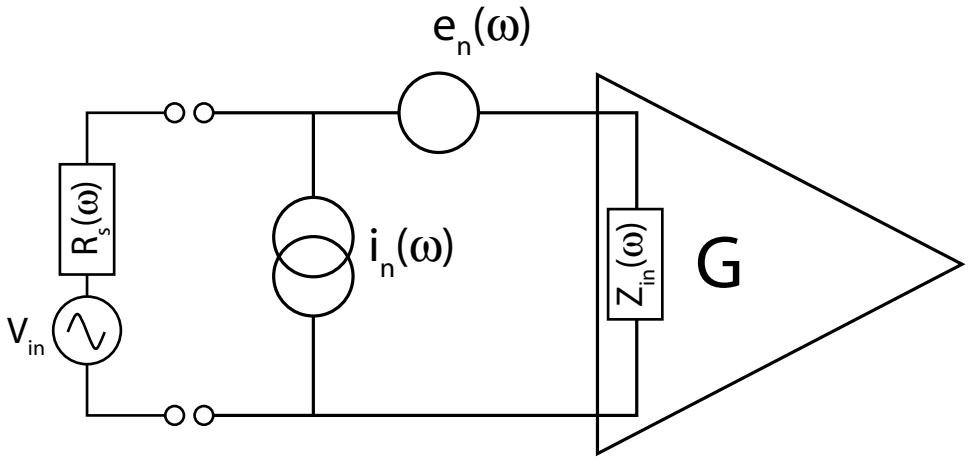

Figure 1.2: Schematic of classical amplifier Showing contributions to total noise. An ideal amplifier with gain G and input impedance $Z_{\text{in}}(\omega)$ amplifies an input signal and contributions from two fictitious noise sources, e_n and i_n. The "voltage noise" e_n can be considered to only add noise to the output of an amplifier, while the "current noise" i_n adds an amount of noise that is dependent on the impedance $R_S(\omega)$ of the object being measured by the amplifier. Noises are typically considered to be dependent on frequency.

the squared magnitude of that signal's fourier transform. It is important to note that we require that the power spectral density contain information about the amplitude content of the signal, but not about the phase; squaring the magnitude of the FFT accomplishes precisely this.

1.2.2 Classical Amplifier Noise

The noise of a classical amplifier is expressed in the language of spectral densities; however, quoting an amplifier's noise only as a single spectral density is an oversimplification. When real amplifiers are measured, the spectral density of their output noise is seen to vary with the impedance on their input. A simple model that accurately captures this variation, however, is shown in figure 1.2. In this representation, the noise of an amplifier is the sum of the effects of two different noise sources, a voltage and a current noise. The voltage noise source, whose spectral density is written either as $e_n(\omega)$ or $S_V(\omega)$, adds noise only to the output of the amplifier, and is completely independent of the system coupled to the amplifier's input. The other noise source, the current noise spectral density, [$i_n(\omega)$ or $S_I(\omega)$] adds noise to the output of the amplifier that is proportional to the parallel combination of the impedances on the amplifier's input. In figure 1.2 both of these noise sources are described as being on the amplifier's input, but in real physical systems they may be anywhere

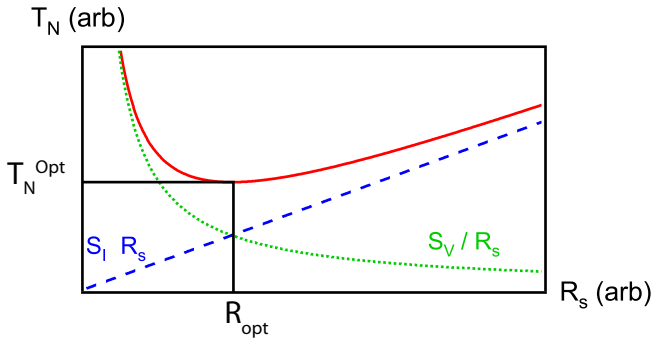

Figure 1.3: Variation of amplifier noise temperature with source impedance R_S. The total noise temperature of an amplifier (solid red line) includes contributions from its current noise (blue dashed line) and its voltage noise (green dotted line). The minimum value of this noise temperature, $T_{N,opt}$, occurs at an optimal source resistance R_{opt}.

within the machinery of the amplifier[1].

The total noise spectral density output by an amplifier is then the sum of the contributions of these two different terms. If the input impedance of the amplifier is large, then this is expressed as:

$$S_{V,\text{out}}(\omega) = G\left[S_V(\omega) + R_S^2 S_I(\omega)\right] \tag{1.2}$$

Alternately, one can divide by the gain and express this quantity as an equivalent noise on the input of the amplifier:

$$S_{V,\text{in}}(\omega) = S_V(\omega) + R_S^2 S_I(\omega) \tag{1.3}$$

Clearly, the minimum signal-to noise ratio achieved by a particular amplifier will occur for some optimum value of R_S that varies with the relative magnitudes of S_V and S_I. A computational tool that is frequently used to calculate this minimum noise is the "noise temperature."

The noise temperature T_N is defined as the temperature of a resistance R_S on the amplifier input with Johnson noise ($= 4k_B T_N R_S$) equal to the input noise of an amplifier. From equation (1.3), this may be simply calculated:

$$T_N = \frac{1}{4k_B}\left[\frac{S_V}{R_S} + S_I R_S\right] \tag{1.4}$$

For a given amplifier, this will vary with the source impedance (see figure 1.3), but will attain a minimum noise temperature T_N^{opt} with a source resistance R_{opt}. These may be trivially calculated

[1] In addition to S_V and S_I, the spectral densities from the autocorrelations functions of the two fictitious noise sources, there may also be a term arising from the correlations of these two sources, usually written S_{IV}. In our experiments, the current and the voltage noise are considered to be uncorrelated, and this term is therefore assumed to be zero.

to be:

$$T_N^{\text{opt}} = \sqrt{S_V S_I}/4k_B \tag{1.5}$$

Attained with a source resistance given by:

$$R_{\text{opt}} = \sqrt{S_V/S_I} \tag{1.6}$$

Amplifier current and voltage noise may also be considered in another context: as related to the sensitivity and backaction of measurements made by a particular amplifier. The voltage noise, first, expresses a limit on the sensitivity of an amplifier's measurement: even if the effects of i_n were entirely discarded (by, for example, a short circuit), the amplifier output will have an uncertainty from e_n. Similarly, i_n can be thought of as expressing an amplifier's backaction: independent of the measured output noise, i_n forces a physical current through a measured system. Considered in this way, these two sources are similar to the quantities Δx and Δp in the "Heisenberg microscope."

As with the Hesisenberg microscope, furthermore, both of these noise sources are required at some level by quantum mechanics (Caves, 1982), and all amplifiers must have at least as much noise as an amplifier operating at the "quantum limit," with ($\sqrt{S_V S_I} = \hbar/2$). In most practical systems, however, measurements are far from this limit, and both the current and the voltage noise are a consequence of some mechanism of the amplifier's operation. Although the SET is capable of approaching this limit (Devoret and Schoelkopf, 2000), the noise of measurements in this thesis was dominated by other effects. Our measurements will therefore not be considered in the context of quantum limited measurement.

1.2.3 Backaction and Sensitivity in Mesoscopic Measurements

In most amplifiers that one would use on a lab bench, the idea of separating current and voltage noise is relevant only as a means to determine an overall noise level. In the most common macroscopic case, the output impedance of the signal source (R_S in figure 1.2) is a real, linear resistance, and any noise driven through it modifies only the system noise. In other words, i_n may add noise to a measurement of the voltage source in figure 1.2, but, if repeated measurements are taken and averaged together, then the result will converge towards the "correct" value of V_{in}.

If R_S is nonlinear, however, the situation is far more complicated. Current noise driven across a nonlinear resistor will produce a voltage signal that does not average to zero, and can alter the ultimate result of an averaged measurement. The current noise, in other words, represents a

physical current passed through R_S, and can change the result of a measurement. This is termed the backaction of an amplifier, because noise properties of the amplifier are causing real physical consequences on the system that is being measured – acting "backwards" to the direction of the normal signal flow in a circuit.

The effects of backaction, however, can range beyond simple distortion of one's measurement: if the system coupled to the input of an amplifier is particularly delicate, then amplifier backaction may even fundamentally alter it's behavior. In the simplest case, a signal source with a small heat capacity may be warmed by the amplifier that measures it. In more complicated systems, backaction can produce a wide range of effects, which may even dominate the dynamics of the measured system. It is the study of such effects in a single mesoscopic system, the RF-SET/Cooper-pair box, that comprises the majority of the work done for this thesis.

As an element of the global dialog on amplifier noise, these results may not have a great deal of consequence: the SET is a very particular amplifier that is used in a comparatively limited number of measurements. However, this work represents an important contribution to the SET community, which illustrates the nature and variety of the possible backaction effects possible with SET measurement. It also contains an excellent illustration of the sorts of tools and formalisms that may be used to anticipate, analyze, and predict backaction in more general mesoscopic systems.

1.3 The SET and the RF-SET

The measurements in this thesis considered the noise and the backaction of the Single Electron Transistor operated as a mesoscopic charge amplifier. The SET was invented in the late 1980s, in metallic systems at Bell Laboratories (Fulton and Dolan, 1987), and in semiconductor systems in the Kastner group (Kastner, 1992). At its heart, it consists of a nanoscale island contacted through two tunnel junctions to two different leads (see figure 1.4); these leads are called the drain and source, by analogy with ordinary transistors. Tunnel junctions are thin insulating barriers sandwiched between larger conductors. An electron fluid cannot flow continuously through the barrier, but individual electrons may still pass through the barrier in discrete tunneling events. A voltage applied across the drain source leads (henceforth V_{DS}) will drive these tunneling events preferentially in one direction, and will cause a measurable current to pass through the SET island; this current is read out as the SET's response.

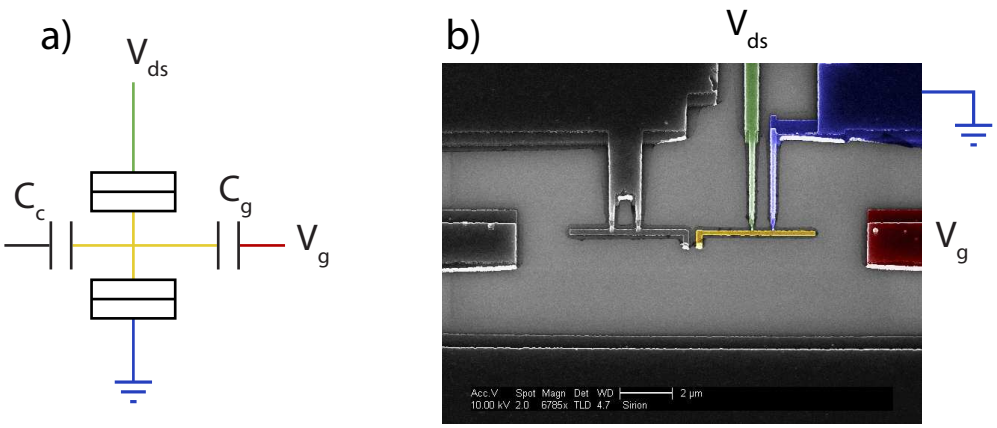

Figure 1.4: a) Circuit diagram for Single Electron Transistor only. Leads are color coded to correspond to the Scanning Electron Microscope image in figure 1.4b. The boxes with horizontal lines in the circuit diagram represent normal-state tunnel junctions. The gate capacitor (C_g) couples the SET island to the externally applied gate voltage V_g, while the coupling capacitor (C_c) provides coupling to the system that the SET is measuring (not shown in this schematic). b) Image of SET sample fabricated at Yale. Artificial coloration demonstrates the correspondence between the SET in this sample and the circuit diagram at left; uncolored elements will be discussed later.

1.3.1 Coulomb Blockade

Amplification of the charge signal on the SET input is achieved through an effect termed "Coulomb blockade." In Coulomb blockade systems, the electrostatic energy increase with the addition of a single electron is so large that it creates an energetic barrier forbidding the addition of further charge to an isolated node (in our system, the "island"). Coulomb blockade systems are usually parameterized by a charging energy, $E_C = e^2/2C_\Sigma$, where C_Σ is the total capacitance of the SET island to all other leads. This charging energy sets the characteristic energy scale for the addition of a single electron to an uncharged island. In order for Coulomb blockade effects to manifest themselves, E_c must be larger than all other relevant energy scales in the problem. Our SET samples, which consist of μm size metallic islands with total capacitances around 0.5 fF, therefore require temperatures below $\sim$ 0.5 K, voltages less than $\sim$ 40 μV, and the elimination of spurious environmental radiation at frequencies above $\sim$ 10 GHz, which might provide energy to excite electrons on to the island.

SET amplification occurs when Coulomb blockade is modulated by a capacitively coupled voltage. In our systems, this can be either an externally applied gating voltage (V_g) coupled through a gate capacitor (C_g), or a voltage from a microelectronic system that is connected to the SET via a coupling capacitance (C_c). C_c and C_g form capacitive voltage dividers with the island's capacitance

to ground, and a simple application of Kirchoff's laws can be used to show that voltages coupled across these capacitors modulate the potential of the island. From the potential of the SET island, we calculate changes in E_{el}, the electrostatic energy cost for the addition of a single electron to the SET island, and electron tunneling rates onto and off of the island. When operated as an amplifier, the SET is tuned in a regime such that the current flowing from the drain lead to the source lead – calculated from tunneling rates on to and off of the SET island – is a sensitive function of the coupled voltages.

Considered by most usual figures of merit, however, the SET is not a very good amplifier. The SET output varies linearly with its input only over an extremely limited range in voltage; even when techniques such as those described in chapter 5 are used to compensate for nonlinearities in the SET's gain, it is still saturated by signals corresponding to $\lesssim 1$ electron of polarization charge on C_c. The voltage gain of the SET is also unremarkable: because C_c and C_g must be small, voltages on the SET's input are not significantly different from the SET output voltage.

The SET is still very useful as an amplifier, however, for one very important reason: the same small capacitance that diminishes the SET's voltage gain presents a very high impedance to any signal source. A delicate microscopic system, with a limited ability to drive current through a measuring apparatus (a high output impedance), can be coupled to the SET without being "short circuited." In addition, the smallness of C_c minimizes the SET's effects on the signal source. For these reasons, the SET has proved very useful for the analog measurement of delicate micro- and mesoscopic systems.

1.3.2 Coulomb Blockade and Band Structure

To quantitatively understand the patterns in SET transport caused by Coulomb blockade, the energetics of island charging must be combined with an understanding of the band structure of the conductors in the SET. Conversely, the subtle differences in the response of different Coulomb blockade systems may be understood only as a product of the states in the conductors comprising the system, and not of any change in the Coulomb blockade physics itself. In this thesis, we consider Coulomb blockade in metallic systems in both the normal and superconducting states. Important results from the study of Coulomb blockade in semiconductors, however, have contributed a great deal to the background of this thesis. Coulomb blockade has also been investigated in other systems – nanotubes, nanoparticles, and organic molecules – but they are not considered here, as they are

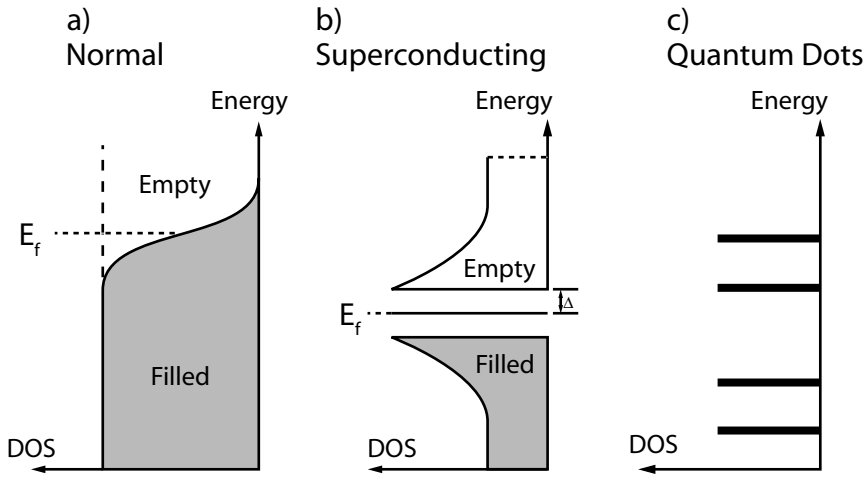

Figure 1.5: Density of states available for tunneling in different Coulomb blockade systems. a) Empty and filled states in a normal metal are determined by Fermi statistics. b) Empty and filled states in a superconductor are understood through BCS theory, and consist of bands of states at an energy $\pm\Delta$ away from the Fermi energy. c) Available states in a quantum dot system are discrete levels that include the charging energy of the quantum dot and the (comparable) energy of different single-electron states.

beyond the scope of this work.

The occupation of states in a normal metal (see figure 1.5a) is described by Fermi statistics, where a continuous density of single electron states that is completely filled until energies approaching E_F, the Fermi energy of the metal. Tunneling into normal metals in Coulomb blockade systems is therefore a threshold process: a tunneling electron must have enough energy to overcome E_{el}, the Coulomb blockade electrostatic energy cost, but electrons with any arbitrary additional amount of energy can tunnel into empty electron states above the Fermi energy.

Our experiments also consider metallic systems in the superconducting state, with a density of states given by BCS theory, illustrated in figure 1.5b. In superconductors, electrons form a condensate of "Cooper pairs," which exist at the Fermi energy of a sample. A Cooper pair can only tunnel between superconductors when, after paying the electrostatic energy cost E_{el}, it can tunnel into the Cooper pair state at the Fermi energy of the target electrode. Tunneling between superconductors also occurs, however, via broken Cooper pairs ("quasiparticles"), which are excitations above the superconducting ground state that require an additional energy Δ, known as the superconducting gap. The combined effects of these two different types of tunneling, at different bias conditions, will give rise to many of the interesting characteristics of the superconducting SET, discussed in detail in section 3.4.

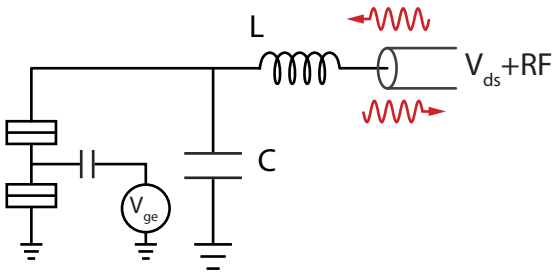

Figure 1.6: Circuit schematic for RF-SET. A lumped-element LC resonant circuit is placed near the SET, and SET response is measured as modulation of the reflected RF power.

Finally, a great deal of related research has considered Coulomb blockade physics in semiconductor systems (Kouwenhoven and Marcus, 1998). These systems, constructed either of "quantum dots" in two dimensional electron gases, or nanoscale heterostructure pillars, can be so small that the level spacing for individual electronic wavefunctions is comparable to E_C, and semiconductor energy spectra (figure 1.5c) therefore consist of discrete energy levels with a generally nonuniform spacing. Semiconductor systems are also notable because their tunnel coupling can be tunable in-situ.

1.3.3 The RF-SET

As originally designed, the SET was a very precise amplifier, but also a very slow one. Drain-source currents flowing in the SET are typically related to applied voltages by effective resistances which are $\gtrsim 100$ kΩ; when measured in a cryostat, with $\sim$ nF of capacitance in the leads, RC times will limit measurement bandwidth to kHz. This is unacceptably slow for many SET applications, and, in particular, this meant that SET measurements were susceptible to low-frequency noise from any of a variety of sources. For this reason, precision measurements in early SET experiments were not possible.

This problem was solved in 1998, however, with the invention of the Radio-Frequency Single Electron Transistor ("RF-SET"), by Rob Schoelkopf and Peter Wahlgren (Schoelkopf et al., 1998). In the RF-SET, a microwave resonant circuit ($f_0 \sim 500$ MHz; design of such circuits is discussed in chapter 5) is placed in close proximity to a SET (see figure 1.6). A microwave carrier signal at the resonant frequency of this circuit is then launched down transmission line leads and reflected from the combination. The output of the SET is inferred from amplitude of the reflected microwave signal.

Wave propagation down transmission line leads effectively "removes" lead capacitance from the

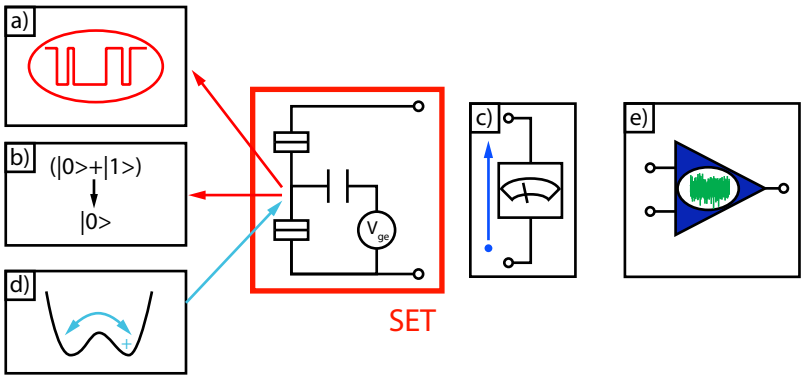

Figure 1.7: Schematic of different noise sources in SET measurements. Charge state fluctuations of the SET island (a) are a necessary consequence of SET operation, and are the primary source of backaction that this thesis discusses. These fluctuations are treated differently in the normal and superconducting states. The operation of the SET may also dephase (b) a superposition of quantum states measured by the SET, although our experiments did not probe this effect. The sensitivity of the SET was limited by the shot noise (c) of the current that is used to read out the SET. Charged fluctuators (d) and other noise sources with a 1/f spectrum couple to the SET input and effectively modulate the gain of the SET. Noise from the following amplifiers (e), finally, adds white noise to the entire measurement.

problem. The bandwidth of the RF-SET, therefore, is limited only by the SET's resistance and the capacitance local to a SET device; bandwidths of $\geq$ 100MHz have been measured (Schoelkopf et al., 1998), and higher bandwidths are theoretically possible.

The increased bandwidth afforded by the RF-SET allowed, indirectly, for the field of ultrafast SET measurements: because SET data could now be captured many orders of magnitude faster than the characteristic timescale of slow gain variations in the SET, those gain variations could now be identified and removed.

1.4 Noise Processes in SET measurements

There are many different noise processes at work in an operating RF-SET; at its heart, this thesis describes attempts to measure and separate their effects. The characteristic timescales of these processes lie throughout an enormous range, from much slower than RF-SET measurement to much faster than the RF-SET could hope to observe. In this section, I will briefly describe the sources and phenomenologies of the major types of noise present in a SET measurement, which are diagrammatically represented in figure 1.7.

These noise sources may be loosely separated into categories motivated by the current noise/voltage noise discussion of section 1.2.2: Noise sources may either appear on the input of an amplifier, where

they comprise the amplifier's backaction, or on the output of the amplifier, where they affect the amplifier's sensitivity. In addition to these two types of noise, however, there was a third type of noise in our experiments, which I will call "technical noise" – noise that was not intrinsic to the SET's operation, but which was nevertheless capable of disturbing the SET's measurement.

1.4.1 Backaction: SET Island Charge State Fluctuations

Classical amplifier backaction consists of a noisy current signal i_n which is forced through the impedance of a measured system. Charge on the SET island, capacitively coupled to the system that the SET measures, imposes exactly such a signal [box (a) in figure 1.7]. As electrons tunnel on and off of the SET island, the charge state of the SET island will switch, typically between two states, in a random telegraph noise pattern. These charge state fluctuations cause the current noise of the SET. Their nature and variation will be analyzed in detail in chapter 2.

The timescale of these fluctuations is typically very fast; in regimes where the SET is useful as an amplifier it is never less than GHz. It is worth noting that the current in the SET is effectively a long-time average of the tunneling rates, and so we cannot expect to be able to measure SET tunneling in real time using a SET. However, several time-averaged properties of this noise have effects that do not need to be observed at high frequencies. These effects are investigated and discussed at length in chapter 6.

1.4.2 Backaction: Superconducting State Island Charge Fluctuations

In the superconducting state, the potential of the SET island capacitively couples to the Cooper pair box, and causes backaction in the same way as the charge state fluctuations in the normal state. Because of the superconductivity in the box and SET islands, however, this noise must be treated in a very different theoretical framework. In chapter 3, I will discuss how the quantum mechanical coherence of the Cooper pair box motivates a quantum treatment of the effects of SET noise, and how the SET can be operated to produce noise with striking nonclassical effects.

1.4.3 Backaction: Dephasing

In the study of measurements of quantum two level systems, an important concept is that of the dephasing of a quantum state by a measurement. Analyses that discuss dephasing treat the phase of a superposition of states in a quantum two-level system as a variable conjugate to the state of that

system. According to this scheme, a measurement of a qubit charge state will necessarily disturb the phase of a superposition of such states [box (b) in figure 1.7].

Dephasing from SET measurement, however, was not visible in our experiments. In the superconducting state, when the SET was measuring a system that could maintain quantum coherence, other forms of SET backaction – particularly, noise from the potential on the SET island – dominated the box's response, and obscured any direct observation of dephasing effects.

1.4.4 Sensitivity limitation: Shot Noise on SET Output

The ultimate limit on the sensitivity of a SET measurement is a consequence of the nature of charge transport in a SET: because SET current flows through discrete tunneling events, any current that serves as a SET readout will necessarily have shot noise [box (c) in figure 1.7]. This shot noise imposes the ultimate physical limit on the sensitivity of a SET measurement (Devoret and Schoelkopf, 2000). Measurements in our system, however, were not sensitive to effects on this level: noise at the level of the intrinsic sensitivity of the SET was overwhelmed by the noise of the following amplifiers.

1.4.5 Technical Noise: 1/f Noise on SET Input

Noise with a spectral density that varies as f^{-1} appears in many strange places in nature. Unfortunately, the SET is one such place: so-called 1/f, or "pink" noise has been found to be ubiquitous in SET measurements, and poses one of the strictest limitations on SET measurement. 1/f noise is problematic for an experiment because it cannot be averaged to zero. An experiment that experiences noise with a spectral density that is uniform in frequency may be repeated and averaged: the resultant value will converge towards the "true" value of the measurement. Noise with a 1/f spectrum, however, is not nearly so well-behaved. A 1/f spectrum suggests that the longer you wait, the larger the fluctuations in one's averaged measurement will be. Repeated averaged measurements, therefore, do not converge to a single value.

1/f noise in the SET can come from a variety of sources, and it is generally difficult to separate out the different contributions. One particular source of such noise, however, that is clearly present in our measurements is the fluctuation of charged impurities close to the SET island [box (d) in figure 1.7].

Colloquially called "charge offset noise", "two-level fluctuators", or any of a variety of cursewords, telegraph fluctuations of charge coupled to the SET island are one of the most important problems

confronting SET measurement. Such signals are thought to be charged impurities in close proximity to the SET island which can physically move between two lattice sites near the SET. Because these fluctuators are moving charge closer to and further from the SET island, they couple polarization charge to the SET island, and cause a random signal on the SET input.

A pure random telegraph signal with a characteristic switching time τ has a power spectrum that is flat up to the corresponding characteristic frequency $1/(2\pi\tau)$, above which the power spectrum rolls off as $1/f^2$. An ensemble of such switchers, however, with the correct distribution of relaxation times and amplitudes, can collectively produce noise with a 1/f spectrum. This behavior is reasonably generic, and has been noted in a variety of condensed matter systems (Van der Ziel, 1979); theorists have attempted to explain it with a wide variety of theoretical models (Weissman, 1988). Other quantum computing groups have even claimed to have seen the signature of a coupling between such two-level fluctuators and their qubits (Cooper et al., 2004)(Simmonds et al., 2004), and claim that these effects can be reduced by careful control of the fabrication of Josephson junction barriers (Martinis et al., 2005).

In measurements with the SET, it is not uncommon to find that a single two-level fluctuator is particularly strongly coupled to the SET island, with an ability to couple a telegraph signal of 3-10% of an electron, or more, of polarization charge. Such a fluctuator can render a SET measurement impossible, as the SET gain will certainly vary, and may even vanish with this amount of additional gate charge. An important component of the work done for this thesis, discussed in Section 5.7, involves properly designing software to track and remove the effects of this charge offset noise. In Section 8.2, also, I discuss measurements of this noise for its own sake, and our attempts to create an understanding of this noise that could confirm or disprove various mechanisms of its operation.

1.4.6 Technical Noise: Following Amplifiers

A final form of noise that was present in our systems was entirely independent of the SET: noise from the postamplifiers [box (e) in figure 1.7] appeared in addition to all of the noises intrinsic or local to the SET. This noise can be understood in the sense of a classical noise described in section 1.2.2; in our experiments, it was little more than a nuisance. This noise did not act back on our measurement, had a white spectrum, and could be averaged away. Low noise HEMT amplifiers, built by the National Radio Astronomy Observatory (NRAO) were used to provide an impressively low system noise temperature of $\approx$ 5K. Nevertheless, this noise still provided the dominant contribution

to the uncertainty of our measurements. Future experiments have been proposed that use lower-noise SQUID postamplifiers to lessen this effect, but such experiments are not discussed in this thesis. Because following amplifier noise is not an intrinsic effect, it will not be treated in this thesis.

1.5 Overview of Thesis

The measurements performed for this thesis span a wide range of topics that could easily have been considered independently. Measurements performed in the Normal and Superconducting state used the same apparatus and the same device, but were radically different in the nature of the effects seen and the formalisms that were used to treat the effects. Nevertheless, analogous portions of the two measurements will be treated together; thus I will discuss both superconducting and normal theory before I discuss any experiment.

The first part of this thesis treats the theory of the SET and box operation. Chapter 2 discusses this in the normal state; chapter 3 discusses this in the more complicated superconducting state.

The next part of the thesis discusses the practical matters important to the implementation of these measurements. In chapter 4, I speak about the fabrication and design of the samples measured. In chapter 5, I speak about the equipment and setup used to measure our samples.

The remainder of the thesis explains and interprets the measurements that were made. In chapter 6, I discuss the measurement of backaction in the normal state. In chapter 7.8, I discuss the backaction measured in the superconducting state. Preparation for the superconducting state measurements involved a few side investigations which broadened our understanding of the SET; these discussions are contained in chapter 8. Finally, in chapter 9.3, I summarize the work and discuss the conclusions that I have drawn.

Chapter 2

Single Electron Systems in the Normal State

2.1 Introduction

The Single Electron Transistor can be treated theoretically far more simply in the normal state than in the superconducting state; in this regime, charge transport occurs through single electron tunneling events, whose rates are simple functions of the temperature and the energy gained or lost when an electron tunnels. To model the response of the Single Electron Transistor, we consider an ensemble of such rates, connecting different charge states on the SET and box island. From the tunneling rates into and out of each SET charge state we can infer the time-averaged occupation of that charge state, and from this, the measured behavior of the Single Electron Transistor and the Single Electron Box. This remarkably simple model, usually referred to as the "sequential tunneling model," "orthodox theory," or the "global rule" can account for all of the backaction effects seen in our normal state observations of the Single Electron Transistor.

In this chapter, I will build a detailed understanding of the mechanics of the model used to understand and predict backaction in our SET-Box system when operated in the normal state. I will begin by describing the calculation of the single electron tunneling rates which are used in the sequential tunneling model. In section 2.3, I will describe the setup of a master equation to model the Single Electron Box. In Section 2.5, I will describe how these ideas are adapted to the modeling of the response of the Single Electron Transistor, and then, in section 2.6 I will describe how the full-box SET system is modeled and how effects are measured. Finally, in section 2.7, I will discuss higher-order tunneling processes, and the effects that these cause in box and SET measurements.

2.2 Single Electron Tunneling Rates

2.2.1 Fermi's Golden Rule

The tunneling rates used in the sequential tunneling model to reproduce the behavior of the SET and the box follow quite simply from Fermi's golden rule. To build an understanding of the sequential tunneling model, therefore, I will start by developing an understanding of single electron tunneling in an isolated tunnel junction. In section 2.2.2, I will discuss the modifications that are made to this calculation in situations where Coulomb blockade can modify tunneling rates.

We will consider charge transport to occur only through sequential tunneling of single electrons, corresponding to the inclusion of only first-order terms in the perturbative calculation of tunneling rates. This is somewhat of an oversimplification of the problem: higher-order tunneling processes, usually referred to as "cotunneling", are known to occur in our system in both the SET and the Single Electron Box, and cause a variety of different effects. The relative magnitude of these higher order effects, however, diminishes in proportion to the dimensionless conductance of the junction, g. This conductance is usually written in dimensionless form as:

$$g = \frac{e^2}{hR_T} \tag{2.1}$$

where R_T is the normal state resistance of a tunnel junction. The small parameter for the perturbative expansion of higher order tunneling effects is simply expressed as:

$$\frac{g}{4\pi^2} = \frac{R_K}{4\pi^2 R_T} \tag{2.2}$$

where $R_K = e^2/h$ is the inverse of the so-called conductance quantum. For the SET and box samples used for measurements in the normal state, this expansion parameter was small (typically $g/4\pi^2 \sim 0.05$ for both the box and SET), and our model was able to recreate the behavior of the box and the SET without taking higher order effects into account. A more detailed discussion of the consequences and measurement of cotunneling effects in the normal state will be undertaken in Section 2.7.

Single electron tunneling rates in the normal state are found through simple application of Fermi's Golden Rule. From (Sakurai, 1994), we have Fermi's Golden Rule as:

$$w_{i\to n} = \left(\frac{2\pi}{\hbar}\right) |\langle n|V|i\rangle|^2 \, \delta(E_n - E_i) \tag{2.3}$$

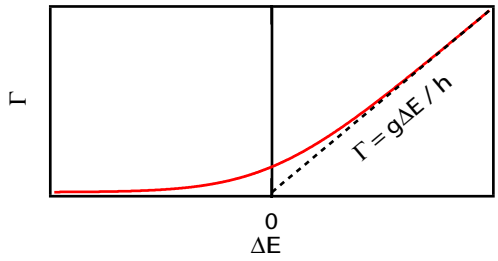

Figure 2.1: Single electron tunneling rate for a tunnel junction as a function of the imposed energy difference ΔE. At negative ΔE, only thermally excited electrons may tunnel, and the tunneling rate exponentially falls as ΔE decreases. At positive ΔE, the tunneling rate asymptotically approaches the zero-temperature result, which predicts a tunneling rate that is linear in the energy difference.

This is understood to mean that the transition rate for tunneling from an initial state $|i\rangle$ to some final state $|n\rangle$ is proportional to the square of the matrix element for that process ($|\langle n|V|i\rangle|^2$). The net transition rate out of some state, then, can be found by integrating this single-transition rate over all final states weighted by $\rho(E)$, the density of such states available to a tunneling electron.

For the case of single electron tunneling, the calculation of these rates is particularly simple. The matrix element in the above equation, which describes the strength of the coupling between the two metallic leads introduced by the tunnel junction, is simply determined by the thickness and the area of the tunnel junction; numerically, it is expressed as the junction's conductance.

The density of available states for a tunneling process can be calculated from the Fermi occupations of the two metallic leads. This calculation is performed in detail in Chapter 2 of (Grabert and Devoret, 1992); we report only the result. Assuming that the density of states (including both filled and empty states) in the two metals does not vary with energy, the total rate at which electrons tunnel (which is proportional to the current flowing between the two conductors) is found to be:

$$\Gamma = \frac{g}{h}\left(\frac{\Delta E}{1 - e^{-\Delta E/k_B T}}\right) \tag{2.4}$$

This equation describes the rate at which electrons tunnel from one side of a tunnel junction to the other, as a function of the energetic difference (ΔE) between the two leads. In the simplest case, ΔE may be imposed by an external voltage source, as in a purely DC voltage-biased junction. However, when considering multi-junction circuits, where the tunneling of a single electron requires energy to charge the capacitance of an isolated island, ΔE also accounts for the energy that a tunneling electron loses or gains to the charging of those capacitances.

A plot of this rate as a function of ΔE is shown in Figure 2.1. A tunneling rate calculated

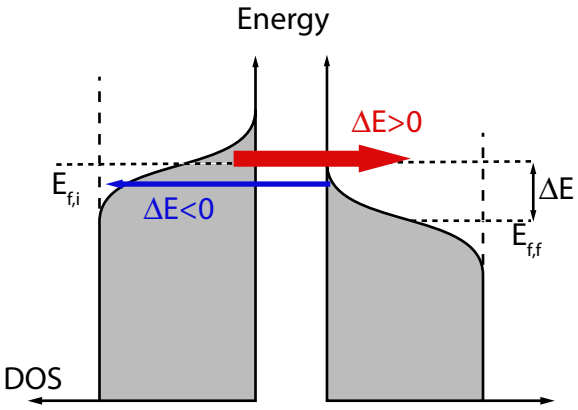

Figure 2.2: Tunneling between two normal metal leads with an energetic difference between the fermi levels. Electrons in filled states in the left reservoir find more empty states in the right reservoir with increasing ΔE, and the rate of left-to-right tunneling therefore increases as ΔE is increased. Only electrons above the fermi energy in the right lead can find empty states to tunnel into at the same energy in the left reservoir, and the right-to-left tunneling rate is therefore exponentially suppressed as $\Delta E/k_B T$.

with a positive ΔE may be considered to describe an energetically favored process, where electrons tunneling from the Fermi energy of an initial lead would tunnel into states above the Fermi energy of the target lead. An example of such a tunneling process is illustrated by the red arrow in figure 2.2. Tunneling occurs when an electron in a filled state on the left reservoir is coupled to an empty state on the right reservoir; clearly, the number of such possible couplings (and, therefore, the rate of single electron tunneling) increases rapidly with ΔE. Asymptotically, this tunneling rate will tend towards $g\Delta E/h$ (see figure 2.1), the forward tunneling rate that one might infer from a linear I-V characteristic.

A tunneling rate calculated with a negative value of ΔE is comprised of tunneling events that are represented by the blue arrow in figure 2.2. These correspond to tunneling events where an electron tunneling from the Fermi energy of an initial reservoir would tunnel into a state below the Fermi energy of the target reservoir. Tunneling events contributing to this tunneling rate therefore come predominantly from the tail of the Fermi function, and, as ΔE becomes more negative, become exponentially small (see figure 2.1).

2.2.2 Energy Difference for Single Electron Tunneling

At a fixed temperature, the single electron tunneling rates described above are a function of a single parameter: the energy difference ΔE for a tunneling event. For the example of a voltage-biased

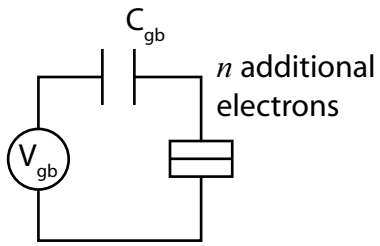

Figure 2.3: Circuit diagram for the Single Electron Box. The box gate voltage, V_{gb} is coupled to the box island via the box gate capacitor, which is referred to as C_{gb}.

junction discussed above this ΔE can be directly imposed with an external voltage bias, and will accurately predict the linear current-voltage characteristic that is experimentally measured.

When small tunnel junctions are fabricated with isolated islands, however, calculation of the ΔE for a single electron tunneling event becomes more complicated, and gives rise to an array of interesting physical consequences. In these situations, an electron tunneling on to an isolated island stores energy electrostatically in the capacitance of the island which can be comparable to, or greater than, the available thermal energy $k_B T$. This electrostatic energy increase, which increases with the square of the charge on an isolated island, adds an additional term to the externally imposed energy difference, and can cause ΔE to change from positive (suggesting energetically favored tunneling) to negative (indicating energetically inhibited tunneling) with the addition of one, or a few electrons. Phenomena that are a consequence of this effect are described with the term Coulomb blockade, because the Coulombic charging energy of a nanoelectronic island has blocked the addition of further charge to that island.

A precise determination of the ΔE for a tunneling process can be somewhat nontrivial; as an electron tunnels, one must account for the energy gained or lost from both externally applied voltages and electrostatically stored energy. In multi-junction circuits, an understanding of where energy is gained or lost from an externally applied voltage is sometimes tricky to calculate, and must be carefully attended to. In this thesis, I will report and interpret, but not derive, expressions for the tunneling energy in both the Single Electron Box and the SET; the precise derivation of these expressions may be found in (Grabert and Devoret, 1992) or in (Lafarge, 1993). One may also find a more general treatment of this problem in Chapter 7 of (Tinkham, 1996).

The single electron box is the simplest circuit where our sequential tunneling model may be used to analyze Coulomb blockade effects. A circuit diagram of the Single Electron Box is shown in figure

2.3; it consists of an isolated metallic island that is capacitively gated by an external voltage. The only control parameter that may be varied is the voltage capacitively coupled to the box. This box gate voltage is shown on the above diagram as V_{gb}, but may also include contributions from charged fluctuators in the substrate (see Section 1.4.5) and coupling to other nanoelectronic devices (i.e. the backaction of the SET). The only degree of freedom of the box, meanwhile, is the number of additional electrons on the box island, usually indicated as n. It is worth noting that the conduction band of the metallic island does not contain only n electrons – there are billions, or more, aluminum atoms in the metallic island, each of which has a positively charged nucleus and a corresponding number of electrons. However, because each aluminum atom contributes no net charge to the island, these charges do not charge the capacitors, and are irrelevant to our discussion of the energetics of the single electron box; we only concern ourselves with the few additional electrons that tunnel onto the island.

The energy of the box, as a function of the box gate voltage, V_{gb} and the number of additional electrons on the island n, is expressed as:

$$E = \frac{1}{2C_\Sigma}(C_{gb}V_{gb} + ne)^2 + \frac{1}{2}C_{gb}(1 - 2C_{gb}/C_\Sigma)V_{gb}^2 \tag{2.5}$$

The second term in this expression is frequently omitted, as we are interested in the relative energies of different charge states on the box island, and this term does not vary with the charge state n of the island. Practically, we may consider it to describe the work done by the gate voltage V_{gb} in placing polarization charge on the gate capacitor. This is, again, independent of the charge state of the box island, and irrelevant for the calculations that follow.

For simplicity, and in anticipation of the known physical result, we also express the gate voltage V_{gb}, in dimensionless units of electrons of polarization charge on the box gate capacitor, $n_{gb} = C_{gb}V_{gb}/e$. Note that n_{gb} represents a polarization charge, which can take a continuum of values, while the charge on the island (n) is still constrained to integer values.

The energy of the single electron box thus becomes:

$$E = \frac{e^2}{2C_\Sigma}(n_{gb} + n)^2 \tag{2.6}$$

This may be interpreted as follows: for any fixed number of additional electrons on the box island, the electrostatic energy is parabolic in the applied gate charge (as we expect it to be, as

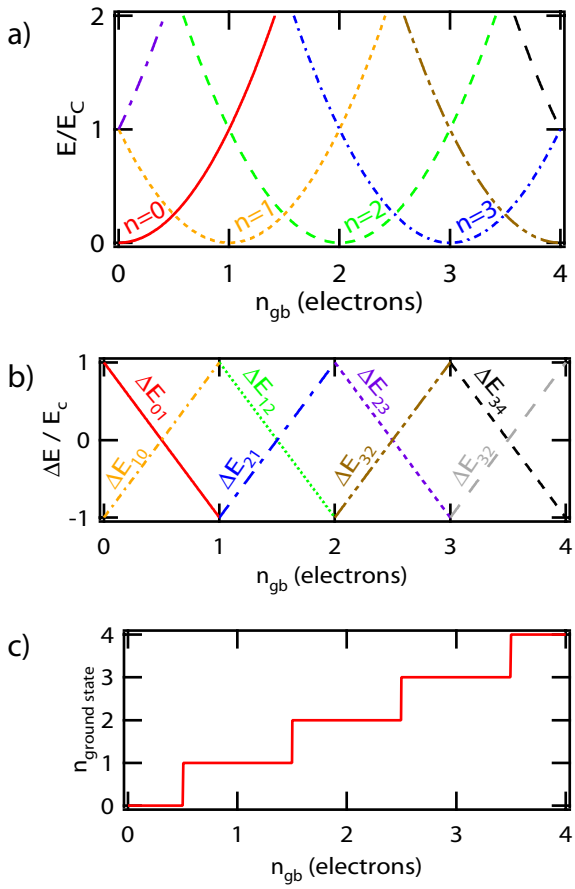

Figure 2.4: a) Energy of the Single electron box. For a fixed number n of additional electrons on the box island, the electrostatic energy is parabolic in the applied gate voltage. b) Energy difference between box charge states differing by one electron, used to determine box tunneling rates. c) charge of the energetic ground state of the box island, plotted as a function of box gate charge n_{gb}. As the gate voltage is increased, the charge state of minimum energy changes.

it consists of two capacitors placed in series and voltage biased; see figure 2.4). For clarity, the quantity $\frac{e^2}{2C_\Sigma}$ is often written as E_c, and referred to as the charging energy; it represents the energy that would be required to add a single electron to the island in the absence of any gate voltage, and provides a convenient energy scale for many calculations we perform.

If an additional electron is added to the island, the energy remains parabolic in the applied gate charge, but the energetic minimum of that parabola occurs at a different value of n_{gb} (see figure 2.4). The difference in the energy of two charge states differing by one electron, which is used for the ΔE that determines tunneling rates on to and off of the island, thus varies linearly with n_{gb}, vanishing at half-integer values of n_{gb}.

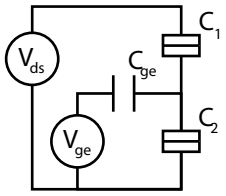

Figure 2.5: Circuit diagram of the Single Electron Transistor. An isolated island is contacted to two external leads (the Drain and the Source) through two different tunnel junctions. A voltage applied across the drain-source leads can give a directionality to the current flowing, which varies dramatically with V_{ge}, the SET gate voltage.

The single electron transistor is formed by adding another junction and another voltage (the drain-source voltage, V_{ds}) to the above circuit (see figure 2.5). At $V_{ds} = 0$ this circuit is similar to the single electron box, and the charge state of the SET island changes with gate voltage exactly as the single electron box would. However, because the two junctions couple the SET island to different reservoirs, we may now think of a measurable current that passes through the SET island (and a voltage that drives it), leading to more complicated and interesting behavior in the SET. In all further discussions of the single electron transistor, in both the normal and the superconducting state, the symbol V_{ge} will be used to refer to the SET gate voltage (Voltage on the Gate of the Electrometer), to differentiate it from V_{gb}, the box gate voltage. This terminology was used because it was deemed to provide the best differentiation from V_{ds} and V_{gb}, the other control voltages in the system.

In the SET, the energy ΔE for single electron tunneling events on to and off of the island can be summarized as:

$$\begin{aligned} \Delta E_1^{\pm} &= -\frac{e^2}{C_\Sigma}\left\{\left[\tfrac{1}{2} \pm (n - n_{ge})\right] \pm \tfrac{C_2 V_{ds}}{e}\right\} \\ \Delta E_2^{\pm} &= -\frac{e^2}{C_\Sigma}\left\{\left[\tfrac{1}{2} \pm (n - n_{ge})\right] \mp \tfrac{C_1 V_{ds}}{e}\right\} \end{aligned} \tag{2.7}$$

Where the subscript 1 (2) suggests tunneling across the top (bottom) junction, and the plus(minus) indicates whether an electron is tunneling onto the island or off of it.

As we expect, at $V_{ds} = 0$ this expression reduces to the difference of parabolas that can be inferred from equation 2.6, but for finite V_{ds} an increased rate for electrons to tunnel on to the island through one junction and off through the other can lead to a measurable current passing through the Single Electron transistor. Because these rates vary with the gate voltage (see equation 2.7), the current through the SET is a sensitive function of the polarization charge capacitively

coupled to the SET island; this is the effect that we will use for SET measurement.

2.3 The Sequential Tunneling Model

The full phenomenology of both the SET and the single electron box is reproduced by considering the combined effects of all of the different rates for electrons to tunnel on to and off of the SET/box island. In practice, this is done through a standard formalism that is mathematically referred to as a "master equation" treatment of the problem. When applied to transitions between discrete charge states, this is referred to as "orthodox theory" or a "sequential tunneling model." In this section, I will build an understanding of the construction of such a model as it might be undertaken by an experimental physicist.

A sequential tunneling model recreates the phenomenology of a single-electron system by finding a mixture of charge states whose relative proportions are preserved by the combined effects of all tunneling processes – in effect, a steady-state solution to the system of coupled rates. The relative proportions of different charge states in this mixture are then identified with the occupation probabilities of the represented charge states. This somewhat abstract prescription may be seen as a generalization of a more obvious principle: if a two-level system (with states A and B) has an equal probability, per unit time, to tunnel from A to B and from B to A, then we expect that the long-time-averaged behavior of that system will tend to show the system 50% of the time in state A, and 50% of the time in state B; if one of these transition rates increases relative to the other, then we expect that this will be reflected in a correspondingly larger population in the target state of the increased rate. This is typically referred to as "detailed balance." A sequential tunneling model accounts for these effects with an arbitrarily large number of charge states.

We calculate this rigorously by considering an ensemble of systems occupying various charge states; let the population in each charge state be P_i. If the rate for charge state i to transition into charge state j is $\Gamma_{i\to j}$, then the rate of change of the population in a given charge state may be expressed as:

$$\frac{d}{dt}P_i = \sum_{i\neq j}\Gamma_{j\to i}P_j - \sum_{i\neq j}\Gamma_{i\to j}P_i \tag{2.8}$$

which is the difference between the transition rate into state i [represented by the first term in (2.8)] and the total transition rate out of that state (which is expressed in the second term).

The system of transition rates between all available charge states may therefore be represented as a system of linear equations, which we express in matrix form:

$$\frac{d}{dt}\vec{P} = \mathbf{M}\vec{P} \tag{2.9}$$

$$M_{ij} = (1 - \delta_{ij})\,\Gamma_{j\to i} - \sum_{k\neq i} \delta_{ij}\Gamma_{i\to k} \tag{2.10}$$

Where the matrix $\mathbf{M}$, the transition rate matrix, is seen to calculate the time evolution of an ensemble containing a mixture of states.

The steady-state solution $\vec{P}_{ss}$ to this system of equations corresponds to the occupation probability distribution that is unchanged by the combined effects of the possible transitions, i.e.:

$$\mathbf{M}\vec{P}_{ss} = \frac{d}{dt}\vec{P}_{ss} = 0 \tag{2.11}$$

It is clear that this steady state solution is simply an eigenvector of the transition rate matrix $\mathbf{M}$ with eigenvalue zero.

Because single electron tunneling is an ergodic process, we may identify the steady-state population of each charge state in an ensemble of such systems with the time-averaged occupation probability of the corresponding charge state in a single system governed by the same transition rates. In other words, the solution to the above equations – which was derived by considering the evolution of an ensemble of systems – also gives the state occupation probability distribution for a single system governed by the same rates.

Our determination of the charge state of the system therefore becomes simple: given a particular nanoelectronic system, with known bias voltages, we choose a set of charge states that the system might potentially occupy, and calculate all transition rates between these charge states. We then use these rates to construct a matrix, and find the zero eigenvector of that matrix. The components of this vector represent the probability of occupation of the corresponding charge state.

2.4 Theory of the Single Electron Box in the Normal State

A trivial application of this technique is seen in the modeling of the response of the Single Electron Box. We will consider, for simplicity, only two charge states of the box (which will have 0 and 1 additional electrons on the box island). We will also only consider values of the gate voltage for which between 0 and 1 electrons of polarization charge are used to gate the box island; if our model is

restricted to these gate voltages and to comparatively low temperatures, then it may be reasonably assumed that only two charge states of the box have any significant probability to be populated.

In this model, the energy may be taken from equation (2.6); the difference in the energy between the ground and excited state is therefore:

$$\Delta E_{01} = E_C(1 - 2n_{gb}) \tag{2.12}$$

$$\Delta E_{10} = -E_C(1 - 2n_{gb}) = -E_{01} \tag{2.13}$$

The matrix describing the rates for our master equation is therefore:

$$M = \begin{pmatrix} -\Gamma(E_{01}) & \Gamma(-E_{01}) \\ \Gamma(E_{01}) & -\Gamma(-E_{01}) \end{pmatrix} \tag{2.14}$$

where Γ is the rate for single electron tunneling, which we know from equation (2.4):

$$\Gamma = \frac{g}{h}\left(\frac{\Delta E}{1 - e^{-\Delta E/k_B T}}\right) \tag{2.15}$$

Combining equations 2.14, 2.12, and 2.15, and calculating the null space of the resulting matrix, we find the vector:

$$\begin{pmatrix} e^{2E_c(n_{gb}-\frac{1}{2})} \\ 1 \end{pmatrix} \tag{2.16}$$

The relative magnitude of the two elements of this vector tells us the relative probability of occupation of the two different charge states of our box; we can divide these probabilities of occupation by their sum to find a "normalized" vector, which expresses the absolute probability of occupying each charge state:

$$\begin{pmatrix} \dfrac{e^{E_{01}/2k_BT}}{e^{E_{01}/2k_BT} + e^{-E_{01}/2k_BT}} \\ \dfrac{e^{-E_{01}/2k_BT}}{e^{-E_{01}/2k_BT} + e^{-E_{01}/2k_BT}} \end{pmatrix} \tag{2.17}$$

It is worth noting that this equation describes the relative weights of the two charge states of the box as given, simply, by their Boltzmann weights, precisely as one might expect.

The average charge measured on the box will then be an average of the two charge states ($n = 0$ and 1 electrons) weighted by the occupation probabilities in equation (2.17). After a small amount of algebra, we find that this yields:

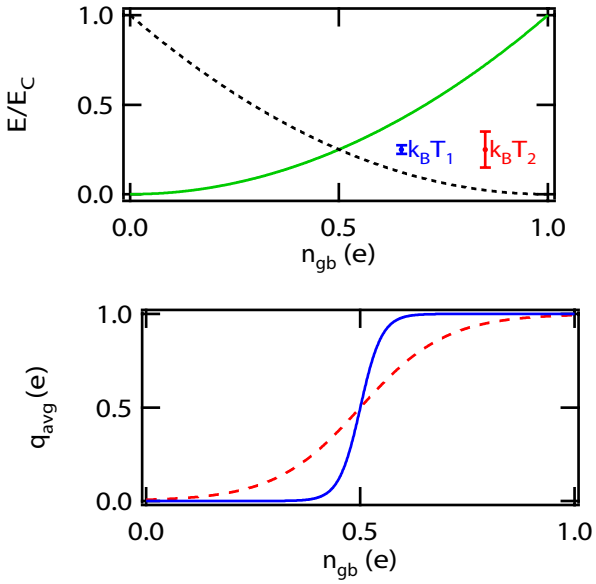

Figure 2.6: a) Parabolic energy bands for single electron box in the states with 0 (green) and 1 (black dotted) additional electrons on the island. b) Coulomb staircases calculated using the sequential tunneling model at a temperatures indicated by bars in part (a)

$$\bar{n} = \frac{1}{2}\left\{\tanh\left[\frac{E_c}{k_B T}(n_{gb} - \frac{1}{2})\right] + 1\right\} \tag{2.18}$$

If more charge states are considered, then the sequential tunneling model still yields a Boltzmann weighted average of the available charge states, but the expression of the averaged charge on the box is not nearly as simple as equation (2.18).

This time-averaged box charge is plotted as a function of the box gate in figure 2.6b. This plot is usually referred to as the "Coulomb Staircase." For values of the gate charge where the energetic differences between adjacent charge states is large (see figure 2.4), the Coulomb staircase indicates that repeated measurements of the charge state of the box island nearly always yield the energetically favorable ground state. However, at values of n_g where the energy difference between two adjacent charge states is comparable to or smaller than $k_B T$, the average charge measured on the box will be somewhere between the two charge states, indicating that both charge states are occupied some fraction of the time. When exactly half an electron of polarization charge is applied to the box, we say that the box is at electrostatic degeneracy, or simply at "degeneracy". In this case, we are equally likely to measure 0 or 1 additional electrons on the box, and the time-averaged charge is therefore $\frac{1}{2}$. Finally, once the gate voltage is swept well past the degeneracy point, the charge state

on the box island will once again strongly prefer a single charge state – now, however, with a single additional electron on the box island.

The majority of the measurements performed for this thesis consist of Coulomb Staircases, measured with the Single Electron Transistor. Considered theoretically as above, these staircases are very simple: for a given sample with a fixed E_c, a Coulomb staircase may vary only in the width of the transition between charge states, which is a function only of the temperature of the electron reservoirs.

Alternately, this relationship may be inverted, and the width of the transition between charge states in a Coulomb staircase may be taken as a measure of the "temperature" of the Coulomb staircase. For the purposes of our measurements, we quantify the width of the transition between charge states by considering the maximum slope of the Coulomb staircase; this may be found quite simply from the derivative of the function for the simply thermally broadened Coulomb staircase:

$$\frac{d\bar{n}}{dn_g} = \frac{1}{2}\mathrm{sech}^2\left(\frac{\mathrm{E_c}}{\mathrm{k_B T}}(\mathrm{n_{gb}} - \frac{1}{2})\right) \tag{2.19}$$

This attains a maximum value at $n_g = \frac{1}{2}$, where it has a value of $E_c/(2k_BT)$.

As we will see in later chapters, however, this simple model of a thermally broadened staircase is not sufficient. There are many subtle variations that add to and modify this simple functional form. This thesis is primarily concerned with the backaction of the SET, which is one such effect; to build an understanding of how the backaction effects the Single Electron Box, I will next describe our theoretical understanding of the operation of the SET.

2.5 Theory of the SET in the Normal State

A full theoretical treatment of the operation of the SET does not yield the same simple, closed form solution that we saw for the single electron box in equation (2.18), and the actual mechanics of the calculation of SET charge state occupancy is therefore somewhat less illuminating. For this reason, I will not work through a calculation of the stationary state of the SET in the same fashion that I did for the single electron box. Construction of a model to do so, however, proceeds from equation (2.7) in exactly the same fashion as an analysis of the single electron box proceeded from equation (2.6), and can be solved using the same computational techniques.

When the SET is used to measure an electrical signal, we do not read the measurement out by

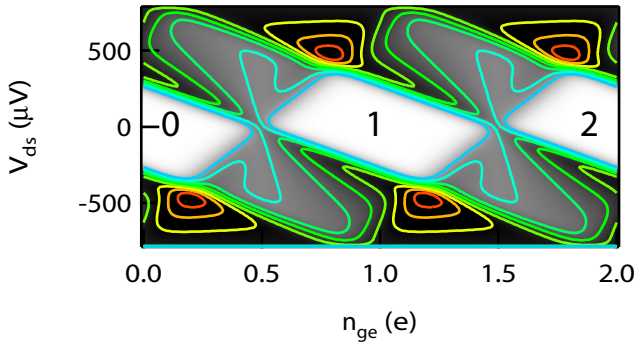

Figure 2.7: Theoretical prediction of the conductance of the normal-state SET. Smaller conductance is shown in white; larger conductance is shown in black; contours show lines of constant conductance. Black numerals identify combinations of gate and drain-source voltage where the SET island is blockaded in a particular charge state, and identify that state. This plot is typically referred to as a SET charging diamond, or, simply, "diamond."

observing the mean charge on the SET island, but rather by measuring the macroscopic current that flows between the drain and the source lead of the SET. This current, however, may be simply found within the framework of the existing model that we have outlined: it is simply the product of the tunneling rate off of the SET island and the occupation probability of the SET island. This may be intuitively grasped through a simple example: If the SET island is in the "0" charge state half of the time, and the "1" charge state half of the time, and charge may only leave through one junction, then the rate at which current flows through the SET is exactly half of the tunneling rate for charge leaving the island; the actual current rates through the SET, although more complicated and arising from more charge states, are calculated in exactly the same spirit. Finally, the data are differentiated with respect to V_{ds} to yield a plot of SET conductance, which may be more directly compared to the experimentally measured results.

The response of the SET, as a function of the two control voltages, is plotted in figure 2.7. For a given combination of the gate and drain source voltage, the conductance may be inferred from the color on the density plot; colors that tend towards white indicate a low conductance, and darker colors indicate a larger conductance. The large white regions in the middle of the plot are "blockaded regions," where Coulomb blockade inhibits current flow through the SET, and a correspondingly lower conductance is measured.

The response of the SET may be rather simply understood. With $V_{ds} = 0$, the SET behaves exactly as the box would; for most values of V_{ge} it is in a fixed charge state because of the Coulomb blockade effects preventing the addition of further electrons to the island. In regions around half-

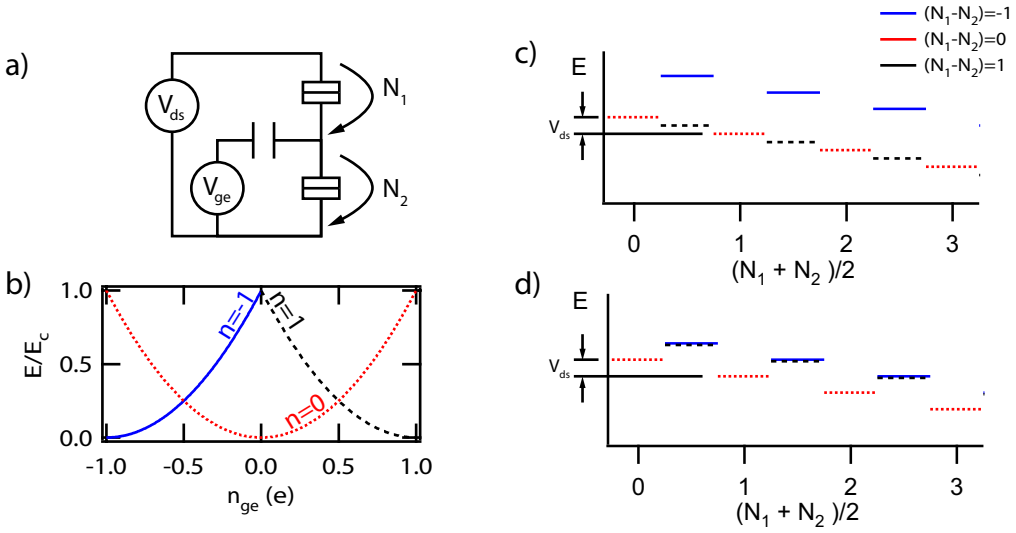

Figure 2.8: a) circuit diagram of SET, showing $N_1(N_2)$, the total number of electrons which have tunneled across junction 1(2). b) Electrostatic energy for SET charge states with -1, 0, and 1 additional electrons on the SET island. c) Schematic diagram for ΔE between SET charge states when the SET is operated at degeneracy ($n_{gb} = \frac{1}{2}$). The change in energy for a tunneling event is calculated from the energetic difference between the corresponding parabolas in part (b) and the additional energy supplied by V_{ds}. At degeneracy, sequential tunneling between the $n = 0$ and $n = 1$ charge states is always energetically favorable, and current flows as the SET charge state "cascades" to the right. d) schematic showing ΔE between adjacent charge states with the SET biased maximally far from degeneracy. The energetic cost for an electron to tunnel on to the island is large, and current is exponentially small. The measurable conductance of the SET is correspondingly small.

integer values of the gate charge coupled to the SET island, however, more than one charge state is accessible (the energy for electron tunneling can be supplied by thermal excitations, or by a small V_{ds}).

In the blockaded region, therefore, no current will flow, and the SET conductance will be very low; in regions where two charge states are accessible, current will flow with any infinitesimally small voltage, and the SET will register a measurable conductance.

The conductance away from $V_{ds} = 0$ may be understood within this framework as well. For current to flow, tunneling across both junctions of the SET must be energetically favorable. At zero temperature, the threshold for this occurs when V_{ds} is large enough that the energy imparted to a single electron tunneling across one junction compensates for the electrostatic energy cost for that electron to tunnel on to the island.

A convenient method for an understanding of the energetic favorability is shown in figure 2.8. The number of electrons that have tunneled across junction 1(2) are taken to be $N_1(N_2)$; the total

number of electrons that have passed from the drain to the source is therefore $(N_1 + N_2)/2$. If the charge state of the island was initially at $n = 0$, then the charge state of the SET island at some later time is the difference between these two numbers, i.e. $n = (N_1 - N_2)$.

For any SET island charge state n, the electrostatic energy of that charge state (expressed as a function of $n_g e$) is shown in figure 2.8b; it is parabolic, exactly as in the case of the Single electron box. The ΔE used to calculate the rate for single electron tunneling is found by adding this electrostatic energy difference to the energy gain(loss) from tunneling with(against) the SET drain-source voltage. A schematic of the relative energies of three SET charge states is shown in figure 2.8c and d.

When the SET is operated at $n_{ge} = \frac{1}{2}$ (figure 2.8c), then the electrostatic energy difference between SET charge states is zero, and the ΔE used to calculate tunneling rates is a consequence entirely of the drain-source voltage. A "cascade" of states is available, and by undergoing sequential transitions between these charge states current will flow through the SET (see arrows in figure 2.8c)

In the maximally blockaded state (at $n_{ge} = 0$) (see figure 2.8d), no such cascade exists – transitions from $n = 0$ to any charge state incur an energy cost, and will be exponentially suppressed.

It is worthy of note that, in general, the capacitances of the two SET junctions (C_1 and C_2 in figure 2.5) are not equal in size, and that a V_{ds} applied to the SET will therefore impart unequal amounts of energy to electrons tunneling across either of the two SET junctions. Practically, we see this in the diamonds of figure 2.7: at a fixed value of n_{ge}, the drain source voltage required to break blockade the positive V_{ds} direction will, in general, be different from the voltage required to break blockade in the negative V_{ds} direction. Put differently, when a Coulomb diamond is measured, the ratio of the slopes of the lines comprising each diamond may be used to infer the ratio of the capacitances of the SET junction; however, some caution must be exercised when doing so.

In addition to asymmetry in the capacitances of the Single Electron Transistor, there may also be differences in the resistances of the junctions of the SET. These, however, are somewhat more difficult to measure, and, for the purposes of our calculations, were never known to any particularly high accuracy. Generally, it was presumed that the relative resistances of the SET junctions was proportional to the junction area, and that the capacitance of the junctions could be used as a measure of the junction area – that, therefore, the ratio in junction conductances was proportional to the ratio of junction capacitances. Some attempts were also made to infer the resistive asymmetry of the junctions from differences in current flowing through certain features in the Superconducting SET.

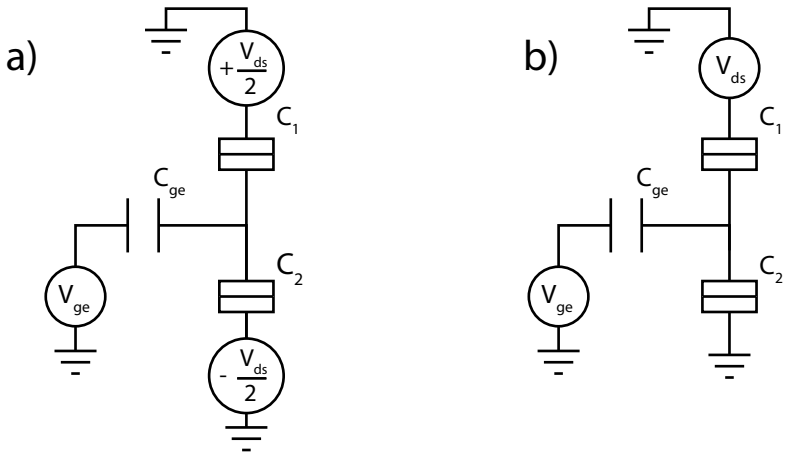

Figure 2.9: a) Symmetric and b) Asymmetric biasing schemes for the SET. Most theoretical treatments presume a symmetric biasing scheme, but practical considerations in many experiments require or prefer an asymmetric biasing scheme, which may be theoretically treated with a minimal modification.

In neither case, however, were variations or errors in our knowledge of the resistive asymmetry of the SET junctions found to cause significant differences in the outcome of SET modeling predictions.

Another potential problem in the matching of theoretical predictions to the model arose because of the method in which the SET was biased with a drain-source voltage. Theoretical treatments of the SET typically presume that it is operated in the "symmetric bias" mode (see figure 2.9a), while in an experimental realization of the SET, it is frequently preferable to operate in an "asymmetric bias" mode (see figure 2.9b). Although theoretical predictions for the SET current may still be produced and used, one must attend to the fact that the gate capacitance (C_g in figure 2.9) will add to the capacitance C_2 in the asymmetric bias case, while it will not affect the junction asymmetry in the symmetric bias case.

2.6 Modeling the SET-Box system in the Normal State

The models discussed above can accurately reproduce the effects of the SET and the single electron box alone, but the effects that we are interested in arise from the coupling between the two. Happily, a model that accounts for the behavior of the coupled SET-box system is conceptually no more difficult than either of the two models alone. I am greatly indebted to Aash Clerk, who initially provided the code that modeled the response of the coupled SET-box system and explained to me its structure as I will describe in this section.

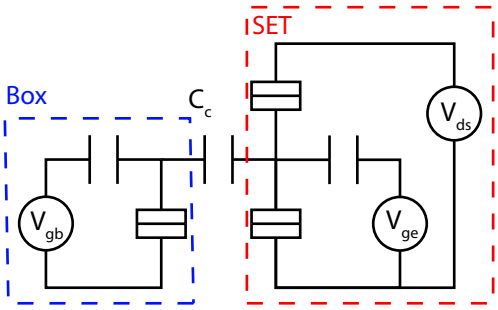

Figure 2.10: Circuit schematic for the coupled box-SET system. The Single Electron Box is measured by the SET through a simple capacitive coupling, shown on the above diagram as C_c, the "coupling capacitor."

The box couples to the SET through the geometrical capacitance between the box and SET island; on a circuit schematic, this is represented by a simple capacitive coupling, shown as the coupling capacitor C_c in figure 2.10.

When modeling the SET or the box alone, the possible states of the system were indexed by the number of additional electrons on either the SET or the box island. In the coupled SET-box system, we must consider all reasonable combinations of Box and SET charge states. While this may increase the computational complexity of the problem by a large amount, it does not complicate the setup conceptually. We still create a rate matrix out of single-electron tunneling rates, which may only couple states differing by a single electron on either the SET or the box. This is to say, the matrix that we are diagonalizing may be far larger than it was in the case of the isolated SET or box, but the matrix is nevertheless sparsely filled, and the calculation of the tunneling rates does not involve any steps more profound than those already taken in the filling of matrices for the isolated box or SET.

The coupling capacitor allows the charge state of one island to affect tunneling rates in the other island by modifying (slightly) the electrostatic stored energy of a each combination of box/island charge states. Naively, one might expect the total electrostatic energy of the box-SET system to be the simple sum of the electrostatic energy of the box island (with n additional electrons):

$$E_{box} = E_{c,box}(n - n_{gb})^2 \tag{2.20}$$

and that of the SET (with m additional electrons):

$$E_{SET} = E_{c,SET}(m - n_{ge})^2 \tag{2.21}$$

Fully calculating the energy stored in the coupled system, one finds an additional term, cor-

responding to the energy stored in the coupling capacitance; the total electrostatic energy of the Box-SET system thus becomes:

$$E_{total} = E_{c,SET}(m - n_{ge})^2 + E_{c,box}(n - n_{gb})^2 + \frac{e^2 C_c}{C_{\Sigma,box} C_{\Sigma,SET}}(m - n_{ge})(n - n_{gb}) \tag{2.22}$$

This is often expressed in terms of $E_{c,box}$, and $\kappa = C_c/C_{\Sigma,SET}$, the fraction of the total SET island capacitance comprised by the coupling capacitor. In later analyses it will become clear that, when a single electron tunnels onto the SET island, κ represents the fraction of that electron which appears as polarization charge gating the box island.

2.7 Higher Order effects in the Single Electron Transistor and Single Electron Box

For the above described model, electron tunneling is presumed to consist of sequential, discrete tunneling events of single electrons between states localized on either side of a single junction, with a tunneling rate given by the Fermi's Golden Rule expression of equation (2.4).

This is, however, only an approximation. Quantum mechanically, tunneling events are thought of as a perturbative coupling between two possible charge states of a nanoelectronic device. If the size of this perturbation becomes large, then first-order perturbation theory is no longer adequate to understand the effects that are seen. Second order processes, which may be thought of as simultaneous tunneling events through two different junctions, will occur; this process is usually referred to as "cotunneling." In addition, charge states of the island state of the system will be "dressed" by their quantum mechanical coupling to other charge states; in other words, the ground state of the single electron box will no longer be a pure charge state, but instead a quantum mechanical superposition of several different charge states. The perturbative small parameter that determines the magnitude of these effects is simply proportional to the product of a junction conductance to the resistance quantum, $R_k = 25.8\,\mathrm{k}\Omega$

2.7.1 Cotunneling in the SET

The sequential tunneling model outlined predicts that the current through a sufficiently cold SET in Coulomb blockade is exponentially small in the temperature. However, this is known not to be true: second order effects, where electrons simultaneously tunnel on to the SET island through one

junction and off through another (Averin and Odintsov, 1989) are known to occur, and have been measured (Geerligs et al., 1990). These effects diminish rapidly with increasing junction resistance; they are a result of an expansion in the small parameter[1] $(g/4\pi^2)$, where

$$g/4\pi^2 = \frac{R_K}{4\pi^2 R_T} \tag{2.23}$$

For a tunnel junction with normal state resistance $R_T = R_k/4\pi^2 = 650\Omega$, this factor will be of order unity, and cotunneling processes to all orders will have to be considered. Happily, however, our SETs were designed to have large charging energies, with correspondingly small tunnel junctions, and hence large tunneling resistance; the effects of cotunneling in our samples were therefore minimal.

We do not, therefore, make any attempt to model the effects of cotunneling in the operation of the SET. This is in part for practical reasons – theoretical modeling that simultaneously accounts for first- and second-order tunneling effects is significantly more complicated than the tunneling model that we have used (Konig et al., 1997) – but also because, for all measurements performed in the normal state for this thesis, the SET was operated in a region where tunneling enabled by thermal excitations or by an imposed voltage was expected to dominate cotunneling effects. In the regime where our measurements were made, it will be seen in Chapter 6, orthodox theory calculations fully account for the effects seen.

2.7.2 Quantum Fluctuations on the Single Electron box

Higher order terms in the perturbative expansion of single electron tunnel coupling lead to the SET cotunneling effects discussed above, in Section 2.7.1. The box experiences a similar coupling between charge states on the island and charge states in the leads; however, because the box cannot pass current, the signature of this coupling is different from the SET. Nevertheless, as in the SET, these effects are calculated as a perturbative expansion in the small parameter g, described in equation 2.23. This small parameter was found to be of a similar magnitude in both the box and the SET samples measured, approximately 0.05.

A theoretical analysis of the problem of quantum fluctuations considers the coupling between the localized charge state of the box and single electron states in the leads. Because this coupling is not infinitesimally small, the states in the lead "dress" the quantum mechanical ground state of

[1] N.B. some references use $g = R_K/4\pi^2 RT$, which is to say that they explicitly include the 4π in their expression for a junction's conductance. This was not done in this thesis for the sake of a uniform notation, but may cause some confusion when these expressions are compared to other references

the single electron box. This may be thought of as quantum mechanical ground state of the single electron box not being a pure charge state, but rather a superposition containing small amplitudes of charge states other than the ground charge state. The expectation value of the charge on the box island is then calculated as a function of the free energy difference between the box island and the leads, which varies with the box gate. One can therefore recalculate the expectation value of the charge on the box island for every box island potential – or, in our experiment, for every value of gate voltage.

At points near the electrostatic degeneracy of the box ($n_{gb} = \frac{1}{2}$), terms in this perturbative calculation diverge, and the calculation breaks down. This problem was solved in 1991 (Matveev, 1991), by an explicit resummation of the leading divergent terms. Matveev is also notable for his comparison of this problem to the Kondo effect, where a coupling between a localized state and a large number of nearby states "dresses" the ground state of the localized system.

Later analyses use graphical expansion techniques to calculate these effects to second (Grabert, 1994) and to third (Goppert and Grabert, 2001) order in the tunneling conductance; notable comparisons have also been made between this theory and quantum Monte Carlo data (Goppert et al., 1998). A concise overview of these results, appropriate for an experimentalist exploring these problems, may be found in (Lafarge, 1993).

The experimental consequence of these analyses is that a measured Coulomb staircase does not have the simple tanh functional form predicted by equation 2.18. To first order in g, the functional form of the Coulomb staircases is instead:

$$\langle n \rangle_1 = \frac{g}{4\pi^2} \ln \frac{1 + 2n_{gb}}{1 - 2n_{gb}} \tag{2.24}$$

Higher order expansions of this expression are not included for the sake of brevity, but may be found in (Grabert, 1994) and (Goppert and Grabert, 2001).

The predicted functional form of a quantum broadened staircase cannot be fit by a thermally broadened staircase at any single temperature (see figure 2.11). The quantum broadening, instead, causes the measured charge on the single electron box to approach an integer value much more slowly than a simple thermal model at a reasonable temperature would normally predict (see figure 2.11). Quantum fluctuations were therefore measured by matching the precise functional form of our measured Coulomb staircases to the staircase shape predicted by equation (2.24). Some difficulty arises in the practical measurement of such a quantum broadened staircase, as there does not exist a

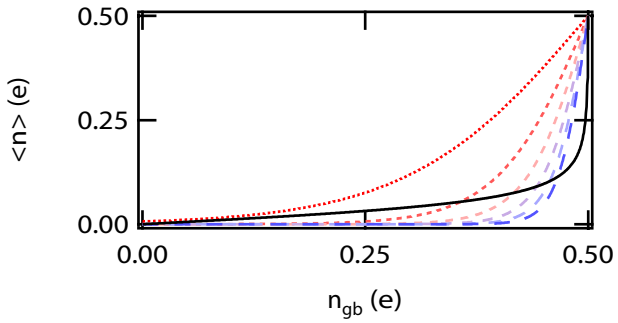

Figure 2.11: Thermally broadened Coulomb staircases and a quantum-broadened Coulomb staircase (black solid line) calculated for our device parameters. Thermal steps are calculated for temperatures ranging from $k_BT = E_C/25$ (blue, long dashes) to $k_BT = E_C/5$ (red, short dashes). The quantum broadening modifies the shape of the staircase in a way that cannot be accounted for by any single temperature.

theory that simultaneously accounts for these quantum fluctuations and the thermal broadening of the staircase. However, as will be demonstrated in Chapter 6, our samples were still sufficiently cold that, for certain regimes, the thermal broadening of the staircase could be negligible, permitting an accurate measurement of the quantum fluctuations.

Chapter 3

Single Electron Systems in the Superconducting State

3.1 Introduction

When operated in the superconducting state, the behavior of the SET-box circuit is markedly different from its normal-state behavior. The aluminum comprising the leads and island of both the SET and the box is described by a BCS ground state, instead of a Fermi sea of electrons, and shows effects due to the coherent nature of that state [first noted in (Buettiker, 1987); first studied in detail in (Bouchiat, 1997)]. The box, which is renamed the "Cooper pair box," is able to support coherent superpositions of different charge states and is capable of operation as a coherent quantum two-level system. The response of the SET, meanwhile, is complicated by tunneling processes that combine both quasiparticle and single electron tunneling. The combined effects of these changes motivate an understanding of SET backaction in the superconducting state that is entirely different from the normal state theory presented in chapter 2.

In this chapter, I will provide theoretical background for the understanding of our system in the superconducting state. In section 3.2, I begin by describing our understanding of how tunneling between superconductors differs from the normal metal tunneling described in chapter 2. In section 3.3, the operation of the Cooper pair box will be explained within this framework. Section 3.4 will treat the changes that superconductivity introduces into the operation of the SET. Finally, in section 3.5, I will combine our understanding of these two systems within a density matrix framework to describe the backaction of the superconducting SET on the Cooper pair box.

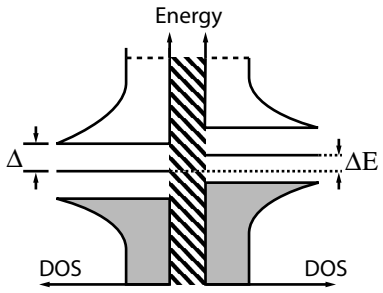

Figure 3.1: "Semiconductor model" of tunneling in superconductors. The density of quasiparticle states in a superconductor is shown as a function of energy for two superconductors separated by an insulating barrier. Filled states are indicated in gray, while empty states are indicated in white. Quasiparticle tunneling between superconductors will occur when a quasiparticle can tunnel from a filled state in one superconductor to an empty state in the other superconductor at the same energy.

3.2 Tunneling in the Superconducting State

In a superconductor, free electrons join together to form Cooper pairs, which form a condensate and give rise to the unique behaviors that characterize superconductors. Because of this new charge carrier, tunneling between superconductors is more complicated than in the normal state, and two different tunneling processes contribute to an overall current: depending on the bias conditions, charge moves across an insulating barrier either as Cooper pairs (understood through the Josephson Effect) or as broken Cooper pairs (which we consider to be electron-like excitations above the superconducting condensate called "quasiparticles"). In this section, I will describe the conditions required for each of these two different types of tunneling, in order to motivate our understanding of the operation of the SET and Cooper pair box.

3.2.1 Quasiparticle Tunneling

In the normal state (see section 2.2), we understood tunneling through consideration of a perturbative coupling between electron states in the leads on either side of a tunnel junction. In what was essentially a Fermi's golden rule calculation, this coupling was integrated over the density of states in either lead to yield a total single electron tunneling rate. We showed this graphically by considering a density of filled and empty states on either side of a tunnel barrier, where tunneling events could bring electrons from a filled state on one side of the barrier to an empty state on the other side (see figure 2.2).

Broken Cooper pairs – "quasiparticles" – are considered to be electron- (or hole-) like excitations

above the superconducting condensate, and their tunneling may be understood through a similar picture. In this picture, usually called the "semiconductor model," quasiparticles occupy states in a superconductor that are considered in the same manner as the single electron states in a normal metal (Tinkham, 1996; Van Duzer and Turner, 1981). Available states for these quasiparticles are represented by two bands, which start an energy Δ away from the Fermi energy of a superconductor (see figure 3.1); The density of states in these bands varies with energy as:

$$N(E) \propto \frac{|E|}{\sqrt{E^2 - \Delta^2}} \tag{3.1}$$

With E=0 at the Fermi energy of the superconductor. Δ is referred to as the superconducting energy gap of the superconductor. The occupation of these states can be calculated using simple Fermi statistics; at zero temperature (or at $k_B T \ll \Delta$), we may consider that all of the states in the bottom band are occupied and all of the states in the top band are filled.

Tunneling between the quasiparticle bands is then analyzed exactly as in the normal state. Electrons can tunnel from a filled state in one lead to an empty state at the same energy in the other lead, and will in general do so at a rate that is calculated with Fermi's Golden rule from the density of states in equation (3.1) (see figure 3.1). At temperatures typical for our experiments, quasiparticle tunneling is generally negligible until ΔE, the energy difference between the Fermi levels in two superconductors, is equal to 2Δ, which is twice the superconducting gap energy. When the energy difference is greater than 2Δ, quasiparticles from the full band of one superconductor can freely tunnel into the empty band of the other superconductor. This model makes excellent intuitive sense as well, as it predicts that a current of broken Cooper pairs will flow only when the available bias voltage is high enough to break Cooper pairs.

3.2.2 Cooper Pair Tunneling

Current may also flow through an SIS junction as Cooper pairs, in a process called the Josephson effect. A DC Cooper pair current will only flow, however, if the Fermi energies of two superconducting leads are aligned. In the semiconductor model diagram of figure 3.1, this is illustrated as a density of Cooper pair states at the Fermi energy of each superconductor, which allows a DC Cooper pair current only if it is aligned with the Cooper pair state in an adjacent superconductor. Drawn as such, however, the semiconductor picture is slightly misleading, as the Cooper pair level at the Fermi energy cannot tunnel into any of the other quasiparticle states shown in the diagram. It is

included in the semiconductor model primarily to indicate the conditions for Cooper pair tunneling, and should not be confused with the quasiparticle bands or any of the calculations that use them. Because DC Cooper pair tunneling will only occur when the free energy difference between two leads is zero, we say that Cooper pair tunneling is a resonant process, and will frequently refer to either "resonant Cooper pair tunneling" or a "Cooper pair resonance."

Calculation of the rate of Cooper pair tunneling between two superconducting leads is more complicated than the corresponding quasiparticle tunneling rate calculation. A discussion of a Cooper pair current will usually begin by considering the coupling of the superconducting wavefunctions on either side of a voltage-biased junction. Each side of the junction is taken to have a single wavefunction describing the superconductor, expressed as:

$$\psi = n^{1/2} e^{i\theta} \tag{3.2}$$

where n is the density of Cooper pairs in a superconducting lead, and θ is the so-called phase of the superconductor. A relatively simple consideration of the coupling between two such leads (Van Duzer and Turner, 1981) will yield the two Josephson relations:

$$I = I_c \sin(\phi) \tag{3.3}$$

$$\dot{\phi} = \frac{2e}{\hbar} V \tag{3.4}$$

which express the current through a junction, I, as a function of ϕ, the gauge-invariant difference of the phase across the junction. The gauge-invariant phase difference is calculated from the superconducting phase as:

$$\phi \equiv \Delta\theta - \frac{2\pi}{\Phi_0} \int \mathbf{A} \cdot d\mathbf{s} \tag{3.5}$$

and allows Josephson junction behavior that is independent of the choice of mathematical gauge in which the system is analyzed. The evolution of ϕ is given by equation (3.4) as a simple function of the applied voltage bias.

Consideration of the evolution of this gauge invariant phase difference is an important tool for understanding many effects in superconducting Josephson junction circuits [see e.g. (Tinkham, 1996)]. The dynamics of the evolution of this phase are usually calculated in the context of the RCSJ ("resistively and capacitively shunted junction") model, which treats the current through a real Josephson junction as coming from the combined effects of three different elements (see figure 3.2): a resistance, a capacitance, and a pure Josephson element that is governed by the Josephson

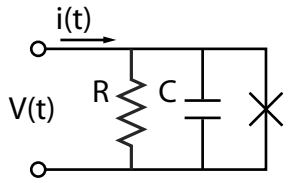

Figure 3.2: RCSJ (resistively and capacitively shunted junction) model used to find the current-voltage characteristic of a Josephson junction. A pure Josephson element, governed by equations (3.3) and (3.4), is connected in parallel to a pure resistance and a pure capacitance.

relations [equations (3.3) and (3.4)]. The total current through this combination can be rather simply expressed as:

$$I = I_c \sin(\phi) + \frac{V}{R} + C\frac{dV}{dt} \tag{3.6}$$

For clarity, the second Josephson equation (3.4) is used to express this entirely as a function of ϕ, and the time is expressed dimensionlessly as $\tau = \omega_p t$, with:

$$\omega_p = (2eI_c/\hbar C)^{1/2} \tag{3.7}$$

which is called the "plasma frequency" of the junction. The RCSJ equation then becomes:

$$\frac{I}{I_C} = \frac{d^2\phi}{d\tau^2} + \frac{1}{\omega_p RC}\frac{d\phi}{d\tau} + \sin\phi \tag{3.8}$$

This equation for ϕ is analogous to the differential equation governing the position of a massive particle, experiencing viscous drag, moving in a "tilted washboard" potential that is functionally expressed as:

$$U(\phi) = -E_J \cos\phi - \frac{\hbar I}{2e}\phi \tag{3.9}$$

Here we have defined E_J, the Josephson coupling energy of the junction, as

$$E_J = (\hbar/2e)I_C \tag{3.10}$$

Although the discussion above involves a purely classical consideration of the junction phase ϕ, the quantum mechanical understanding underlying the experiments in this thesis proceeds in the exact same fashion, and considers a quantum mechanical phase variable moving in the same tilted washboard potential [equation (3.9)]. An alternate derivation of the potential landscape in phase space of a Josephson junction is given in (Devoret, 1997) where this potential is derived from a purely quantum-mechanical consideration of the coupling across a Josephson junction; the results, however, are equivalent.

In the discussion that follows, we will interest ourselves primarily with the junction phase, ϕ in the above equation, rather than the current that was of classical interest. This phase is considered as a quantum variable and is conjugate to n, the number of Cooper pairs in a superconducting condensate.

3.2.3 Tunneling in Superconductors and Quantum Coherence

Perhaps the most important difference between single electron and Cooper pair tunneling is a consequence of the "coherence" maintained by a Cooper pair tunneling event, which introduces effects that are unique to the superconducting state. Disregarding coherence, Cooper pair or single electron tunneling events appear quite similar: a quantum mechanical coupling between two states (with electrons/Cooper pairs on different sides of a tunnel junction) couples a wavefunction on one side of a junction to the wavefunction of a target state. After some time, this coupling may bring sufficient amplitude of a wavefunction into a target state that a charge measurement would likely observe an electron/Cooper pair in the target state instead of the source state; we say that the species has tunneled. Because of the coherence of a superconducting condensate, however, the subsequent evolution is very different for electrons and for Cooper pairs.

In the normal state, a single electron will tunnel into an empty state within a Fermi sea of electrons. A single electron in an state above a Fermi sea may be thought of as a small excitation above the expected thermal state of the Fermi sea. Because of electron-electron interaction, however, this excitation decays very rapidly, and the Fermi sea will relax to a normal thermal Fermi distribution. This relaxation occurs on a timescale that is much faster than the characteristic time for subsequent tunneling events, and so coherent effects in quasiparticle tunneling are not observed.

In the superconducting state, a tunneling Cooper pair moves into the coherent BCS ground state of a superconductor. A BCS ground state is a single, coherent, macroscopic quantum state, which, in express contrast to a normal metal, does not have many different degrees of freedom. A Cooper pair that has tunneled into a superconducting reservoir, therefore, will not "relax into the Fermi sea," and can stay coherent with its source state long after it has tunneled.

It is important to note that, in this language of coherence, quasiparticle states in a superconductor are more like single electron states than they are like the macroscopic quantum coherent state of a superconductor. According to the BCS theory, quasiparticle states exist as continuous densities of states above and below the superconducting ground state (this may be seen in the band

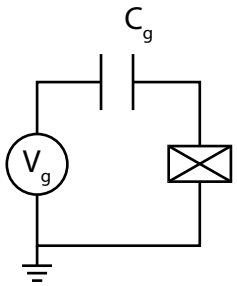

Figure 3.3: Schematic of the Cooper pair box. An isolated island is connected, via a tunnel junction, to a superconducting reservoir. A gate lead may capacitively couple a voltage to the island.

structure of the "semiconductor model" of a superconductor in figure 3.1). As in a normal metal, furthermore, a quasiparticle which has tunneled into one of these states may be expected to scatter, relax, and rapidly lose its coherence with the state from which it came. This fact will be important in our consideration of superconducting SET backaction, in section 3.5, where it will motivate our understanding of SET backaction as the noise from a nonequilibrium reservoir.

3.3 Theory of the Superconducting Cooper Pair Box

As in the normal state, the simplest Josephson junction circuit that we can construct consists of a single island, connected to ground with a Josephson junction, and capacitively coupled to a voltage bias (see figure 3.3); in the superconducting state, this circuit is usually termed the "Cooper pair box." As we have drawn it, this circuit does not differ from the single electron box discussed in chapter 2. However, because of the coherence of the superconductors discussed in section (3.2.3), the Cooper pair box can show markedly different behavior from the analogous normal state system. It has been shown to operate as a coherent quantum two-level system, with an energy level splitting that may be probed spectroscopically (Nakamura et al., 1997). The group of Nakamura has demonstrated coherent control of the Cooper pair box (Nakamura et al., 1999), and earlier measurements in our lab have measured its excited state lifetime (Lehnert et al., 2003b). Current studies of the Cooper pair box focus on its manipulation and use as a candidate component of a quantum computer (Devoret et al., 2004).

In this section, I will describe the operation of the Cooper pair box within the larger context of the study of quantum two-level systems. I will provide only the background necessary for an understanding of the experiments performed in this thesis; the reader is referred to (Abragam,

1983; Slichter, 1990) for more extensive discussions of possible experiments that may be performed with quantum two-level systems, and to (Cottet, 2002; Schuster, 2007) for descriptions of recent experiments that have been performed on superconducting two-level systems.

3.3.1 Hamiltonian of the Cooper pair box

Following (Cottet, 2002), we consider the Cooper pair box as a coherent quantum two-level system in the basis of charge states of the box island; let $|N\rangle$ denote the state with N additional Cooper pairs on the box island. The Hamiltonian of the Cooper pair box may then be decomposed into two separate portions: an electrostatic energy, which is diagonal in the basis of the charge states of the box island, and a Josephson coupling that couples island states of different charge.

$$\hat{H}_{total} = \hat{H}_{el} + \hat{H}_J \tag{3.11}$$

The electrostatic energy of different number states of the Cooper pair box island is calculated exactly as in the normal state, and is found to vary parabolically with n_{gb}, the gate voltage applied to the Cooper pair box; we find that

$$\hat{H}_{el} = E_C(n_{gb} - 2\hat{N})^2 \tag{3.12}$$

Where $\hat{N}$, the number of additional Cooper pairs on the box island is now taken to be an operator in the Hilbert space of box island charge states described above. Rather trivially, this operator may be expressed as:

$$\hat{N} = \sum_N N \left|N\right\rangle \left\langle N\right| \tag{3.13}$$

Note that, as in the normal (non-superconducting) state, we express the externally applied gate voltage in dimensionless units as $n_{gb} = C_{gb}V_{gb}/e$, which may be interpreted as electrons of polarization charge on the box gate capacitor. Note, also, that to avoid confusion with the normal state, we do not express this gate voltage in terms of Cooper pairs. In a similar spirit, the charging energy in this section is still expressed as $E_C = e^2/2C_\Sigma$, the energy to add a single electron to the box island. In this section, the number of Cooper pairs on the box island is denoted by a capital N, to distinguish it from the number of additional single electrons on the island in our normal state calculations. For calculations where the total *charge* on the Cooper pair box is important, it will

be expressed in units of electrons – either as $2N$ (twice the number of Cooper pairs) or as n (the number of additional single electron charges, which may be restricted to even values only).

To express the Josephson coupling of the junction in our box in the basis of box island charge states, we first expand the cosine term in the energy of our Josephson junction in exponentials:

$$\hat{H}_J = -E_J \cos(\hat{\phi}) = \frac{E_J}{2}\left(e^{i\hat{\phi}} + e^{-i\hat{\phi}}\right) \tag{3.14}$$

We may then identify the operator $e^{\pm i\hat{\phi}}$ as the operator that adds a single Cooper pair to or removes a single Cooper pair from the box island, i.e.:

$$e^{-i\hat{\phi}} = \sum_N |N\rangle \langle N+1| \tag{3.15}$$

Equations (3.12) and (3.14) are combined to write the Hamiltonian for the Cooper pair box system. For simplicity of calculation, we will restrict ourselves to the $|N=0\rangle$ and $|N=1\rangle$ charge states of the Cooper pair box, in a region between $n_{gb} = 0$ and 2 electrons. This approximation is valid, and higher charge states do not need to be considered in samples where $E_J \lesssim E_C$; readers are referred to (Cottet, 2002) for an analysis of the Cooper pair box involving all charge states. In this basis, we find that the full Hamiltonian of the Cooper pair box is expressed as:

$$\hat{H} = \begin{pmatrix} E_C(n_{gb})^2 & -E_J/2 \\ -E_J/2 & E_C(n_{gb}-2)^2 \end{pmatrix} \tag{3.16}$$

This Hamiltonian is placed in a more symmetric form by subtracting $E_C\left[(n_{gb})^2 - 2n_{gb} + 2\right] I$, effectively subtracting constant energy from both states:

$$\hat{H} = \begin{pmatrix} 2E_C(n_{gb}-1) & -E_J/2 \\ -E_J/2 & -2E_C(n_{gb}-1) \end{pmatrix} \tag{3.17}$$

This Hamiltonian is frequently identified with the Hamiltonian of a spin - 1/2 particle, as:

$$\hat{H} = 2E_C\left(n_{gb}-1\right)\hat{\sigma}_z - \frac{E_J}{2}\hat{\sigma}_x \tag{3.18}$$

The eigenvalues of this Hamiltonian are:

$$E_{e,g} = \pm\sqrt{\left(\frac{E_J}{2}\right)^2 + \left[2E_C(n_{gb}-1)\right]^2} \tag{3.19}$$

Corresponding to an energy difference between the excited and the ground state of the Cooper pair box of:

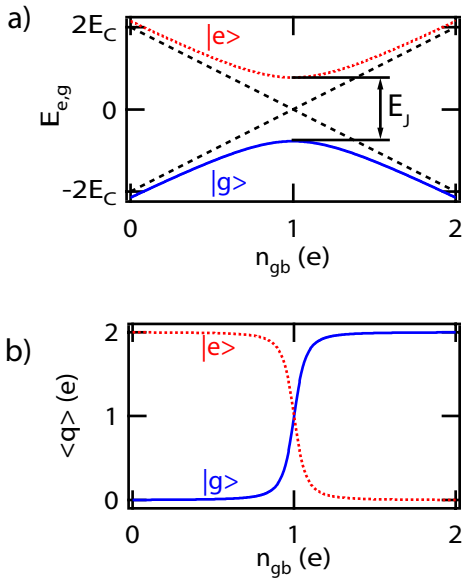

Figure 3.4: a) Relative energy of the excited and ground state of the Cooper pair box, plotted vs n_{gb}, the externally applied gate voltage. The ground state is indicated by a solid blue line, while the excited state is indicated by a red dotted line. Black dashed lines show the electrostatic energy of states with $N = 0$ and 1 additional Cooper pairs on the island; the Josephson coupling introduces an avoided crossing. b) Expectation value of the measured charge on the box island, expressed in electrons. The measured response of the box gives the expected Coulomb staircase. Color coding is the same as in part a. Data are generated with $E_J = 0.6E_C$

$$\Delta E_{e,g} = \sqrt{E_J^2 + \left[4E_C(n_{gb} - 1)\right]^2} \tag{3.20}$$

The relative energies of the ground and excited eigenstates of the Cooper pair box, calculated from this equation, are plotted in figure 3.4a. The black dashed lines on that plot show the electrostatic energy difference between the two states in the absence of a Josephson coupling; when introduced, the Josephson coupling creates the expected avoided crossing.

3.3.2 The Coulomb Staircase of the Cooper Pair Box

The expectation value of the charge on the Cooper pair box in its ground and excited states is calculated from the eigenvectors of the Hamiltonian described in equation (3.17):

$$\langle q \rangle_g = \langle g \left| \hat{\sigma}_z \right| g \rangle + 1 = \frac{(n_{gb} - 1)}{\sqrt{\left(\frac{E_J}{4E_C}\right)^2 + (n_{gb} - 1)^2}} + 1 \tag{3.21}$$

$$\langle q \rangle_e = \langle e \left| \hat{\sigma}_z \right| e \rangle + 1 = -\frac{(n_{gb} - 1)}{\sqrt{\left(\frac{E_J}{4E_C}\right)^2 + (n_{gb} - 1)^2}} + 1 \tag{3.22}$$

In these expressions, both n_{gb} and $\langle q \rangle$ are expressed in electrons. These expectation values are plotted in figure 3.4b, as a function of n_{gb}, the externally applied box gate voltage. As in the normal state, we see that the measured charge on the box island increases with n_{gb} in a "staircase" fashion; also as before, these measurements are called Coulomb staircases.

The superconducting Coulomb staircase, however, differs from the normal state Coulomb staircase in several important ways. First and foremost, an increase in charge on the Coulomb staircase – a "step" – occurs when 2 electrons of charge have been applied to the box gate, while staircases measured in the normal state showed a staircase step for every 1 electron increase in n_{gb}. Experimentally, this was not always found to be the case: staircases were sometimes measured with steps occurring with every 1 electron of charge coupled to the box gate. This was generally presumed to be due to the additional quasiparticles which are available to tunnel on to the box island (Lafarge et al., 1993); when seen, it was referred to as "quasiparticle poisoning." Observations of this poisoning, and our theories about its causes, will be presented section 7.5.

In addition, the width of the superconducting Coulomb staircase is understood differently than the width of the corresponding normal state Coulomb staircase. In the normal state, the width of the Coulomb staircase was a function of $k_B T/E_C$, the temperature of the single electron box normalized to the box charging energy (see section 2.3). In the superconducting state, when $k_B T \ll E_J$, the width of the Coulomb staircase is determined by the range in n_{gb} over which the Josephson energy is comparable to the electrostatic energy difference between Cooper pair box charge states; this may be inferred graphically from figure 3.4. Alternately, from equation (3.21), we note that the width of a superconducting Coulomb staircase in its ground state is proportional to the quantity $(E_J/4E_C)$, which expresses the ratio between the charging energy and the Josephson coupling energy of the Cooper pair box.

For the circuit depicted in the schematic of figure 3.3, this Josephson coupling energy is determined only by the geometry of the Josephson junctions, and is a fixed quantity. In our experiments, however, we wished to be able to vary the Josephson coupling energy of our Cooper pair box. This was accomplished by splitting the single junction in our Cooper pair box into two different junctions that encircled an externally applied magnetic flux (see figure 3.5). This loop was then operated as

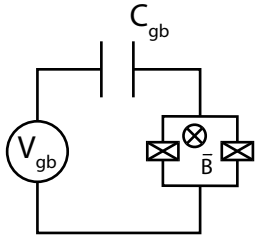

Figure 3.5: Schematic for "split box" Cooper pair box design. The single junction connecting the box island to ground from figure 3.3 is split into two junctions on the perimeter of an open loop, forming a Superconducting Quantum Interference Device (SQUID). When a magnetic field is threaded through this loop, the effective Josephson coupling energy of the combination can be modulated.

a Superconducting Quantum Interference Device (SQUID), where the effective Josephson coupling energy of the combination varied with magnetic flux Φ_B as [see e.g. (Tinkham, 1996)]:

$$E_J(\Phi_B) = E_{J,tot} \left|\cos\left(\pi\Phi_B/\Phi_0\right)\right| \tag{3.23}$$

Observations of Coulomb staircases measured as E_J is varied are presented in section 7.3.2, where they were interpreted as an early indicator that the behavior of the Cooper pair box was well understood.

3.3.3 Bloch Sphere

Because of the similarity between the Cooper pair box Hamiltonian and the Hamiltonian of a spin-1/2 particle [noted in equation (3.18)], the behavior of the Cooper pair box is sometimes modeled using the so-called "Bloch sphere," which was developed for the understanding of NMR two-level systems. Because this understanding was not directly used for most of the calculations in this thesis, I present only a brief summary of its results; readers are referred to (Cottet, 2002) for more information on the analogies between solid state and NMR systems, and to (Abragam, 1983) or (Allen and Eberly, 1987) for descriptions of two-level system manipulations understood within this context.

The Bloch sphere considers an NMR spin as an archetype for any quantum two-level system. Ignoring a global phase factor that is not physically observable, the normalized state of a quantum system restricted to the states $|0\rangle$ and $|1\rangle$ may be most generally described as:

$$|\psi\rangle = \cos(\theta/2)e^{-i\phi/2}\,|0\rangle + \sin(\theta/2)e^{i\phi/2}\,|1\rangle \tag{3.24}$$

We apply this language to the Cooper pair box considered in the basis of charge states, where the

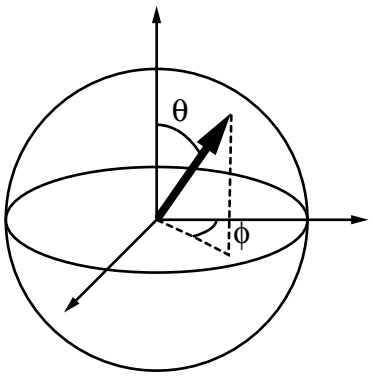

Figure 3.6: The "Bloch sphere" representation of the state of a quantum two-level system. The state of a quantum two-level system is represented as a vector on a unit sphere. The expectation value of a measurement of σ_z is represented by the projection of this state vector on the z-axis. The Hamiltonian of the Cooper pair box is represented by a fictitious magnetic field, and the time evolution of the quantum state of the Cooper pair box is a simple precession about the fictitious magnetic field vector.

$|0\rangle$ and $|1\rangle$ states refer to states with 0 or 1 additional Cooper pairs on the box island. In this basis a measurement of σ_z corresponds to a measurement of the charge state of the Cooper pair box island.

When the two-level system form of equation (3.24) is applied to an NMR spin, the angles θ and ϕ are identified with the polar and azimuthal angles describing the orientation of the spin (see figure 3.6). In this picture, the projection of the Bloch vector onto the $\hat{x}$, $\hat{y}$, or $\hat{z}$ axis denotes the expectation value of a measurement of the polarization of the system in the corresponding direction. When a time-independent Hamiltonian governing the time evolution of the state of such a system is then decomposed as:

$$\hat{H} = H_x\sigma_x + H_y\sigma_y + H_z\sigma_z \tag{3.25}$$

one finds that the the time evolution corresponds to simple precession of the Bloch vector around the static magnetic field described by $\vec{H} = (H_x, H_y, H_z)$. The frequency of this precession, furthermore, is simply the Larmor frequency $\omega = E_{01}/\hbar$ determined by the energy splitting of the two-level system.

Comparing with equation (3.18), we see that the Josephson energy and the electrostatic energy of the Cooper pair box may be identified with, respectively, the $\hat{x}$ and $\hat{z}$ components of a fictitious magnetic field. Furthermore, by considering the variation of this fictitious magnetic field with n_{gb}, we can recreate the Coulomb staircase. As n_{gb}, the voltage capacitively coupled to the Cooper pair box, is changed from 0 to 2 electrons, the $\hat{z}$ component of the fictitious magnetic field changes from

positive, to zero, and then negative. If the quantum two-level system has been permitted to relax into its ground state, aligned with the fictitious magnetic field $\vec{H}$, then the calculated expectation value of the charge on the Cooper pair box – the projection of a unit vector aligned with $\vec{H}$ onto the z axis – reproduces the Coulomb staircase of the Cooper pair box that was calculated in section 3.3.2.

3.3.4 Spectroscopy

The Bloch sphere may also be used to understand the effects of an oscillating RF signal applied to the gate of the Cooper pair box. Detailed mathematical calculations of this result may be found in any of a number of texts; see, for example, (Sakurai, 1994) or (Allen and Eberly, 1987). We include only the graphical Bloch sphere picture here at a level appropriate to motivate the experiments that we perform. An oscillating RF charge [expressed as $\delta n_{RF} \cos(\omega t)$] on the gate of the Cooper pair box is included in the Hamiltonian as:

$$\hat{H}_{RF}(t) = 2E_C \ \delta n_{RF} \ \cos(\omega_{RF} t) \ \sigma_z \tag{3.26}$$

This is understood as a small oscillating magnetic field in the z direction of the Bloch sphere. This term is considered perturbatively in the so-called "rotating frame," a reference frame co-rotating with the Larmor precession of the quantum two-level system. In this frame, all time evolution of a quantum state due to the static Hamiltonian is removed, and we consider the effects of the perturbation independent of the Larmor precession of the two-level system.

The only component of this field that will affect the state of our system is the component oscillating at the Larmor frequency of the system that is perpendicular to the static magnetic field. The magnitude of the component of (3.26) that is perpendicular to the static magnetic field in our system is simply $[2E_C \ \delta n_{RF} \sin(\theta/2)]$, where θ is the angle between the $\hat{z}$ axis and the fictitious static magnetic field. In the rotating frame, this appears as a DC perturbing field perpendicular to the eigenstates of the fictitious spin, and will cause the state of the fictitious spin to oscillate between the ground and excited state. This so-called "Rabi oscillation" is one of the hallmarks of quantum coherence in a quantum two-level system, and has been an early goal of many groups studying superconducting qubit systems (Martinis et al., 2002; Vion et al., 2002; Wallraff et al., 2005). We did not measure Rabi oscillations in our experiments because the backaction of the SET disturbed the state of the qubit before it could undergo coherent oscillations. Nevertheless, we were

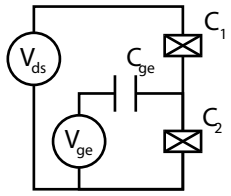

Figure 3.7: Schematic of the SET in the superconducting state. The fabrication and the circuit structure are exactly as in the normal state, shown in figure 2.5. Instead of normal state tunnel junctions, however, this circuit diagram shows Josephson junctions connecting the SET island to the drain and source leads.

still able to see effects that were a consequence of this effect: although we did not observe coherent excitation of our qubit, we were able to see that an RF voltage applied to the gate of our Cooper pair box would excite some population into an excited charge state, but only where the applied RF signal was resonant with the energy splitting of the box. This spectroscopic probing of the Cooper pair box will be discussed in chapter 7.8 as an important tool for understanding and interrogating the energy spectrum of our system.

3.4 Theory of the Superconducting Single Electron Transistor

As with the box, the physical layout of the superconducting SET does not differ from its normal state analog; the only physical difference between the superconducting and the normal SET is the state of the metal comprising the device. The method of superconducting SET measurement, furthermore, is exactly the same as in the normal state: a response curve of the SET alone is measured, and then used to calibrate the response of the SET to an external voltage signal. A detailed description of this methodology may be found in section 5.5. While the methodology of SET measurement is the same, the processes underlying its operation are quite different. Because of the increased complexity of tunneling in the superconducting state, the response and the backaction of the superconducting SET are understood in a different and more complex fashion than that of the normal state SET.

In this section, I discuss the basic mechanisms of current flow in the superconducting SET. This is not intended to be an exhaustive treatment of the subject, but rather to provide suitable background for our analysis of superconducting SET backaction. I will focus my discussion on the mechanisms of tunneling in the superconducting SET, and the conditions under which different types of tunneling will occur. Readers who are interested in a more thorough explanation are referred to (Pohlen, 1999)

for further information.

3.4.1 Conditions for Tunneling in the Superconducting SET

As in the case of the normal state SET, current flows in the superconducting SET through a series of tunneling events that bring charge from the drain onto the island, and then to the source lead. In the normal state this tunneling consisted of incoherent sequential tunneling events that were simply treated with first-order perturbation theory. In the superconducting state, this tunneling occurs through a variety of different combinations of Cooper pair and quasiparticle tunneling events. As a consequence, the measured response of the superconducting SET (see figure 3.8) is considerably more complicated than the normal state SET response (see figure 2.7.) Nevertheless, there are strong parallels between the two, and we still term the response of the superconducting SET (shown in figure 3.8) a "diamond."

In section 3.2, we noted that tunneling in superconducting Josephson junctions can occur through resonant tunneling of Cooper pairs, or through the tunneling of single quasiparticles. In general, these processes are allowed or disallowed for certain combinations of SET gate and drain-source voltages; in order to fully understand the operation of the SET, it is instructive to calculate the conditions that these tunneling processes must satisfy.

Quasiparticle tunneling in a superconductor is similar to single electron tunneling in the normal state: it is a threshold process that will occur at a rapidly increasing rate for biases above a "turn-on" voltage. Unlike the normal state, however, the turn-on bias difference is nonzero – arising from the 2Δ of energy of a quasiparticle excitation above the superconducting condensate.

We calculate the conditions where quasiparticle tunneling will occur by accounting for all of the energy gained and lost by each tunneling quasiparticle. As before, this includes factors from the applied drain-source voltage and from the charging of the SET island. The energy imparted by the drain-source voltage is calculated by considering the capacitances of the SET junctions as a simple capacitive voltage divider:

$$E_{Vds} = \kappa_i e V_{ds} \tag{3.27}$$

Where κ_i describes the fraction of the drain-source voltage across each junction, calculated as:

$$\kappa_1 = \frac{C_2 + C_g/2}{C_\Sigma} \tag{3.28}$$

$$\kappa_2 = \frac{C_1 + C_g/2}{C_\Sigma} \tag{3.29}$$

Here C_1 and C_2 refer to the capacitances of the two tunnel junctions comprising the SET, while C_g is the gate capacitance, and C_Σ is the total capacitance of the SET island. Note that this formulation describes a symmetric SET bias (see section 2.5); in an asymmetric bias mode, the gate capacitance would appear to be entirely in parallel with C_2.

The electrostatic energy gained or lost in a quasiparticle tunneling event is calculated exactly as in the normal state. If the electrostatic energy of the SET island with n additional electrons and a capacitively coupled gate charge of n_{ge} is:

$$E_n = \frac{e^2 \left(n_{ge} - n\right)^2}{2C_\Sigma} \tag{3.30}$$

Then the net electrostatic energy gained or lost when a single quasiparticle tunnels on to the SET island may may be calculated as:

$$\Delta E_{el} = E_{n+1} - E_n \tag{3.31}$$

Tunneling will occur if the drain source voltage is large enough to supply this energy and the 2Δ of energy necessary to split a Cooper pair into quasiparticles. Mathematically expressed, this requirement is:

$$\kappa_i e V_{ds} \geq E_{n+1} - E_n + 2\Delta \tag{3.32}$$

Identifying $E_C = e^2/2C_\Sigma$ and expanding,

$$\kappa_i e V_{ds} \geq E_c \left(2n - 2n_{ge} + 1\right) + 2\Delta \tag{3.33}$$

The threshold in V_{ds} for a quasiparticle to leave the SET island may be derived by repeating the above derivation considering the transition from the $n+1$ charge state to the n charge state (and using the κ value for the other junction).

In a similar fashion, we may calculate the conditions that n_{ge} and V_{ds} must satisfy for Cooper pairs to tunnel onto and off of the SET island. As discussed in section 3.2, Cooper pair tunneling is a resonant process that will only occur when the Fermi energies of the source and target leads are aligned. We account for this mathematically by enforcing that the energy imparted by the drain-source voltage to a tunneling Cooper pair ($= 2e\kappa_i V$) is equal to the change in electrostatic energy from the tunneling of that Cooper pair, i.e.:

$$2\kappa_i e V_{ds} = E_{n+2} - E_n \tag{3.34}$$

Unlike quasiparticle tunneling, Cooper pair tunneling is not a threshold process, and will only occur at combinations of n_{ge} and V_{ds} where this Cooper pair resonance condition is satisfied. In

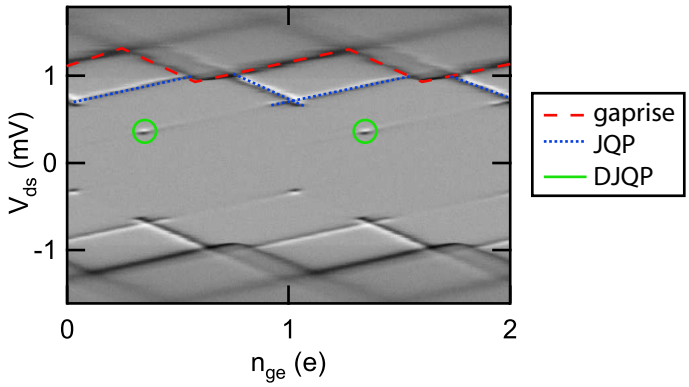

Figure 3.8: Response of the SET in the superconducting state, shown as RF-SET reflected power (greyscale) vs drain-source voltage (V_{ds}, left axis) and gate voltage (n_{ge}, bottom axis). Current-transport processes that were studied in this thesis are illustrated with colored lines in the positive-V_{ds} half of the plot.

equation (3.34), we see this in the fact that the Cooper pair resonance condition is expressed as an equality, which may be contrasted with the inequality of the quasiparticle tunneling threshold expressed in equation (3.33).

Current transport through the SET is understood to occur in "charge cycles," where sequences of quasiparticle and Cooper pair tunneling events bring charge on to the SET island through one junction, and then off of the island through the other junction. These charge cycles are typically described by a cyclical series of charge states that the SET occupies during the different steps of the charge cycle. For the measurements made in this thesis, the SET was operated at each of three different charge cycles which are illustrated on the diamond shown in figure 3.8. The "gaprise"[1], which appears as a black ridge at drain source voltages between ± 1 and ± 1.1 mV, is caused by sequential quasiparticle tunneling in the SET. The Josephson quasiparticle ("JQP") process, which is highlighted with a blue dotted line in figure 3.8, involves a combination of Cooper pair and quasiparticle tunneling. In the diamond of figure 3.8, the JQP appears as parallel white and black lines – because the RF-SET response, which essentially measures the differential conductance of the SET, is increased when the JQP is turning on, and negative at voltages above the JQP, where the JQP process is turning off. Finally, the Double Josephson quasiparticle ("DJQP") process occurs as a point-like feature in SET current at comparatively low drain-source voltages; in figure 3.8 it is circled in green.

[1] So called because it causes an abrupt *rise* in current when the applied V_{ds} can overcome the superconducting *gap*.

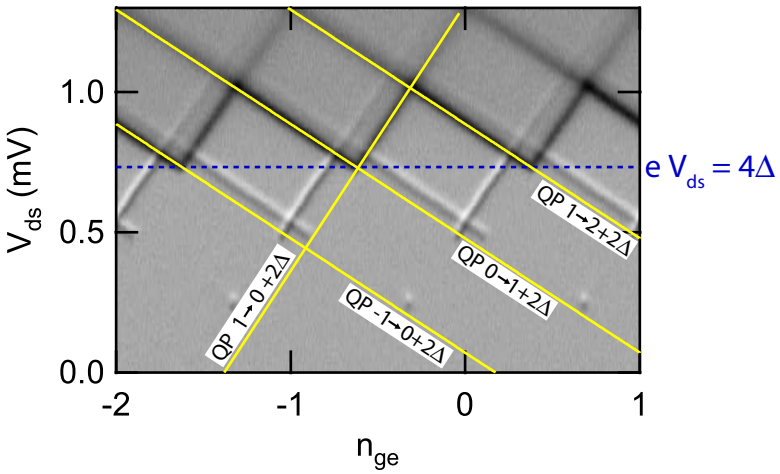

Figure 3.9: Superconducting diamond with illustrated thresholds for quasiparticle tunneling processes. Solid yellow lines show quasiparticle tunneling thresholds calculated from equation (3.33). The dashed blue line shows where $eV_{ds} = 4\Delta$, at which point the drain source voltage can break Cooper pairs. In regions of the diamond where the drain-source voltage can supply enough energy to break Cooper pairs, and the tunneling of the resulting quasiparticles is energetically favorable, conductance is seen in the SET response. Note that the gate voltage, n_{ge}, shown on the bottom axis, contains an arbitrary offset (from background charge coupled to the SET island), and should therefore not be construed to indicate the absolute total charge coupled to the SET island.

3.4.2 Quasiparticle Current in the Superconducting SET

The simplest current transport process in the superconducting SET, quasiparticle tunneling, can be understood by direct analogy to single electron tunneling in the normal state SET. In both cases, a current flows through incoherent sequential tunneling events that are energetically favored above a threshold in V_{ds}, the drain-source voltage. This threshold is modulated in the exact same way as single electron tunneling in the normal state with n_{ge}, the electrometer gate voltage. Quasiparticle tunneling in the superconducting state, however, requires an energy difference driving each tunneling process that is not merely positive – as in the normal state – but greater than 2Δ, to break the Cooper pairs that form the quasiparticle current.

In figure 3.9, quasiparticle tunneling threshold voltages calculated from equation (3.33) are plotted as yellow lines superimposed on a plot of the SET response. It is immediately apparent that the structure of the onset of quasiparticle tunneling, along these thresholds, is similar to the pattern in the onset of current in the normal state SET, offset by 4Δ (the reader is invited to compare the diamond-shaped profile demarcated by the red dashed line in figure 3.8 with the diamond shaped profile in figure 2.7). Because of the region where no current flows (where V_{ds} is less than the su-

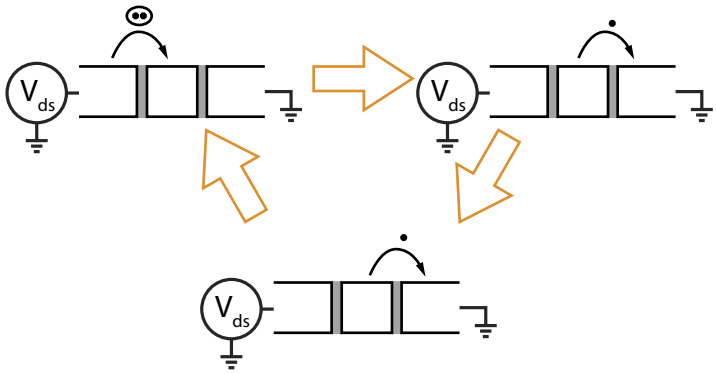

Figure 3.10: Illustration of the tunneling processes comprising the JQP cycle. A Cooper pair first tunnels across one junction, followed by two quasiparticle tunneling events across the other junction. At different bias conditions, similar cycles proceed (also termed JQP cycles) where the Cooper pair tunneling event brings a Cooper pair off of the island; processes may also occur with the Cooper pair tunneling across the other junction.

perconducting energy gap), and because of the pronounced nature of the onset of the quasiparticle current in the SET, operating points on or near the onset of quasiparticle current are colloquially said to be "on the gaprise" (see figure 3.8). The onset of the gaprise occurs at $V_{ds} = 4\Delta/e$, where the drain-source voltage supplies the 2Δ of energy necessary for a Cooper pair to be broken and to tunnel across either of the two junctions in the SET.

3.4.3 The JQP Current Cycle

At voltages less than $eV_{ds} = 4\Delta$, the drain-source voltage cannot supply the energy necessary to break Cooper pairs and allow quasiparticle tunneling across both SET junctions. However, current may still flow if at least one of the tunneling processes involves Cooper pair tunneling, which does not require the 2Δ of energy that quasiparticle tunneling would. One such process is the Josephson Quasiparticle, or "JQP" current cycle, indicated by a blue dotted line in figure 3.8.

The JQP current cycle involves a single resonant Cooper pair tunneling event across one junction, followed by two quasiparticle tunneling events across the other junction (shown schematically in figure 3.10). Because of the first of these steps, the JQP process will only occur at settings of V_{ds} and n_{ge} where Cooper pairs may resonantly tunnel across one of the SET junctions. From equation (3.34) it is apparent that such settings define a family of diagonal lines in a plot of SET conductance against n_{ge} and V_{ds} ("left-diagonal" and "right-diagonal" lines correspond to Cooper pair tunneling across the two different junctions; see figure 3.8). Combinations of V_{ds} and n_{ge} that satisfy this

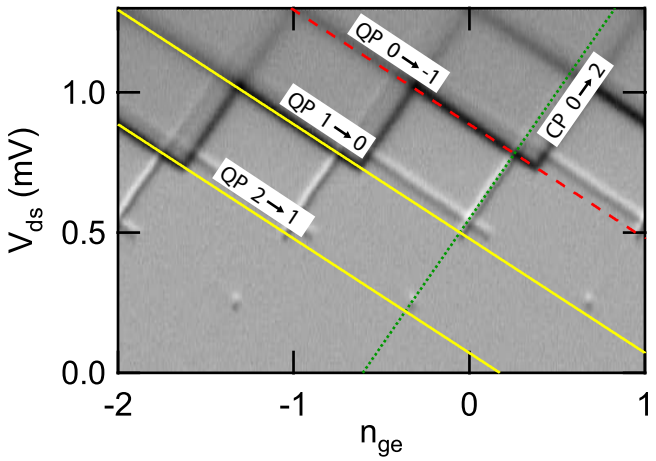

Figure 3.11: Superconducting SET Diamond with overlay showing thresholds for the tunneling processes in a JQP current cycle. The green dotted line shows combinations of V_{ds} and n_{ge} that satisfy the resonance condition between the SET island charge states with 0 and 2 additional electrons on the island. A Cooper pair that resonantly tunnels onto the SET island tunnels off in two sequential quasiparticle tunneling events. The threshold voltages for the required quasiparticle tunneling processes are illustrated by two solid yellow lines. The red long-dashed line indicates the threshold for a third quasiparticle tunneling event onto the SET island, which brings the island in a charge state where the Cooper pair resonance condition is no longer satisfied. It can be shown that this "poisoning" occurs at voltages less than the gaprise in samples where $E_C < \frac{2}{3}\Delta$.

condition for one such resonant tunneling process are indicated by a green dotted line in figure 3.11. For the JQP process to occur, the two quasiparticle tunneling processes off of the SET island must also be energetically favorable; the thresholds for these processes are indicated by solid yellow lines in figure 3.11. The JQP will therefore occur along the Cooper pair resonance line (the green dotted in figure 3.11) above both of the relevant quasiparticle tunneling thresholds (indicated by solid yellow lines).

In some samples, a third quasiparticle tunneling event may become energetically favorable at voltages below the gaprise. It can be shown (Pohlen, 1999) that this third quasiparticle tunneling process, indicated by a red dashed line in figure 3.11, will cross the Cooper pair resonance at drain-source voltages less than that of the gaprise only in samples with $E_C < \frac{2}{3}\Delta$. If this third quasiparticle tunneling event occurs, then the SET island will transition into a charge state for which a Cooper pair resonance condition is not satisfied (in figure 3.11, the $n = -1$ charge state). In this case, the JQP process will no longer be able to proceed, and we say that the JQP process has become "poisoned".

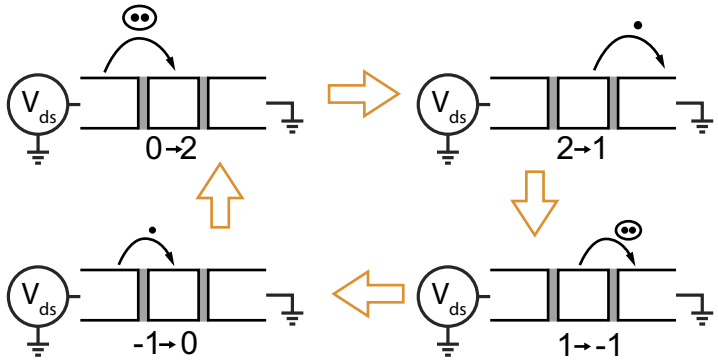

Figure 3.12: Illustration of the tunneling processes that occur in the DJQP current cycle. A Cooper pair resonantly tunnels across the left junction, followed by a quasiparticle across the right junction. A Cooper pair then tunnels across the right junction, and then a quasiparticle tunnels across the left junction. Because, in total, 3 electrons of charge are transferred during each cycle, this process is sometimes termed the "3e" process. Numbers under each illustration show the number of additional electrons on the SET island before and after each depicted tunneling process.

3.4.4 The DJQP Current Cycle

The final feature visible in the superconducting diamond of figure 3.8 is the Double Josephson Quasiparticle, or "DJQP,"[2] feature, which is circled in green. This feature occurs at the intersection of two Cooper pair resonance lines, at a far lower absolute drain source voltage than any other visible feature. It was first observed by the Delft group (van den Brink et al., 1991). Because of its combination of low power dissipation and large gain, the DJQP process is the favorite operating point for measurements made in our lab.

The DJQP process proceeds via the four tunneling events depicted in figure 3.12: two resonant Cooper pair tunneling events (of different parity), and two quasiparticle tunneling events. As with the JQP, we may deduce the location of the DJQP in a SET diamond from the conditions on V_{ds} and n_{ge} required for these processes to occur. In section 3.2.2 we noted that Cooper pair tunneling will only occur for combinations of n_{ge} and V_{ds} that define diagonal lines on the superconducting SET diamond. The DJQP process requires Cooper pair tunneling across both junctions – and will therefore lie along a right-diagonal Cooper pair resonance line and a left-diagonal Cooper pair resonance line. Two such Cooper pair resonance conditions that could comprise a DJQP cycle are illustrated with green dotted lines in figure 3.13. Their point of intersection, at $eV_{ds} = 2E_C$, is where the DJQP process occurs.

[2]Other sources refer to this process by a variety of different names. References discussing the "3e" process, the "eye," or the "Lehnert feature" are all referring to the DJQP process.

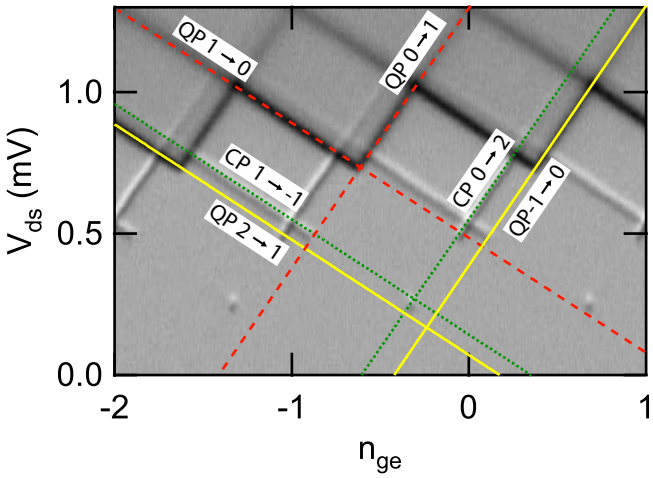

Figure 3.13: Illustration of thresholds for the tunneling processes that comprise the DJQP cycle. The DJQP cycle requires four separate tunneling processes to occur (see figure 3.12). The green dotted lines indicate the values of V_{ds} and n_{ge} that satisfy the two Cooper pair resonance conditions, while the yellow solid lines show thresholds for the two required quasiparticle tunneling processes. The red dashed lines indicate thresholds for additional quasiparticle tunneling processes onto the SET island that will "poison" the DJQP process.

In addition to the requirement that both Cooper pair tunneling processes are resonant, the DJQP feature also requires that its two component quasiparticle tunneling processes are energetically favorable. Again, we may gain intuition about the satisfaction of this requirement from the SET diamond plot; the two quasiparticle tunneling thresholds, illustrated by solid yellow lines in figure 3.13, may be simply linearly extrapolated from the SET gaprise. If the intersection of the Cooper pair resonance lines occurs at a higher V_{ds} than both of these lines, then the quasiparticle tunneling processes required for the DJQP will be energetically favorable, and the DJQP process will occur. Mathematically requiring this, from equations (3.33) and (3.34), we find that the condition for this energetic favorability is met only in samples with $E_C > \frac{2}{3}\Delta$, i.e. a charging energy that is greater than two-thirds of the superconducting gap.

In figure 3.13, two further quasiparticle tunneling thresholds are shown as red dashed lines. For appropriately high SET charging energies[3] ($E_C > 2\Delta$), the intersection of the two Cooper pair resonances will lie above these red lines, and the DJQP will be said to be poisoned. In this case, after each quasiparticle tunneling event in the schematic of the DJQP process in figure 3.12, two tunneling events will be possible: a Cooper pair resonance may occur, permitting the SET to complete the

[3]It should be emphasized that none of the SET charging diamonds shown in this thesis are in this regime. In particular, figure 3.13 is quite far from this regime

DJQP process, or a quasiparticle tunneling event may occur, allowing another quasiparticle to tunnel off of the island. If the second quasiparticle tunnels, then the current cycle will look exactly like the JQP process; in essence, when the DJQP process is poisoned, then it is only because the JQP process can proceed concurrently with the DJQP process and effectively competes with it. For this reason, however, SET samples were designed with charging energies in the range $\frac{2}{3}\Delta < E_C < 2\Delta$, so as to show a DJQP process.

The fact that the existence of a DJQP feature could be inferred from the relative positions of the JQP and the gaprise was important for our experiment. We frequently would make preliminary measurements of samples in a pumped Helium 3 refrigerator (at T=250 mK) prior to measurement in our dilution refrigerator. Oftentimes it was difficult to make precise measurements of E_c and Δ in these higher-temperature measurements, and the DJQP feature was not always directly visible. In these situations, the relative positions of the JQP and gaprise features could be used to directly test whether or not a sample would, if measured at lower temperatures, have a DJQP feature that could be used for our measurements of superconducting SET backaction.

In addition to the above described processes, it is also possible for current to flow through the SET entirely via Cooper pair tunneling events. Because this would require energy-conserving Cooper pair tunneling through both junctions, this process would only occur near $V_{ds} = 0$. Precisely because it occurs at very low applied drain-source voltage, and does not involve the creation of any quasiparticles, one might naively imagine that this process would provide ideal operating points for the SET to measure a sample while minimally disturbing it. Unfortunately, however, this is not the case. The resonant nature of the Cooper pair tunneling does not provide any directionality to the current passed through the SET, and the effects of this process on SET conductance were therefore usually not measurable. Even if it were possible to make measurements at operating points on or near this process, they would still be susceptible to the superconducting SET backaction that we will describe in section 3.5.

3.5 Theoretical description of SET Backaction in the Superconducting State

In this section, I will treat the mathematical details of the model used to predict the superconducting SET's backaction. This discussion will focus on the technical details underlying the calculations that we performed; a more phenomenological discussion of these results, oriented towards experimentally

measurable effects, will follow in section 3.6.

There are two fundamental differences between our calculation of superconducting state backaction and the backaction modeling performed in the normal state. First, because the Cooper pair box is a coherent quantum two level system (TLS), we must account for backaction and noise within the context of quantum mechanics. In order to simplify the resulting calculation, we introduce a second change: we consider the backaction in the weak coupling limit. Before launching into a full description of our model, I should briefly explain the content and the ramifications of these two statements.

To understand our treatment of backaction in the superconducting state, it is instructive to contrast superconducting tunneling with our treatment of tunneling in the normal state. Tunneling rates in the normal state were calculated from the quantum mechanical coupling of single electron states in the leads to states on the box island. There are a fantastic number of such states, and our calculations considered the combined effects of many couplings between individual states and a continuum; each such coupling is very weak[4]. The weak tunnel coupling and the continuous density of target states allowed us to presume that, once an electron had tunneled onto the island, it would lose coherence with the state from which it had tunneled; sequential tunneling events were therefore incoherent. We thus could describe our normal state treatment of the backaction as semi-classical: a quantum-mechanical coupling predicted tunneling rates, but this coupling was considered only as a weak perturbation that did not govern the evolution of an electron after it had tunneled. Tunneling events were considered as completely uncorrelated, and our rate equation considered discrete transitions between essentially classical charge states.

In the superconducting state, the presuppositions that allowed us to assume uncorrelated tunneling do not hold. The Cooper pair box is capable of maintaining quantum coherence for long times (Nakamura et al., 1999);(Lehnert et al., 2003b), and Cooper pair states on the box do not lose coherence in the same way as single electron states on the normal box[5]. To account for this, we consider the evolution of the state of the island using quantum mechanics, considering the macroscopic BCS wavefunction of the collective Cooper pair state of the box island.

[4] In particular, we considered the timescale of single electron tunneling, which is inversely proportional to the tunnel coupling, to be longer than τ_{rel}, the relaxation time of the Fermi sea of electrons, generated by electron-electron and electron-phonon interactions.

[5] Quasiparticles tunneling onto the box island, however, tunnel into a continuum in the same way as electrons in a normal metal, and quasiparticle tunneling is therefore incoherent in the same way as normal-metal single electron tunneling.

A desire to simplify this model motivated the second large difference in the superconducting modeling: we considered the SET-box interaction in the "weak coupling limit." Again, we can understand weak coupling by contrast with the the strong coupling calculation performed in the normal state. In the normal state, we considered the coupled box-SET system in its entirety; the two components could not be treated separately. When the SET caused backaction that affected the box, that in turn modified the SET's measurement. Our model accounted for the full interacting system and would reproduce these effects – with arbitrarily high coupling.

In the superconducting state, however, solving our system in this way would be complicated, and is beyond the scope of this thesis. Instead, we modeled our system in the weak coupling limit, where the SET was considered as a noise source independent of the box. At each SET operating point, we solved for a quantum noise spectrum produced by the SET, and calculated the effects of this noise spectrum on the box. At the level of the results that we will present in this thesis, such a consideration is appropriate: we looked only for the signatures of SET backaction, and do not claim to have made a precise quantitative comparison of the shape of backaction-affected Coulomb staircases.

The following subsections will treat the different facets of the quantum noise calculations performed for this thesis. First, in section 3.5.1, I will discuss how the coherence of the Cooper pair box motivates an analysis of SET noise in the frequency domain, understood as a spectral density like that introduced in section 1.2.1. In the superconducting state, however, the noise must be treated in a quantum-mechanical fashion, and so I will discuss the particularities of quantum noise. This entire section will closely follow a similar discussion included in (Schoelkopf et al., 2002). The first logical application of quantum-mechanical noise is a consideration of the noise of a resistor, also presented in (Schoelkopf et al., 2002). In Appendix A I provide a detailed derivation of the expression for this noise, and I discuss the practical ramifications of our understanding of this noise in section 3.5.2.

In section 3.5.3 I will provide an overview of the methodology used to calculate the quantum noise of the SET. This analysis will describe the use of a density matrix to account for the combined evolution of a qubit state and the complex many-body state of the SET. The underpinnings of this formalism ares described in detail in (Redfield, 1957) and (Blum, 1996); my discussion will follow the treatment of a normal SET-qubit system in (Schoelkopf et al., 2002). Detailed descriptions of the extension of this technique to treat the superconducting SET can be found in (Clerk et al., 2002; Clerk and Bennett, 2005), and especially (Clerk, 2003).

3.5.1 Quantum Noise and Two Level System Dynamics

Our first task in understanding the effect of the SET on our qubit is to understand the generic effects of noise on coherent two level systems. The calculation of these effects was introduced to me by (Schoelkopf et al., 2002); the following derivation is reproduced from that work. Our analysis proceeds directly from elementary perturbation theory. We consider a qubit acted upon by a static Hamiltonian ($\hat{H}_0$) and a perturbation from a noise source, $\hat{V}$, which will be discussed more below. In the energy eigenbasis of the static Hamiltonian, the qubit state may be represented as:

$$|\psi(t)\rangle = \begin{pmatrix} \alpha_g(t) \\ \alpha_e(t) \end{pmatrix} \tag{3.35}$$

The static Hamiltonian of our qubit ($\hat{H}_0$) is proportional to $\hat{\sigma_z}$, and we consider the perturbing effects of noise in a transverse direction:

$$\hat{V} = Af(t)\hat{\sigma}_x \tag{3.36}$$

Here, we have taken A to be a scalar variable indicating the magnitude of the coupling between the qubit and the noise source. The variable $f(t)$ indicates the value of our noisy signal; it is properly an operator in the Hilbert space of a noise source.

We are interested in isolating the response of our external noise source from the normal precession of our qubit, and so this problem is properly treated in the interaction picture, where the evolution of qubit states is governed only by the perturbing Hamiltonian. Starting from the Schroedinger picture state ket, which is expressed as:

$$|\psi_S(t)\rangle = e^{-iHt/\hbar}\,|\psi(0)\rangle \tag{3.37}$$

we create the interaction picture ket by removing the time dependence caused by the bare Hamiltonian:

$$|\psi_I(t)\rangle = e^{iH_0t/\hbar}\,|\psi_S(t)\rangle \tag{3.38}$$

In the interaction picture, this bare Hamiltonian time dependence term appears instead in the operators.

We then calculate the time evolution of the state of the qubit, using first-order time-dependent perturbation theory [see, e.g. (Sakurai, 1994)]. This gives the usual result, with the time evolution is generated purely by the perturbing Hamiltonian:

$$|\psi_I(t)\rangle = |\psi(0)\rangle - \frac{i}{\hbar}\int_0^t d\tau\ \hat{V}(\tau)\,|\psi(0)\rangle \tag{3.39}$$

To find the excitation rate of this system, we imagine a two-level system initialized in its ground state. We want to calculate the probability of finding it in its excited state as a function of time. The amplitude that the perturbation couples into the excited state is calculated as:

$$\alpha_e = \langle e|\, \psi_I(t)\rangle = -\frac{iA}{\hbar}\int_0^t d\tau\, \langle e|\, \hat{\sigma}_x(\tau)\, |g\rangle\, f(\tau) \tag{3.40}$$

Because we are in the interaction picture, the time dependence in the operator $\hat{\sigma}_x$ is generated by the static Hamiltonian $\hat{H}_0$, and may be explicitly accounted for:

$$\alpha_e = -\frac{iA}{\hbar}\int_0^t d\tau\ \langle e|\, e^{iH_0\tau/\hbar}\hat{\sigma}_x e^{-iH_0\tau/\hbar}\, |g\rangle\, f(\tau) \tag{3.41}$$

The two exponential terms, however can act directly on the $|g\rangle$ and $|e\rangle$ kets to reduce the time dependent terms to scalars. Identifying $\omega_{01} = (E_1 - E_0)/\hbar$, we find:

$$\alpha_e = -\frac{iA}{\hbar}\int_0^t d\tau\, e^{i\,\omega_{01}\tau}\, \langle e|\, \hat{\sigma}_x\, |g\rangle\, f(\tau) \tag{3.42}$$

Trivially, the term $\langle e|\, \hat{\sigma}_x\, |g\rangle$ is equal to 1. The probability of a measurement registering the qubit in its excited state is then simply the square of this amplitude:

$$p_e(t) \equiv |\alpha_e(t)|^2 = -\frac{A^2}{\hbar^2}\int_0^t\int_0^t d\tau_1\, d\tau_2\, e^{-i\,\omega_{01}(\tau_1-\tau_2)} f(\tau_1) f(\tau_2) \tag{3.43}$$

The averaged behavior of many such measurements corresponds to an ensemble average of this expression, written:

$$\bar{p}_e(t) = -\frac{A^2}{\hbar^2}\int_0^t\int_0^t d\tau_1\, d\tau_2\, e^{-i\,\omega_{01}(\tau_1-\tau_2)}\, \langle f(\tau_1) f(\tau_2)\rangle \tag{3.44}$$

This double integral describes a square in the (τ_1, τ_2) plane, as illustrated in figure 3.44. The quantity in brackets – $\langle f(\tau_1) f(\tau_2)\rangle$ – is essentially an ensemble average of the product of two measurements of the noise function $f(t)$ at τ_1 and τ_2. If the separation of these two times is longer than any correlation time in $f(t)$, then this average will be zero. In figure 3.44 this has been indicated with an orange shaded region near $\tau_1 = \tau_2$: this is the only portion of the entire domain of integration that will contribute to the final value of the integral.

To simplify the expression, we shift to the coordinates $T = (\tau_1 + \tau_2)/2$ and $\tau = (\tau_1 - \tau_2)$, illustrated as rotated axes on figure 3.44. The only portion of the integration that contributes to our result is now centered around $\tau = 0$, and we may extend the limits of integration to $\tau = \pm\infty$. Thus we find that the integral has become:

$$\bar{p}_e(t) = \frac{A^2}{\hbar^2}\int_0^t dT \int_{-\infty}^{\infty} d\tau e^{-i\,\omega_{01}\tau}\, \langle f(T + \tau/2) f(T - \tau/2)\rangle \tag{3.45}$$

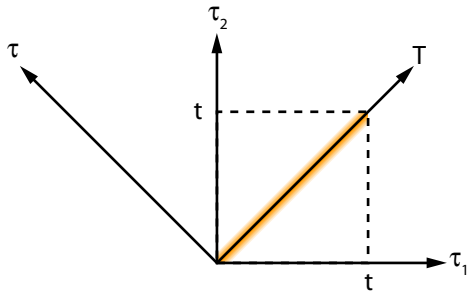

Figure 3.14: Illustration of the domain of the double integral expressed in equation (3.44). The integrals over the variables τ_1 and τ_2 in equation (3.44) cover the region described by the dashed box. Because of the small but finite autocorrelation time of the signal $f(t)$, nonzero contributions to the integral only occur in a region near $\tau_1 = \tau_2$, illustrated by an orange gradient. We transform to the difference coordinates T and τ, and then extend the limits of the integration in τ to $\pm\infty$. Because contributions to the integrand far from $\tau = 0$ are negligible, this leaves the calculated value of the integral unchanged.

If the noise process is stationary then the ensemble average of the correlation terms is dependent only on the difference in the two times, i.e.:

$$\langle f(T+\tau/2)f(T-\tau/2)\rangle = \langle f(0)f(\tau)\rangle \tag{3.46}$$

Allowing us to express the excitation probability as:

$$\bar{p}_e(t) = \frac{A^2}{\hbar^2}\int_0^t dT \int_{-\infty}^{\infty} d\tau e^{-i\,\omega_{01}\tau}\,\langle f(0)f(\tau)\rangle \tag{3.47}$$

The integral in dT may now be trivially done, as there is no T dependence in the integrand. Finally, the remaining integral, over the variable τ, is identified as a spectral density as:

$$S_f(\omega) = \int_{-\infty}^{\infty} d\tau e^{i\omega\tau}\,\langle f(0)f(\tau)\rangle \tag{3.48}$$

yielding our final expression:

$$\bar{p}_e(t) = t\frac{A^2}{\hbar^2}S_f(-\omega_{01}) \tag{3.49}$$

This predicts that an ensemble of measurements will show a linear increase in the excited state population. From this, we identify the excitation rate of our TLS:

$$\Gamma_\uparrow = \frac{A^2}{\hbar^2}S_f(-\omega_{01}) \tag{3.50}$$

as proportional to the spectral density of the quantum noise at negative frequencies. A similar analysis of this situation that treats a TLS initialized in its excited state can be used to calculate

the expected relaxation rate of a system, which we find to be:

$$\Gamma_{\downarrow} = \frac{A^2}{\hbar^2} S_f(+\omega_{01}) \tag{3.51}$$

This is proportional to the spectral density of our noise source at positive frequencies.

In classical calculations of noise, there would be no difference between these two expressions, because classical noise does not distinguish between positive and negative frequency components. The difference in our quantum mechanical calculations arises from the ordering of the operators f in equation (3.48). Because $f(t)$ is a quantum mechanical operator, the two terms in equation (3.48) do not necessarily commute, and the excitation (3.50) and relaxation (3.51) rates that a noise source impose upon a system are, in general, different. We say that the noise at positive frequency can only relax a qubit, and the noise at negative frequency can only excite a qubit; the combined spectrum which contains both of these effects is sometimes referred to as the "two-sided noise spectrum."[6]. The separation of excitation and relaxation that this derivation describes will lead to the peculiarities of the effects of noise on our qubit: we will find that noise may either selectively excite or selectively relax our qubit, and that the SET may be tuned so that its noise preferentially has either one of these effects.

In a weak measurement that is not capable of "single-shot" detection of a qubit state, we cannot observe these rates directly. Such a measurement can only report the change of an ensemble-averaged measurement; as we will see in a moment, the rate of change of an ensemble-averaged polarization is subtly different from the individual excitation and relaxation rates for a qubit. To transpose the pure excitation and relaxation rates to experimentally measurable quantities, we consider an ensemble of systems, where the probability that an element of the ensemble is found in its excited state is p_e, and the probability that one is found in its excited state is p_g. The time evolution of these ensemble-averaged populations is calculated as:

$$\frac{dp_e}{dt} = p_g\Gamma_{\uparrow} - p_e\Gamma_{\downarrow} \tag{3.52}$$

$$\frac{dp_g}{dt} = p_e\Gamma_{\downarrow} - p_g\Gamma_{\uparrow} \tag{3.53}$$

where the excitation and relaxation rates, extrapolated from equations (3.50) and (3.51), are:

$$\Gamma_{\uparrow/\downarrow} = \frac{A^2}{\hbar^2} S_f(\pm\omega) \tag{3.54}$$

[6] A classical noise that a voltmeter might measure at angular frequency ω would consist of the sum of the corresponding positive and negative frequency quantum noises, i.e. $S_{\text{classical}}(\omega) = S_{\text{quantum}}(\omega) + S_{\text{quantum}}(-\omega)$.

It is worth noting that the equations governing the time evolution of the state occupation probabilities are the same as those governing the occupations of various charge states in the normal state. A similar balancing of these rates ("detailed balance"), furthermore, can be used to find the steady state occupation probabilities towards which these rates will drive a system. If an ensemble of systems is in this steady state mixture, then the $\Gamma_{\uparrow/\downarrow}$ transitions will leave the relative populations of the two states unchanged. We can solve for these steady state populations, then, by setting the time derivatives in equations (3.52) and (3.53) to zero:

$$p_g = (\Gamma_\downarrow/\Gamma_\uparrow)p_e \tag{3.55}$$

Enforcing that the sum of the state occupation probabilities is 1, we find:

$$p_g = \frac{\Gamma_\downarrow}{\Gamma_\downarrow + \Gamma_\uparrow} \tag{3.56}$$

$$p_e = \frac{\Gamma_\uparrow}{\Gamma_\downarrow + \Gamma_\uparrow} \tag{3.57}$$

Instead of considering the separate probabilities for the ground and excited states, we consider the experimentally accessible polarization of a state P, which is simply calculated from the occupation probabilities of our two states:

$$P = (p_g - p_e) \tag{3.58}$$

In the steady state, this polarization takes the value:

$$P_{SS} = \frac{\Gamma_\downarrow - \Gamma_\uparrow}{\Gamma_\downarrow + \Gamma_\uparrow} \tag{3.59}$$

We may also calculate another experimentally relevant quantity, the rate of decay of an arbitrary mixture of states towards this steady state polarization. We solve for this by considering the time evolution of a polarization that differs from the steady state value. Given a polarization expressed as

$$P(t) = P_{SS} + \Delta P(t) \tag{3.60}$$

We will solve for the evolution of $\Delta P(t)$ in time, and, therefore, the relaxation of the mixture. First, the normalized ground and excited state occupation probabilities that produce this polarization are:

$$p_e(t) = p_{e_{ss}} - \Delta P(t)/2 \tag{3.61}$$

$$p_g(t) = p_{g_{ss}} + \Delta P(t)/2 \tag{3.62}$$

We wish to find the rate of change of $\Delta P(t)$. By differentiating (3.58), we see that the rate of change of the excess polarization is equal to the rate of change of the total polarization (trivially, the $\frac{d}{dt}P_{SS}$ term this generates vanishes). The rate of change of the total polarization, meanwhile, may be calculated as the difference of equations (3.52) and (3.53):

$$\frac{d}{dt}\Delta P(t) = \frac{d}{dt}P(t) = 2p_e\Gamma_\downarrow - 2p_g\Gamma_\uparrow \tag{3.63}$$

Substituting the expressions for p_e and p_g from equations (3.61) and (3.62), we can show that:

$$\frac{d}{dt}\Delta P(t) = -\Delta P(t)\left(\Gamma_\uparrow + \Gamma_\downarrow\right) \tag{3.64}$$

This equation predicts a decay of the excess polarization ΔP that is proportional to the magnitude of ΔP. It may be concisely interpreted to say that a nonequilibrium polarization will exponentially relax to its equilibrium value, with a time constant that is proportional to the sum of the quantum noise at positive and negative frequencies corresponding to a qubit's splitting.

Equations (3.59) and (3.64), together with the expression relating quantum noise to transition rates [equation (3.54)] summarize the major results of this section. They show that quantum noise is capable of either selectively exciting or selectively relaxing a qubit, and that, in measurements, excitation and relaxation effects may be separated through observations of the polarization and relaxation time of a qubit.

3.5.2 Quantum Noise Effects of the Environment

Having understood the effects of quantum noise in section 3.5.1, our next task is to explain the calculation and interpretation of such noise. In this section, we will discuss the quantum noise generated by a simple resistor, which is derived in detail in Appendix A. This calculation is immediately relevant to our experiment, as it predicts the noise effects of the transmission lines that bring signals to our qubit. The understanding that proceeds from these calculations motivated our attempts to carefully design our qubit environmental impedance (described in section 4.2.2), and also provided an impetus for the measurements of the qubit's environment that are described in section 8.1.

From equation A.17 in appendix A, the two-sided noise spectrum of a resistor is expressed as:

$$S_V(\omega) = \frac{2R_0\hbar\omega}{1 - e^{-\hbar\omega/k_BT}} \tag{3.65}$$

This function is plotted in figure 3.15 at several different temperatures. We consider first the plot of the quantum noise of a resistor at zero temperature, shown as a solid blue line. Both the positive

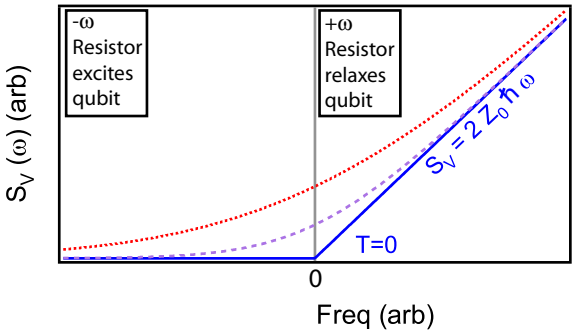

Figure 3.15: Quantum Noise spectrum of a simple resistor. Different curves show spectra calculated at T=0 (blue solid line) and at two warmer temperatures (purple dashed and red dotted lines). The positive frequency quantum noise of the resistor is always larger than the corresponding negative-frequency component, but, for $\hbar\omega \approx k_B T$ the difference between the two is small. Thus a cold resistor can only relax a qubit, while a hot resistor can drive both exciting and relaxing transitions in a qubit.

and negative frequency structure of this spectrum may be interpreted within our understanding of the physics of a resistor. The spectral density at negative frequencies is zero, which mathematically expresses the fact that a zero temperature resistor is unable to give up energy to any other system. At positive frequencies, we see a linear rise in the noise spectral density, which we understand as the voltage fluctuations from the zero-point motion of the harmonic oscillators that we have considered to comprise our resistor. This positive frequency noise will stimulate the relaxation of a two level system coupled to a resistor, even when that resistor is at zero temperature. In the limit where $\hbar\omega \gg k_B T$, this remains true: a cold resistor, in other words, can absorb a photon to relax a qubit, but cannot excite it. This expression may be combined with equation (3.50) or equation (3.51) to predict the excitation or relaxation rate of a system. At zero temperature, we see that this predicts qubit relaxation rates that linearly increase with the frequency splitting of the qubit. Because the time required for qubit operations has the same scaling, however, we may discuss a "Q" ($= \omega_{01}/\Gamma_{\downarrow}$) imposed by the environment that describes the typical number of qubit operations possible before the environment disturbs the qubit state. For a pure resistor at zero temperature, this does not vary with frequency.

The scaling of the quantum noise spectrum with resistance provided the motivation for our design of the Cooper pair box's environmental impedance. A resistor coupled to a qubit does not change the steady state polarization of the qubit when in equilibrium, because, when equation (3.65) is inserted into equation (3.59), the factors of resistance cancel. However, when calculating the rate at which

this equilibrium is approached [inserting (3.65) into (3.64)], it becomes apparent that increasing a resistance coupled to a qubit causes a corresponding increase in the timescale of the qubit relaxation at all frequencies.

When designing our Cooper pair box samples, this fact motivated the careful consideration of the environmental impedance. The transmission lines bringing signals to our box appeared as an impedance with a quantum noise spectrum that would affect the state of our qubit. We designed our box to have an environmental impedance that was $50\,\Omega$ at all relevant frequencies. By doing this, we hoped to limit the relaxing effects of the environment on our qubit, and to determine variations in the qubit relaxation rate that were proportional to the SET operation alone.

The expression for the quantum noise of a resistor also lends itself to physical interpretation in the opposite limit, where $\hbar\omega \ll k_B T$. In this regime, $S_V(+\omega)$ and $S_V(-\omega)$ are nearly equal, and can be shown to be equal to $S_V(|\omega|) = 2R_0 k_B T$. When calculated as a symmetrized noise $[S_V(+\omega) + S_V(-\omega)]$, which may be measured classically, this gives the familiar Johnson noise result.

3.5.3 Calculation of SET Quantum Noise

The calculation of the quantum noise of the SET is more complicated than the corresponding calculation for a simple resistor. For this reason I will only provide a sketch of the structure of the theory underlying our modeling. My discussion is based on the formalism for the treatment of the quantum noise of the normal state SET included in (Schoelkopf et al., 2002). The superconducting SET near the DJQP feature can be treated in a very similar fashion, and is explained briefly in (Clerk et al., 2002) and in more detail in (Clerk, 2003). Additional notes about superconducting SET backaction modeling may also be found in (Clerk and Bennett, 2005), although the treatment therein is more relevant for an understanding of backaction effects in nanomechanical systems.

To understand the equilibrium state and transition rates in the SET-box system, we will use an equation that, by analogy with equation (2.9), encapsulates the time evolution behavior of all relevant SET-box charge state combinations. In the normal state, such an equation was simple to conceive and to construct: we built it directly from the transition rates between discrete states. Our superconducting treatment is necessarily more complicated, as the evolution of the state of the box is quantum mechanical, and cannot be described simply by uncorrelated transitions between discrete states. Still, we wish our treatment to reproduce the probabilistic consideration of an ensemble of measurements that was understood to motivate our calculations in the normal state. The correct

formalism for the consideration of an ensemble of quantum systems is the density matrix. An excellent explanation of density matrices applied to similar systems can be found in (Blum, 1996).

Quantum noise can be calculated from the time evolution of a density matrix for the full SET/qubit system [see e.g. (Schoelkopf et al., 2002) for a treatment using a normal SET]. Such a density matrix must account for all degrees of freedom in this system, including the qubit, individual fermion states in the SET, and the coupling between the two[7]. When the time evolution of this density matrix is calculated using standard quantum mechanical techniques, the quantum noise produced by the SET can then be inferred from the resulting behavior of the qubit.

Our SET backaction modeling is based on techniques outlined in (Schoelkopf et al., 2002), where the full time evolution of the density matrix for the SET-box system is not explicitly calculated. Instead, several approximations are made to produce a simplified expression of the state of our system that involves only the relevant degrees of freedom. The calculation begins with a consideration of single electron tunneling in the normal SET as a weak perturbation to the full system Hamiltonian. This tunneling perturbation, written $\hat{H}_T$, is separated from the remaining terms which constitute the "bare" Hamiltonian $\hat{H}_0$ of the system. A von Neumann equation is derived [(58) in (Schoelkopf et al., 2002)] that expresses exactly the evolution of the system affected by the SET tunneling perturbation in the interaction picture. This equation is then simplified by tracing out the microscopic fermion degrees of freedom.

To further simplify the resulting expression, two assumptions are made. First, it is assumed that the time scale for electron relaxation in the SET is faster than any other time scale in the problem. Because of this fact, we assume that the states of the SET island and leads are at all times expressed as Fermi distributions. This approximation, known as a Born approximation [see e.g. (Carmichael, 1999)], eliminates the possibility of coherent dynamics of single electron states in the Fermi seas on the SET. The second approximation, a Markov approximation, assumes that the behavior of the qubit is a function only of its current state, and not of its past history. This approximation is also allowed by the fast decay of the fermion states in the SET leads, which cannot "store" information from the qubit – so that the qubit's current evolution is not affected by any consequence of its past dynamics.

Working with these two approximations, a master equation is derived that predicts the evolution

[7] This coupling is parameterized by a coupling strength A, which is taken to be a small parameter so that strong coupling effects can be ignored.

of the density matrix as a function of its state. We state this in simple matrix form:

$$\frac{d}{dt}\vec{\rho} = \mathbf{M}\vec{\rho} \tag{3.66}$$

to emphasize its similarity to the master equation underlying our normal state backaction calculations [see equation (2.9)]. In (Schoelkopf et al., 2002) a similar expression appears as equation (63), where the matrix $\mathbf{M}$ is expressed as a power series in the qubit-SET coupling parameter A. The code that we used to model the backaction of the superconducting SET was based on calculations using a similar matrix. Because the microscopic Fermion degrees of freedom have been traced out, these treatments use reduced density matrices with only 8 elements, corresponding to the usual 4 density matrix elements for a two level system, repeated for each of the 2 SET charge states[8]. To compute SET quantum noise, the elements of this density matrix are combined into an 8×1 vector. If a state with qubit state g and SET charge state n is represented as $|g_n\rangle$, then this density matrix vector can be written as:

$$\vec{\rho} = (\langle g_0|\,\rho\,|g_0\rangle\,, \langle g_1|\,\rho\,|g_1\rangle\,, \langle e_0|\,\rho\,|e_0\rangle\,, \langle e_1|\,\rho\,|e_1\rangle\,, \langle g_0|\,\rho\,|e_0\rangle\,, \langle g_1|\,\rho\,|e_1\rangle\,, \langle e_0|\,\rho\,|g_0\rangle\,, \langle e_1|\,\rho\,|g_1\rangle)$$

The diagonal elements of a density matrix correspond to classical state occupation probabilities, and we may therefore construe the first four elements of this "density matrix vector" as the occupation probabilities for the corresponding states. The last four elements of this vector describe superposition states of the qubit, and cannot be interpreted so simply.

The time evolution of this density matrix vector, in equation (3.66), is then used to calculate the quantum noise of our SET. We solve for the steady state polarization and relaxation time of our qubit while it is coupled to the SET, and, from the relations in section 3.5.1, explicitly calculate the SET quantum noise that produces them. Computationally, this is done by considering how the two steady-state density matrices calculated in the zero-coupling case mix together when a finite (but small) coupling is introduced.

With zero SET-box coupling, the evolution of the SET and the box are independent. In this case our system has two steady states, which correspond to the zero-eigenvalue eigenvectors of $\mathbf{M}$; they are expressed in equation (66) of (Schoelkopf et al., 2002). These vectors correspond to mixtures of SET charge states[9] with the qubit in either the ground (1st eigenvector) or excited (2nd

[8] In the normal state SET, tunneling may be considered where the SET switches between two different charge states only. Because electron states in the SET are taken to decay very quickly to a Fermi distribution, we do not consider superpositions of SET charge states.

[9] determined by tunneling rates on and off of the SET island

eigenvector) state. When we then "turn on" the qubit-SET coupling, the degeneracy of these two modes is broken. We find a zero-eigenvalue mode from which we infer the steady state polarization of the qubit, and a slow relaxation (least negative eigenvalue) mode that describes the rate at which linear combinations of box states relax to their steady state steady-state mixture. This calculation is performed in detail in (Schoelkopf et al., 2002). Implemented computationally, it was the core of the calculations that that motivated our experiments.

3.6 Modeling of SET Quantum Noise: Phenomenological Results

The backaction predicted by the model described in section 3.5 may be understood nearly independently of an understanding of the mathematical details of the model. A simple phenomenological understanding of the mechanism of superconducting SET backaction proceeds as follows: on the DJQP, current is understood to flow through a current cycle described in 3.4.4, combining two Cooper pair tunneling events and two quasiparticle tunneling events. At SET operating points near (but not on) the DJQP feature, one or both of the Cooper pair tunneling processes will be slightly off-resonance, and the SET will therefore have a tendency to absorb or emit quanta of energy to bring these tunneling processes closer to resonance. If a Cooper pair tunneling event requires additional energy to satisfy the resonant Cooper pair tunneling condition, we say that this tunneling process is "below resonance." If, after accounting for the energy gained from the applied voltage and lost to the charging energy, a Cooper pair tunneling event has more energy than the resonant condition requires, we say that it is detuned "above resonance." When the SET is tuned to be above or below resonance, it will have a tendency to emit or absorb quanta of energy to compensate for this detuning and effectively bring a process back into resonance. This tendency to absorb or emit photons across a narrow range of frequencies (which correspond to the detuning of a Cooper pair resonance) may be identified with the quantum noise of the SET, so that an operating point below resonance contributes to the positive frequency quantum noise of the SET, and an operating point above resonance contributes to the negative frequency quantum noise of the SET.

The box polarization and relaxation time is affected by this purely quantum component of the SET's noise, but may also be affected by noise from two other sources. First, the resistive environment of the Cooper pair box may be modeled as a quantum noise source with a predominantly relaxing effect on the qubit. Second, the classical noise from the fluctuating voltage on the SET

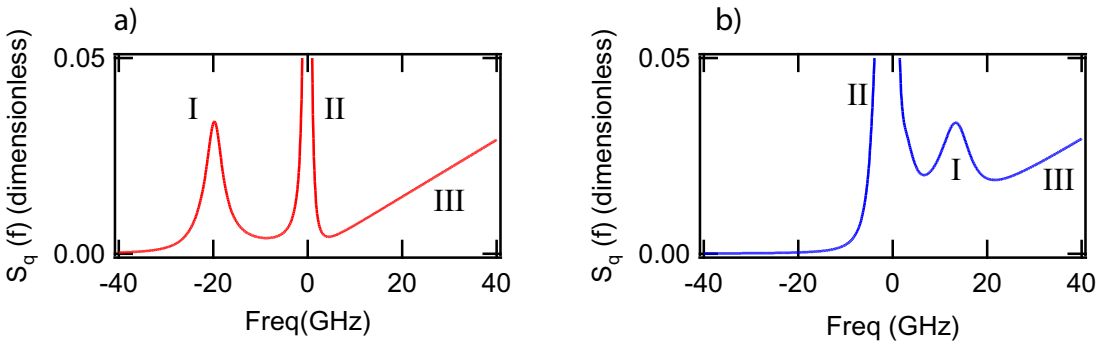

Figure 3.16: Sample quantum noise spectra of the SET generated at two different operating points. Contributions to these spectra may be generally decomposed into contributions from 3 different sources. A large resonance (I) can appear at negative (a) or positive (b) frequencies, where one of the Cooper pair resonances in the DJQP cycle strongly emits or strongly absorbs energy from the Cooper pair box. A large peak (II) at low frequencies that is roughly symmetric across $f = 0$ appears because of the classical charge state fluctuations of the SET island. Finally, a linear rise in the charge spectral density at positive frequencies (III) is due to the quantum noise of the resistive environment of the Cooper pair box. The noise is expressed in dimensionless units of charge noise, obtained by normalization to (e^2/Γ_{qp}), where Γ_{qp} is the quasiparticle tunneling rate at the DJQP. The operating points where these spectra are generated are $\sim 3\%$ of an electron away from the center of the DJQP; the data in part a were modeled at a voltage .084 mV above the center of the DJQP, while the data in part b were generated for a voltage .024 mV below the center.

island, coupled to the Cooper pair box, adds noise that is symmetric at positive and negative frequencies, and therefore equally likely to excite or relax the Cooper pair box. The modeling code used to calculate the noise acting upon our box accounted for both of these effects.

The combined effects of these sources are expressed as a spectral density across a range of both positive and negative frequencies. Figure 3.16 shows two such spectra where the qualitative difference in the spectral signatures of these three different effects is apparent. The first effect, the pure quantum noise of the detuned Cooper pair resonances, appears as a peak in the calculated quantum noise of the SET (labelled as I in figure 3.16). This peak may be at positive frequency (if the SET is tuned below a resonance) or at negative frequency (when the SET is tuned above a resonance). The frequency at which these peaks occur is determined by the frequency detuning of the corresponding Cooper pair resonance, and varies linearly with SET operating point. The width of these peaks is proportional to Γ_{qp}, the quasiparticle tunneling rate off of the SET island at the DJQP feature.

The classical voltage noise due to the charge state fluctuations on the SET island appears as a large peak in the spectral density of the SET (II on figure 3.16). This signal is symmetric in

frequency, reflecting the fact that this noise is equally capable of exciting and relaxing a two-level system to which it is coupled.

The relaxing effect of the radiative environment on the Cooper pair box qubit causes a feature in the calculated quantum noise spectrum that is denoted with a III in figure 3.16. This noise is calculated from the usual expression for the quantum noise of a resistor (Schoelkopf et al., 2002):

$$S_V(\omega) = \frac{2R\hbar\omega}{1 - e^{-\hbar\omega/k_B T}} \tag{3.67}$$

For the purposes of our modeling, the resistive environment was presumed to be at zero temperature, where equation (3.67) reduces to a simple linear rise in the environmental noise at only positive frequencies. The magnitude of this effect is proportional to the characteristic impedance of the environment at the qubit frequency, and, expressed in units of charge noise, includes a factor proportional to the square of the box gate capacitance (C_B^2) from the capacitive coupling of this voltage to the Cooper pair box island.

Spectra such as that in figure 3.16 were useful for understanding the quantum noise in a range of frequencies for a single SET operating point, but, for the purposes of our experiment, they lent little insight into trends that might provide an unmistakable signature of the backaction of the SET. For this reason, when attempting to motivate experiments searching for the signatures of SET backaction, we considered the variation of SET quantum noise at an array of operating points, with the frequency of the noise held fixed. Furthermore, rather than presenting the noise as a spectral density – which is not directly accessible experimentally – we considered the noise at each operating point symmetrized $[S_V(+\omega) + S_V(-\omega)]$ or antisymmetrized $[S_V(+\omega) - S_V(-\omega)]$ so as to be proportional to the relaxation rate or the polarization of a qubit acted upon by the SET, respectively[10]. This allowed us to calculate the effects of SET noise as a quantity measurable in the Cooper pair box, as a function of SET controls that could be directly set experimentally.

A plot of the predicted antisymmetrized SET quantum noise of the SET at 20 GHz shown in figure 3.17 (n.b. this plot does not include the relaxing effect of the Cooper pair box's environment. While those effects were included in our calculations, they obscured the SET quantum noise effects we wish to demonstrate with figure 3.17). The effects discussed in relation to the noise spectrum of 3.16 may be readily interpreted in the context of the calculations made for this plot.

[10] Properly, from section 3.5.1, we know that it is the *fractional* asymmetry of the noise, $\{[S_V(+\omega) - S_V(-\omega)] / [S_V(+\omega) + S_V(-\omega)]\}$ which determines the polarization of the qubit. Our plots, nevertheless, use the plain antisymmetrized noise, which better illustrates the trends in the backaction of the SET.

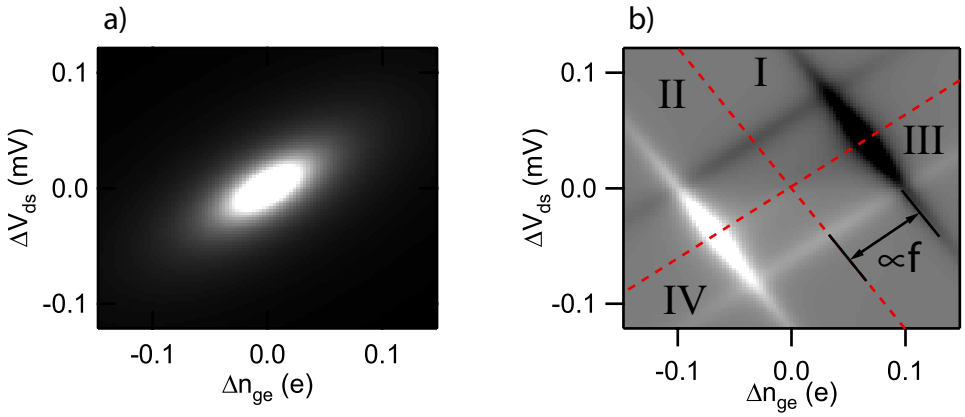

Figure 3.17: Current and Antisymmetrized SET quantum noise at 20 GHz, plotted against SET operating point relative to the center of the DJQP feature. a) The calculated current through the SET DJQP feature, as a function of operating point. This approximates the measured current in our SET samples; the SET could only be used to make measurements at operating points at or near the central white region. b) Antisymmetrized SET quantum noise vs. operating point. Red dotted lines identify the location of the Cooper pair resonances, while roman numerals identify regions of operating point space where I) both Cooper pair tunneling processes are detuned so as to have more energy than the resonant condition requires, II and III) one of the Cooper pair tunneling processes is above resonance, and the other is below, and IV) both Cooper pair tunneling processes are below resonance. In regions I and IV, the Quantum noise of the SET will predominantly excite or relax the qubit, whereas in regions II and III the SET may have an exciting and a relaxing effect. At a given operating point, the preferred frequency at which the SET will relax or excite a qubit is proportional to the distance from each of the resonance lines.

Selective excitation or relaxation due to detuned Cooper pair resonances, in the quantum noise spectrum of figure 3.16, produced a peak in the SET quantum noise proportional to the frequency detuning of a Cooper pair resonance. In figure 3.17, we only see this peak in quantum noise at operating points where the detuning of a Cooper pair resonance matches the frequency of the quantum noise being considered. The two Cooper pair resonances are indicated in figure 3.17 by diagonal dashed red lines, and the energy detuning from each of these resonances may be inferred from the perpendicular distance between an operating point and one of these lines. Running parallel to the Cooper pair resonance lines, we therefore observe strong peaks in the quantum noise for lines of operating points where the detuning of a Cooper pair resonance matches 20 GHz, the frequency of the quantum noise that is being considered in figure 3.17.

Antisymmetrized quantum noise reflects the tendency of off-resonance Cooper pair tunneling to either excite or relax the qubit measured by the SET. Where the SET has a tendency to excite a qubit – above resonance – the antisymmetrized quantum noise will be strongly negative, which is reflected by the black regions in figure 3.17. Similarly, where the SET has a strong tendency to relax

a qubit, below resonance, the strong asymmetry of the quantum noise towards positive frequency is reflected in a range of points that appear in white.

The plot in figure 3.17 is divided into four regions by the two Cooper pair resonance lines. For operating points in region I, Cooper pair tunneling across either junction is above resonance, and the quantum noise effects of the SET are only at negative frequencies. Similarly, in region IV, Cooper pair tunneling across both junctions is below resonance, and the purely quantum part of the SET's noise is seen only at positive frequencies. When a SET is tuned to an operating point in region II or region III it will demonstrate a tendency to emit during one part of the DJQP cycle, and to absorb during another part. Because these two competing effects are difficult to vary and to measure independently, this is deemed to be a less experimentally interesting region.

This analysis indicates a perimeter of operating points surrounding the DJQP feature which can reset the state of a qubit with a 20 GHz energy splitting. Because they present a closed ring of SET operating points that spell death for our qubit, we have termed this family of operating points "the moat." If the antisymmetrized noise is plotted at a different frequency, this moat occurs at a different radius around the DJQP feature, and so, when planning SET operation, one must consider a family of moats that can reset qubits at different energy splitting. In figure 3.17 I have suggested this with bars showing that the size of the moat is proportional to the frequency of the quantum noise considered in the plot.

It is important to note that the moat feature, for appropriately high frequencies, extends beyond the region in SET operating point space where current flows. At such operating points, the SET is unable to complete the DJQP process – because at least one of the Cooper pair resonances is so far detuned that it effectively does not occur. Still, however, at these operating points the SET may absorb or emit single quanta of energy to step through one (or half) of a DJQP cycle. For operating points where this is the case, the SET will show strong quantum noise effects even if its measurement is effectively "turned off."

The SET noise spectra in figure 3.16 also showed an increase at both positive and negative low frequencies from the classical noise of charge fluctuations on the SET island. Signatures of this effect are difficult to see on plots such as figure 3.17, precisely because there is not a marked asymmetry in the noise that they produce, but they are readily apparent when the symmetrized quantum noise of the SET is plotted in the same way, as in figure 3.18. There, the large classical noise from the fluctuating charge state of the SET island appears as a white region at the intersection of the two

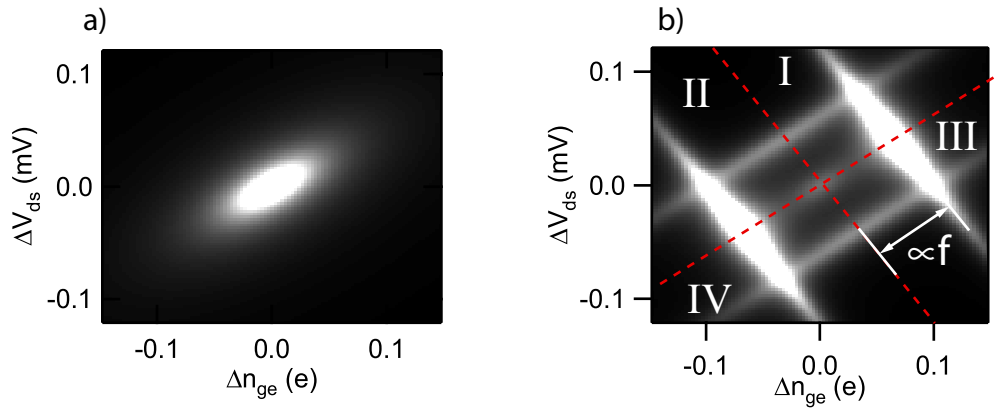

Figure 3.18: Symmetrized SET quantum noise at 20 GHz, plotted vs SET operating point. a) Current through the SET at operating points near the DJQP feature. b) The symmetrized quantum noise of the SET, which is proportional to the SET-induced relaxation rate, is large where large currents are flowing in the SET (center of plot), or where the SET detuning matches the qubit frequency.

resonance lines. The symmetrized SET quantum noise in figure 3.18 shows the same "moat" feature that we discussed in relation to figure 3.17, which is due to the purely quantum part of the SET's noise.

Chapter 4

Fabrication of Samples

Samples for the normal state measurements described in this thesis, and for the first superconducting measurements, were fabricated at Chalmers University in Sweden, by David Gunnarsson, in the group of Per Delsing. For later measurements (after 2003), and particularly for those where the environmental impedance of the Cooper-pair box was considered and carefully engineered, samples were fabricated at Yale. The vast majority of the fabrication work at Yale was completed by Hannes Majer, to whom I am indebted; the following description, of the work done at Yale, is little more than an overview of his process, distilled from the few months where I was assisting him.

4.1 Dolan Bridge Fabrication Process

All samples measured were fabricated out of Aluminum-Aluminum Oxide-Aluminum tunnel junctions, using the Dolan bridge double-angle evaporation technique and electron-beam lithography. The Dolan bridge uses a bilayer of two different resists: A thick ($\sim 700\,\mathrm{nm}$) bottom layer of easily-developed resist is first deposited, followed by a thinner ($\sim 100\,\mathrm{nm}$) upper layer which requires a much larger dose to be developed. The two different resists used were different formulations of Polymethyl Methacrylate (PMMA).

An electron beam then selectively exposed a pattern in the resist corresponding to our sample design. The electron beam was provided by a Sirion FEI scanning electron microscope, converted for electron-beam lithography using the Nanometer Pattern Generator System (NPGS) software produced JC Nabity Lithography Systems, Inc. (http://www.jcnabity.com/). Beam doses were adjusted so that the pattern was faithfully represented in the upper layer of resist, while the lower layer of resist was developed over a much wider area – thus producing a region of "undercut." In

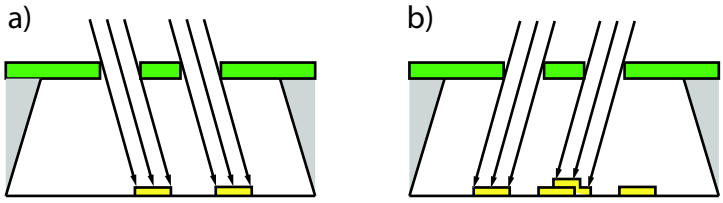

Figure 4.1: Schematic of Dolan Bridge/double angle evaporation technique for fabrication of Josephson junctions. A bridge of resist (shown in cross section) is suspended above a silicon substrate. Aluminum is evaporated at two different angles, with an oxidation between the evaporations, to produce two metal reservoirs connected by a tunnel junction.

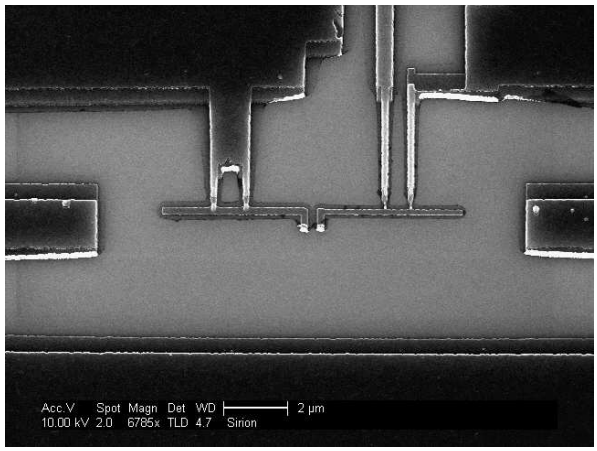

Figure 4.2: SEM Image of Box-SET Sample. The box is in the left half of the image, while the SET is in the right half of the image. The "ghost" image from the double-angle evaporation process is clearly visible.

regions where two exposed areas are nearby, this undercut can create suspended bridges (see figure 4.1)

Aluminum was then evaporated at two different angles onto the resulting mask. If the bridge is designed correctly, then images of these two separate evaporations will overlap in the area underneath the bridge (see figure 4.1b). If a small amount of an argon-oxygen mixture is introduced into the evaporator between the two evaporations, a thin oxide barrier will grow on the surface of the bottom evaporation. This oxide barrier will have a typical thickness of a few atomic layers: thick enough that fluctuations in thickness do not create short circuits between the two leads, and yet thin enough that electrons are able to tunnel between the two aluminum reservoirs.

The resulting samples could then be viewed in the SEM, although doing so usually destroyed the Josephson junctions in our devices. An SEM image of one of our samples is shown in figure 4.2, where the "ghost" image from the double angle evaporation process is clearly visible. Junctions are

formed where the two evaporations overlap – where the leads, extending from the top of the image, overlie the islands, which are in the middle of the image.

4.2 Design considerations

While the theory of SET fabrication may be simple, in practice it proved to be one of the most difficult tasks encountered in the completion of this thesis. This was due, however, largely to the strict requirements for devices: our design required that electron-beam lithography be accurately executed at an extremely wide range of size scales. Small junctions in the SET required accurate lithographical features smaller than 100 nm, while careful engineering of the environmental impedance required wide scale exposure across a 5 mm chip. The following sections describe the various requirements imposed by different facets of our experiment, how these requirements translated into considerations for our fabrication process.

4.2.1 SET Design Considerations

Modulations in conductance in the SET are caused by Coulomb blockade (see section 2.2.2), where a single electron added to the SET island causes an increase in electrostatic energy that forbids the addition of further electrons. The characteristic energy for this process is the charging energy of the SET ($E_C = \frac{e^2}{2C_\Sigma}$), typically expressed in Kelvin. We require that this energy scale be large relative to the other relevant energy scales in the problem. In particular, this charging energy must be much larger than the available thermal energy ($k_B T$), so that thermal excitations cannot bring additional electrons onto a blockaded island.

Measurements in the superconducting state imposed a further, stricter restriction on the charging energy of the device: for a SET to have a DJQP feature, the preferred operating point for our superconducting measurements, its charging energy must satisfy $2\Delta > E_C > \frac{2}{3}\Delta$(Pohlen, 1999), where Δ, the superconducting gap of Aluminum, was typically found to be $190\,\mu$V. For the purposes of our fabrication, this meant that SETs must be fabricated with $E_C > 1.45\,$K or, more practically, must have a total island capacitance less than approximately 600 aF.

The total capacitance of the SET island contained contributions from the geometric capacitance of the SET island, and from the SET junctions. The geometric capacitance of the SET island to grounded leads nearby was typically 200 aF. This number would vary somewhat with our particular design, but could be effectively calculated using electrostatic modeling software such as Ansoft

Maxwell.

The capacitance of the junctions, which consist of a thin insulating barrier between two large conductors, is typically proportional to their area. The limit on the total island capacitance therefore translated into a requirement that the Josephson junctions in the SET be small. For the junctions fabricated at Chalmers, the junction capacitance was found to be approximately $50\,\mathrm{fF}/\mu\mathrm{m}^2$ of junction area; The capacitance per area of junctions fabricated at Yale was probably not significantly different. After accounting for the 200 aF geometric capacitance of our SET island, we found ourselves constrained to fabricate SET junctions with a total capacitance less than 400 aF – which could therefore be no larger than approximately 70 nm square.

Fabricating such small junctions is a difficult task; it requires very precise electron beam doses, patterned with extreme accuracy. The requirements of our particular junctions were at the limits of the capabilities of the electron-beam pattern generating system we used.

4.2.2 Cooper Pair Box Design Considerations

Controlling the electron beam sufficiently well to design correctly sized junctions for our SET was a difficult task, but it was made more so by the competing design constraints of our Cooper pair box. The design for the Yale-fabricated Cooper pair box samples required large features (see figure 4.3) that both introduced additional geometric capacitance to the SET island, and degraded the precision with which the SET pattern could be applied.

In an attempt to control the environmental impedance seen by the Cooper pair box, leads controlling the box and the SET were carefully engineered as tapered transmission lines (see figure 4.3). High frequency signals propagating down electrical leads do so as waves travelling down transmission lines(Pozar, 2005). For signals on a chip, there are a variety of conductor geometries that can support wave propagation(K.C. Gupta and Bhartia, 1996). Coplanar Waveguide (CPW)(Simons, 2001) was chosen these experiments for several reasons. Most importantly, a CPW transmission line is scalable: if the center trace width and the gap of a coplanar waveguide transmission line are tapered in the correct proportions, then the physical size of a transmission line can be changed while the characteristic impedance of that line remains constant. In our samples, because of the high dielectric constant of the silicon chips and circuit board substrates, this scaling was particularly easy. Our coplanar waveguide structures could be considered in the limit of an infinitely far removed back ground plane, and tapering the size of the coplanar waveguide leads was accomplished via a

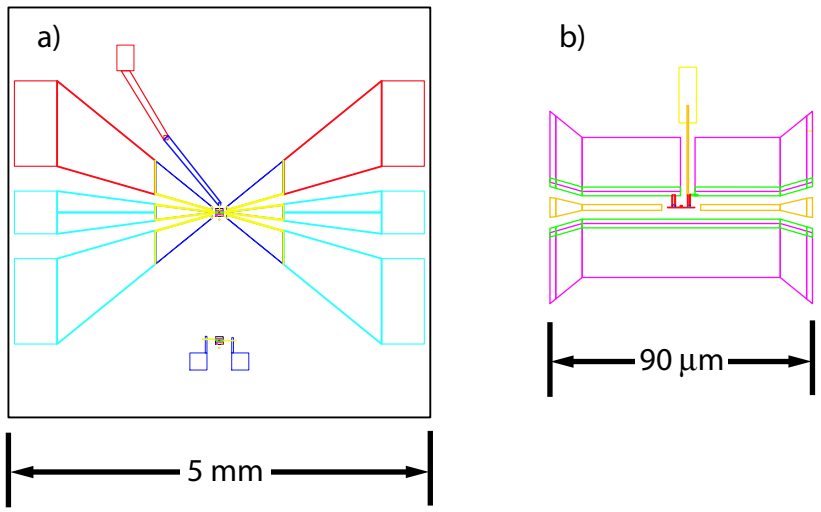

Figure 4.3: a) Diagram of large-scale e-beam pattern used for Box-SET samples. b) Enlarged diagram showing small features and device. Different colors in the same diagram indicate different e-beam writing steps.

simple linear taper of all of the relevant CPW dimensions.

A CPW transmission line also has a geometry reminiscent of coaxial cable, with a center lead that is surrounded by two grounded conductors. Because of this geometrical similarity, many launchers exist that can smoothly transition between coaxial and CPW geometries; smooth geometrical transitions minimize discontinues in impedance, and, therefore, reflections.

While CPW transmission lines were an indispensable part of the design of our experiment, they did significantly complicate the fabrication. The large-scale CPW structure required by our experiment (see figure 4.3) were written with a different beam current in the SET, in a separate step, and significantly increased the time required to write each sample. Because of this additional writing time, and because of the large physical area of each chip occupied by the CPW structures, it was impossible to write dose arrays, which might otherwise be used to fine-tune the e-beam current and carefully adjust junction size.

Furthermore, our fabrication suffered from the proximity effect, where scattered electrons during the writing process contributed exposure to resist with an approximately 3 μm radius of any desired feature. CPW structures near the device (see figure 4.3b), through the proximity effect, added a small amount of exposure to the region where devices were fabricated, and rendered an already unstable process less so.

The large CPW ground planes close to our fabricated device caused one further problem: they

introduced additional capacitance to the SET island and lowered its charging energy. As described above, the requirement of a large charging energy placed an upper limit of approximately 600 aF on the total capacitance of the island. Estimates from electrostatic modeling of our design suggested that a large fraction of the geometric capacitance of our SET island was introduced by the large CPW ground planes.

4.3 Additional Fabrication Ventures

Of the many side inquiries and blind alleys explored in the fabrication of samples for this thesis, one particular venture deserves mention in this work. This work, done as an attempt to fix problems seen in the penultimate round of Yale-made samples, ultimately proved unsuccessful. We report it here so that future work does not fall prey to the same trap.

All circuit diagrams shown thus far in this thesis, and all diagrams used for fabrication, show the Cooper-pair box as an isolated metal island, connected via tunnel junctions to a very large grounded reservoir. When samples with this design were measured the Coulomb staircase was almost always purely periodic in 1 electron of gate charge (detailed measurements of this "quasiparticle poisoning" are discussed in section 7.5). This is a situation that is by no means universally true of Cooper-pair box samples: Cooper pair box samples measured in 2003 at Yale, and samples measured by other groups have shown pure Cooper-pair periodicity in the box response(Bladh, 2005). Nevertheless, for reasons that are poorly understood, all of the samples fabricated at Yale were affected by this poisoning to some degree

It has been suggested that this poisoning was due to a ready availability of quasiparticles from the Cooper-pair box's reservoir (a theoretical explanation of this idea is provided in section 7.5). According to this thinking, the 2Δ free energy cost for the addition of a quasiparticle to the Cooper pair box's island does not need to be paid if a population of quasiparticles is readily available in the superconducting reservoirs. Such analyses typically describe a new, "effective" superconducting gap which describes the apparent energy required to create quasiparticles, as a pure a posteriori consideration.

On initially seeing quasiparticle poisoning in Yale-fabricated Cooper-pair box samples, it was hypothesized that this was due to the large CPW ground planes. The SET, according to this argument, is breaking and recombining Cooper pairs as current is flowing (see section 3.4 for a description of SET operation); when these Cooper pairs recombine, the binding energy is released

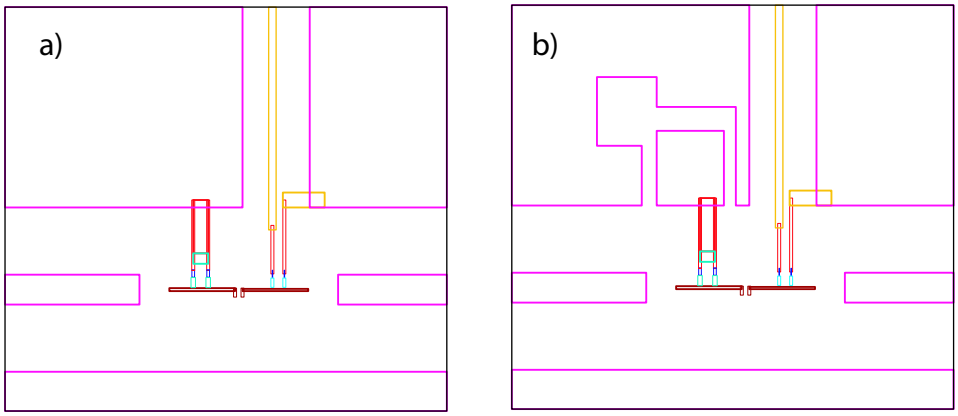

Figure 4.4: a) Traditional Cooper-pair box design, where the CPB box island is directly connected to the large CPW ground planes. b) "Floating Island" sample design, where the reservoir for the Cooper-pair box is a small cutout of the larger CPW ground plane.

into the substrate as phonons, each with exactly 2Δ of energy. The large ground planes in the Yale-fabricated samples are thought to act as "antennas" for these 2Δ phonons; their larger area creates a larger cross-section for the phonons to poison the CPB reservoir.

A proposed remedy to this was the so-called "Floating Island" Cooper-pair box design (see figure 4.4b). In this design, a path is cut through the CPW ground plane near the CPB, so that the reservoir coupled to the box is significantly smaller than the entire CPW ground plane. According to this logic, the smaller reservoir will have a smaller cross-section for absorbtion of 2Δ phonons from the substrate, and may be more immune to quasiparticle poisoning.

In designing the floating island, careful consideration was paid to the effects of this new design on the coupling capacitances within the circuit. In the "standard" Box-SET design (figure 4.4a), the reservoir of the box was grounded, and voltages coupled to the box increased its potential relative to ground. In the "floating island" design, however, box gate voltages couple to both the box island and its reservoir. The charge coupled to the box, n_{gb}, will then be determined by the difference in these two voltages; if the island is poorly designed, then this difference may be small, and we may effectively lose control of our box. In the same manner, we require that the island and the reservoir are coupled to the SET island by significantly different capacitances, so that the SET response from an additional Cooper pair on the box island is not cancelled by the capacitively coupled loss of charge from the reservoir. These capacitances were modeled using Ansoft Maxwell, and were found to be different enough that a measurement was deemed possible.

Unfortunately, measurement of a "floating island" sample still showed quasiparticle poisoning.

These results are in sad agreement with other groups' attempts to engineer around quasiparticle poisoning (Gunnarsson, 2005), and serve, above all, to illustrate how poorly quasiparticle poisoning in these systems is understood.

Chapter 5

Apparatus and Measurement Techniques

The experimental design underlying the measurements made for this thesis integrated careful engineering from many different disciplines. Samples were measured in a precisely machined cryogenic apparatus and controlled by leads that could transmit accurate electrical impulses across a wide band of frequencies. Careful microwave engineering was required for the readout of our RF-SETs. The entire measurement was then controlled by complicated suites of software that coordinated the control of our measurement. This chapter will discuss the design of each of these facets of our experiment, and will explain our motivation for assembling our experiment as we did.

In the first part of this chapter, I will describe our physical setup, and how we engineered it to the requirements of our experiment. This will involve a discussion of the cryogenic (section 5.1.1), electrical (section 5.1.2), and RF (section 5.2) engineering considerations that were taken into account when physically assembling our experimental apparatus.

I will then move on to the specific details of the electrical control and readout of our measurement. This will involve a discussion of the electronics used to generate signals and measure our experiment's response (section 5.3), followed by a discussion of the RF tank circuit design that permitted SET readout with high bandwidth (section 5.4).

The final part of this chapter will explain the software and algorithms that were used to measure our system's response in various ways. I will start, in section 5.5, with a discussion of the basic methodology we used to make calibrated RF-SET measurements. This basic software was developed to circumvent the effects of parasitic capacitances in our system; the methodology by which we measured and compensated for these capacitances is described in section 5.6. Section 5.7 will describe

how, using our ability to compensate for parasitic capacitances and independently control the box and the SET, we were able to implement slow feedback techniques that counteracted the effects of charge noise on our sample. Finally, in section 5.8, I will close with a brief discussion of techniques that were used for more exotic measurements of our experiment, including time-domain observation of the state of the Cooper pair box.

5.1 Physical Setup and Wiring

5.1.1 Cryogenic Setups

Data for this thesis were taken in three different cryogenic fridges. For the purposes of testing fabrication, samples were cooled in an Oxford Heliox pumped He3 refrigerator, which was capable of attaining a base temperature of approximately 250 mK. At these temperatures ($k_BT < E_C$) Coulomb blockade effects were visible in the single electron transistor, but could not be measured in the box. This was because of the box charging energies that were somewhat lower than the corresponding SETs [typically, $E_{C,box} = k_B(0.5\text{K})$], which allowed thermal fluctuations to obscure the box response. Also, at temperatures of 250 mK, the SET's response was broadened in n_{ge}. The gain of the SET is proportional to the slope of a SET response feature in n_{ge}, and thermal broadening of these features therefore reduced the gain to the point where the box could not be accurately measured in a reasonable time.

Normal state box-SET measurements, and the first measurements in the superconducting state, were taken in a Kelvinox 400 dilution refrigerator at a base temperature of approximately 12 mK. While the fridge was at its base temperature of 12 mK, the electron temperature was presumed to be comparably low: estimates suggest that the effective temperature of the electrons in our devices was around 28 mK. The elevation of this temperature is due to the poor coupling between the electronic heat capacity of our devices and the cooling power of the fridge; however, 28 mK is by no means a poor figure.

Later measurements of the SET-box system in the superconducting state were made in a Cryoconcept dilution refrigerator, which was capable of reaching a similar base temperature of 14 mK.

5.1.2 Wiring and Filtering

Wiring in the two dilution refrigerators was dutifully attended to, and is, in large part, to thank for the low base electron temperature that was achieved. Wiring was designed to simultaneously

minimize the heat leak into the cryostat, filter the signals that were presented to the devices, and provide a 50 ohm environment to the qubit across a wide range of frequencies.

Signals were brought into the cryostat on .085" semi-rigid coaxial lines, designed to present a well-behaved characteristic impedance of 50Ω to RF signals propagating into the cryostat. Because of this, the amplitude of signals reaching our devices did not vary much with frequency, and we were able to know with reasonable accuracy the amount of signal power applied to a sample. A well defined environmental impedance was also shown to be important to our understanding of the effects of the radiative environment on the Cooper-pair box. Semi-rigid cables were made out of copper (with a PTFE dielectric) when their thermal conductivity did not pose a problem; when connecting components anchored to dissimilar temperatures, cables with stainless steel conducting surfaces were used. Signals are understood to travel only within a skin-depth of the surface of the metals used in these cables. At high frequencies, this can cause significant attenuation, as a thin cross section of already-resistive stainless steel will rapidly attenuate a signal. This effect is more pronounced on the center pin of a coaxial cable, where the cross-sectional area carrying the signal current is smaller. For this reason, certain long cables spanning a thermal gradient were made with coaxial cable that used a stainless steel outer conductor and a silver plated copper weld (SPCW) inner conductor. This was found to provide the optimum combination of low thermal conductivity and high electrical conductivity. The bulk of the cross sectional area of the cable, in the outer conductor, was made of high thermal resistivity stainless steel, while the inner conductor, whose electrical resistivity had a more pronounced effect on the attenuation of a given cable, was made with the lower electrical resistivity SPCW.

Careful attention was paid to cryogenic noise filtering (Bladh et al., 2003) at all temperatures in the cryostat (see figure 5.1). Broadband Johnson noise from a 300 K source could dominate and obscure control voltages applied to the SET and the box, and were therefore filtered or attenuated at cryogenic temperatures. DC lines, which generally would not accommodate the resistances to ground present in an attenuator, were passed through 2 or 3 powder filters, which were usually measured to have a sharp cutoff in transmission above 100 MHz (typical copper powder filter thruput is shown in figure 5.2). A powder filter consists of a long conducting wire potted in a paste of epoxy and fine metal powder (Martinis et al., 1987). A powder filter is generally understood to operate as a lossy RC line, with the fine metal powder providing a large lossy capacitance to ground. Multiple powder filters, with different metal powders (copper and stainless steel) were used to provide redundant

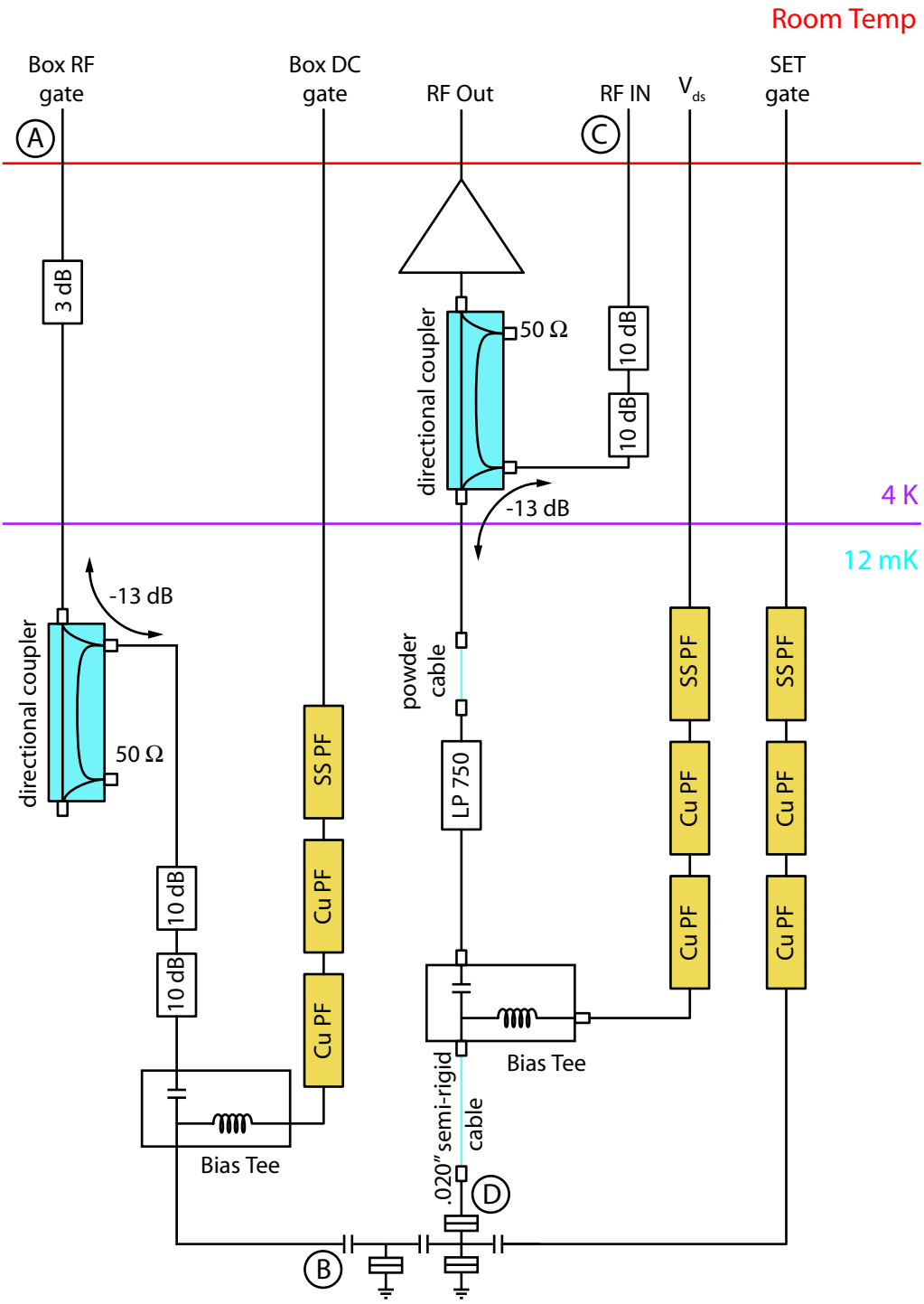

Figure 5.1: Schematic of cryogenic wiring used with box-SET experiments.

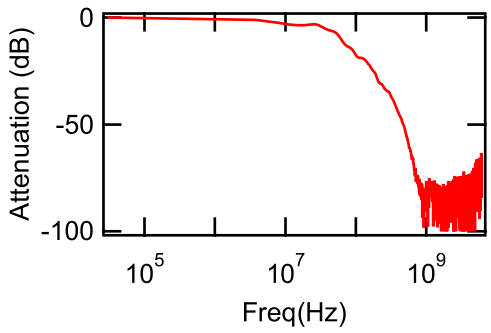

Figure 5.2: Typical RF thruput of a Copper powder filter. Loss is low, and varies slowly with frequency, until $\sim 100\,\mathrm{MHz}$, where the transmission drops rapidly to the noise floor of our measurement.

protection against suspected variations in the temperature response of the two filters. The higher thermal conductivity of the copper powder at low temperatures is thought to aid in the heat sinking of the electrically isolated center pin. Stainless powder, on the other hand, retains its low conductivity at low temperatures, and therefore protects against any loss in filter performance with cooling.

On lines designed to carry broadband RF signals, attenuation was strategically placed to dampen room temperature Johnson noise. The attenuators used were manufactured by either Midwest Microwave[1] or XMA[2], and were found not to superconduct at low temperatures. Attenuation was designed to attenuate Johnson noise from outside of the cryostat so that it was of comparable or smaller magnitude than the Johnson noise of the attenuator itself; the amount of power dissipated in each attenuator was also computed and compared to the available cooling power of that stage in the fridge. RF lines used either a directional coupler or a bias tee to break the DC continuity of the center pin and therefore reduce direct thermal conduction from room temperature.

The combined effects of all of these RF engineering efforts are shown in figure 5.3, where the microwave transmission (S_{21}) of the box gate and SET tank-circuit lines is plotted against frequency. Except where filtering artificially imposes a cutoff (to filter out broadband noise on the SET drain-source lead), these plots show that signals transmitted into the cryostat vary slowly and in a well-controlled manner with frequency.

[1] Midwest Microwave part numbers ATT-0298-XX-HEX-02 or ATT-0550-XX-35m-02, where XX is the attenuation in dB. See http://www.midwest-microwave.com

[2] XMA part number 2782-6051-XX, where, again, XX is the attenuation in dB. See http://www.xmacorp.com/attenuators.html

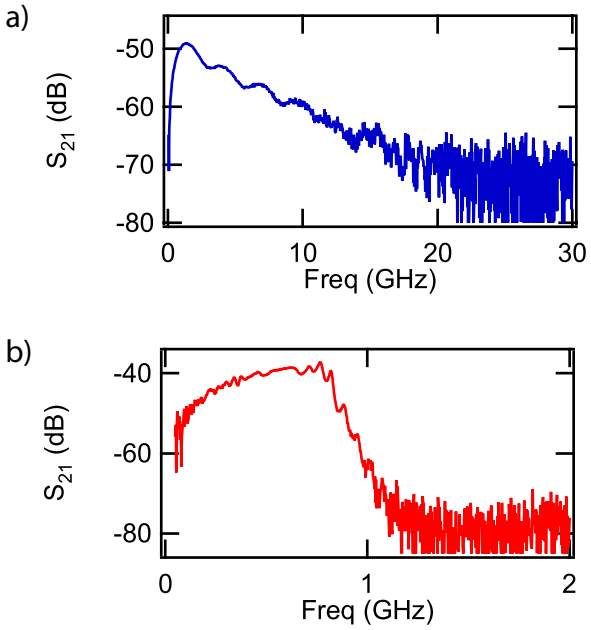

Figure 5.3: RF Thruput of a) the box RF Bias (between points A and B in figure 5.1) and b) the SET tank circuit bias lines (between points C and D in figure 5.1). While attenuation used for heat sinking reduced the transmission of these lines to a rather low level, the transmission of these lines nevertheless varies little with frequency, suggesting that there are few impedance discontinuities in the lines. The sharp cutoff in transmission in the SET bias line is due to a low-pass filter, designed to filter broadband thermal noise, which may be seen in figure 5.1.

5.2 Sample Mounting and RF Engineering

Samples were mounted in a standardized board used in the Schoelkopf lab called the "jellyhog." (see figure 5.4) The sample mount earned its name because, in its original conception, it allowed connectors to exit the sample mount both downwards (hanging as would the tentacles of a jellyfish) and outwards (as the legs of a hedgehog). In most recent incarnations, however, the jellyhog has been more jellyfish than hedgehog. The jellyhog has been useful for our lab because of its modularity: experiments can be swapped in and out of a cryogenic apparatus with a potential for minimum rewiring. It also satisfies a number of important requirements: It is a closed space that is reasonably impervious to RF interference, and yet it is not so sealed that it risks exploding because of trapped gas. Boards have been designed that will permit a large number of RF and DC signals to be routed to a sample, and, because it is a standard component in the Schoelkopf lab, these boards have been mass-produced.

Boards used for mounting samples have at all times been made out of low-RF-loss substrates.

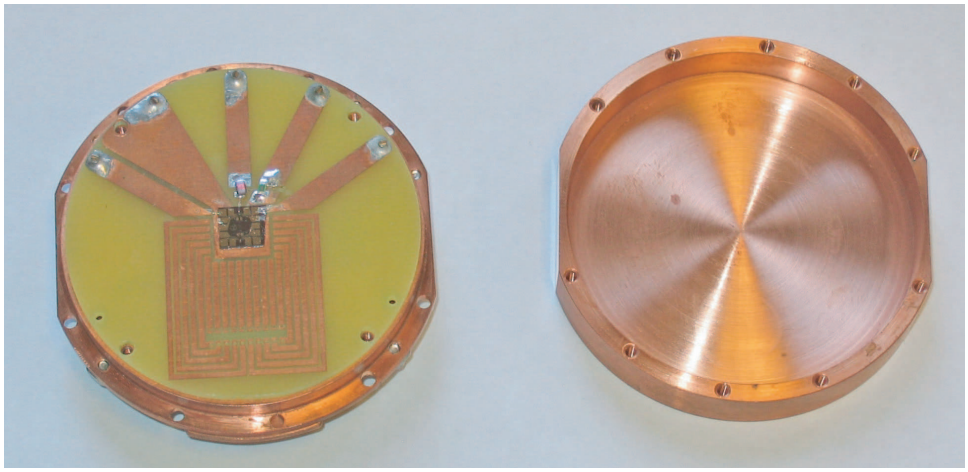

Figure 5.4: Jellyhog sample mount with low frequency chip mount. SMA posts launch input signals onto 50Ω lines.

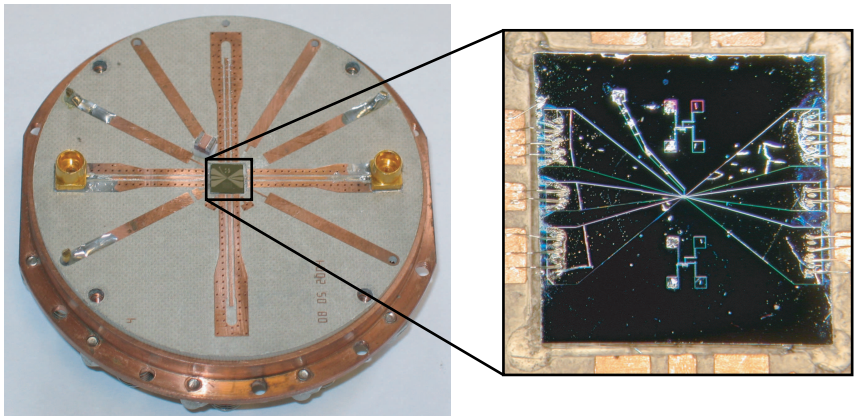

Figure 5.5: Arlon AR1000 jellyhog board for high frequency experiments. Inset shows matching between CPW on-board and CPW on-chip

For the measurements made in the normal state, the only high-frequency signal was the carrier used for the tank circuit, typically around 400 MHz. Chips were mounted on boards made of FR4, a hard substrate with a dielectric constant of approximately 4. Signals were launched using simple blunt-post launchers, and brought to the chip with 50 Ω microstrip lines. (see figure 5.4).

For measurements in the superconducting state, good RF engineering was required to much higher frequencies (up to 40 GHz). Signals on-chip were propagated via coplanar waveguide (CPW) transmission lines, which could easily be scaled in size. Circuit boards inserted into the jellyhog were made of Arlon (see figure 5.5), a high dielectric ($\epsilon_r = 10$) microwave substrate designed to be comparable to silicon($\epsilon_r = 11.7$). A recess was milled in the board to minimize the impedance

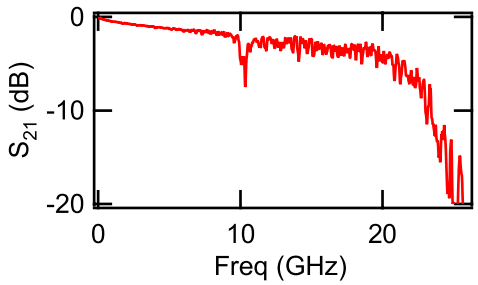

Figure 5.6: RF Thruput of SMP launchers. The careful RF engineering bringing signals to our samples (see figure 5.5) provided RF transmission that varied little with frequency for the range of frequencies used to control our Cooper pair boxes. A large drop in transmission at 26 GHz is due to the low-quality SMA connectors used to make this particular measurement; a small ripple at ~ 10 GHz is of unknown origin.

discontinuity at the chip-board interface. Vias were drilled through the Arlon board to tie the CPW ground planes together and suppress parasitic stripline modes. Signals were launched with SMP surface-launch connectors that could provide clean launching to 10s of GHz. A plot of the RF thruput of these connectors is shown in figure 5.6. For this measurement, RF transmission was measured for a signal launched, via an SMP surface-launch connector, onto an Arlon board. This signal then passed through a simple CPW transmission line and off of the board through another SMP connector. This measurement shows a laudably featureless transmission spectrum; the feature at 10 GHz is unexplained, while the broad dip around 26.5 GHz is due to external connectors used to make this particular measurement.

5.3 Experiment Control and Readout

5.3.1 DC Experiment Control and Readout

Control voltages applied to the gates of the box and the SET were generated with Agilent 33250A arbitrary waveform generators (AWGs), attenuated to an appropriate level (typically by 40 dB) outside of the cryostat, and passed to the sample via the wiring described above.

The drain-source lead of the SET was treated somewhat different because we wished to measure the current through the SET. Voltages to be applied to the SET were generated by a Yokogawa 7651 DC voltage source (see figure 5.7). These were then divided (typically by a factor of 1000), and passed over a selectable bias resistor(R_{bias} in figure 5.7). The voltage measured across R_{bias} was amplified to provide a measure of the current through the SET. The current was then fed to the device; the voltage over the device was measured so that I vs V curves of the SET could be

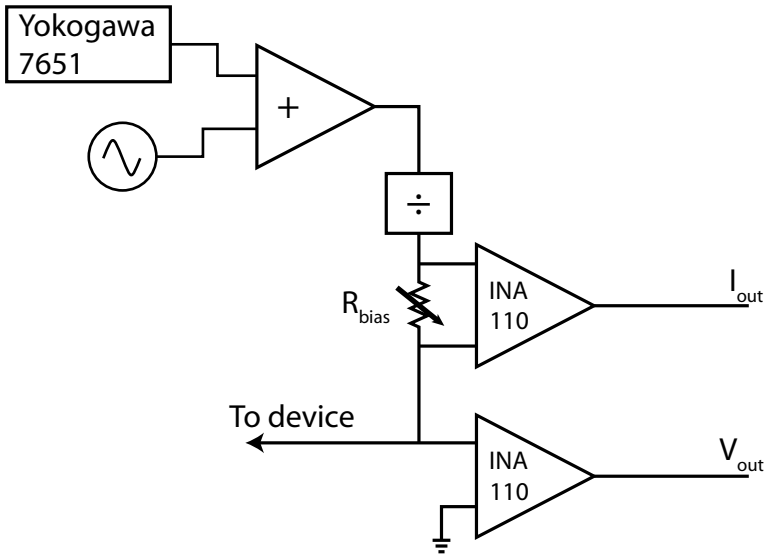

Figure 5.7: DC biasing circuitry for SET drain-source.

measured.

5.3.2 RF Hardware setup

Carrier signals to be reflected off of the tank circuit were generated externally to the cryostat, using one of several available CW sources. These were typically attenuated outside of the cryostat, passed through a DC block to break ground loops, and inserted via a line RF-engineered to 1 GHz (see figure 5.1). This signal was combined with the SET DC bias via a bias tee (see figure 5.1), reflected from the SET, and once again separated with the same bias tee. The signal was amplified with an NRAO cold amplifier (typical gain of 23 dB, typical $T_N = 2.5\,\mathrm{K}$) and brought outside of the cryostat.

Once outside of the cryostat, signals were amplified to easily measurable levels using a combination of NRAO and Mini-Circuits Room-temperature amplifiers (see figure 5.8). The gain and noise temperature of these amplifiers was chosen such that the noise of each amplifier, referred to its input, was dominated by the noise of the amplifier that preceded it. Thus, the total system noise temperature for this measurement was typically < 10 K.

After sufficient amplification, the amplitude of this RF signal was converted to a voltage, and digitized using an Acqiris DP110 fast PCI digitizer. Three different methods, illustrated in figure 5.8, were used to convert an RF output signal to a measurable voltage.

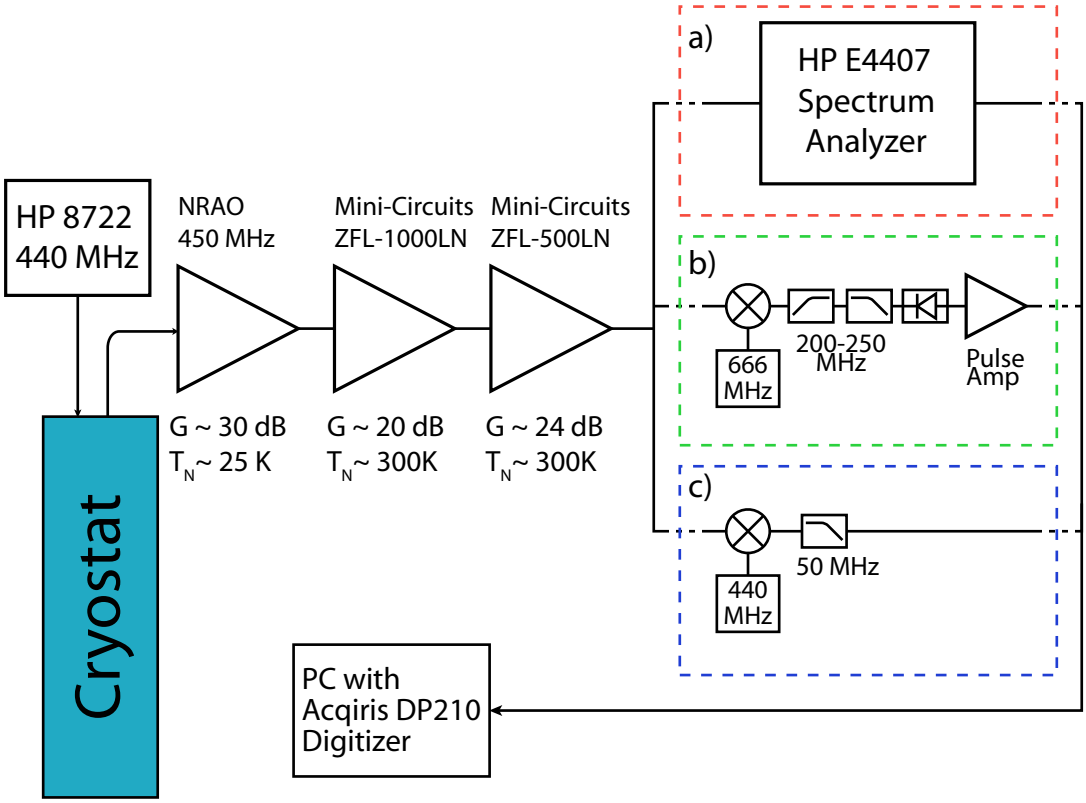

Figure 5.8: Schematic of room-temperature RF electronics. The magnitude of the RF signal output is converted to a voltage to be read by a computer one of three ways: a) HP E4407B Spectrum analyzer outputs a voltage proportional to the power in a specified band about a specified frequency. b) RF output is mixed down, band-passed, and rectified with a RF rectifying diode. A pulse amplifier is used to amplify the (DC) output of the diode to levels that can be read by the Acqiris card. c) RF output is mixed to DC and low-passed to the expected bandwidth of the experiment. Note that the signal used to mix down the RF output must be phase-locked with

For slow measurements, a HP E4407B superheterodyne spectrum analyzer was used (figure 5.8a). The "aux video out" output of this spectrum analyzer provided a voltage that was proportional to the power input to the spectrum analyzer within a chosen band around a chosen frequency. This was, by far, the simplest of the readout methods used; the frequency and bandwidth of our measurement could be changed rapidly without physically disturbing the RF setup. The spectrum analyzer used, however, did not permit measurements with a bandwidth greater than 3 MHz, which required alternate methods for some of the faster measurements we wished to make.

For faster measurements, we initially attempted a power measurement with a commercially available RF power diode (fig 5.8b). This measurement used a mixer to convert the carrier signal (440 MHz) to a lower frequency (approx. 225 MHz). The signal was then band-passed and rectified

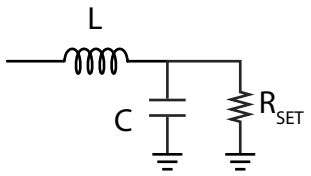

Figure 5.9: Schematic for RF-SET tank circuit. A lumped element inductor is placed in series with the drain of the SET, represented on the above schematic by the differential resistance R_{SET} (for reasons of brevity, in the derivations that follow R_{SET} will be simply abbreviated R). The capacitance between the drain of the SET and the grounded source creates an LC resonant circuit which is damped by the SET's conductance.

with a Herotek DT0110 diode. The diode's response was low-passed (not shown) and amplified by an Analog devices AD8009 amplifier. This setup permitted fast measurements of the SET response, but was plagued by fluctuations in output caused by the physical instability of the interconnects.

We finally attempted a homodyne measurement of the RF output of our experiment(fig 5.8b). In this measurement scheme, the output of our warm amplifier chain was mixed with a CW signal at the same frequency as the carrier signal input into the cryostat. The phase of the LO (local oscillator) signal, which was phase-locked to the input signal, was adjusted to yield the maximum response in the amplitude of diode output, which was low-passed and input to the usual Acqiris digitizer. This implementation was useful for fast measurments, and occasionally for experiments where we wished to see variations in the phase of the signal output by our experiment.

5.4 RF-SET Tank Circuit Design and Theory

In Chapters 2 and 3 I spoke at length about the operation of the normal and superconducting SET, and how we understood and modeled the current through the SET as a function of its various operating parameters. Measurements of the current through the SET, however, are not very useful, as the high characteristic resistance of SET samples ($\gtrsim 100\,\mathrm{k}\Omega$) combined with the typical capacitance of bias lines in our cryostats ($\sim$ nF) yields very limited bandwidth. This problem was solved in 1998 with the invention of the Radio Frequency SET (colloquially, the RF-SET) (Schoelkopf et al., 1998).

The RF-SET consists of a lumped-element impedance-transforming resonator coupled to the drain-source of the SET (shown schematically in figure 5.9). This circuit, usually termed a "tank circuit," transforms the impedance of the SET (at a high frequency, ω_0) to an impedance that is better matched to the $50\,\Omega$ transmission lines bringing signals into our cryostats[3]. The SET

[3]Typically, in our experiments, $\frac{\omega_0}{2\pi} \sim 400\,\mathrm{MHz}$

response is then measured as the amplitude of an RF signal reflected from the tank circuit at this high frequency. The bandwidth of this RF-SET measurement is limited by the resistance and capacitance local to the SET sample, and can be far higher than a corresponding DC measurement. This increased bandwidth, in turn, allowed measurements to be made on faster timescales than some of the slow 1/f noise sources in our system, and permitted the high precision measurements described in this thesis.

In this section, I will present the theory underlying the construction of the tank circuits used in our experiments, and explain how our tank circuits were optimized for the readout of our measurements. For a more comprehensive discussion of the design of impedance-transforming RF tank circuits, the reader is referred to (Teufel, 2007).

The effects of a tank circuit are understood by calculating the combined impedance of L, the lumped-element inductor, R, the differential resistance of the SET, and C, the capacitance between the SET drain lead and ground, as shown in figure 5.9. Most generally, this can be expressed as:

$$Z(\omega) = j\omega L + \frac{1}{j\omega C + \frac{1}{R}} \tag{5.1}$$

Rationalizing the denominator of the second term, we find:

$$Z(\omega) = j\omega L + \frac{R\left(1 - j\omega RC\right)}{1 + \left(\omega RC\right)^2} \tag{5.2}$$

At the resonance frequency ω_0 the imaginary part of this expression vanishes, and equation 5.2 may be solved to find the effective impedance of the combined circuit:

$$Z(\omega_0) = \frac{R}{1 + \left(\omega_0 RC\right)^2} \tag{5.3}$$

While the requirement that the imaginary part of 5.2 vanish is used to solve for the resonant frequency:

$$\omega_0 = \sqrt{\frac{1}{LC} - \frac{1}{\left(RC\right)^2}} \tag{5.4}$$

Inserting equation (5.4) into equation (5.3), we find a closed form solution for $Z(\omega_0)$ expressed as a function of the circuit parameters in figure 5.9:

$$Z(\omega_0) = \frac{L}{RC} = \frac{Z_{LC}^2}{R} \tag{5.5}$$

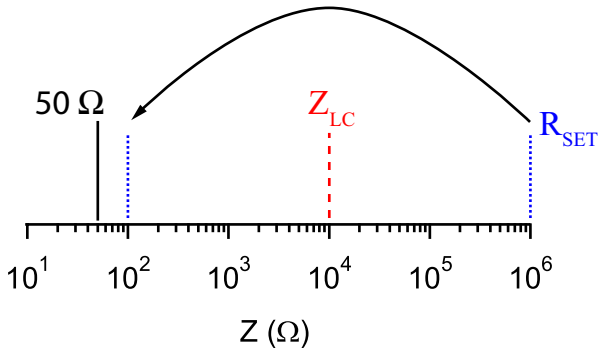

Figure 5.10: Plot showing the relative magnitudes of the impedances used in an RF-SET tank circuit impedance transformation. A device impedance R_{SET}, shown here as $1M\Omega$, is transformed to a lower impedance by a tank circuit with characteristic impedance Z_{LC}, shown here as $100\,\mathrm{k}\Omega$. The relative magnitudes of R_{SET} and the transformed impedance may be understood by "reflecting" R_{SET} across Z_{LC} when the two are plotted on a log axis.

Where we have defined the quantity $Z_{LC} = \sqrt{L/C}$, the "characteristic impedance" of our resonant circuit, as the factor instrumental in determining the transformed impedance of the SET-tank circuit combination. Insight may then be gained into the transforming effect of this tank circuit by graphically observing the relative magnitudes of these impedances, as in figure (5.10). From equation (5.5), it is apparent that Z_{LC} is simply the geometric mean of R_{SET} and the transformed impedance. When plotted on a log-spaced number line, then, (see figure 5.10), these three impedances are evenly spaced. In a real circuit, where we are given a resistance R and design a tank circuit with impedance Z_{LC}, we may think of the transformed impedance as the "reflection" of the source impedance across Z_{LC}.

This understanding motivated the design of the tank circuits used to match the impedance of our devices to the 50Ω coaxial cables in our cryostat. Most often, however, we were not entirely free to choose a tank circuit with any arbitrary Z_{LC}: the large SET drain capacitance (increased by the high ϵ_r of the Arlon microwave substrate) and the available selection of lumped-element inductors generally limited the value of Z_{LC} to a few kΩ. The corresponding transformed impedance of our SETs, typically hundreds of Ohms, provided a better match to the RF coaxial input lines than the bare SET, but the match was nevertheless not always good.

In addition to transforming the impedance of the SET, the microwave tank circuits also determined the bandwidth available for RF-SET measurement. Whereas the inherent bandwidth, set by the RC time of the SET resistance and the SET capacitance, could be very large ($>$ 1 GHz), the bandwidth of a practical readout was set by the time necessary for the RF-SET tank circuit to

change in amplitude. This bandwidth[4] can be shown to be ω_0/Q, where Q is the quality factor of the tank circuit. For the tank circuits used in our samples, where Z_{LC} was less than the geometric mean of the device resistance and the characteristic impedance of the lines, this Q could be approximated as:

$$Q \approx \frac{Z_{LC}}{Z_0} \tag{5.6}$$

Where Z_0 is the characteristic impedance of the transmission lines bringing signals to the tank circuit. The bandwidth available to an RF-SET measurement was therefore:

$$(\Delta\omega) = \frac{Z_0\omega_0}{Z_{LC}} \tag{5.7}$$

This form for the functional dependence of the bandwidth may be simply intuitively understood: the Q of a resonant circuit is a dimensionless number proportional to the number of free oscillation cycles that a resonator will undergo before its amplitude decays away, which is, in turn, a function of the quality of the impedance match between the resonant circuit and the damping effects of the transmission line. A resonator with a low Z_{LC} is well matched to the external transmission line, has a low Q, and will therefore adjust to a change in fewer oscillation cycles, i.e. quicker, than a high Q resonator. For the fast measurements performed to probe the relaxation of our superconducting qubit, the increased bandwidth that came with a low Z_{LC} and a correspondingly low Q was occasionally desirable, but low-Q tank circuits were designed with the understanding that lowering the Q involved trading off the matching of the microwave signal for the bandwidth available for measurement. A worse match between a tank circuit and a $50\,\Omega$ coaxial line, in turn, lowers the signal-to-noise ratio of an RF-SET measurement [detailed discussions and calculations of the variation in signal-to-noise ratio with the Z_{LC} of a SET tank circuit can be found in (Roschier et al., 2004) and (Teufel, 2007)]. Several of the measurements described in this thesis suffered from low signal-to-noise ratios due to precisely this effect.

5.5 Algorithms for Calibrated Box and SET Measurement

A calibrated measurement of charge using the SET consisted of two discrete measurements: first, the SET response was measured, and the nonlinear gain profile of the SET was noted; afterwards, the SET's response to a signal from the box was measured. After every such pair of measurements, the SET response function (the first measurement) was used to calibrate the measurement of the

[4] In units of $\sec^{-1}$, i.e. the effective exponential settling time of the measurement

charge on the box (the second measurement). In this section, I will provide a detailed description of the methodology used to measure these two different responses, first from the SET (5.5.1) and then from the box (5.5.2).

5.5.1 Measuring the SET Response: The "Transfer Function"

In order to make the high-precision, calibrated measurements of charge required for the experiments pursued in this thesis, one must take the output of the SET, often a complicated, noisy, and non-intuitive signal, and calibrate it to make a measurement of real charge. Our calibration relies on the fact that the response of the SET, which is in general very complicated, is periodically repeated with each additional electron of polarization charge coupled to the SET island. The SET's response is summarized in the SET diamond, a plot of the measured output of the SET (typically in units of current or reflected power) as a function of the charge coupled to the SET island (n_{ge}) and the drain-source voltage (V_{ds}). A typical superconducting SET diamond is shown in Figure 5.11. A detailed description of the structure of SET diamonds in the normal state is included in section 2.5; theory of the superconducting SET is discussed briefly in section 3.4 and at length in (Pohlen, 1999).

A calibrated charge measurement using the RF-SET consisted of two discrete steps: First, a drain-source voltage setting for the SET is identified, usually chosen to optimize the SET's gain, or to produce a particular backaction artifact. One such possible drain-source voltage is shown by a red line in Figure 5.11a. The SET drain-source voltage is fixed to this value, and the SET response is measured as the gate charge is swept. The output of the SET, shown in figure 5.11b, is typically referred to as a "transfer function."

The transfer function is the key to the calibration of measurements made with the SET. The SET response is reported in units that are very difficult to untangle: information about the conductance of the SET is converted into a RF-carrier amplitude, which is measured by a spectrum analyzer and converted to a voltage. Typically, when a graph of a transfer function is plotted, the x axis is expressed in units of polarization charge coupled to the SET island – which is proportional to the applied gate voltage by the gate capacitance which can be fabricated with a precision of, at best, $\sim 10\%$. Our measurement of the transfer function, however, allows us to calibrate these factors out, and therefore to make a charge measurement with an accuracy much higher than our a priori knowledge of any of the system parameters.

The transfer function directly measures the SET response (in arbitrary units) as a function of the

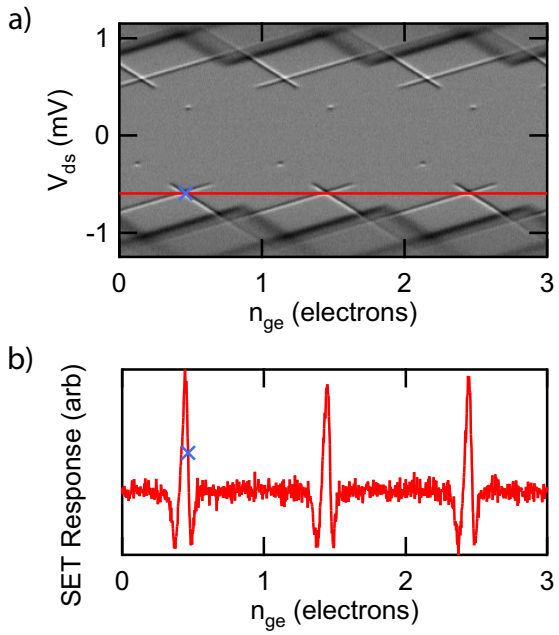

Figure 5.11: a) SET Response (RF reflected power) plotted as a function of the gate charge n_{ge} and the drain-source voltage V_{ds}. This plot is usually referred to as a "diamond." b) slice of the diamond shown in part (a) measured at the drain-source voltage indicated by a red line. This is usually referred to as a "transfer function". The SET is fixed at an operating point (blue X), and then variations of the response around that point can be calibrated in units of charge.

voltage coupled to the SET island; because the transfer function is periodic in exactly one electron, we know the exact conversion between the SET response and charge coupled to the island. Changes in the response of the SET (in the y direction, in figure 5.11b) may therefore be used to make extremely accurate measurements of any additional charge coupled to the SET island, expressed as a fraction of the (very accurately known) periodicity of the transfer function. In other words, an additional charge coupled to the SET that causes the SET response to shift by an amount known to be $\frac{1}{100}$th of a SET period is reported as a coupled polarization charge of $\frac{1}{100}$th of an electron, and can be reported as such without explicit reference to any of the gain factors in the readout system.

Once a transfer function has been measured and the noise has been averaged to an acceptably low level, the gate charge applied to the SET island is set to a fixed value. The resulting combination of n_{ge} and V_{ds} settings is usually termed an "operating point"; one such operating point is plotted as a blue "X" in both parts of figure 5.11. With these external voltages coupled to the SET fixed, an box signal is coupled to the SET island.

A box signal coupled to the SET will cause a change in SET response whose magnitude is related

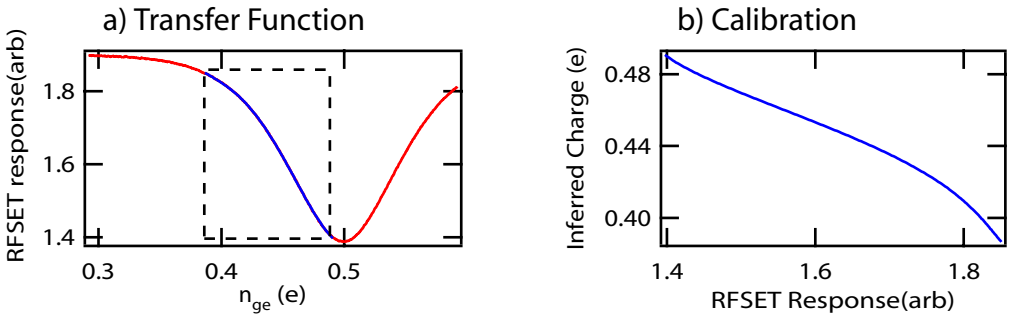

Figure 5.12: Demonstration of the processing of a measured transfer function to create a monotonic SET-Response-to-charge calibration function. a) A section of a measured transfer function is selected around the chosen operating point where the SET response varies monotonically with the charge coupled to the SET. A 5th-order polynomial is fit to this data. b) This polynomial fit is then inverted, to give a lookup table, which can be used to find the charge coupled to the SET from the SET response.

to the slope of the transfer function. One may naively consider the slope of the transfer function to be the gain of the SET. It should be emphasized, however, that this interpretation is in fact an oversimplification of the situation: the SET is not, in fact, a linear amplifier. Indeed, transfer functions that have been used to measure data in this thesis were frequently very nonlinear, even on the small ($.03e$) charge scales of a signal from the box. However, because the full transfer function of the SET can be measured, its nonlinearity is immaterial: the (nonlinear) transfer function that we measure (SET response vs. externally coupled charge) is the same function that determines the SET response to charge coupled from the box. Independent of the shape of the transfer function, our conversion is faithful.

In order to use the transfer function to calibrate the measured signal in charge units, we reduced it to a function that expressed the SET response as a monotonic, single-valued function of the charge coupled to the SET island. Our measurement of the SET's response, however, could be quite noisy, and reducing it to a monotonic function through simple averaging took prohibitively long. This was solved by fitting a low (typically 4th- or 5th-order) polynomial to a region of the transfer function in the vicinity of the chosen operating point (see figure 5.12). A monotonic section of this polynomial was then taken and used as a function to convert SET response into charge coupled to the SET. Empirically, this method of using a polynomial to smooth the noise in a transfer function was found to qualitatively reproduce all relevant features in the transfer functions measured, while being quite insensitive to fluctuations caused noise on the measurement of the transfer function.

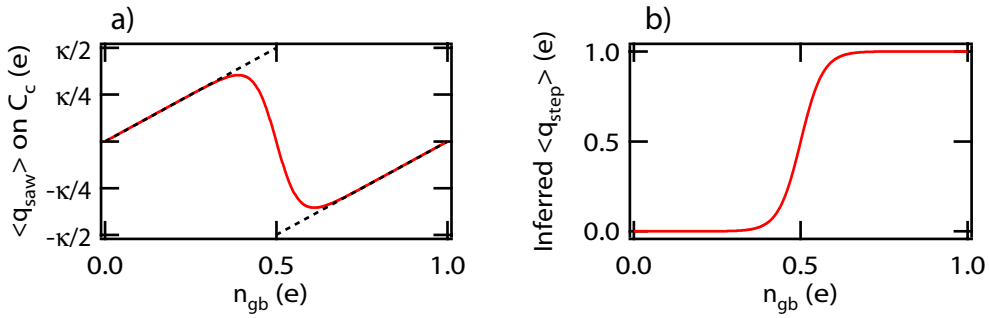

Figure 5.13: Single Electron Box Sawtooth response and Coulomb Staircase Calculation. a) Sawtooth variation of the charge on C_c measured by the SET. Dashed black lines indicate the charge on C_c in the absence of tunneling onto the box island for $n = 0$ (bottom) and $n = 1$ (top) additional electrons on the box island; these lines have a slope of κ_{box}. b) A Coulomb staircase is inferred from the sawtooth in part a using equation (5.8)

5.5.2 Measuring the Box Response: The Coulomb Sawtooth/Staircase

In our experiments, the signal coupled from the box to the SET island was the potential of the box island, which was used to infer the Coulomb staircases described in chapters 2 and 3. This potential varied as a sawtooth function as n_{gb}, the box gate voltage. This sawtooth function may easily be inferred from a simple Kirchoff's laws analysis of the potential of the box island, and, using this understanding, we may very easily convert this sawtooth potential into a Coulomb staircase.

To gain an intuitive understanding of this sawtooth response, we first imagine the potential of the box island as the box gate voltage is swept with a fixed number of electrons on the island. In this situation, which is a reasonable approximation of the box's behavior far away from electrostatic degeneracy, the box may be thought of as a simple capacitive voltage divider. The potential on the blockaded box island will therefore rise linearly with the applied box gate voltage. (see figure 5.13). When the box gate voltage is swept far past the degeneracy point, however, then an additional electron will have tunneled on to the box island to keep the island in its energetic ground state (see figure 2.6a), and the potential of the box will have decreased by an amount corresponding to one electron of charge on the sum capacitance of the box island. Once past this degeneracy point, then, the island is again in a fixed charge state, and the potential of the island rises linearly with the applied box gate voltage n_{gb}.

This has been discussed as a discrete-electron "screening" of n_{gb}, the applied box gate voltage. For large voltages (corresponding to many electrons of polarization charge) applied to the box gate, the potential of the box island does not rise appreciably; we say that the tunneling of single electrons

onto the box island has screened the potential coupled to the box island. However, as seen above, for small voltages, the discrete tunneling of a single electron cannot screen the applied voltage, and the island potential increases by an amount proportional to the applied voltage.

Far from degeneracy, where the potential of the box island rises linearly with the applied gate voltage n_{gb}, the charge coupled to the SET island via the coupling capacitor can be calculated simply using Kirchoff's laws. From this calculation, we find that an electron tunneling on to the box island couples κ_{box} electrons on to the SET island

Knowing this fact, we may calculate $\langle q \rangle$, the averaged number of additional electrons on the box island, from $\langle q_{Cc} \rangle$, the amount of polarization charge on the coupling capacitor (for clarity, I will term the potential on the coupling capacitor q_{saw} and the number of additional electrons on the SET island q_{step}, because of their respective functional forms). The total potential of the box island is inferred from the charge on C_c by dividing by the factor κ_{box}; this resulting sawtooth is converted to a staircase function by adding the linear variation in potential that is expected from the simple no-tunneling case. This gives the expression:

$$q_{step} = n_{gb} - \frac{q_{saw}}{\kappa_{box}} \tag{5.8}$$

Which is used to convert the measured charge sawtooth functions into Coulomb staircases.

It is important to note that κ_{box} in this equation is a parameter that is measured from the slope of the flat part of the Coulomb sawtooth (see figure 5.13). This will be important in section 6.6, where the quantum fluctuations of charge on the single electron box introduce a slope in the Coulomb staircase that is misread as an error in κ_{box}.

5.6 Using Cancelling Sweeps to Circumvent Parasitic Capacitances

A serious complication to measurements made with the Single Electron Transistor is posed by the cross-capacitance of the various control leads. Ideally, the two control leads in our experiment (for the SET and the box) would couple only to their respective islands. In practice, however, the small size and physical proximity of our leads and devices led to unintended capacitive coupling between each device's gate and the other's island. We called such capacitances – such as that between the box gate and the SET island – "cross capacitances" (see figure 5.14). These capacitances coupled signals intended for a single island to both, so that our two control leads were not orthogonal. (In figure

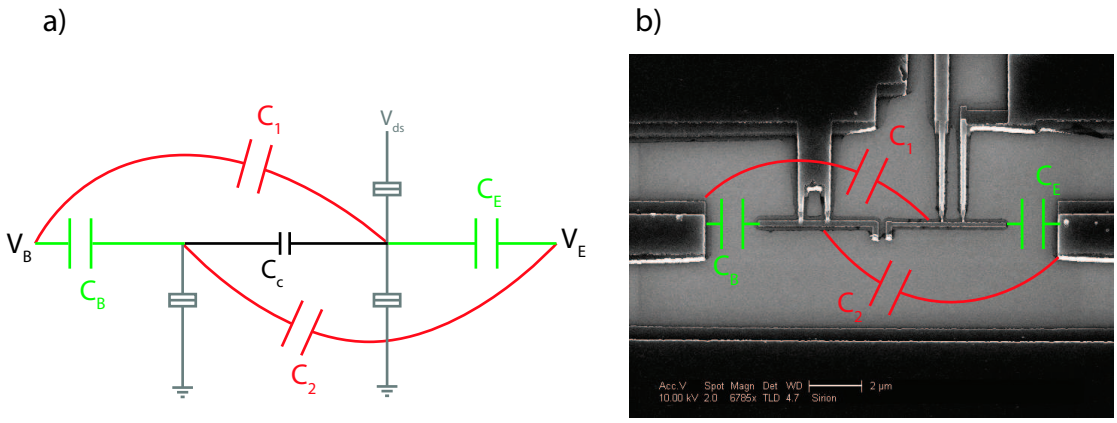

Figure 5.14: Box-SET circuit schematic with cross capacitances. The unintended cross capacitances (C_1 and C_2) are shown in red, while the "direct" capacitances (C_B and C_E) are shown in green. The Box and SET junctions are shown in gray for comparison with other box-SET schematics. b) SEM image of a sample. All capacitances shown in part a) arise from the geometric proximity of the leads and islands; the capacitances from part a) are drawn on the image for reference.

5.14, the SET gate capacitance is denoted as V_{ge}, signifying the "electrometer" gate. Similarly, in our discussion, the term "electrometer" will be used interchangeably with "SET". This terminology arose so V_{ge} would not be confused with other voltages in the system.)

We eliminated the effects of these cross capacitances and isolated charge signals to single islands by applying two sweeps, correctly proportioned but in opposite directions, to the two different control leads. Colloquially, we called this "countersweeping." The magnitude of these sweeps is derived by considering a matrix of capacitances, which can be used to express the charges induced on the two islands as a function of the voltages applied to the two gate leads:

$$\begin{pmatrix} q_E \\ q_B \end{pmatrix} = \begin{pmatrix} C_E & C_1 \\ C_2 & C_B \end{pmatrix} \begin{pmatrix} V_E \\ V_B \end{pmatrix} \tag{5.9}$$

Or, expressed in terms of the matrices themselves:

$$\mathbf{q} = \mathbf{CV} \tag{5.10}$$

Inverting this matrix, we can express the voltages that one would need to apply as a function of the polarization charge that one desires to induce on either island:

$$\mathbf{V} = \mathbf{C^{-1}q} \tag{5.11}$$

This equation can be used to find the voltages required to induce an absolute charge on either the SET or the box island, but it can also be used to find the change in voltages required to produce a corresponding change in charge on either of the given islands:

$$\begin{pmatrix} \Delta V_E \\ \Delta V_B \end{pmatrix} = \mathbf{C^{-1}} \begin{pmatrix} \Delta q_E \\ \Delta q_B \end{pmatrix} \tag{5.12}$$

During the acquisition of data from the SET or the box, we will typically apply a linear ramp in the charge coupled to one of the islands and hold the charge coupled to the other island constant. This is accomplished by solving the above equation twice – once for the amplitude and once for the DC offset voltage of the sweeps required to produce charge signals with the appropriate charge amplitude and offset. This calculation is performed frequently, and is therefore entirely incorporated into our measurement software, so that, with a knowledge of the capacitances in our system, we may apply sweeps in voltage directly to either island.

5.6.1 Determination of Cross Capacitances

In order to countersweep correctly, however, it is important that each of the capacitances in the above matrix are accurately determined. While these values can usually be modeled in electrostatic capacitance software to within approximately 10%, higher accuracy is required if a well-controlled charge signal is to be applied to either the SET or the box. The total charge coupled to each of the islands is effectively the difference between the charge capacitively applied by each of the gates, and small errors in those capacitances can propagate to large errors in their difference, potentially ruining an experiment. Such errors are typically referred to as artifacts of "bad cancelling"; their precise phenomenological manifestations will be discussed below.

Our algorithm for determining the four capacitances shown in figure 5.14 consisted of four discrete measurements:

1) Determination of C_E: First, a linear ramp in voltage is applied to the electrometer gate lead without any countersweeping. This sweep couples capacitively to both islands: On the SET, it sweeps out a transfer function, and on the box, it sweeps out a sawtooth. A measurement of the SET response probes the total potential coupled to the SET island, which is a sum of these effects. The response to this sweep is therefore a transfer function where the x axis is swept nonuninformly: instead of a linear ramp, it is swept with a linear ramp with a κ_{box} sized wiggle added. Fortunately, the periods of the SET and the box response are generally incommensurate, and the wiggle is

generally so small that these effects will not appreciably degrade the accuracy of a capacitance determination.

The electrometer response is then fit to a Fourier series, typically with 5 terms. We know that SET has a response that is 1-electron periodic in the total applied polarization charge, and so the fit periodicity of the SET's response can be used to find the conversion between V_{ge} and n_{ge}. Rather simply, if a measured voltage ΔV_E offsets the electrometer response by exactly one electron, then the capacitance C_E, expressed in electrons/V, is just $(1/\Delta V_E)$[5].

2) Determination of C_1: The capacitance C_1 is determined in the same fashion as C_E: the box gate lead (V_B) is swept over some large range, yielding a periodic response. A Fourier series is fit to this response, and the period ΔV_B of the fit is noted. The capacitance between the box gate and the SET island is again simply $(1/\Delta V_B)$. Once again, there will be a slight error from the box response coupled to the SET island during this sweep, but this will again average away if V_{gb} is swept over a range corresponding to many electrons.

3 & 4) Determination of C_2 and C_B: The capacitances C_2 and C_B must still be determined; their determination is somewhat more problematic than the direct capacitances C_E and C_1. Naively, one would think that it would be possible to determine the box gate periodicity by sweeping the box gate, and, using a knowledge of C_E and C_1, cancelling the effect of this sweep on the electrometer island. The combined effects of these two sweeps would be a linear ramp in the charge coupled to the box island, with no change in the charge coupled to the box island.

In practice, such a measurement can isolate the box's response, but it does not provide a direct measure of C_B. Put differently, if a sweep of V_B is applied to the box gate lead, and a countersweep is applied to the electrometer gate lead to keep the electrometer island at a fixed operating point, then the charge coupled to the box island is no longer simply simply $C_B V_B$; instead, it is decremented by the charge coupled to the box island by the countersweep. This will introduce errors of order $(\frac{C_1 C_2}{C_B C_E})$. One could imagine approaching the physical values of these capacitances by measurements of successive approximations of these values, but, happily, it is possible to find their values in a closed-form manner.

Imagine that the physical capacitances in our experiment are given by the matrix:

$$\mathbf{C} = \begin{pmatrix} C_E & C_1 \\ C_2 & C_B \end{pmatrix} \tag{5.13}$$

[5]Note that attenuation on the gate voltage lines must be taken into account if one wishes to convert these values into a physical capacitance value.

And our best guesses for the values of these capacitances are expressed in the matrix:

$$\mathbf{C^{guess}} = \begin{pmatrix} C_E^g & C_1^g \\ C_2^g & C_B^g \end{pmatrix} \tag{5.14}$$

Upon completing the first two capacitance determination steps, we know two elements of C_{guess}, and the remaining two are unknown:

$$\mathbf{C^{guess}} = \begin{pmatrix} C_E^g & C_1^g \\ ? & ? \end{pmatrix} \tag{5.15}$$

To proceed, we insert the artificial value of 1 electron/Volt in the above matrix for the value of C_B^g, so that a sweep that is nominally 1 electron will apply a 1 volt sweep to the box gate. We then set the measurement software to apply a cancelled sweep of S_B electrons to the box island. The software will then automatically set the sweeps using equation (5.12):

$$\mathbf{C^{guess}} = \begin{pmatrix} C_E^g & C_1^g \\ 0 & 1 \end{pmatrix} \tag{5.16}$$

$$\begin{pmatrix} \Delta V_E \\ \Delta V_B \end{pmatrix} = \mathbf{C_{guess}^{-1}} \begin{pmatrix} 0 \\ S_B \end{pmatrix} = \begin{pmatrix} -\frac{C_1^g}{C_E^g} S_B \\ S_B \end{pmatrix} \tag{5.17}$$

The actual charge that is coupled to the two islands can be determined by multiplying these real voltages by the real capacitance matrix:

$$\begin{pmatrix} n_E \\ n_B \end{pmatrix} = \begin{pmatrix} C_E & C_1 \\ C_2 & C_B \end{pmatrix} \begin{pmatrix} \Delta V_E \\ \Delta V_B \end{pmatrix} = \begin{pmatrix} -\frac{C_1^g C_E}{C_E^g} S_B + C_1 S_B \\ -\frac{C_1^g C_2}{C_E^g} S_B + C_B S_B \end{pmatrix} \tag{5.18}$$

Let us presume that our determinations of C_1^g and C_E^g are perfectly accurate, in which case this expression reduces to:

$$\begin{pmatrix} n_E \\ n_B \end{pmatrix} = \begin{pmatrix} 0 \\ \left(-\frac{C_1 C_2}{C_E} + C_B\right) S_B \end{pmatrix} \tag{5.19}$$

This equation indicates that the countersweeping has worked, and our voltages couple charge only to the box island, but the magnitude of the charge coupled by this sweep is not simply $S_B C_B$. If we experimentally find that a sweep of P_B volts on teh box gate moves the electrometer's response through one electron, then:

$$n_{gb} = 1 = C_B P_B \left(1 - \frac{C_1 C_2}{C_B C_E}\right) \tag{5.20}$$

The periodicity of the box's response is thus related to the two known quantities and two unknown quantities. For a complete solution, we require a second equation. We find the second equation by measuring the response of the box with the SET voltage shifted by exactly one electron.

The response of the electrometer, when shifted by exactly one electron, should be completely indistinguishable from the original electrometer response. However, this shift in electrometer DC offset is not cancelled on the box island (because we do not know C_2), and will therefore cause an offset in n_{gb} in the box's response. Let us call this shift X_B (measured in volts); alternately, this shift can be expressed as a fraction of an electron by dividing X_B by the measured periodicity of the box response, P_B. This shift can be measured, and, when combined with our measured value of P_B and equation (5.20), can be used to find C_B and C_2. We solve analytically for this value in terms of the unknown capacitances by imposing a 1 electron shift in the electrometer sweep DC offset. This shifts the voltages applied by:

$$\begin{pmatrix} V_E \\ V_B \end{pmatrix} = \mathbf{C_{guess}^{-1}} \begin{pmatrix} 1 \\ 0 \end{pmatrix} = \begin{pmatrix} \frac{1}{C_E} \\ 0 \end{pmatrix} \tag{5.21}$$

Which will, in turn, cause a shift in the DC charge coupled to the box and the electrometer of:

$$\begin{pmatrix} n_E \\ n_B \end{pmatrix} = \begin{pmatrix} C_E & C_1 \\ C_2 & C_B \end{pmatrix} \begin{pmatrix} \frac{1}{C_E} \\ 0 \end{pmatrix} = \begin{pmatrix} 1 \\ \frac{C_2}{C_E} \end{pmatrix} \tag{5.22}$$

We identify this calculated shift in the DC component of the box charge sweep with the shift in n_{gb} measured experimentally, expressed in electrons:

$$X_B/P_B = \frac{C_2}{C_E} \tag{5.23}$$

When this is combined with equation 5.20), the result is a closed-form solution for the remaining two capacitances:

$$C_2 = C_E \frac{X_B}{P_B} \tag{5.24}$$

$$C_B = \frac{1}{P_B} + \frac{C_1 C_2}{C_E} \tag{5.25}$$

Once these capacitances have been determined, sweeps can be applied purely to the box island or the electrometer island. In our experiments, this was done with a LabVIEW program called the "stairmaster," a software oscilloscope that allowed real-time control of the Box-SET system in the correct, diagonal coordinates. A screenshot of the stairmaster is shown in figure 5.15. By automating two important tasks – the countersweeping to eliminate the effects of cross-capacitances, and the calibration of applied sweeps in units of charge – the stairmaster allowed us to work with our experiment on a much higher level and to directly interface with our theoretical understanding of our system.

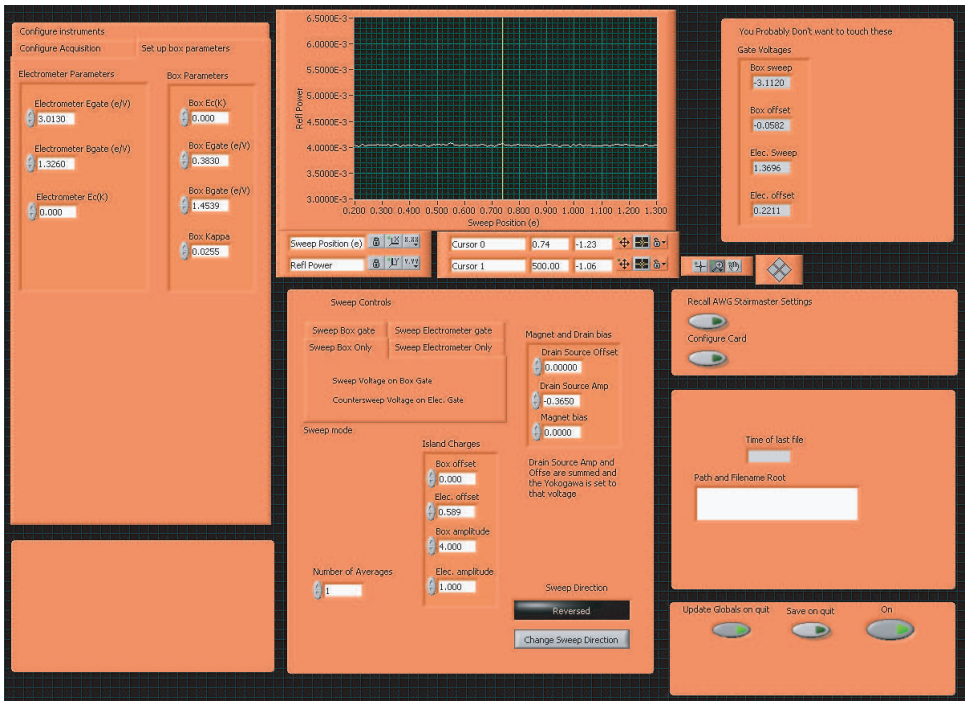

Figure 5.15: Screenshot of the "stairmaster", which allowed real time variation of sweeps that could be isolated to only the box or the SET islands.

5.6.2 Consequences of Errors in Cross-Capacitance Determination

The method of determining the capacitances outlined above does not introduce any systematic errors in the capacitance values that one finds; however, because of the noise inherent in the system, there will invariably be random errors in these values. Because of the role of each of these capacitances, errors in particular capacitances lead to recognizable behavior in the phenomenological response of the system. For the four different capacitances, these errors are:

– The electrometer gate capacitance C_E determines, most importantly, the proportionality between the voltage applied to the electrometer gate and the charge induced on the electrometer island. An error in C_E will cause the response of the electrometer to not appear 1e periodic. Also, because a precise knowledge of the SET response periodicity is used for the calibration of charge measurements made with the SET, errors in C_E will also cause a scaling error in box charge measurements.

– For the same reasons, errors in the box gate capacitance C_B manifest themselves in a periodicity of the box response that is different from 1e (or, if the box is in the superconducting state, 2e).

– The capacitance C_1 determines, to lowest order, the magnitude of the countersweep applied

to the electrometer to hold the SET operating point fixed while a signal is applied to the box. Practically this means that, if C_1 is erroneously determined, then a sweep that is intended to couple a ramp in charge to only the box island will instead couple a small ramp in charge to the SET island as well. The total charge coupled to the electrometer island will therefore show a linear variation added to the response of the box. This is one of the most commonly seen errors in our system, and is typically referred to as "bad cancelling."

– The capacitance C_2 causes only second-order effects in most relevant measurements. Errors in C_2 can be seen while measuring the response of the box to a sweep in charge. If C_2 is determined incorrectly, than offsetting the electrometer will cause some change in the DC value of the charge sweep coupled to the box, and will cause a phase shift of the box response. This is a small effect, however, and quite difficult to see unless the operating point of the electrometer is shifted by several electrons of polarization charge.

5.7 Charge Noise and Slow Feedback

A precise determination of the cross-capacitances in the SET-box system allowed us to directly apply signals to a single island in our experiment. This ability was a necessary precursor for the charge noise rejection algorithm that I will describe in this section, which enabled the unprecedented high precision of our measurements.

As noted previously, the SET is plagued by slow charge noise on its input, typically showing a telegraph or 1/f characteristic, with timescales between 10s and 100s of seconds. This can be seen in real-time in repeated sweeps of the electrometer gate: repeated sweeps, in the absence of charge noise, should be noisy replicas of each other. However, in the presence of charge noise, one will find that repeated sweeps exhibit random offsets in the n_{ge} direction. Microscopically, this is thought to be due to charged impurities that are weakly bound to either the substrate or the metallic lattice. When these charged impurities move between two available lattice sites, they can capacitively couple additional polarization charge to either the box or the SET island.

Our measurements suggest that each such charged impurity was localized near one of the two islands; charge fluctuations were seen to affect either the box or the SET, but would typically not affect both devices simultaneously. For the purposes of our experiment, this was beneficial: the charge noise affecting the SET was typically found to be more severe than that affecting the box, and was perhaps even activated by SET operation. The greater signal-to-noise of the SET's response,

however, allowed this charge noise to be monitored and removed on a relatively short timescale.

In fact, in order to make a precise measurement with the SET, it was imperative that we remove it. A charge fluctuation on the input of the SET shifts the operating point of the SET. A central contention of this thesis is that the backaction of the SET is a very sensitive function of the SET's operating point; shifts in the SET's operating point must therefore be carefully monitored and diligently rejected if one is to report the SET as having been operated at a consistent operating point. Even if this were not the case, the effects of charge noise must be removed to make a precise measurement: shifts in n_{ge} introduce changes in the nonlinear gain of the SET as a charge amplifier.

As mentioned before, a calibrated charge measurement made with the SET consisted of two sequential measurements, first of the SET's response to the box, and then of the SET's response to an external charge sweep. In order to counter the effects of charge noise, this pair of measurements was repeated on a comparatively short timescale – typically 1-3 minutes. Each time a transfer function was measured, it was fit to a simple Lorentzian function, and its center was found[6]. Any shift in the center of the transfer function was inferred to be due to a shift in the background charge coupled to the SET. Such shifts were removed with the application of an offset in charge to the SET island to bring the SET back to the desired operating point.

In cases where the change in the background charge noise was found to be large (more than .02 or .03 e, typically), the associated sawtooth measurement was discarded for fear of it not being at a consistent operating point, and the measurement was repeated. In this way, we can say with certainty that a data set consisting of many averaged Coulomb staircases was measured with the SET at a consistent operating point.

5.8 Advanced Measurement Techniques

5.8.1 Audio Frequency Feedback

Slow feedback as described above has proven useful at making precise measurements with the SET, but it is not without limitations. Feedback operating on a time scale of minutes risks missing (or averaging the effects of) charge fluctuations occurring on much shorter timescales, potentially causing erroneous transfer functions, miscalibrated data, or imprecision in the operating point.

[6] For most measurements made with the SET, the transfer function was found to be a peaked function which could be reasonably fit with a Lorentzian. For some settings of V_{ds}, though, the transfer function did not have a very Lorentzian lineshape. Nevertheless, repeated fits of a Lorentzian to a consistently misshapen peak would find the same center, and our methodology was therefore found to be robust.

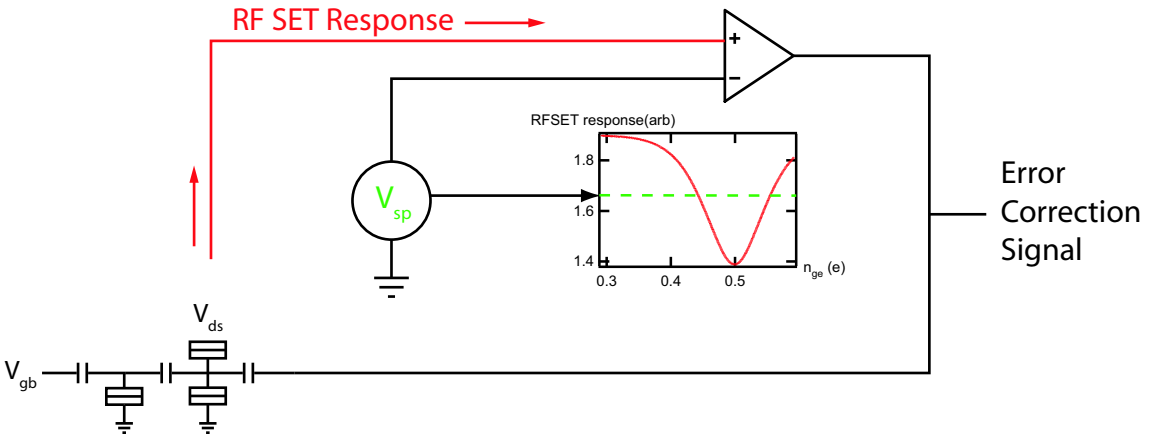

Figure 5.16: Schematic setup for audio frequency feedback loop to circumvent charge noise. The compensating signal that is applied to the SET gate is also is read out as a measure of the total charge coupled to the SET island.

One possible modification to our experiment that would address the slowness of our instrument's response to charge noise is audio frequency feedback, where the SET is adjusted, at $\sim$ kHz, to stay at a single operating point. The magnitude of the signal required to keep the SET at its fixed operating point could then be read as an indication of the total charge coupled to the SET (see figure 5.16). We typically referred to operation of the SET in this fashion as a "charge-lock loop", where an external, analog hardware loop maintained the SET at an operating point of constant charge.

This audio-frequency feedback has the added advantage of solving another problem with SET measurements, caused by the poor dynamic range of the SET. During a correctly cancelled box measurement, the linear sweep applied to the box island does not couple to the SET island. During this measurement, however, the SET does not remain at a constant operating point. Instead, as the box gate is varied, $\pm\kappa_{box}$ of charge is coupled from the box island to the SET, and it is this deviation in charge that we measure as the SET response. If this amount of charge causes the SET to shift to an operating point where there is no gain, then part of the measurement is rendered useless. Practically, this means that the SET can only be operated at a point where the transfer function is monotonic over a range in gate charge corresponding to $\pm\kappa_{box}$ electrons. Perhaps more seriously, this constrains the range of operating points available. If the Coulomb staircase couples 3% of an electron of charge, than one can only find 2 independent operating points on a transfer function that is 6% of an electron wide.

Implementing a charge-lock loop, however, is difficult because of the cross-capacitances in the

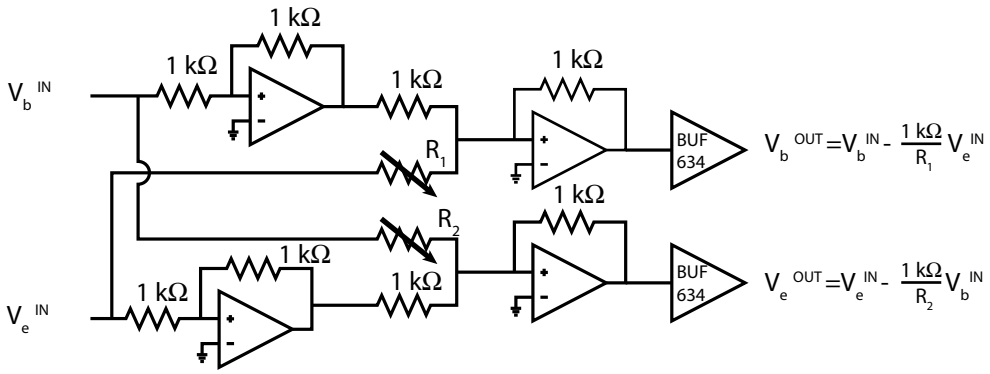

Figure 5.17: Electrical schematic for the stairbox. Each input is inverted and then added to the other input. R_1 and R_2 determine the relative amplitudes of the two inputs combined to make each output. Unity gain buffers on the output allow the circuit to drive a 50Ω load.

system. A feedback signal to eliminate drifts in the SET would have to be applied as a voltage only to the SET island. In our system, this would mean that the error signal that we would apply to the SET would have to be counterswept to eliminate its effect on the box. And, whereas using a linear amplifier for feedback is a small matter, inserting a feedback signal in arbitrary proportion on two different leads is somewhat more difficult.

A solution to this problem was implemented in hardware, in a device that has been termed, by analogy with the "stairmaster" data taking software, the"stairbox." (schematic shown in figure 5.17). The stairbox accepts two input voltages, and outputs two different linear combinations of those voltages. The relative proportions of each input added to create each output can be adjusted by adjusting R_1 and R_2; in this way, the box can be adjusted in hardware to correctly cancel for any given set of capacitances. It is worthy of note that there are 4 free parameters in the capacitance matrix, but only two dials on the stairbox; this is because the normalization of each sweep (volts per electron) is arbitrary, and can be included in software. The box seeks only to accomplish the correct linear combination of the sweeps; for the sake of simplicity it consciously ignores their magnitudes.

The stairbox was shown to work robustly on the bench, but, unfortunately, did not work when inserted into the apparatus. Preliminary tests suggest that there was some problem with the grounding setup of the apparatus, but a full understanding of these problems was not pursued.

It is also worth noting that another graduate student in this lab, John Teufel, had attempted to implement a charge-lock loop in a SET measurement system where the cross-capacitances were not considered. His attempts, however, were ultimately unsuccessful: he found that the feedback loop

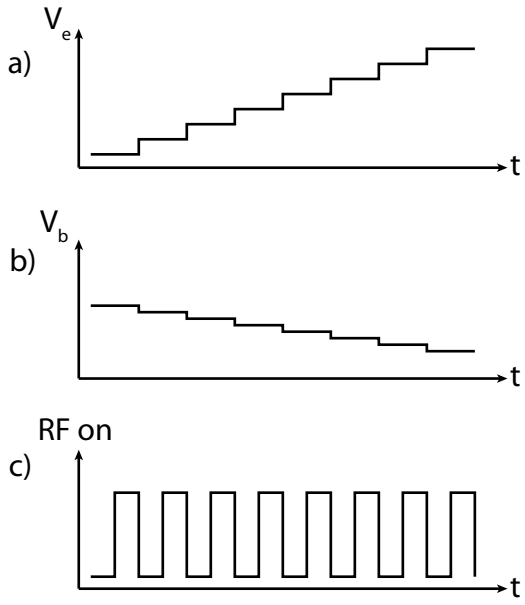

Figure 5.18: Timing scheme for voltages applied while measuring fast response. a,b) Stepped voltages applied to the box and SET gates sweep the charge coupled to the islands as before. c) For each voltage value applied to the box and electrometer gates, the qubit is irradiated with CW microwaves for $5\mu s$ and then measured for $5\mu s$ as it relaxes.

he created was quite unstable. This was typically due to the large noise and the low dynamic range of the SET: corrective signals applied by a simple, linear feedback loop would often apply shifts to the SET of an electron or more; the system simply did not have a linear response on the scale required by the feedback loop.

5.8.2 Rapid Time-domain measurements

Another problem with Coulomb staircase measurement scheme outlined in section 5.5 is its inability to produce rapid, time-domain measurements. If the Cooper-pair box is to be measured as a qubit, then the evolution of a charge measurement must be continuously monitored in time. While no aspect of the measurement design explicitly prohibits measurements made at moderately high frequencies (up to about 10 MHz, the bandwidth of the tank circuit), the particular algorithm described above – applying linear voltage ramps to the box and SET islands – does not simply extend to measurements of box dynamics.

A second suite of measurement software was therefore designed specifically to make repeated measurements of the SET/box system's response on fast timescales. Where the stairmaster applied linear ramps to the two islands, the time-domain software would apply the sweeps as a sequence of

fixed voltages, each applied for $10\mu s$ (see figure 5.18a and b). At each voltage level in these sweeps, a CW RF signal was applied for 5μs, and then turned off for 5μs (figure 5.18c). The SET measured continuously throughout the entire sequence. This allowed us to continuously monitor the response of the Cooper pair box across a Coulomb staircase as the applied RF spectroscopically excited our system, and then as it relaxed. Measurements made using this scheme are presented in section 7.7.

Chapter 6

Measurements in the Normal State

6.1 Introduction

The advanced normal state measurements described in this chapter were the first notable success of the work for this thesis. These measurements were enabled by the charge noise feedback methodology described in Section 5.7, and produced research that led to published measurements of SET backaction (Turek et al., 2005) and the polarizability of the single electron box (Lehnert et al., 2003a).

Both of these observations were based on detailed measurements of the Coulomb staircase in the normal state using the measurement and calibration techniques described in section 5.5. In both cases, independent measurements of the parameters of the box and the SET were used to forecast effects – due to backaction, or to quantum fluctuations – which were found to agree with the measured data.

In this chapter, I will first describe our determination of the physical parameters of the box and the SET which entered into the backaction and quantum fluctuation models. I will then proceed to discuss each of these two phenomena.

I will first treat the backaction of the single electron transistor. In section 6.3.1, I will discuss the magnitude and the phenomenology of the effects that our sequential tunneling model predicts in a system with our measured parameters. The systematic changes in SET backaction with SET operating point require precise control of the SET operating point; in section 6.4 I will therefore discuss the implementation and precision of our normal state algorithm to remove drifts and jumps in the SET operating point. Finally, in section 6.5, I will discuss our experimental measurements of systematic changes of SET backaction with SET operating point.

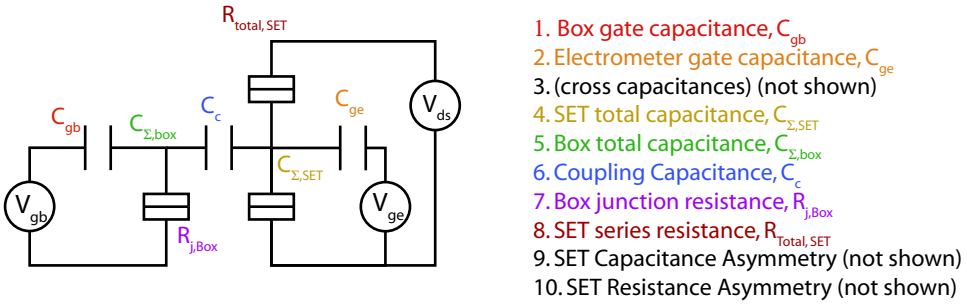

Figure 6.1: Parameters to determine in the Box-SET system. Accurate determination of these parameters usually resulted from a combination of normal state and superconducting state measurements.

Finally, I will close this chapter with a brief treatment of the measurement of the polarizability of the Single Electron Box, whose theoretical underpinnings were laid out in section 2.7.2.

6.2 Determination of Box and SET parameters

A precise determination of the SET and box parameters was required to accurately model any of the effects studied in this thesis. Practically, there were 10 different parameters that needed to be known to fully describe the SET (see figure 6.1). These parameters were determined from a variety of normal and superconducting state measurements.

The SET and box gate and cross capacitances (1,2,and 3 in figure 6.1) were found from the periodicity of the SET response, as discussed in section 5.6.

The series resistance of the SET junctions, also, may be trivially measured by probing the resistance of the SET at room temperature, or, when the SET is cold enough that Coulomb blockade effects are manifest, by measuring the differential resistance of the SET at a high drain-source voltage where Coulomb blockade effects are irrelevant.

Several other important parameters describing the SET may be extracted from the SET's diamonds (for more information about charging diamonds, see Section 2.5). In particular, Coulomb blockade can be always be overcome when V_{ds} is so large that an electron tunneling on to or off of the SET island receives at least as much energy from the drain source voltage as is required to electrostatically charge the sum capacitance of the SET island (i.e. $E_c = e^2/2C_\Sigma$). For $e\,V_{ds} > 2E_c$, even with an arbitrary capacitive division of V_{ds}, there will always be at least E_c of energy available for an electron to tunnel off of or on to to the SET island and initiate current flow through the SET. The charging energy of a SET may therefore be measured by finding the range, in V_{ds}, of the

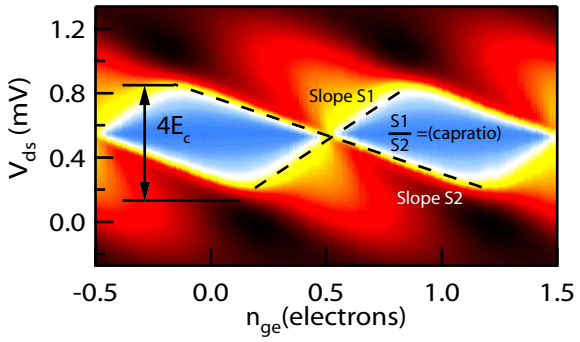

Figure 6.2: The charging energy of the SET island and the capacitance asymmetry of the SET junctions may be determined from normal state charging diamonds. More accurate results may generally be found from superconducting SET diamonds.

Coulomb blockade. A measurement of the charging energy using this technique, however, is often inaccurate, as the effects of temperature and the uncertainty in V_{ds} from the RF voltage on the SET tank circuit tend to blur the edge of the Coulomb blockaded region. This measurement was therefore used only to corroborate results measured in the superconducting state.

The charging diamond may also be used to determine the ratio of the capacitances of the two SET junctions. As discussed in section 2.5, the ratio of the two slopes in a charging diamond is a direct measure of the ratio of junction capacitances in the SET.

When the SET response is modeled using the parameters so determined, one finds that the match between the generated diamonds and the measured diamonds is comparatively poor. This is because the temperature of the SET is difficult to measure, and is probably not fixed. Because of weak thermal linkage between the electrons in the SET leads and the cooling of the dilution refrigerator, the SET probably has difficulty cooling to the base temperature of the cryostat. In addition, electron tunneling in the SET dissipates power, which may be calculated as the product of the SET current and the SET voltage. This current can heat the SET and electrons in the SET leads. This was accounted for by fitting the temperature of our modeled diamonds to the measured data for each distinct V_{ds} value. By this method, the temperature of the modeled SET response that best matched the experimentally measured data was found to vary from 100 mK at $V_{ds} = 0$ to approximately 400 mK at large ($\sim 1mV$) applied drain source voltages.

Although this is clearly not a complete solution to the problem – the power dissipated by the SET, and presumably the temperature to which the SET heats itself, clearly varies with n_{ge} at constant V_{ds} – it did improve the accuracy of the match between the generated and experimental

Attribute	Symbol	Value
Box Gate Capacitance	C_B	25.5 aF
Electrometer Gate Capacitance	C_E	16 aF
SET Island Capacitance	$C_{\Sigma,SET}$	0.40 fF
SET Charging Energy	$E_{C,SET}/k_B$	2.3 K
Box Island Capacitance	$C_{\Sigma,box}$	0.57 fF
Box Charging Energy	$E_{C,box}/k_B$	1.62 K
Coupling Capacitance	C_c	20 aF
Box Charge Coupling	κ_{box}	.034
Box Junction Resistance	$R_{j,box}$	15.4 kΩ
SET Normal State Resistance	R_N	94 kΩ
SET Resistance/Capacitance Asymmetry	a	1.7

Table 6.1: Sample parameters for the SET-box device measured in the normal state. The device was fabricated at Chalmers Institute for Technology, in the group of Per Delsing.

diamonds.

It is also worth noting that this variation in temperature of the SET island had little or no effect on the temperature of the single electron box. The Single electron box was found to consistently show widths consistent with an electron temperature of 25-35 mK, and attempts to correlate variations in the effective box temperature with the power dissipated in the SET were inconclusive (see section 6.5.4). From this, we presumed that the SET and the box were well thermally isolated from each other, and that the elevated apparent temperature observed in the response of the SET may have also been partially due to non-thermal effects, such smearing of our measured response from imprecision in our control voltages.

Attributes of the single electron box were found from measurements of the box staircases. Capacitances between external leads and the box island were found using the techniques described in section 5.6. The charging energy of the box was found by fitting the width of staircases at an array of temperatures, which we know from section 2.4 to be a function of the ratio E_c/k_BT. A linear regression of the fit value of E_c/k_BT vs $1/T$ therefore yields a slope corresponding to the charging energy of the box. It is noteworthy that this must be done at higher temperatures, as the effects of backaction and quantum fluctuations on the box island both cause broadening of the Coulomb staircase that may be erroneously misinterpreted as a saturation of the temperature on the box island. At high temperatures ($T \sim 100 - 300\,\mathrm{mK}$), however, these effects are negligible when compared to the thermal broadening, and the width of the steps was found to vary as expected with temperature. These measurements were corroborated with measurements in the superconducting

state, which were generally able to produce more accurate measurements of both the box charging energy and junction capacitance.

All of the parameters for the sample that was measured in the normal state are summarized in table (6.1). Data in this table are inferred from both superconducting state and normal state measurements.

6.3 Normal State Backaction Phenomenology

We measure the effects of SET backaction as small differences in the Coulomb staircase of the single electron box. These small differences will be shown to agree with predictions from the sequential tunneling model developed in chapter 2, which will provide the ultimate proof of the correctness of our methods. Before this comparison is made, however, we will physically motivate the phenomenology of the backaction effects we observe by considering the effects of fluctuations of the SET island charge state capacitively coupled to the single electron box. In section 6.3.2, we will discuss how these fluctuations vary with SET operating point, before moving on to the details of the measurement of their effects.

6.3.1 Backaction Effects on the Coulomb Staircase

The physical source of the backaction of the SET on the single electron box is quite easy to understand: when an electron tunnels on to either the SET or the box island, it increases the potential of that island. This potential will capacitively couple to the other island; we may think of it as a change in the polarization charge on the coupling capacitor, C_c, which connects the two. A tunneling event onto the box island will therefore change the charge coupled to the SET, and will permit the SET to measure the box. This same mechanism, however, undesirably couples the potential on the SET island to the single electron box, and causes backaction. It is effects from this simple coupling that we will measure.

As the SET operates, the charge on the SET island switches between discrete charge states typically differing by a few, or only one, electron of charge. We consider the potential of the SET island, then, to be a random telegraph signal, whose characteristic timescale is related to the current flowing through the SET, and whose amplitude is the fraction of a single electron on the SET island that couples as polarization charge to the box (rather simply expressed as $\kappa_{SET} = C_c/C_{\Sigma,SET}$). This telegraph signal is the sole source of SET backaction that we consider in the normal (non-

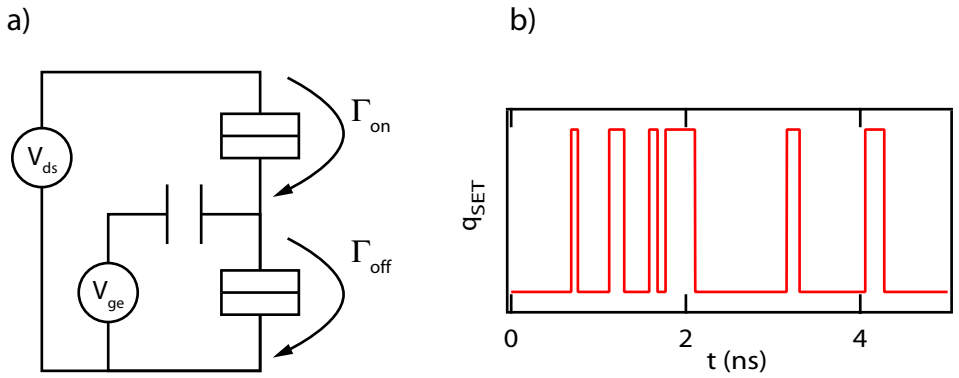

Figure 6.3: a) Schematic of SET island, showing electron tunneling rates on to and off of the SET island. These rates vary with the operating point of the SET. b) Plot of SET island potential fluctuations as a function of time. The duty cycle of these fluctuations may be found from the ratio of Γ_{off} and Γ_{on}, the single electron tunneling rates shown schematically in part a).

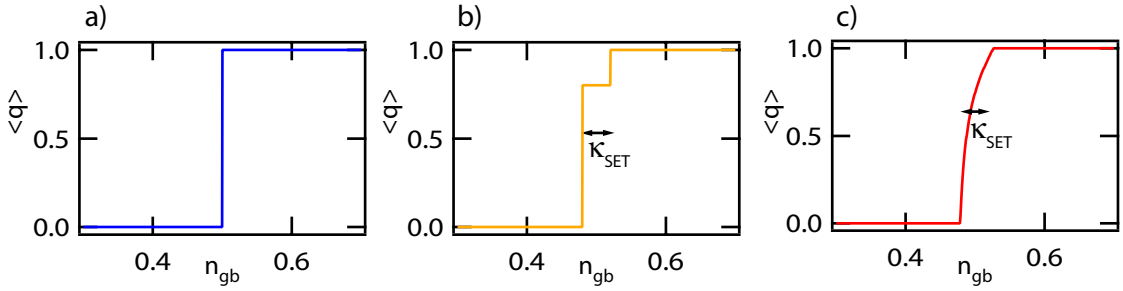

Figure 6.4: Backaction of the SET at zero temperature. a) A zero temperature Coulomb staircase of the Single electron box is a sharp step function. b) A naive expectation, true in the limit where SET tunneling rates are very slow, gives a weighted average of two staircases shifted in box gate charge by κ_{SET}. c) A staircase modeled at zero temperature using the sequential tunneling model described in chapter 2, which takes the tunneling rates of both the SET and the box into account.

superconducting) state. We identify the effects of backaction by observing predictable variations with SET operating point: as the SET operating point is varied, the characteristic frequency and duty cycle of the telegraph signal coupled to the box change, causing subtle changes in the signature of the backaction seen on the Coulomb staircases.

A naive interpretation of the consequence of this telegraph signal might be considered as follows: the Single Electron Box's response is a known function of the gate voltage coupled to the box island (shown, for simplicity, at zero temperature in figure 6.4a). If the gate charge coupled to the box island now switches between two values separated by κ_{SET}, then we might naively expect the response of the box to appear to be a weighted average of two staircases, shifted by κ_{SET} in n_{gb} (see Figure 6.4b). In the limit of very slow tunneling on to and off of the SET island, this would in

fact be what is observed. However, for any practical system, this will not be the case. Transitions in the SET, which are driven by an external voltage, will typically occur at a similar or faster rate than transitions between charge states on the box. Thus, the true response of the box, while retaining some of the phenomenological features of the simple "weighted average" intuitive model discussed above, bears a markedly different functional form. In figure 6.4c, a staircase generated by the sequential tunneling model described in chapter 2 to show the effects of this backaction at zero temperature is reproduced.

This model-generated staircase, like the weighted-average intuitive model discussed above, demonstrates the main signatures of SET backaction. First, because the fluctuating signal coupling to the box does not average to zero, there is an offset in the center of the Coulomb staircase. This shift, which can be as large as κ_{SET}, will vary directly with the duty cycle of the charge state fluctuations of the SET island.

Second, one will note that the transition between the two charge states of the SET island is broadened by a width of κ_{SET}, measured in electron charge coupled to the single electron box. This, again, may be deduced from our model of charge state fluctuations on the SET island: a fluctuating signal on the gate of the box that is κ_{SET} in size can be expected to broaden the Coulomb staircase by as many electrons. Once again, we find that the broadening predicted by the model is more complicated than that predicted by a simple weighted average of different box gate voltages, but nevertheless phenomenologically the same. We recall that broadening of the staircase was predicted in section 2.4, in the absence of backaction effects, to be a measure of the temperature of the Single Electron Box. For temperatures where the thermal broadening is equal to or less than κ_{SET}, however, we see that backaction will cause additional broadening of the staircase that may be misconstrued as an elevated temperature.

The final backaction artifact that we note is an asymmetry of the Coulomb staircase. A Coulomb staircase that is subject to thermal broadening but not to backaction will be perfectly point-symmetric about its midpoint (see figure 2.6). The staircase in Figure 6.4c, however, is clearly not. This may be heuristically thought of as a consequence of "asymmetric broadening" of the charge fluctuations on the box gate: the charge state fluctuations of the SET island about their mean value consist of infrequent ventures far across one side of the mean charge coupled to the box. If these fluctuations are to be seen as broadening the Coulomb Staircase, then we imagine that the Coulomb staircase will be broadened "more" in one direction than in another direction.

It should be emphasized that this is only a cartoon picture of the situation. The full behavior of the system is only produced by a full consideration of all of the coupled rates in both the SET and the box. An analysis of the full coupled system, which takes into account the effects of the box on the SET's operation as well as the effects of the SET on the box's operation, is typically said to be analyzed in the context of "strong coupling."; a simple analysis that considers the SET as a static noise source (as this discussion does) is said to be discussing in the context of "weak coupling". For the precise functional presentations we will present later, strong coupling effects will be taken into account; for our simple heuristic model here, a weak coupling analysis will suffice.

If the measured Coulomb Staircases appeared as in Figure 6.4c, then a measurement of the backaction of the SET would be trivial. When real thermal fluctuations are added, however, these effects are diluted, and their observation becomes much more difficult.

6.3.2 Variation of Backaction with SET operating point

The preceding discussion considered the backaction of the SET by presuming a telegraph signal coupled to the input of the box. This produced a simple mental model that was useful for predicting the nature of the effects of backaction on the single electron box, but, because it did not take into account the fact that rates in the SET and the box are coupled, it produced results that were only an approximation of the expected behavior of the SET-box system. In this section, I will discuss trends that we expect in the noise of the SET as its operating point is varied. As before, however, it should be understood that this discussion is only an approximation to the true behavior of the SET-box system. Backaction in the SET-box system is only correctly considered when one thinks of a fully coupled system; descriptions of the SET as an independent noise source or the box as an independent measurement are therefore more useful in divining the nature of the backaction effects than in finding their precise numerical signature.

As discussed in section 2.5, the full response of the SET is usually presented as "charging diamonds". Inside of the diamonds, the SET is in blockade: the energetic barrier caused by the charging of the SET causes current flow to be exponentially suppressed. For typical SET measurements, the SET is operated on the edge of the region of Coulomb blockade, where dramatic changes in SET current (or conductance) with the total polarization charge coupled to the SET translate into a high SET gain.

At low drain-source voltages, for current to flow through the SET, two tunneling events must

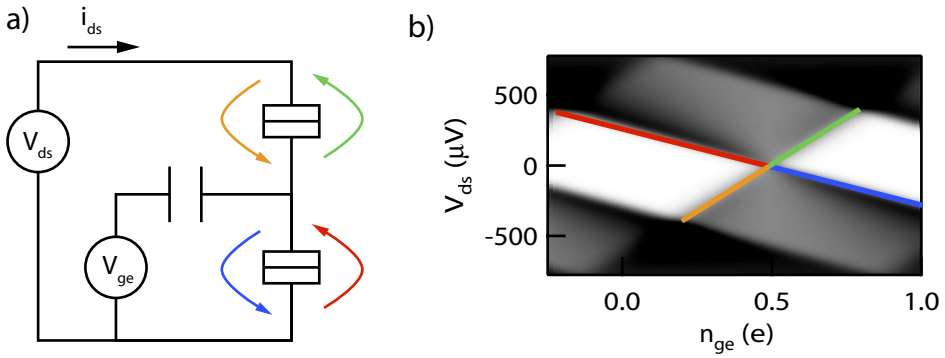

Figure 6.5: a) Normal State SET circuit diagram, and b) model-generated charging diamond of the SET (at very low temperature, for clarity). The lines on part b) represent thresholds for the tunneling processes indicated by the corresponding arrows in part a).

be energetically allowed: electrons must be energetically permitted to tunnel both on to and off of the SET island. Each of these processes becomes activated when a threshold on the charging diagrams is crossed; Figure 6.5 shows thresholds for four such processes. When the SET is operated on the edge of blockade, then, one of the required tunneling processes is barely allowed, or may occur only through thermal excitation, while the other process will happen freely, at a much faster rate. For example, at an operating point near the red line in figure 6.5b, electron tunneling onto the SET island is barely allowed (across the bottom junction), but, once an electron is on the SET island, it will rapidly tunnel off through the top junction. The charge state of the SET island will therefore spend most time with zero electrons on the SET island, with infrequent rapid fluctuations to a charge state with 1 additional electron on the SET island.

More generally, we may infer from this the nature of the charge state fluctuations: at operating points near any Coulomb blockade diamond, the charge state fluctuations of the SET have a duty cycle that is very close to 0 (or 1); in regions of higher current, the duty cycle of these fluctuations is far closer to 50%.

Figure 6.5b also suggests a symmetry in the tunneling rates that is important to note: for any operating point (n_{ge},V_{ds}) on the charging diagram, there exists another operating point ($(1 - n_{ge})$,$-V_{ds}$) where the voltage biases across each of the junctions is exactly inverted. The tunneling rates that determine the SET island charge state fluctuations at these two operating points will be exactly the same, and so both of these operating points will have the same SET backaction – except that a preference for a higher charge state at one operating point will translate into a preference for a lower charge state at the other operating point. Practically, we expect that the effects of backaction

at such paired points will be equal in magnitude, but opposite in the sign of the backaction signal.

6.4 Noise and Drift Rejection

To observe minute variations of SET backaction with operating point, the operating point of the SET must be fixed very precisely. Precisely fixing the SET operating point, however, was found to be far from trivial. Charge noise in the SET could apply random shifts of as much as 10% of an electron to the gate of the SET on timescales that ranged from seconds to 10s of minutes (a more detailed discussion of charge noise can be found in section 1.4.5; Measurements of the charge noise in our system are presented in section 8.2.2). The applied V_{ds} was also found to vary by as much as 100 μV on a timescale of hours or 10s of hours, probably due to thermal offset voltages in the biasing leads. Finally, the box was found to be susceptible to charge noise, which would induce offsets in the box gate voltage n_{gb} of order .05e on timescales that were much longer (10s of minutes to hours) than the corresponding SET charge noise timescales.

Measurement and removal of these three drifts was necessary for the precision Coulomb staircase measurements in this thesis, and was accomplished through three calibration measurements which were repeated frequently ($\sim$ once per minute) during the collection of our data.

SET charge noise occurred on the fastest timescale of these three drifts, and generally posed the greatest threat to the consistency of our measurements. Fortunately, however, it was very easy to remove using algorithms very similar to those discussed in section 5.7: during each recalibration interlaced with our measurements, the response of the SET was measured, and a Lorentzian fit to the resulting data. Any change in the applied voltage at the center of this function was inferred to be due to charge noise in the substrate, and a cancelling signal was applied to the SET gate to remove its effect.

To protect against drifts in the drain source voltage V_{ds}, the response of the SET to a sweep in n_{ge} was measured at an array of drain-source voltages. At each drain source voltage, a Lorentzian was fit to the SET response vs n_{ge} curve. The width of that Lorentzian was taken as a measure of the range in n_{ge} over which current flows through the SET. This width will attain a minimum when the voltage applied across the drain-source of a SET is zero, and the size of the blockaded region of the SET is maximally large (see figure 6.6). This allowed us to find the external voltage required to counteract the thermal offset voltages in the system; any further voltages applied to the SET were then referenced as differences from this found $V_{ds} = 0$ point.

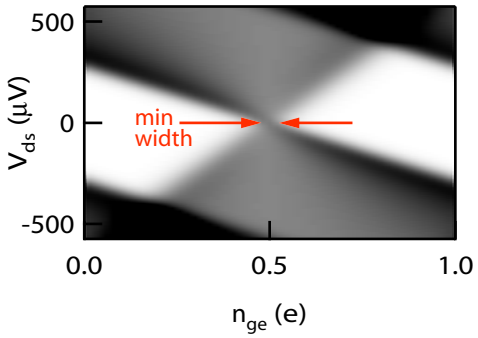

Figure 6.6: Illustration of technique to find external voltage corresponding to $V_{ds} = 0$ on device. The SET response is measured as n_{ge} is swept for an array of V_{ds} values; this may be thought of as taking horizontal slices of the above plot. A Lorentzian is fit to each measured trace. The Lorentzian width will be a minimum at the external voltage corresponding to $V_{ds} = 0$, illustrated with red arrows. Because of thermal offset voltages in the system, the external voltage corresponding to zero volts on the device was generally not zero.

Finally, because the position of the step center was an important metric of the effects of backaction, it was important that we accurately measure and understand drifts and noise in the applied box gate voltage n_{gb}, which will add to the backaction-imposed shift of the Coulomb staircase. This was accomplished by setting the SET to a "fiducial operating point" (at $V_{ds} = 0$, and with n_{ge} adjusted to be 6% of an electron less than the point of maximum conductance), and measuring a Coulomb staircase. The center of this Coulomb staircase was then found. Because this calibration staircase was always measured with the SET at the same operating point (the fiducial operating point), the backaction effects of the SET were presumed to be the same on all calibration staircases, and any offsets in the box gate voltage n_{gb} were presumed to be due to charge noise coupled to the box island. These offsets were counteracted with an externally applied n_{gb}. Backaction-induced shifts of staircases at other operating points were then referenced as changes from the position of this fiducial step.

Removing offsets in this way, extremely precise control of SET measurements was obtained. Staircases measured hours apart with the SET at the same operating point were shown to be exactly alike; staircases measured at different operating points were shown to have consistent differences that did not change with time [see figure 6.7; part (a) shows the location of the box steps without drifts in n_{gb} removed, while in part (b), the drifts have been removed].

From records of the noise rejected by these algorithms, estimates of the precision of our SET control and the uncertainty of our measurements could then be made.

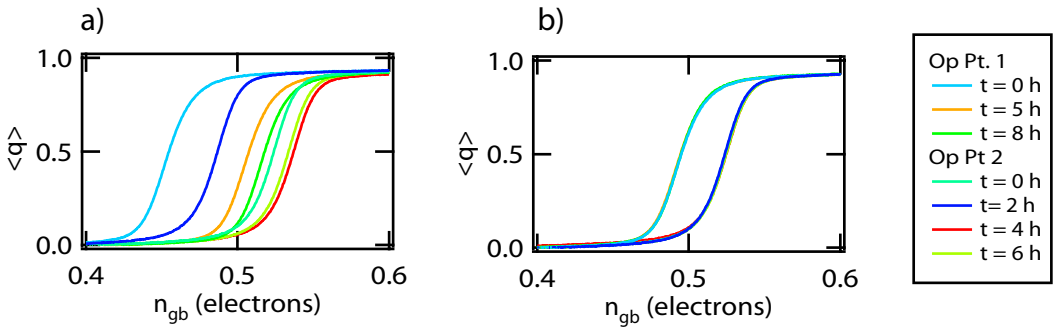

Figure 6.7: a) Repeated measurements of Coulomb staircases of the single electron box taken at two different SET operating points over an 8 hour period. b) When the box gate drift, inferred from interlaced measurements of a fiducial step, is removed, the staircases are shown to overlie exactly, demonstrating the precision of n_{gb}, the applied box gate bias.

The precision of the voltage applied to the SET gate (n_{ge}) was estimated from repeated measurements of the SET transfer function to vary by approximately $5 \times 10^{-3}e$. This was presumed to be due to charge noise causing fluctuations in the total charge coupled to the SET island on a timescale faster than that of our noise rejection algorithm. In our plots of SET backaction vs operating point, this measured uncertainty was reported as an imprecision in the set operating point of the SET.

Repeated Coulomb staircase measurements with the SET at a fixed operating point were found to differ in n_{gb}, or in their horizontal position, by, on average, $5.5 \times 10^{-4}e$, which was reported as the uncertainty of our determination of the "location" of a Coulomb staircase (see section 6.5.3). This effect was again due to charge noise coupling to n_{gb} on a timescale faster than our noise rejection algorithm could remove it.

Finally, measured Coulomb staircases were typically averaged so that the uncertainty in the measurement of the box charge (i.e. noise on the box staircase) was $1 \times 10^{-3}e$.

6.5 Measurement of Backaction

6.5.1 Measurement Overview

Coulomb staircases were measured at an array of operating points in an attempt to sample the full variety of backaction effects that could be produced by the SET (see figure 6.8). Five values of V_{ds} were chosen for five separate series of Coulomb staircases. For each value of V_{ds}, n_{ge} was progressively incremented through a series of distinct SET operating points (see figure 6.8); no measurements are reported at operating points where the SET response did not vary with n_{ge}; thus, the step series

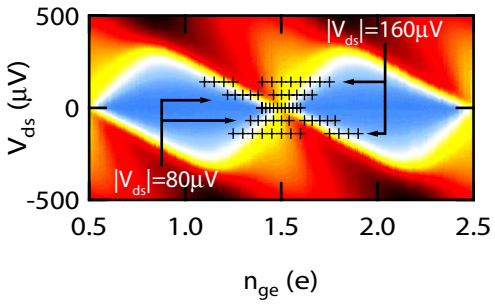

Figure 6.8: Operating points where the backaction of the normal state SET was measured.

have gaps in them at the peak of each transfer function, where the SET gain was zero.

As each Coulomb staircase was measured, the charge coupled from the single electron box to the SET varied the SET's operating point slightly. Thus, a Coulomb staircase measured with the SET fixed at a particular operating point actually samples a range of n_{ge} on the SET. In order to accurately reproduce these results, our sequential tunneling model was used to generate Coulomb staircases in precisely the same way. This is to say, rather than fixing the SET operating point and calculating the time-averaged charge on the single electron box island, the sequential tunneling model was used to calculate the variation in SET current as the single electron box was swept through a Coulomb staircase. This variation in SET output was then calibrated, via a theoretically generated SET current-vs-n_{ge} function, into measured charge on the box island. In this way, the measurement that we physically performed was accurately replicated, and any effects that arose from the coupling of the box and the SET were reproduced in the modeled Coulomb staircases exactly as they were in an experimentally measured Coulomb staircase. This was found to be necessary because of effects arising when the SET and the box were both tuned to be near electrostatic degeneracy – near the so-called "double degeneracy" operating point. At such operating points, the SET's transfer function was affected by its coupling to the Single electron box, and the SET readout was therefore not a faithful measurement of the charge coupled to the SET input. By replicating the measurement using the method described above, however, these effects were accurately modeled.

6.5.2 Demonstration of intuitive understanding of SET Backaction effects

A first demonstration of the backaction of the SET can be seen in variations in the shape of the Coulomb staircase with SET operating point. In section 6.3.2, I suggested that the backaction from SET operating points that are reflections across the degeneracy point ($V_{ds} = 0$, $n_{ge} = \frac{1}{2}$) should

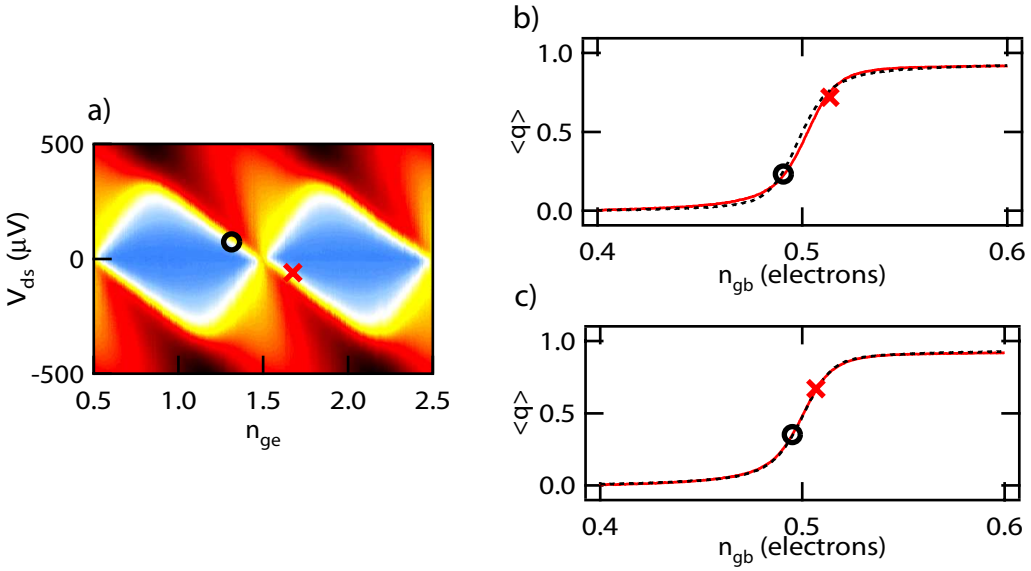

Figure 6.9: a) Diamond of the normal SET showing two operating points where Coulomb staircases were measured. b) Two Coulomb staircases measured at the operating points marked with "X" and "O" symbols of the corresponding colors in part a. As initially measured, these steps showed the expected shift from SET backaction. To demonstrate the asymmetry of these Coulomb staircases, the two staircases have been shifted to that they overlap, which better demonstrates their difference in shape. The two different Coulomb staircases clearly cannot be made to overlie. c) When the red staircase is point-reflected about its center point, the resulting staircase has exactly the same shape as the black staircase. This shows that the asymmetric broadening effects of backaction at the two different operating points have the same magnitude, but act in the opposite direction.

be equivalent, but inverted in magnitude. In figure Figure 6.9a two such operating points have been chosen. The Coulomb staircases measured at these two operating points, shown in Figure 6.9b, cannot be offset to overlay each other. However, when one of these staircases is point reflected about its center, then it exactly overlays the other staircase. We infer from this that the two staircases are asymmetrically broadened by the backaction effects of the SET. The red staircase is preferentially broadened to the left, while the black staircase is preferentially broadened to the right, but the two staircases are nevertheless broadened by charge state fluctuations on the SET island that have the same duty cycle and characteristic frequency. By inverting one staircase, the leftward-broadening of that staircase is shown to exactly overlay the analogous rightward-broadening in the other staircase.

Variations in the position, broadening, and asymmetry of the staircases were seen across all of

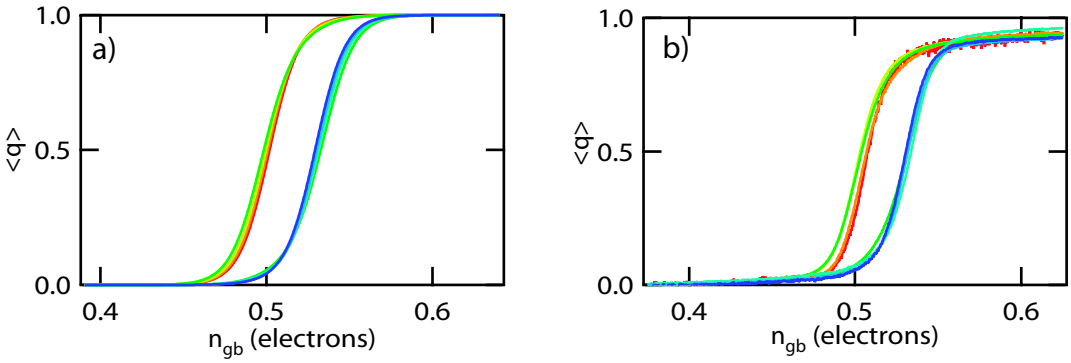

Figure 6.10: a) Theoretically modeled and b) experimentally measured Coulomb staircases for operating points incrementing n_{ge} with $V_{ds} = 0$. The operating points for these staircases are indicated by the markers at $V_{ds} = 0$ in figure 6.8, moving from $n_{ge} = 0.4$ (red) to $n_{ge} = 0.6$ (blue).

the operating points indicated in figure 6.8. For the sake of brevity, I have not included theoretically modeled and experimentally measured steps for each of those operating points. Figure 6.10, however, shows Coulomb staircases taken at a variety of operating points with $V_{ds} = 0$, and is indicative of the excellent agreement between theory and experiment in predicting the trends in staircase offset and shape.

To better quantify these results, numerical measures of the Coulomb staircase shift, broadening, and asymmetry were required.

6.5.3 Location Variations of the Coulomb Staircase

The most obvious variation of the between the Coulomb staircases in figure 6.10 is in their position: depending on the operating point of the SET, these staircases show consistent displacements in n_{gb} of as much as κ_{SET} electrons. The source of this shift is the mean value of the charge on the SET island: when the box gate is swept to measure a Coulomb staircase, the charge from the SET island couples to the box island as well, and may be thought of as adding a DC component to n_{gb}, the externally applied voltage. The time-averaged charge on the SET island may vary by as much as 1 electron, and the fraction of the SET island's charge that is coupled to the box is expressed simply as κ_{SET}. The additional charge coupled to the box by the SET, therefore, may vary by as much as κ_{SET}; it is worthy of note that the staircases in Figure 6.10 show shifts of this magnitude.

More generally, however, the precise shift of a particular staircase is a function of the duty cycle of the charge state fluctuations on the SET island; these fluctuations are, in turn, a complicated function of the SET's operating point. To demonstrate our understanding of the backaction understood with

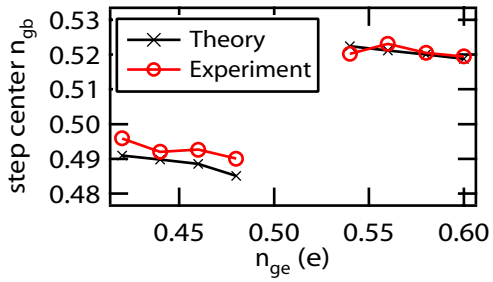

Figure 6.11: Position of the center of Coulomb staircases as a function of the n_{ge} value of the SET when they were measured. All staircases are measured with $V_{ds} = 0$. As n_{ge} is moved through an array of values, the steps show an offset that is in good agreement with theoretical predictions.

the sequential tunneling model, we showed that the experimentally measured trends in Coulomb staircase shift agreed with those predicted by the sequential tunneling model.

We measured the shift of each staircase by finding the value of n_{gb} at the midpoint of the rise of that staircase. It is worthy of note that this measure contained an arbitrary constant offset: because of the thermal offsets in the biasing wiring and the charge noise in the substrate, we could not, with certainty, apply exactly half of an electron of polarization charge to the box gate. However, by referencing all box shifts as shifts relative to the fiducial step (described in section 6.4), we were able to find the shift of each staircase relative to other staircases measured, and accurately reproduce trends in the shift of the staircases. Thus, despite difficulties introduced by the uncertainty of the voltages we applied, our measurement was faithful.

The results of this analysis are shown on the series of steps measured with $V_{ds} = 0$ in figure 6.11. As the gate charge on the SET (n_{ge}) is varied, we find that the variation in position of the measured steps (black crosses) is quite well matched by that of the modeled staircases (red circles). It is worthy of note that this plot amounts to a zero-parameter fit: each of the relevant parameters in the sequential tunneling model was determined from independent measurements of the SET and box. The modeled staircase position, therefore, amounts to less a fit to the data than a prediction from a knowledge of the parameters of the SET and the box, which is seen to agree quite well.

6.5.4 Width Variations of the Coulomb Staircase

The width of a step was similarly difficult to quantify. One can not merely cite the width of a step as the apparent temperature that best fits a measured Coulomb staircase because, as discussed previously, both backaction and quantum fluctuations distort the Coulomb staircase in ways that

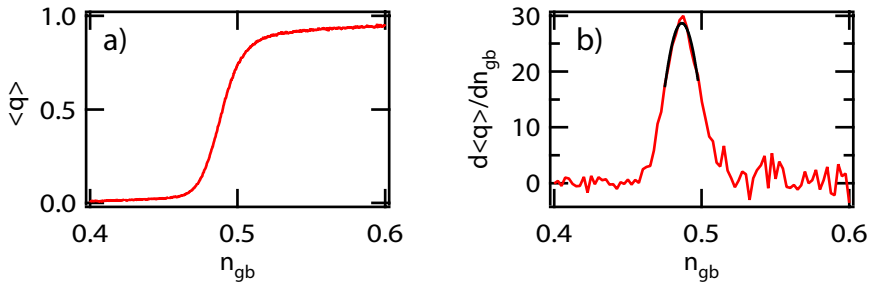

Figure 6.12: Method for calculating the peak derivative of a Coulomb staircase. The raw data (a) is differentiated, and then decimated to produce a step derivative (b). A parabola is fit to the peak of this step derivative (shown in black) to determine the peak value that the derivative approaches.

are fundamentally non-thermal. In order to separate backaction effects from the effects of quantum fluctuations, we report the broadening of a staircase as the maximum slope attained by that staircase. A staircase at zero temperature broadened only by quantum fluctuations will have an infinite slope at $n_{gb} = \frac{1}{2}$ (see figure 2.11). Finite slopes caused by backaction and thermal fluctuations at degeneracy may therefore be considered to contain no additional broadening due to quantum fluctuations of charge on the box, and were used to to provide a measure of the effects of backaction isolated from the effects of quantum fluctuations.

To quantify the maximum slope of a Coulomb staircase, a staircase was first differentiated to yield the staircase slope as a function of n_{gb}. Because differentiating a noisy trace increases the noise on that trace, the resulting staircase derivatives were then decimated, to simplify the fit and remove much of the noise. A parabola was then fit to the peak of the step derivative, so that the noise from individual data points did not yield erroneous values of the step derivative; this may be thought of as inferring the maximum slope of a staircase by using a larger number of data points about the coulomb staircase center. Practically, it was found to yield measurements of the value of the peak derivative of a Coulomb staircase with an uncertainty of approximately 0.4 (in dimensionless units of electrons/electron). This uncertainty in the measured maximum staircase slope was far less than the change in maximum staircase slope predicted by our backaction model.

Using this methodology, the maximum slope of the Coulomb staircase could be plotted as a function of the SET operating point. In figure 6.13, this is shown for the series of SET operating points measured at $V_{ds} = 0$. Coulomb staircases were generated using the sequential tunneling model described in Chapter 2, and analyzed in the same fashion to produce the model curve shown in figure 6.13. The only free parameter in the modeling of the Coulomb staircases is the temperature of the

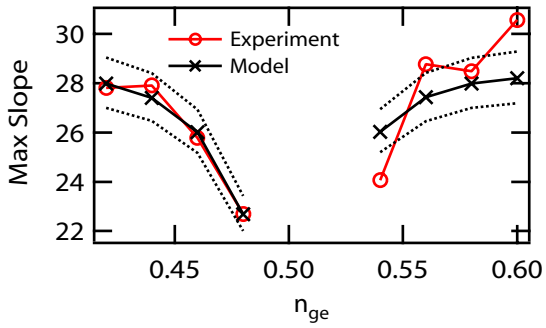

Figure 6.13: Maximum slope of coulomb staircase plotted as a function of n_{ge}, all at $V_{ds} = 0$. A sequential tunneling model accurately predicts the trend in staircase width with operating point. Uncertainty in the modeled Coulomb staircase slope (black dotted lines, corresponding to ± 1 mK) is inferred from the range of box temperatures yielding Coulomb staircases consistent with our results.

single electron box, which could not be found by simple measurement: ideally, one would deduce the electron temperature from the width of the Coulomb staircase, but this requires a measurement of a Coulomb staircase that is not subject to the effects of SET backaction. The electron temperature of the box was therefore used as an adjustable parameter; Coulomb staircases were generated at an array of temperatures and compared to the measured data. It was found that trends in the staircase width were best reproduced by modeled staircases at a temperature of 27 mK, although staircases modeled at temperatures between 26 mK and 28 mK were found to be consistent with the measured staircases (see figure 6.13.) The electron temperature used for the modeling of the single electron box was therefore reported as 27 ± 1 mK, although this does not necessarily reflect the actual electron temperature of our sample. Additional broadening from fast charge noise or from voltage noise on the leads may have also caused homogeneous staircase broadening that was recreated in the model by an increased temperature.

To demonstrate conclusively that Coulomb staircases are broadened by backaction, we must prove that variations in staircase width are not caused by simple heating of the sample. This important check on our data is nontrivial: indeed, heating of the sample by the SET is expected to vary with SET operating point. Heating of the SET is typically thought to be proportional to the power dissipated in the SET, calculated as the product of the drain-source current (I_{ds}) and V_{ds}, the drain-source voltage. At a fixed drain source voltage V_{ds}, heating will be maximal where the current is maximum, which occurs at operating points where electron tunneling rates onto and off of the SET island are equal. At these same operating points, however, the broadening due to backaction, which may be considered to increase as the duty cycle of the charge state fluctuations on the SET

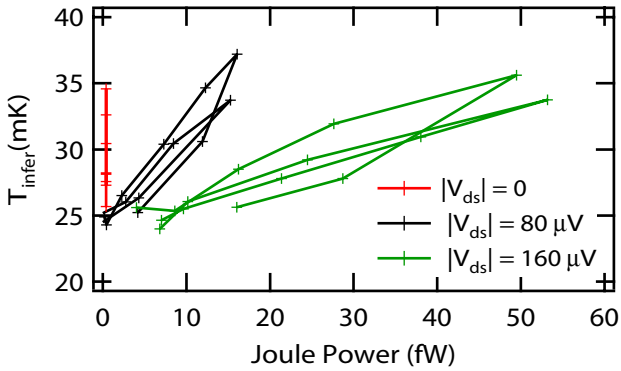

Figure 6.14: Plot of temperature inferred from maximum staircase slope vs Joule power dissipated in the SET. At higher Joule powers, Coulomb staircases are broadened, no thermal conductance can adequately explain the staircase broadening at $V_{ds} = 0$.

island approaches 50%, will also be maximal. Fortunately, however, we were able to show that SET heating was a small effect that could not account for variations in staircase slope comparable to the variations predicted to be due to backaction.

To compare the effects of thermal broadening and backaction broadening, the power dissipated in the SET was calculated as a function of SET operating point by taking the product of V_{ds}, the drain-source voltage, and I_{ds}, the drain-source current. At $V_{ds} = 0$, the power was calculated from the SET conductance and the magnitude of the oscillating voltage from the SET tank circuit, which was taken to be approximately $6\mu V$.

This power was compared to the Coulomb staircase broadening for each operating point indicated in figure 6.8. We express Coulomb staircase broadening as the effective temperature that one would infer from the maximum slope of a Coulomb staircase. From equation (2.19), this is seen to be:

$$T_{infer} = \frac{E_c/k_B}{2\ m_{max}} \tag{6.1}$$

where m_{max} is the maximum slope found at the center of the step of a particular staircase.

The results of this comparison are shown in figure 6.14. At high values of the drain-source voltage V_{ds}, the temperature inferred from the staircase slope is seen to increase with the power dissipated on the SET. However, if we presume a simple linear proportionality between the power dissipated in the SET and the effective box temperature:

$$\Delta T = K \Delta P \tag{6.2}$$

then we find that the inferred temperature correlation, 0.2 mK/fW, predicts that staircases measured

with $V_{ds} = 0$ should experience an immeasurably small amount of heating from SET operation[1]. In publishing our measurements of SET backaction, we therefore presented only data measured at $V_{ds} = 0$, where we could unambiguously say that SET heating did not cause the broadening that we observed, which was therefore entirely due to SET backaction.

6.5.5 Asymmetry of the Coulomb Staircase

Changes in the asymmetry of a Coulomb staircase are perhaps the most unambiguous signature of SET backaction. Changes in the position of the Coulomb staircase may be affected by charge drifts; measurements of the broadening of a Coulomb staircase may be confounded by quantum broadening, heating, or excess noise on the SET sample. Each of these effects, however, is predicted to have no effect on the asymmetry of a Coulomb staircase, which may therefore be considered to be a consequence only of the SET backaction.

The asymmetry of the measured staircases is our staircases was visually apparent (see figure 6.9), but was difficult to quantify. In this section, I will describe our observations of the asymmetry of Coulomb staircases, and the predicted variations staircase asymmetry with SET operating point. I will close with a brief discussion of our attempts to quantify this asymmetry, which ultimately did not yield incontrovertible numerical results.

The source of asymmetric broadening of the Coulomb staircase was discussed at length in section 6.3.1. We imagine it to be a consequence of asymmetric broadening from the charge fluctuations coupled from the SET island. A fluctuating charge coupled to the box gate will broaden a measured Coulomb staircase; the charge fluctuations on the SET island have a peculiar nature that broadens the Coulomb staircase asymmetrically. If we think of the telegraph noise on the SET island as a signal fluctuating about its mean value, then a signal with a duty cycle close to 0 (or 1) will consist of infrequent deviations far to one side of the mean value. When these fluctuations broaden the Coulomb staircase, then they will do so in a way that is "stronger" in one direction (e.g. positive n_{gb}), but which has a "longer range" in the other direction (negative n_{gb}, in this example). This effect, furthermore, is expected to vary with the duty cycle of the charge state fluctuations on the SET.

We see this in the Coulomb staircases of figure 6.15a: the two staircases are functionally different,

[1] The power dissipated in the SET at operating points with $V_{ds} = 0$ was calculated to be always $< 1\,\mathrm{fW}$, and is plotted to scale on figure 6.14. This amount of dissipated power leads us to infer that the SET heats the box by no more than 0.2 mK at $V_{ds} = 0$.

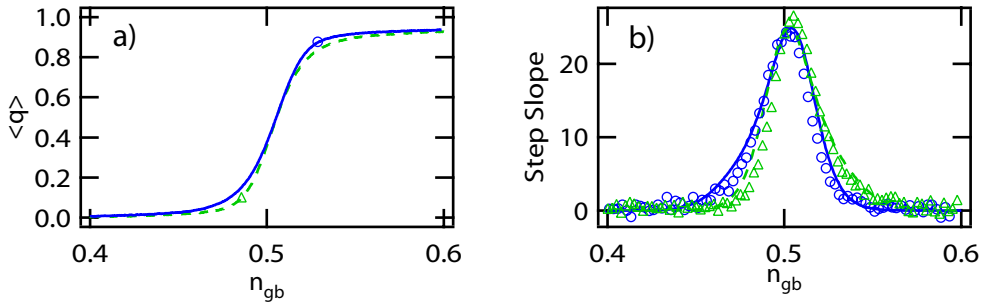

Figure 6.15: a) Coulomb staircases taken at two different operating points where the asymmetry is predicted to be equal in magnitude but opposite in direction. The centers of the Coulomb staircases have been aligned to show their difference in shape b) Derivatives of these Coulomb staircases and of the corresponding model-generated Coulomb staircases, decimated to increase the signal-to-noise. The asymmetry of the steps is clearly seen in the asymmetric tails of the two peaks.

and cannot be shifted to overlay one another. The blue (solid) staircase is broadened over a longer range to the left, while the green (dashed) staircase is broadened over a longer range to the right. This is more apparent, and easier to quantify, when the derivatives of the staircases are compared (see figure 6.15b). In this plot, the data have been aligned by matching the points of peak derivative – that is, the point of the staircase with maximum slope. Clearly the "wings" of the blue function extend preferentially to the left, while the tail of the green function extends preferentially to the right.

To quantify this effect, we compared the values of n_{gb} at the point of maximum derivative (which is the peak of each curve in figure 6.15b) and at the midpoint of each staircase (determined as a measure of the staircase shift). We may think of the first of these two measures as the location of the peak of the function plotted in figure 6.15b; the second of these measures corresponds to the point in n_{gb} that is the "median" value of a distribution represented by the staircase derivative (i.e., half of the integrated area of the function lies to the left of this point, and half of the integrated area of the function lies to the right of this point). These two measures will be coincident if the derivative of a Coulomb staircase is symmetric about its center, and will in general be unequal if it is not; a trend in this quantity may be taken to demonstrate a trend in the asymmetry of the measured Coulomb staircases.

Ultimately, however, our determination of asymmetry in this fashion was lacked the necessary precision make a detailed comparison with theory. This was found to be due to two factors: inaccuracies introduced by noise in our charge measurement, and errors in our determination of the center

of our steps from quantum fluctuations.

Although the uncertainty in our measurement of the charge on the single electron box was averaged to an exceptionally low value – $1 \times 10^{-3}e$ – it was nevertheless a large source of error in the determination of the asymmetry by the scheme outlined above. This is a consequence of our differentiation of the Coulomb staircase: taking the derivative of a noisy signal increases the fractional noise by a large amount. We attempted to circumvent this by decimating the resulting step derivatives, but were still subject to significant errors in the derivatives of the measured steps. (see, for example, figure 6.15b).

Errors were also introduced into the determination of Coulomb staircase midpoints – used to calculate the asymmetry of the Coulomb staircase – by the quantum broadening of our staircases. Ideally, the midpoint of the Coulomb staircase would be the point in n_{gb} where the step attains half of its height. Because of quantum fluctuations of charge, however, the measured charge on a Coulomb staircase was not a pure charge state in the region surrounding the step center; instead, there was a slow tail to the step that extended far away from the measured step center. To find the midpoint of the staircase, we therefore needed to consider a range of the Coulomb staircase symmetric around each step's center. Backaction-induced shifts of the Coulomb staircase, however, meant that our data was generally not taken with the center of a Coulomb staircase precisely in the middle of a sweep.

Because of errors introduced by these two effects, a quantitative comparison of the measured staircase asymmetry to the modeled staircase asymmetry was not completed. Nevertheless, qualitatively, it was found that the asymmetry of the Coulomb staircases varied with operating point exactly as expected; the agrement in shape in magnitude of the asymmetry demonstrated in figures 6.9 and 6.15, is typical of the rest of the data measured, and provides a conclusive demonstration that the observed effects were due to SET backaction.

6.6 Measurement of Single Electron Box Polarizability

The same techniques that were used to measure normal state SET backaction were also used to make measurements demonstrating the effects of quantum fluctuations (Lehnert et al., 2003a) on the single electron box, confirming the theory discussed in section 2.7.2. I will provide only a cursory treatment of these measurements in this thesis, as they were properly the work of Prof. Konrad Lehnert, but they nevertheless deserve mention to elucidate the subtleties of the measurement process.

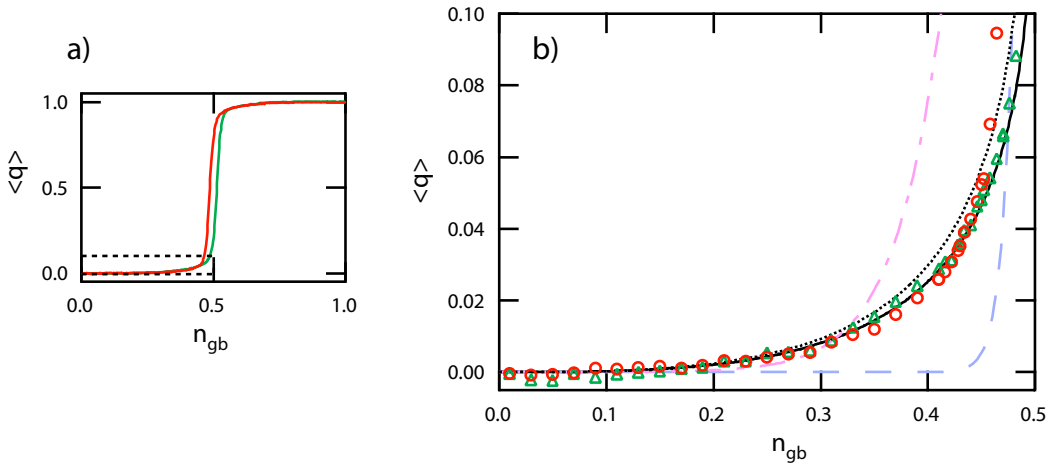

Figure 6.16: Comparison of theoretically predicted quantum broadened staircase and measured Coulomb staircases. a) Two measured Coulomb staircases with different SET backaction effects are shown. We consider quantum fluctuations only in a region of these staircases far from degeneracy, where the measurement is independent of the backaction effects of the SET. b) A precise functional comparison of these staircases (color coded as in a) with theoretical predictions. Neither hot (pink dash-dot) or cold (blue dashed) thermal Coulomb staircases adequately fit the measured functional form. Predictions for quantum broadened Coulomb staircases (black lines) agree much better with the measured data. Dotted black line shows theory to first order. Solid black line shows theoretical prediction calculated to second order in the tunneling conductance g. Figure courtesy of Konrad Lehnert.

Theoretical descriptions of quantum fluctuations on the single electron box predict that the ground state of the single electron box will differ subtly from a charge eigenstate of the box island, and that a measurement of the charge on the box in its ground state will therefore show a non-integer number of electrons in regions of the Coulomb staircase where a simple thermal theory predicts significant population in only one state. This non-integer charge is predicted to vary with the splitting between the energy levels of the single electron box, and therefore has led to predictions of Coulomb staircases which, even at zero temperature, would show a functional form that is broadened in a decidedly non-thermal manner. The functional form of these predicted staircases is presented to lowest order in equation (2.24). To measure quantum fluctuations, we wished to measure the Coulomb staircase with sufficient accuracy to confirm that they followed this functional form.

A comparison of the measured quantum broadened Coulomb staircases, compared with theoretical predictions, is shown in figure 6.16b. Two separate effects complicated the measurement of the quantum broadening of our steps. First, the backaction of the SET, discussed at length above,

distorted the Coulomb staircases in a way that obscured our measurement of quantum fluctuations in certain regimes. Second, our method for the measurement and calibration of Coulomb staircases, discussed at length in chapter 5, artificially removed any linear slope from the flat part of the Coulomb staircases (away from $n_{gb} = \frac{1}{2}$, the degeneracy point). Both of these problems, however, were circumvented, and we were able to make measurements of the quantum broadening of the Coulomb staircase with exquisite precision.

The first complication to these measurements arose because of the backaction that is the subject of this thesis. If a measurement of the quantum fluctuations of the single electron box aims to report anomalous broadening of the Coulomb staircase, then this anomalous broadening must be separated from the broadening due to the backaction described in this thesis.

In our discussion of backaction-induced width variations of the Coulomb staircase, we noted that quantum fluctuations cause broadening of a Coulomb staircase that is most noticeable away from the degeneracy point. We used this fact to our advantage in our measurements of the width variation of the Coulomb staircase (see section 6.5.4), where the slope at the steepest point in a Coulomb staircase was considered to be immune to the effects of quantum fluctuations. Similar reasoning suggests that a measured Coulomb staircase far from the degeneracy point is unaffected by SET backaction or thermal fluctuations. Our measurement of quantum fluctuations on the Coulomb staircase therefore was restricted to a region of the Coulomb staircase far from degeneracy (shown in figure 6.16a), where the effects of backaction were known to be negligible.

The second complication to our measurement of quantum fluctuations arose from the method used to calibrate our Coulomb staircases. As discussed in section 5.5.2, measured Coulomb staircases were inferred from the sawtooth variation in the potential of the box island. A measurement of q_{saw}, the sawtooth potential response of the box island was converted into q_{step}, the Coulomb staircase via the expression:

$$q_{step} = n_{gb} - \frac{q_{saw}}{\kappa_{box}} \tag{6.3}$$

I refer the reader to the discussion in section 5.5.2 to see that variations in κ_{box} will change the slope in the flat part of the measured Coulomb staircase. We typically chose κ_{box} to make the center of our measured Coulomb staircases flat, as would be required by a simple thermal theory of staircase broadening; however, this also artificially removed any linear slope in the staircases that was a consequence of quantum fluctuations. Happily, however, there was sufficient curvature in the

quantum-broadened Coulomb staircases that the quantum broadening still produced a measurable change in the functional form of the Coulomb staircases. The fits to the measured Coulomb staircases in figure 6.16b have subtracted a slope from the Coulomb staircases to force them to have zero slope at $n_{gb} = \frac{1}{2}$, and show excellent agreement with theoretical predictions.

As a consequence of this additional slope, measured values of κ_{box} appeared to differ between the normal and the superconducting state. In the normal state, κ_{box} was measured to be $(3.35 \pm .05) \times 10^{-2}$, while in the superconducting state, the value of κ_{box} inferred from the measured Coulomb sawtooth functions was $(3.70 \pm .05) \times 10^{-2}$, about 10% larger. Because $\kappa_{box} = C_c/C_{\Sigma,box}$ is proportional to the charging energy of the box, and the coupling capacitance C_c is unchanged, we may think of this change in staircase slope as a renormalization of the box capacitance, $C_{\Sigma,box}$, or equivalently of the box's charging energy.

We may understand this effect by considering the relationship between the potential of the box island and the measured charge on the box island. When the box is gated with a potential n_{gb}, it increases the potential of the box island, which may be thought of as increasing the polarization charge on capacitances between the box island and ground. The proportionality between this applied potential and the induced charge may be used to find the capacitance of the box island. Quantum fluctuations of charge have the effect of decreasing the apparent charge on the box island for an applied voltage; this appears in our measurement as an increased island capacitance. Thus, we say that the quantum fluctuations of charge on the box island renormalize the capacitance of the junctions on the box island, and decrease the apparent charging energy.

Our knowledge of the functional form of quantum broadening allows us to infer the "bare" charging energy, and the corresponding "bare" capacitance of the box island, which we would observe if our sample were immune to the effects of quantum fluctuations. For our sample, the bare capacitance measured in this way was inferred to be 498 ± 16 aF. By measuring the island in the superconducting state, however, we may also access this "bare" capacitance, as the gap Δ suppresses the quasiparticle states that contribute to quantum broadening of the Coulomb staircase. Measured in this way, the bare capacitance was calculated to be 478 ± 7 aF, which is consistent with the value inferred from the normal state.

This theory was also empirically verified by comparing the values of κ_{box} inferred from Coulomb staircases measured at different magnetic fields (see figure 6.17), as the magnetic field had mostly – but not entirely – suppressed superconductivity in our samples. As the superconductivity was

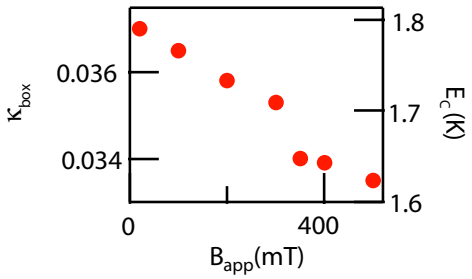

Figure 6.17: Renormalization of κ_{box} and box charging energy by quantum fluctuations, as magnetic field is varied. Increasing the magnetic field from zero suppresses superconductivity, and increases the density of available states to contribute to quantum fluctuations on the box. This causes us to infer a lower value of κ_{box} and a correspondingly lower box charging energy E_C. Figure courtesy of Konrad Lehnert.

gradually suppressed, the density of available quasiparticle states varied. This density of available quasiparticle states figured directly into the calculation of the quantum-fluctuation induced renormalization of the box charging energy. Thus, as the magnetic field suppressed superconductivity, the variation of the quantum fluctuations could be observed

In summary, quantum broadening of the normal state Coulomb staircases was measured to extremely high accuracy, and, where its measurement was not confounded by the effects of SET backaction, was found to agree very well with theoretical predictions calculated to second order in the dimensionless conductance, g, of the box tunnel junction. Our measurements were also used to infer a renormalization of the box junction capacitance from the quantum fluctuations of charge, and this was found to vary as expected when a BCS gap modified the density of quasiparticle states available to participate in the quantum broadening effect.

Chapter 7

Backaction Measurements in the Superconducting State

7.1 Introduction

Measurement of the backaction of the superconducting SET proved to be one of the most elusive goals of the work done for this thesis. In the fall of 2003, we measured a sample fabricated by the group of Per Delsing at Chalmers University in Sweden in the superconducting state, and effects were noted that seemed consistent with superconducting SET backaction that could be described within the formalism of quantum noise outlined in section 3.5. A careful analysis of our results, however, raised questions as to whether or not trends in the backaction effects that we observed were consistent with our theoretical predictions. In addition, ongoing theoretical analysis suggested that the noise effects of the environment acting on the Cooper pair box may have been poorly controlled, and that, within the data set from 2003, it may have been difficult to separate effects of SET noise from the noise effects of a poorly controlled environment.

We therefore attempted to design new samples, at Yale, to correct these shortcomings. The Yale samples were fabricated with coplanar waveguide leads that were designed so that the environment of the Cooper pair box was effectively a well-controlled 50Ω transmission line at all frequencies relevant to its operation. Details of this design are included in section 4.2.2, while measurements of the RF impedance that this design presented to the qubit are described in section 8.1. The samples fabricated at Yale were also designed with E_J, the Josephson coupling energy, and E_C, the box charging energy, in a different regime from the Chalmers sample, in an attempt avoid Cooper-pair breaking effects and to better match the energy splitting of our qubit to our experimental capabilities.

When measured, however, the Yale-made samples were unable to reproduce the results observed in the Chalmers samples in 2003. Measurements of many different samples, at both dilution refrigerator and pumped Helium-3 temperatures, repeatedly showed effects disrupting the superconductivity in the Cooper pair box, breaking Cooper pairs into quasiparticles, and obscuring the backaction effects that we had hoped to measure. The broken Cooper pairs were thought to be a consequence of the operation of the SET, and so we consider this effect to be a very blunt form of SET backaction that ultimately obscured the subtler effects from quantum noise on the SET input.

In this chapter, I will summarize the measurement techniques used in the superconducting state and present the preliminary superconducting backaction measurements made in 2003. First, in section 7.2, I will describe how our understanding of the superconducting SET response was used to precisely determine the parameters of the SET samples that we measured. A precise knowledge of the SET parameters permitted us to implement a charge noise rejection algorithm similar to that used in the normal state to control the SET operating point; the particular implementation of this algorithm in the superconducting state will be described briefly in section 7.2.1.

Using this charge noise rejection algorithm, calibrated measurements of the Cooper pair box were made using the techniques described in section 5.5. In section 7.3.1, I describe how these precision measurements were made while the Cooper pair box was irradiated with microwaves in order to spectroscopically probe the energy splitting of the Cooper Pair box. Then, in section 7.3.2, I will describe how combinations of simple Coulomb staircase measurements and the spectroscopic interrogation of the box energy splitting were used to obtain very accurate measurements of the sample parameters for our Cooper pair box samples. A catalog of the box and SET parameters thus determined for the different samples studied in this thesis will then be presented, in section 7.4.

The remainder of the chapter will focus on the measurements made of various types of SET backaction. The most blunt form of backaction, noted in section 3.3.2, involves the breaking of Cooper pairs on the box island by SET operation. When this occurs, a superconducting Coulomb staircase will not show a "step" with every 2 electrons of polarization charge coupled to the box island, but will instead show steps each electron. Our observations of this so-called "quasiparticle poisoning" will be discussed at length in section 7.5, where I will also discuss certain experimental schemes that were devised in futile attempts to circumvent it.

I will then discuss the quantum noise effects anticipated in section 3.5, and observed in 2003. In section 7.6, I will discuss how the quantum noise of the SET is predicted to be capable of inducing

a population inversion in the Cooper pair box, and how we may have seen this in our measurements of the Cooper pair box. In section 7.7, I will discuss how the quantum noise of the SET is predicted to affect the relaxation time of the Cooper pair box, and how our time-domain measurements of the Cooper pair box showed effects that were thought to be due to the backaction of the SET, but which further investigation cast into doubt.

Finally, in section 7.8, I will summarize our understanding of the theoretical goals of our measurements, of the limitations of the specific measurements that we performed, and will discuss different directions that future work in this field might pursue.

7.2 Determination of SET Parameters

To model and replicate SET backaction in the superconducting state, we required a knowledge of the same parameters that were used in our normal state calculations, all of which are listed in figure 6.1. In practice, many of these parameters were determined in exactly the same way in the superconducting state as in the normal state, and oftentimes the two measurements were corroborated with each other (the response of the SET in the superconducting state was generally sharper, and so the superconducting measurements were generally found to be more accurate, and were usually preferred over normal state measurements of the same quantities). Our description of the measurement of these parameters will therefore be brief, and will focus mostly on measurements where greater accuracy could be attained from measurements of a superconducting device. I will also briefly discuss measurements of the superconducting gap Δ, which could be measured very precisely from the SET's response.

Several of the parameters were determined in exactly the same fashion as in the normal state. In particular, the series resistance of the SET junctions was found from I-V curves of the SET at high drain-source bias, and the relevant capacitances between the two gates and the two islands were found using the periodicity of the response to various combinations of sweeps on the SET and box gate, as described in section 5.6.

Other parameters could be measured in the same way as in the normal state, but, because of the increased sharpness of the superconducting SET response, could be measured more accurately. These include the SET charging energy E_C and the SET junction asymmetry.

The SET charging energy could be found from the range, in V_{ds}, of the SET gaprise feature (see figure 7.1). In section 3.4.2 it was noted that the gaprise in a superconducting SET diamond has the

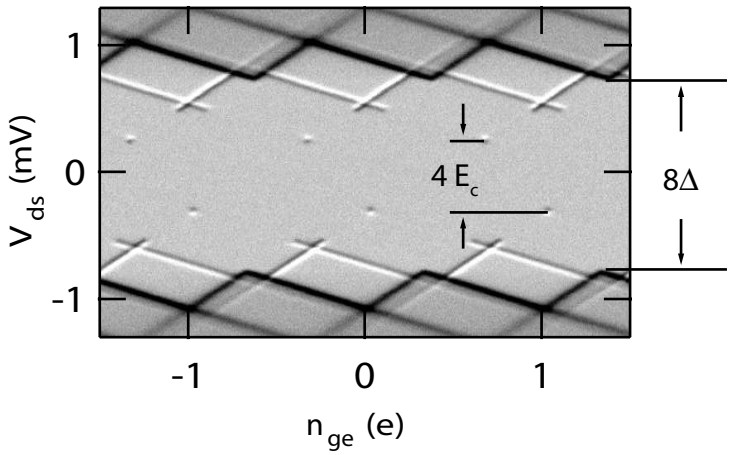

Figure 7.1: Determination of E_J and E_C from superconducting SET response diamond. The difference in V_{ds} between the two DJQP features was used to calculate E_C, while the difference in voltage between the onset of the gaprise was used to calculate Δ, the superconducting gap.

same response pattern as the blockade region in a normal SET's response; as in the normal state, the extent of this feature (in V_{ds}) can therefore be used as a measure of E_C. This provides a more accurate measure of E_c than the corresponding normal state calculations, because the density of states at the onset of superconducting tunneling changes more abruptly than in the normal state. A second measure from the superconducting diamond, however, was found to provide the most accurate measurements of SET charging energies. As discussed in section 3.4.4, the DJQP feature occurs at the intersection of two quasiparticle resonances, each of which occurs at sets of operating points that define a diagonal line in on the superconducting SET response diamond. Solving for the point at which these resonances intersect, we find that we expect the DJQP feature to appear when a drain-source voltage of $eV_{ds} = 2E_C$ is applied to the SET. Because of thermal offset voltages, we cannot directly measure the absolute drain-source voltage that we apply to the SET island, but we do have a precise knowledge of relative voltages that we apply. By looking at the difference in V_{ds} between the two DJQP features (at positive and negative V_{ds} on the sample), therefore, we may infer the charging energy of the SET (see figure 7.1). Because the DJQP is a very sharp feature, this permitted us to obtain very accurate measurements of E_C.

While our measurement of the gaprise was not our best tool for calculating E_C, it was useful for measuring Δ, the gap energy of the superconductor that comprised the SET island. As noted in section 3.4.2, the onset of quasiparticle tunneling occurs when the applied drain source voltage satisfies $eV_{ds} \geq 4\Delta$ – when the drain-source voltage can supply enough energy to break a Cooper pair

and permit quasiparticle tunneling across both SET junctions. As in the case of the DJQP, we did not measure this by applying an absolute voltage of $4\Delta/e$, but instead measured the difference in V_{ds} between the onset of quasiparticle tunneling in the positive-V_{ds} and negative-V_{ds} directions (see figure 7.1). Such measurements of the superconducting gap were an important necessity for our experiment: the gap of the aluminum comprising our samples varied with the cleanliness of the aluminum used, and was lessened when an applied magnetic field began to suppress the superconductivity in our sample.

The SET junction asymmetry could also be found to a much higher precision in the superconducting state than in the normal state. In the normal state, the asymmetry in the size of the SET junctions was found from the ratio of the slopes of the left-diagonal and right-diagonal lines comprising the SET diamonds (see section 6.2). Because the onset of quasiparticle tunneling in the superconducting state is sharper than the onset of single-electron tunneling in the normal state, a similar measurement in the superconducting state yields much more accurate results. We were also able to infer the capacitive asymmetry of the SET junctions from the slopes of the two JQP lines, which were even sharper than the quasiparticle tunneling features and provided an even more accurate measure of junction size differences.

These same parameters could be determined with even higher accuracy from the combined effects of many superconducting SET response features. A library of code was written in IGOR Pro by Dave Schuster which plotted Cooper pair and quasiparticle tunneling thresholds on a SET diamond; see figure 7.2. The parameters that were used to predict the tunneling thresholds, then, could be adjusted until the tunneling thresholds best matched the observed SET response. SET parameters obtained in this way were thought to be more accurate than those obtained through other measurements, because they combined the effects of many different features on the SET diamond; empirically, they were seen to be more precise in repeated measurements.

7.2.1 Charge Noise Rejection and Operating Point Determination

As in the normal state, the ability to make precise measurements with the superconducting SET hinged on our ability to remove drifts and noise in our applied gate voltage at low frequencies. Charge noise in the superconducting SET, like that discussed in section 6.4, appeared as sudden offsets in n_{ge}, the SET gate voltage, and drifts in V_{ds}, the SET drain-source voltage.

Unlike the normal state measurements, our measurements in the superconducting state made no

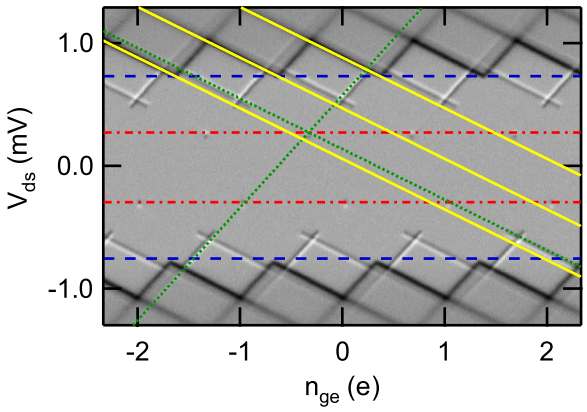

Figure 7.2: Simultaneous determination of E_c, Δ, and capacitance asymmetry in the superconducting SET using overlaid tunneling thresholds. E_c, Δ, C_2/C_1, and offsets and V_{ds} and n_{gb} are adjusted so that the Cooper pair and quasiparticle resonance lines that they predict best overlay a measured superconducting SET response diamond. Parameters are adjusted so that the quasiparticle tunneling thresholds (solid yellow lines) overlay the gaprise, and so that the Cooper pair resonances (dotted green lines) overlay the JQP features at both positive and negative V_{ds}. The charging energy E_C and the V_{ds} offset are adjusted so that the red dash-dotted lines at $\pm 2E_C$ lie on top of the DJQP features, and Δ is adjusted so that the blue dashed line lies at the onset of the gaprise feature.

attempt to measure or correct for drifts in n_{gb}, the box gate charge. This was not for any innate reason, but rather for a technical one: the samples measured in the superconducting state generally suffered from poor signal-to noise ratios[1], and a fast measurement of the Coulomb staircase was too noisy for the Coulomb staircase position to be found accurately. In the samples that were studied in detail, furthermore, the SET charge noise showed large (0.01-0.1e) charged fluctuators that were active on timescales of 10-30 seconds, requiring that the SET response be checked for drifts in n_{ge} after each 30 seconds of averaging. These recalibrations were simply too frequent to measure the box with enough signal-to-noise to accurately reject shifts. Even if it were possible to measure the superconducting staircase accurately during this time, shape variations in the superconducting staircases made it difficult to find a consistent measure of staircase shift.

When searching for effects due to the backaction of the SET, we concentrated our efforts on operating points near the DJQP feature in the SET response (see figure 7.3). For this reason, the remaining discussion of operating point determination and charge noise rejection will focus on this region. Operating points near the DJQP were thought to be advantageous because they involved

[1] Usually due to tank circuits that poorly matched the SET impedance to the 50 Ω lines. See (Roschier et al., 2004) for a full description of the effects of tank circuit design on the signal-to-noise ratio of a SET readout.

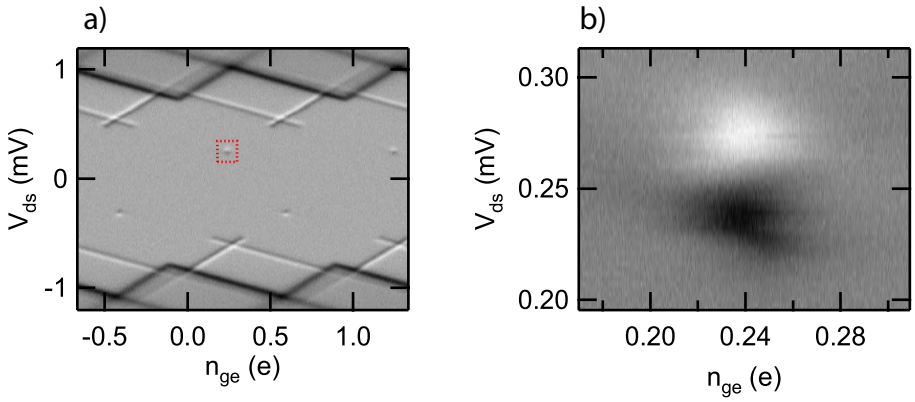

Figure 7.3: a) Superconducting SET response diamond. The dotted red box shows the region of the diamond that is shown in detail in part b). b) Zoom on the DJQP feature from the above diamond. The DJQP feature appears as a peak in SET current, but because the RF-SET effectively probes the conductance of the SET, we see the DJQP feature as a rise and then a dip. Operating points in the remainder of this chapter are shown as points on plots such as this.

comparatively small currents flowing through the SET at comparatively small drain-source voltages – which we had hoped would minimize heating and quasiparticle poisoning in the Cooper pair box. For this reason, instead of reproducing the entire SET response diagram (figure 7.3a), operating points in the remainder of this section will be plotted as points on a more detailed plot of the SET response in the vicinity of the DJQP feature (figure 7.3b).

In these plots, where the SET response is plotted on the z axis as the SET gate (x-axis) and drain-source voltage (y-axis) are varied, the DJQP response appears as two oblong peaks (figure 7.3b). This particular shape may be understood as a consequence of our measurement scheme: If SET current were plotted as a function of n_{ge} and V_{ds} (not shown in figure 7.3), then the DJQP would appear as a simple peak in the resulting density plot. The RF tank circuit that provides the fast readout of the SET, however, effectively measures the conductance of the SET, and the response that we see therefore looks not like a simple peak, but like its derivative (in the V_{ds} direction). The shape of the response in figure 7.3b may therefore be understood as two peaks which correspond to the positive and negative differential conductance on the two sides of the DJQP peak.

The drain-source voltages of operating points near the DJQP feature were referenced as differences from the drain-source voltage at the center of the DJQP. The center of the DJQP was usually measured once for for each Coulomb staircase measured, as drifts in offsets of the drain-source voltage typically occurred on longer time scales (1-2 hours) than a typical measurement of the Coulomb staircase (20 minutes). The drain-source voltage at the center of the Coulomb staircase was found by

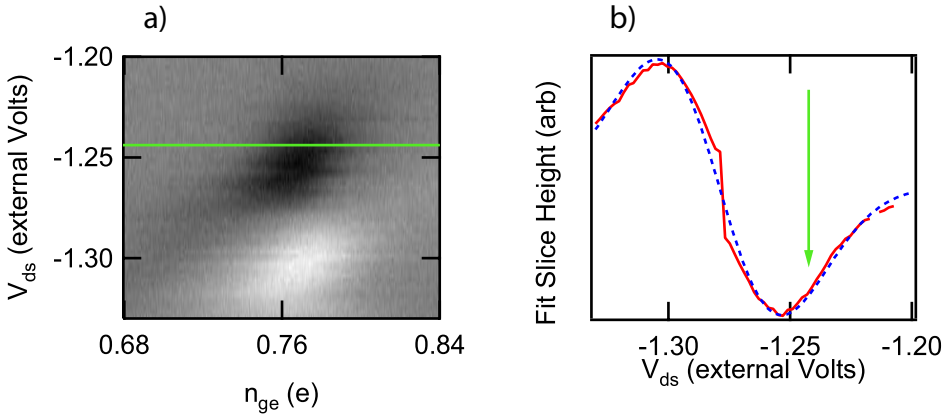

Figure 7.4: Fitting the DJQP Feature to locate operating points. a) An image plot of a DJQP feature. Successive slices (such as that indicated by the green arrow) are taken and fit with a Lorentzian function. b) The height of each of these slices is plotted (red line) as a function of the (externally set) drain source voltage V_{ds} for that slice. The green arrow, for example, shows the plotted point corresponding to to the slice indicated in part (a). The function indicated in equation 7.1 is fit to this profile, and the fit value of Xoff is taken to be the center of the DJQP feature. SET operating points are referenced by their drain-source voltage relative to this point.

a method illustrated in figure 7.4: successive horizontal slices of the image plot of the SET response near the DJQP feature were fit to Lorentzian peaks (one such slice is denoted by a green line in figure 7.4a; the resulting peak in SET response and Lorentzian fit are not shown). The collected peak heights from these fits are then plotted against the drain-source voltage of their corresponding slices, as the red solid line in figure 7.4b. This trend in eye slice heights is then fit to the function:

$$R(V) = A\ (V - V_0)\ e^{-\frac{(V-V_0)^2}{w^2}} \tag{7.1}$$

Which is shown as a blue dashed line in figure 7.4b. It should be emphasized that this fitting function is not derived from a knowledge of the functional form of the current flowing through the SET; it is a purely post-hoc function that fits the measured profile of the DJQP feature response. However, it was found to provide consistent measurements of the center of the DJQP features in our experiments, and was found to be a repeatable metric that could be used to track drifts in the SET operating point.

After a drain-source voltage was selected, and referenced relative to the found center of the DJQP feature, a SET operating point could be uniquely specified by choosing some value of n_{ge}, the SET gate voltage. The value of n_{ge} at a particular SET operating point was usually referenced as the offset, in electrons, from the maximum SET response for that value of V_{ds}. An operating point

could therefore be uniquely and repeatedly specified as, for example, "10 mV above the center of the DJQP feature, $+.03e$ from the center of a Lorentzian fit to the SET response at that voltage.

Coordinates specified in this way were very useful when running experiments on the Cooper pair box, and they possessed the added advantage of interfacing rather simply with our theoretical calculations. Our theoretical modeling code specified the noise of the SET as a function of operating point referenced relative to the center of the DJQP feature, in both the n_{ge} and V_{ds} directions. The voltage settings of our experimental operating points, which were referenced relative to the DJQP center, needed only to be converted into appropriate units to be compared with the output of our model.

7.3 Cooper Pair Box Measurements

After the technology was developed to stably locate operating points on the SET response diamond, and a charge noise rejection algorithm was tuned to reject charged fluctuations coupled to the SET gate, Coulomb staircases of the Cooper pair box were measured. These Coulomb staircases were first used to find accurate estimates of the parameters of the Cooper pair box, and later were measured as part of detailed searches for SET backaction effects.

In this section, I will describe the methods we used to perform measurements on the Cooper pair box, and to produce very accurate estimates of the physical parameters of the Cooper pair boxes in the particular samples that we used. I will begin by a description of the spectroscopic measurements that we performed before describing how these measurements and other measurements of the Coulomb staircase were used to determine the precise parameters of our particular sample.

7.3.1 Spectroscopy Measurements in the Cooper Pair Box

In section 3.3.4, I discussed how an RF voltage applied to the box gate was able to excite bring the Cooper pair box into its excited state when the energy splitting of the Cooper pair box was equal to the photon energy ($h\nu$) of the spectroscopic excitation. In this section, I will describe how such spectroscopic mixing of the box states was used to obtain very precise measurements of the energy splitting of our particular Cooper pair box samples.

In order to use this spectroscopic response to determine the parameters of the Cooper pair box, we first needed to isolate the spectroscopic response from the Coulomb staircases in which it appeared. The process by which we did this is illustrated in figure 7.5: Coulomb staircases were measured

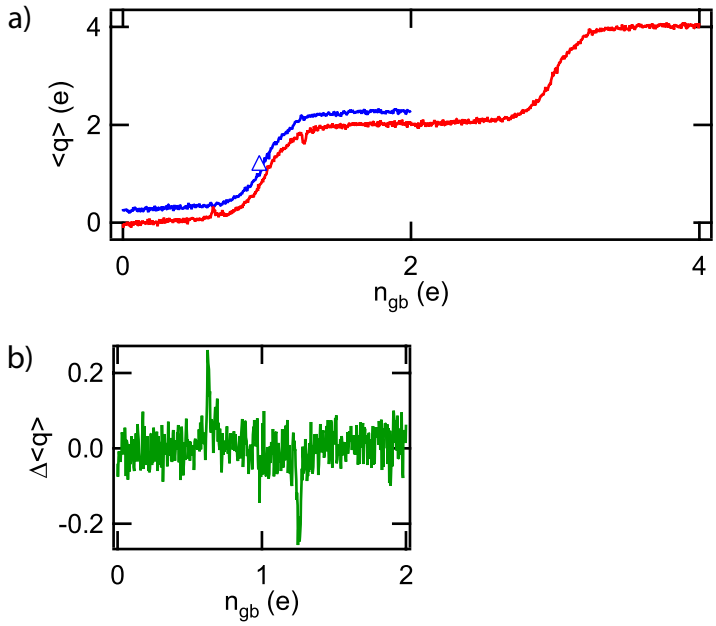

Figure 7.5: Method for isolating the response of the Cooper pair box to an imposed RF spectroscopic signal. a) The gate voltage of the Cooper pair box is swept over a range corresponding to 4 electrons (red curve). During the first half of this sweep, a microwave signal at a fixed frequency is applied to the box; the signal is switched off for the second half of the sweep. The Coulomb staircase from the second half of the sweep, without spectroscopic irradiation, is subtracted from the first half of the sweep (the Coulomb staircase from the second half of the sweep is shown next to the original data trace in blue, demarcated by a triangle and offset for clarity). b) The difference between these two Coulomb staircases is then plotted as the pure spectroscopic response of the Cooper pair box. This permits isolation and accurate measurement of the spectroscopic response peaks, which are generally difficult to observe in staircases like that shown in part a)

over a range corresponding to 4 electrons in n_{gb}, with microwaves on for the first half of this sweep and off for the second half. The second half of this sweep (indicated in figure 7.5 in blue, marked with a triangle and shifted to overlay the first half) was then subtracted from the first half of this sweep (red) to produce the pure spectroscopic response, shown in figure 7.5b. This method was very useful, as we were able to use simple gaussian fits to study the peaks in the resulting spectroscopic response plots, and could isolate spectroscopic response features from the grosser structure of the Coulomb staircase. This was particularly helpful when the Coulomb staircases were very distorted, by either quasiparticle poisoning or backaction effects – where this subtraction still allowed us to isolate the spectroscopy peaks.

It is worth noting that, in many samples, the spectroscopic response appeared as a pair of peaks, or occasionally even triple peaks. This was not entirely understood, but was thought to be due to

charge state fluctuations on the SET island, similar to those studied as the source of normal state SET backaction, offsetting n_{gb} to bring the box into resonance.

7.3.2 Determination of Box Parameters

Measurements of the Coulomb staircase were used to determine the parameters of our Cooper pair box samples in two different ways: the spectroscopy techniques described in section 7.3.1 were used to probe the absolute energy splitting between Cooper pair box energy states, and this was then corroborated with the ratio $(E_J/4E_C)$ which could be inferred from the shape of the Coulomb staircase. In this section, I will describe how these measurements were used to obtain very accurate estimates of the parameters of the Cooper pair box studied in 2003 (as noted above, samples fabricated at Yale always exhibited quasiparticle poisoning, and we were therefore unable to obtain estimates of $(E_J/4E_C)$ from the shape of the staircases. Spectroscopic studies of the Yale-fabricated samples, however, were useful in determining the parameters of these samples.)

Spectroscopically, the energy splitting of the Cooper pair box was matched with theoretical predictions derived from equation 3.20:

$$\Delta E_{e,g} = \sqrt{E_J^2 + \left[4E_C(n_{gb} - 1)\right]^2} \tag{7.2}$$

In particular, for a fixed microwave signal at frequency f, with corresponding energy hf, this can be rearranged to predict the location of the spectroscopic response peaks:

$$n_{gb} = 1 \pm \frac{1}{4E_C}\sqrt{(hf)^2 - E_J^2} \tag{7.3}$$

Our first attempt to use this to measure the parameters of our box is illustrated in figure 7.6. To create this figure, Coulomb staircases were measured with the spectroscopic subtraction described above, varying the frequency of the spectroscopic irradiation from 10 to 35 GHz. The spectroscopic response from each Coulomb staircase was then inserted as a row into a matrix, which was plotted as the image plot in figure 7.6. The red line shows peak location that was calculated, as a function of frequency, from equation (7.3), with E_J and E_C as adjustable parameters. Guesses for E_J and E_C were then taken to be those that produced a hyperbola that best overlaid the spectroscopic response.

While this method did illustrate that our Cooper pair box functioned as a quantum two-level system, it did not yield particularly accurate values for the parameters of our box; in particular,

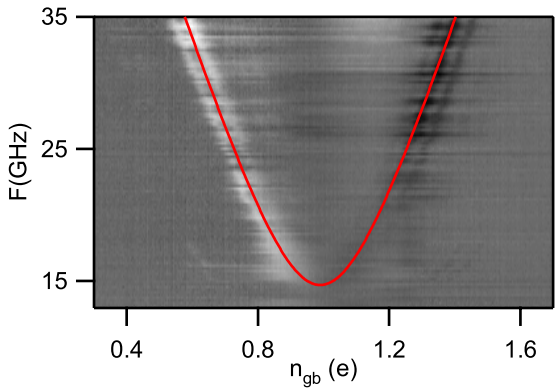

Figure 7.6: Variation of the spectroscopic response of the Cooper pair box as the frequency of the applied spectroscopic signal is varied. Each horizontal slice of the above image plot is a measurement of the spectroscopic response of the Cooper pair box (measured as demonstrated in figure 7.5b) with a spectroscopic signal at a different frequency. Regions of this plot where the response is nonzero show the Cooper pair box energy splitting at a given n_{gb}. A theoretical prediction of the Cooper pair box energy splitting is plotted on the same axis (red line), and the values of E_J and E_C are adjusted to produce the best fit. This produces estimates of E_C, the charging energy, and E_J, the Josephson coupling energy of the Cooper pair box.

the parameter E_J was poorly defined, as the spectroscopic peaks became indistinct when they were close to the center of the step. For this reason, a different method was used to produce our best estimates of the Josephson and charging energies of our Cooper pair box.

Equation (7.3) predicts that the location of spectroscopic response peaks will change with the frequency of the applied microwaves, and also with the Josephson energy of the Cooper pair box (this is shown in the Cooper pair box energy splitting diagram of figure 7.7). By varying the magnetic field through the split-Cooper pair box, we were able to adjust this Josephson energy, and could cause changes in the location of the spectroscopic response peaks that could be measured far from degeneracy, where the spectroscopic peaks were easier to discern. Combined into an image plot in the same fashion as figure 7.6, this spectroscopic response could be fitted to equation 7.3 to provide very accurate estimates of both the E_J and E_C of the box (shown in figure 7.8). From repeated measurements of this type at an array of frequencies, we were able to determine the charging and Josephson energies of our Cooper pair boxes to an accuracy of approximately 1%.

Spectroscopic measurements of the energy splitting of the Cooper pair box were corroborated with measurements of the Cooper pair box energy splitting from the shape of the Coulomb staircase. In section 3.3.2, we described how the shape of the Coulomb staircase was a function of a single parameter, the ratio $(E_J/4E_C)$: Staircases with large Josephson energies had measurably broader

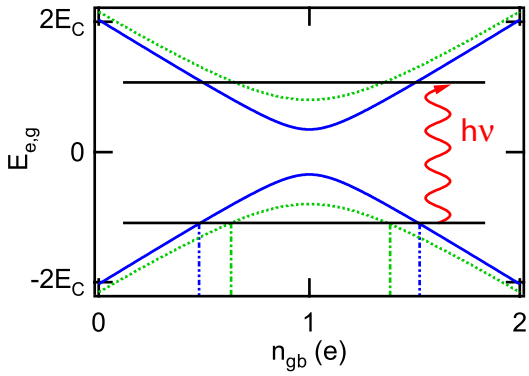

Figure 7.7: Spectroscopy peak location variation with E_J illustrated on box energy splitting diagram. Microwaves at a constant frequency f are applied to the Cooper pair box, and will excite resonant peaks in the Coulomb staircase at values of n_{gb} where they are resonant with the box energy splitting. When the Josephson coupling energy E_J of the Cooper pair box is varied (solid blue hyperbola shows small E_J; dotted green hyperbola shows large E_J), the values of n_{gb} where the microwaves are resonant change. Dashed-dotted lines to the n_{gb} axis show the expected location of spectroscopy peaks for irradiation with microwaves of a frequency corresponding to the energy splitting between the two black horizontal lines. The spectroscopic peaks are maximally separated when E_J is at a minimum.

"steps" than those with low Josephson energies. We observed variation in E_J by measuring staircases at an array of magnetic field values (shown in figure 7.9). Each of these staircases was then fit to equation (3.21), with the quantity $(E_J/4E_C)$ as an adjustable parameter. The resulting measured variation in the Josephson energy (red triangles in figure 7.10) was found to agree with the variation in Josephson energy inferred from spectroscopic measurements (green squares in figure 7.10) everywhere except at the lowest values of E_J. This slight discrepancy may be simply understood in the context of the results presented in chapter 6. Coulomb staircases were probably broadened slightly by a combination of thermal excitations, backaction from the SET (understood as a simple fluctuating gate voltage), and noise on the box gate. This broadening would have caused a negligible change in the Coulomb staircase width for staircases with a large E_J, but will cause the staircase width to saturate as E_J tends to zero. While such effects were certainly present, we infer from the limited range over which they are seen that they did not have Xa significant effect on our Cooper pair box.

7.4 Description of Samples Fabricated and Measured

Our fabrication efforts at Yale simultaneously focused on making large SET charging energies (to allow a DJQP feature) and low box charging energies (to attempt to avoid quasiparticle poisoning, which will be described in section 7.5). The combination of these requirements, and the constraints

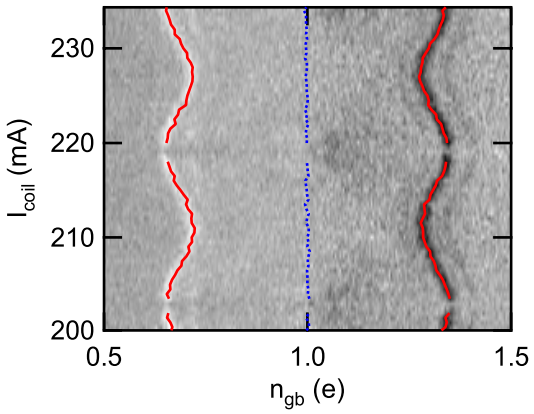

Figure 7.8: Variation of Cooper pair box spectroscopy with applied magnetic field. Each horizontal slice of the above image plot is a measurement of the spectroscopic response of the Cooper pair box (measured as demonstrated in figure 7.5b) with a magnetic field determined by the coil current indicated by the y axis. As the magnetic field is varied, the location of the spectroscopic response peaks on the Coulomb staircase varies. The red lines indicate the location of these peaks, found by fitting gaussian peaks to each spectroscopic response plot. The distance between these peaks is used to accurately find the Josephson energy E_J, while the midpoint of these two peaks (indicated by a blue dotted line) can be used to track slow variations from charge noise coupled to the box island.

imposed by the fabrication of our large coplanar waveguide leads, made our fabrication process complex and unstable. As this process was developed, samples were measured that were deemed unsuitable for the measurements that we wished to make. This section will catalog those samples, and show the evolution of our process towards our ideal samples.

The strictest requirement of our fabrication process was that our SET have a large charging energy. In section 3.4.4 I noted that a SET must satisfy $2\Delta > E_C > \frac{2}{3}\Delta$ to show a DJQP feature; in our samples, this translated into a requirement that the Josephson junctions (which contributed approximately half of the total capacitance of the SET island) be very small. Fortunately, a preliminary estimate of the size of the junctions could be made by measuring the normal state resistance of a SET sample: smaller junctions would generally have proportionately higher resistances. Our first measurement on a sample, therefore, was of its normal state resistance; only samples with a SET resistance $> 250\,\mathrm{k}\Omega$ were considered for further measurement.

A high room-temperature resistance could arise from the series combination of two small junctions (which we desired), or from a single small junction in series with a larger one (which would make it unsuitable for our experiments). To discriminate between these two cases, we measured potentially viable samples in our Helium 3 refrigeration system. Using the techniques described in section 7.2, we would determine a sample's SET parameters, and look for the presence of a DJQP feature.

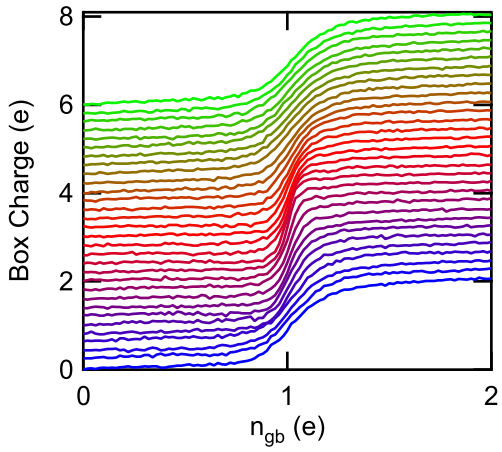

Figure 7.9: Coulomb staircases measured as the magnetic field is swept by an amount corresponding to one flux quantum in the Cooper pair box squid loop. The ratio $E_J/4E_C$ at each magnetic field may be inferred by fitting the shape of each Coulomb staircase.

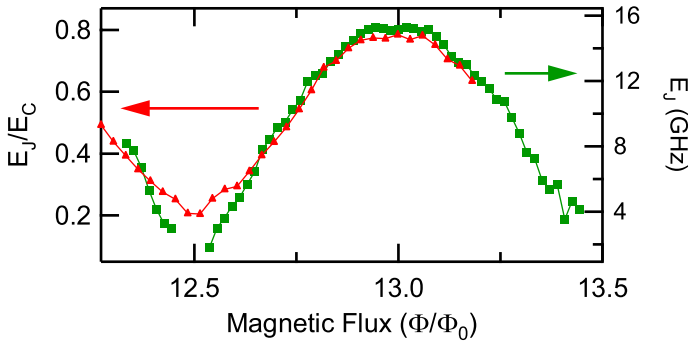

Figure 7.10: Comparison of E_J variation with magnetic field measured via spectroscopy and via fitting of Coulomb staircase shape. As the magnetic field is varied (bottom axis), the broadening of Coulomb staircases can be fit to determine the ratio $E_J/4E_C$. The value inferred from this fit at each magnetic field is plotted as a red triangle, with values indicated on the left axis. The Josephson energy E_J may also be inferred from the splitting of spectroscopy peaks of the Cooper pair box, and is plotted in green squares (corresponding to numbers on the right axis). A comparison between the two shows that the Coulomb staircase may be accurately fit in its ground state, and that the functional form of the variation of the Cooper pair box energy splitting is confirmed.

Samples that were measured at 250 mK and seen to have a DJQP feature were then measured in one of our dilution refrigerators. Using the techniques in section 7.3.2, the parameters of the box could then be measured, and were compared to our target values of $E_C = 5$ GHz and $E_J = 5$ GHz.

Table 7.1 lists the samples that were fabricated and investigated in this way. Each sample is specified by the date it was fabricated and its design version (except where noted, the design versions differ only in minor details of the dose patterns). Samples that were found to be faulty after measurements at room-temperature are omitted from this table. SET charging energies are

Sample Name	R_N	$E_{C,SET}$	DJQP?	$E_{C,Box}$	Comments
Chalmers B42	190 kΩ	2.3 K	Yes	14 GHz	Chalmers fab, measured in 2003
2005-06-22v45	230 kΩ	0.7 K	No		
2005-06-29v45	1.2 MΩ	1.3 K	No		very asymmetric junctions
2005-08-26v49	246 kΩ	1.3 K	No		
2005-11-01v49	403 kΩ	1.65 K	Yes	~ 5 GHz	distorted 1e staircase
2006-02-06v52	347 kΩ	1.51 K	Yes	12 GHz	"floating island"/still 1e
2006-02-10v52	377 kΩ	1.63 K	Yes		problems measuring box

Table 7.1: Catalog of Box-SET samples measured for this thesis. All of the samples were fabricated at Yale except the first, which was fabricated at Chalmers institute for Technology, in the group of Per Delsing. Normal state resistances were measured at room temperature; the resistance of a device was found to increase by $10-20\%$ upon cooling. SET charging energies are measured in Kelvin, to compare to the superconducting gap, while box charging energies are listed in GHz, which is more relevant to the spectroscopic measurements that we performed.

listed in Kelvin, for comparison with the temperature scales in our experiments. The aluminum in our experiments was generally measured to have $\Delta \sim k_B(2.3\text{K})$, so we expected to see a DJQP in samples with $E_C \gtrsim 1.5\,\text{K}$. Box parameters are not listed for samples that were measured only at 250 mK, as a sample found to be inadequate at that temperature was not worth the additional effort required for dilution refrigerator measurements.

It should be noted that the samples fabricated at Yale show an increase in device charging energy that is approximately linear with the room-temperature resistance. This trend suggests that more resistive samples had smaller SET junctions, as per our design. This trend, however, is defied by one sample in table 7.1: the device fabricated at Chalmers has a much higher charging energy than Yale samples with the same resistance. This may be attributed to two factors. First, the group at Chalmers was able to achieve very transparent aluminum oxide tunnel barriers in their fabrication – which caused much lower resistance for the same junction size and junction capacitance. The Chalmers sample also, however, had much less capacitance added to the SET island from nearby metallic structures: unlike the Yale samples, it did not have large coplanar waveguide ground planes near the box and SET. When combined, these two effects adequately explain the aberrantly high charging energy (or, equivalently, aberrantly low resistance) of the "Chalmers B42" sample.

In the end, the last three Yale-fabricated samples listed in table 7.1 were studied in detail. Unfortunately, all of these samples showed severe quasiparticle poisoning and staircase distortion that did not appear to vary with any of the fabrication parameters. The last two of these samples also used the "floating island" design discussed in section 4.3; the samples still showed quasiparticle poisoning.

Scientist/Group	Readout	Poisoning?	Reference
Aumentado/NIST	CP Transistor	Controllable[2]	(Aumentado et al., 2004)
Bouchiat/Saclay	RF-SET	Avoidable[3]	(Lafarge et al., 1993)
Quantronics/Saclay	"Quantronium"	Avoidable[4]	(Vion et al., 2002)
Delsing/Chalmers	RF-SET	Yes (Intermittent)[5]	(Gunnarsson et al., 2004)
Echternach/JPL	RF-SET	Yes (Intermittent)[6]	(Schneiderman et al., 2006)
Devoret/Yale	"Quantronium"	Occasional [7]	Personal communication
Nakamura/NEC	SET	Avoidable[8]	(Yamamoto et al., 2006)
Schoelkopf/Yale	RF-SET	Yes	(this thesis)
Schoelkopf/Yale	CQED	No	(Wallraff et al., 2004)
Welstood/Maryland	RF-SET	Yes	March Meeting Abstract, 2006

Table 7.2: List of different groups that have observed quasiparticle poisoning in superconducting qubit systems. The final column lists resources where interested readers may learn more about the variation in quasiparticle poisoning observed by each group. Groups are listed in alphabetical order.

7.5 Quasiparticle Poisoning of the Superconducting Cooper Pair Box

The quasiparticle poisoning mentioned in the last section is one of the most serious problems affecting charge measurements of superconducting systems. In quasiparticle-poisoned Cooper pair boxes, a measurement does not behave as expected because quasiparticles, instead of Cooper pairs, tunnel on to the box island (Lutchyn et al., 2006). This effect is sometimes referred to as "bad parity," and has been a problem for most other groups studying similar systems (summarized in table 7.2). Cooper pair boxes read out by the RF-SET are nearly always affected by quasiparticle poisoning to some degree. In the RF-SET measurements described in this thesis, poisoning was found to be intermittent in samples fabricated at Chalmers and ubiquitous in those fabricated at Yale; the reasons for this are poorly understood (as noted in table 7.2, many groups have seen quasiparticle poisoning that is intermittent, either as experimental conditions are varied or when different samples

[2] Aumentado found that the degree of quasiparticle poisoning could be adjusted by adjusting the gap in the island with oxygen doping.

[3] In the work done by Bouchiat, quasiparticle poisoning was effectively understood and avoided using the "quasiparticle band" theory that will be discussed later in this chapter.

[4] In the quantronium work done at Saclay, quasiparticle poisoning was found to be a problem, but was solved with the addition of gold quasiparticle traps.

[5] In the work done in the Delsing group, quasiparticle poisoning was found to be very sample-dependent. Quasiparticle traps and "band gap engineering" were employed in an attempt to suppress its effects, but did not appear to consistently eliminate it.

[6] The Echternach group reported elimination of quasiparticle poisoning with increased box gate sweep rates.

[7] In private communications with the Devoret group, I learned that quasiparticle poisoning appeared in some samples, but not in others, but was generally infrequent.

[8] In the Nakamura experiments, quasiparticle poisoning was controlled by an adaptation of the idea of "band gap engineering" that will be discussed later in this chapter, where thin aluminum films in the Cooper pair box island create a region with a higher superconducting gap, and quasiparticles preferentially tunnel off of the island to the lower-gap leads.

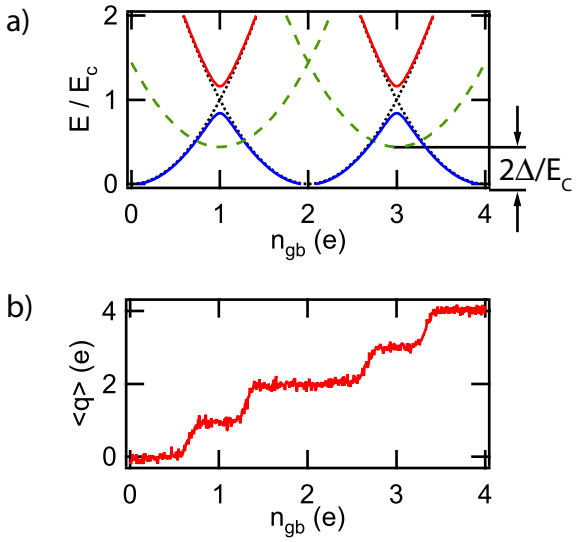

Figure 7.11: "Short step-long step" observed in Coulomb staircase demonstrating quasiparticle poisoning. a) Calculated energy bands for a Coulomb staircase. The solid lines show the calculated excited (red) and ground (blue) state of a Cooper pair box; the black dotted lines show the parabolic energies of the Cooper pair box charge states in the absence of Josephson coupling. Green dashed lines show energy of a quasiparticle band. For $2\Delta < (E_C - E_J/2)$, this band may be at lower energy than the desirable Cooper pair box ground state, and it will be energetically preferable for a quasiparticle to tunnel on to the Cooper pair box island. b) A Coulomb staircase measured with a short step-long-step character, which lead us to infer an energy landscape like that shown in part (a).

with the same design are measured). In this section, I will describe our observations of this effect, as well as our current understanding of its source and our efforts to circumvent it.

Quasiparticle poisoning occurs when a Cooper pair box charge state with a single quasiparticle (an "odd parity state") is energetically preferable to a desired state with only additional Cooper pairs (an "even parity state"). This state is undesirable, as the coupling between Cooper pair box states differing by a single quasiparticle is incoherent, and cannot be treated using the theories developed in chapter 3. Quasiparticle-poisoned islands are typically understood as shown in figure 7.11a, where the normal Cooper pair box energy bands – parabolas with avoided crossings – are interrupted by bands corresponding to a state with a single additional quasiparticle. These quasiparticle bands require additional energy – shown here as 2Δ – to break a Cooper pair; nevertheless, if that 2Δ of energy is less than the energy of the even parity states of the Cooper pair box, it will still be energetically preferable for a quasiparticle to tunnel on to the box island.

Quasiparticle poisoning is observed in measurements of the Coulomb sawtooth (described in section 5.5.2). Coulomb sawtooths are periodic in 2 electrons of applied gate charge if quasiparticles

never tunnel on to the box island. If quasiparticles may freely tunnel on to the box island, then a sawtooth that is 1e periodic in n_{gb} is measured. An intermediate regime was observed in many of our samples, however, where the apparent superconducting gap Δ was reduced, but not eliminated. These samples showed the the "short step-long step" behavior illustrated in figure 7.11b.

In some of our measurements, the nature and the extent of this short step-long step behavior were seen to vary with the rate at which the Coulomb sawtooth was swept. Typically, a staircase would show less poisoning (a shorter short step) with a faster sweep rate. In samples where this was seen, poisoning would typically wane at sweep rates above 100 kHz (our standard sweep rate was 2 kHz). This was interpreted to be a consequence of the relatively slow timescale of quasiparticle poisoning: if the box gate was rapidly swept through the range where quasiparticles tunnel on to the box island, then quasiparticles would not, on average, have time to tunnel onto (and poison) the Cooper pair box.

We attempted to control quasiparticle poisoning involved fabricating Cooper pair boxes with smaller charging energies. According to the "quasiparticle band" theory shown in figure 7.11, poisoning will occur if the energy of an even parity state [$(E_C - E_J/2)$ at $n_{gb} = 1$] is greater than that of the quasiparticle band (2Δ at $n_{gb} = 1$). A Cooper pair box fabricated with a lower charging energy, therefore, might place all relevant Cooper pair box states safely below the quasiparticle bands. Unfortunately, this was not found to work, or even to produce measurable changes in the extent of quasiparticle poisoning effects. We believe that this is due to a ready supply of quasiparticles in the leads which lessens or eliminates the 2Δ "energy cost" to break a Cooper pair, bringing the quasiparticle band in figure 7.11a down to the same level as the Cooper pair bands (so that the quasiparticle band would have an apparent Δ of 0).

We also attempted to eliminate quasiparticle poisoning effects through so-called "band gap engineering", where a small magnetic field was applied to the Cooper pair box sample. A magnetic field suppresses superconductivity and effectively lessens the superconducting gap more dramatically in a large planar superconducting structure than in a small, isolated structure. Quasiparticles on the box island, then, would energetically prefer the lower free energy state on the Cooper pair box leads, and should preferentially tunnel off of the Cooper pair box island. This logic proved effective for the Chalmers sample measured in 2003, where 2e staircase periodicity was possible only with a small ($\sim$ .02 T) applied magnetic field, but had little discernible effect on the samples fabricated at Yale.

During the course of our experiments, we noticed that the operation of the SET seemed to cause

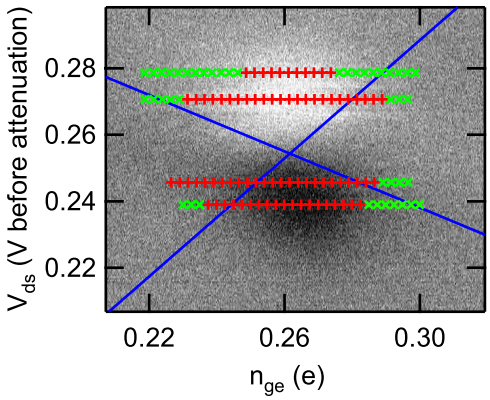

Figure 7.12: Image Plot of DJQP feature with overlay showing operating points where measured Coulomb staircases were not simply 1e periodic. At operating points where a Coulomb staircase was measured and found to have steps every 1 electron, a red cross is shown. At operating points where Coulomb staircases showed short step-long step behavior that repeated every 2 electrons, a green "X" is shown. Blue lines show the location of the Cooper pair resonances that define the DJQP feature. The regions where Coulomb staircases are maximally poisoned, indicated in red, are where the largest current is flowing in the SET, suggesting that the quasiparticle poisoning is a consequence of SET current.

quasiparticle poisoning effects. This was first noted in the sample measured in 2003, where staircases without quasiparticle poisoning could be measured using SET operating points at the DJQP feature, but could not be measured when the SET was operated on the JQP feature or the gaprise. This is thought to be due to phonons from the recombination of Cooper pairs broken during SET operation: as current flows through the SET, recombining Cooper pairs release energy into lattice vibrations that can bridge the electrical gap between the box and the SET[9]. Phonons from SET operation, furthermore, will have precisely the right energy to break Cooper pairs in the box. If these phonons create an adequate supply of quasiparticles in the box leads, then they might completely eliminate the barrier for quasiparticle entry into the Cooper pair box caused by the superconducting gap.

In the samples fabricated at Yale, it was noted that most Coulomb staircases measured showed a response that was periodic in 1e of applied gate charge (and were completely poisoned), but a few were seen to show "short step-long step" behavior (and were "incompletely poisoned"). When Coulomb staircases were systematically measured at an array of operating points near the DJQP feature, it was found that the short step-long step behavior occurred systematically in certain ranges

[9] An alternate explanation holds that the creation of these quasiparticles is a consequence of heating of the sample, either from the AC voltage applied to the tank circuit, or the DC power dissipated in the SET. Varying the AC power on the tank circuit, however, had no effect on quasiparticle poisoning effects, and the differences between the Chalmers and Yale fabricated samples – with comparable DC powers dissipated, but very different quasiparticle poisoning effects – suggest that the quasiparticles were not generated thermally.

of operating points, indicated by green "x"s in figure 7.12, while other regions, indicated by red pluses, were completely poisoned. Consistently, the operating points that showed maximal poisoning were those where higher currents were flowing in the SET. For this reason, we describe quasiparticle poisoning as a coarse SET backaction effect which, like other effects studied in this thesis, can be strongly dependent on the operating point of the SET.

7.6 Superconducting SET Quantum Noise and Population Inversion in the Cooper Pair Box

The first measurement that lead us to believe that we had observed backaction effects due to the quantum noise of the superconducting SET was an apparent population inversion in the Cooper pair box. Our theoretical understanding of the superconducting SET (summarized in section 3.5) suggests that, for certain operating points where one or both of the SET Cooper pair tunneling processes in the DJQP process is tuned to have an excess of energy, the SET may preferentially emit that energy into the Cooper pair box. Our modeling suggested that this SET backaction could dominate the dynamics of the Cooper pair box and produce a population inversion, where an ensemble of measurements would be more likely to find the box in its excited state than its ground state. Staircases affected by backaction in this way would be measured in their ground state everywhere except for a narrow range in n_{gb} (corresponding to a narrow range of box energy splittings), where the coupling to the SET would excite the box into its excited state. In a measurement of a superconducting Coulomb staircase, this would appear as a staircase that crossed over the $\langle q \rangle = 1$ line before $n_{gb} = 1$.

An early observation that appeared to demonstrate this is shown, as a green solid line, in figure 7.13. This curve was thought to show a Coulomb staircase of a Cooper pair box that was in its ground state (shown on that plot as the blue dash-dot-dotted line) everywhere except for a region around $n_{gb} = 1$, where the frequency splitting of the Cooper pair box was thought to match the detuning of a Cooper pair resonance in the SET. In this region, measurements of the charge on the Cooper pair box island seemed to show more population in the excited state (red dash-dotted curve) than in the ground state.

After noting preliminary observations such as that shown in figure 7.13, Coulomb staircases were systematically measured at many operating points near the DJQP feature of the SSET, shown schematically in figure 7.14. These observations were grouped into "step series," identified by markers of different shapes, each of which was designed to test a particular trend in the shape of Coulomb

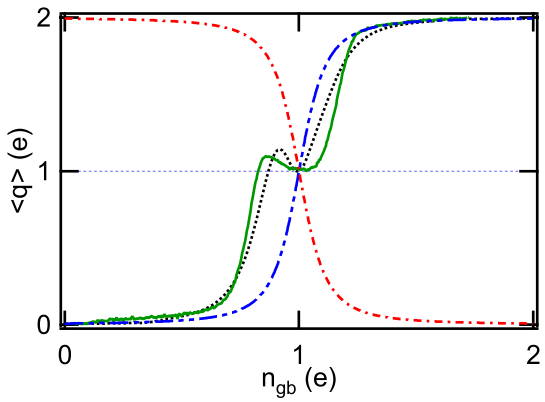

Figure 7.13: Comparison of Population inversion predicted by Quantum Noise model and measured Coulomb staircase. The staircases measured in 2003 (green solid line) show a feature that appears similar to population inversions predicted by our model of superconducting SET backaction (black dotted line). Blue dash-dot-dot line and red dash-dot line show the expectation value of the charge on the Cooper pair box island in the ground and excited states.

staircases with SET operating point.

Coulomb staircases measured as the SET drain-source voltage was varied (green squares, orange triangles, and magenta pluses in figure 7.14) were thought to be the best way to vary the detuning of the two Cooper pair resonances near the DJQP feature. Although the precise detuning of the two DJQP Cooper pair resonances should be calculated at each operating point, it may be generally said that at higher values of V_{ds} both processes were above resonance, and at lower values of V_{ds} both processes were below resonance. In between these extremes, as V_{ds} was varied, we expect that the dominant frequency of SET quantum noise effects will vary systematically. The Coulomb staircases measured during the V_{ds} sweeps indicated in figure 7.14 by green squares and magenta pluses are shown in figure 7.15. These plots each show inversion artifacts similar to those initially noticed in the Coulomb staircase of figure 7.13. However, several problems were noted in the appearance and trends of these measurements that ultimately lead us to question whether or not they were really effects due to the quantum noise of the SET as theoretically described in section 3.6.

First, it was noted in section 3.5 that the quantum noise of the SET was only capable of exciting the Cooper pair box for regions of operating points where one or both of the Cooper pair resonances was detuned above resonance. In figure 7.14, these operating points occur when the magnitude of the applied drain-source voltage is higher (in that plot, more negative) than one or both of the black dotted lines. The Coulomb staircases shown in figure 7.15a were all taken with the SET tuned below both Cooper pair resonances – and should therefore never show any sort of inversion artifact.

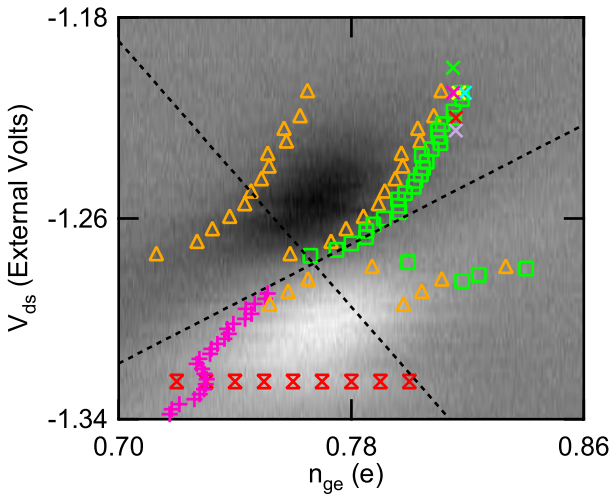

Figure 7.14: Image plot of DJQP feature with operating points marked where Coulomb staircases were measured in 2003 attempts to observe SSET backaction. Crosses indicate operating points where series of staircases were measured while the magnetic field was swept. Other symbols represent series of Coulomb staircases measured with either n_{ge} or V_{ds} varied to observe changes in SET backaction with operating point. Different colors and markers correspond to different measurement series on different days, and will be discussed in the text. Note that the drain source voltage had the lowest magnitude (least negative) for operating points at the top of the graph. Black dashed lines show the inferred positions, on these plots, of the two Cooper pair resonances that contribute to the DJQP cycle.

Instead, however, the majority of the Coulomb staircases in figure 7.15 show some sort of artifact that could be identified as an inversion similar to the expected consequence of asymmetric quantum noise. This suggested to us that the apparent inversion observed in many of our measurements may not have been an inversion at all; we do not know what it could have been. In conversations, we have thought that this effect may have been due to quasiparticle poisoning (as discussed in section 7.5). The trend in the artifacts presented in figure 7.15 clearly supports this hypothesis (with staircase distortions that are most pronounced near the center of the DJQP feature, where SET-induced quasiparticle poisoning is thought to be most severe).

The subset of the data presented in figure 7.15 that is measured furthest from the center of the DJQP feature (the data at the top of figure 7.15a and at the bottom of 7.15b) seem to, at least partially, refute this hypothesis: for this small subset of the total collection of operating points used to measure the Cooper pair box, inversion was seen when the SET was tuned to be far above both resonances (7.15b) and not seen when the SET was tuned below both resonances (7.15a). Stated differently, the "inversion," thought to perhaps be quasiparticle poisoning because

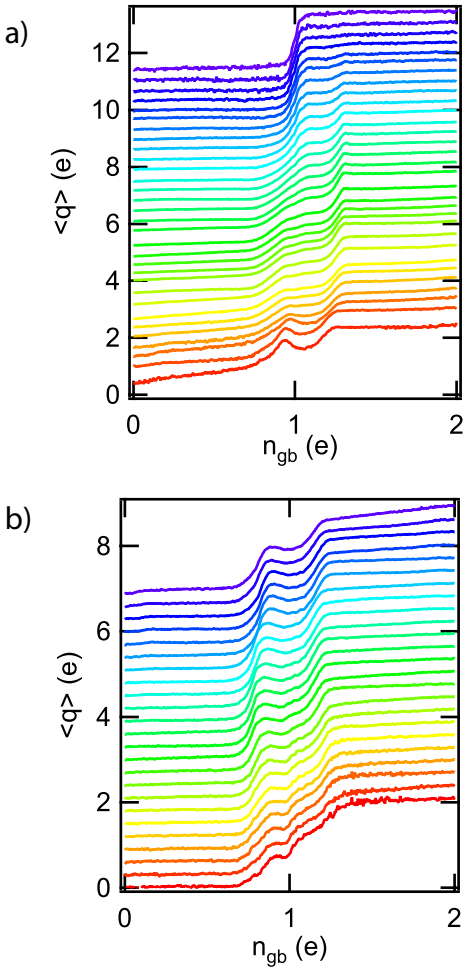

Figure 7.15: Coulomb staircases measured as the drain-source voltage is varied across the DJQP feature. a) A series of steps measured with the drain source voltage providing less energy than is necessary for the Cooper pair resonances (offset for clarity). These Coulomb staircases were measured at the series of operating points indicated by green squares in figure 7.14. Coulomb staircases at the top of the plot correspond to operating points at the top of figure 7.14. b) A series of Coulomb staircases measured with V_{ds} providing more energy than necessary for the Cooper pair resonances. These staircases were measured at the operating points indicated by magenta plus symbols in 7.14. As before, the ordering of the traces corresponds to the relative locations of the operating points in figure 7.14. The inversion artifact does not disappear for any V_{ds} where measurements were possible.

it appeared at operating points near the center of the eye where theory predicted it should not, nevertheless disappeared or persisted, in accordance with theory, at operating points far below or above the center of the DJQP. For these reasons, we did not choose to publish the measurements described here, but we believe that the measurements are suggestive of the effects of SET backaction.

An additional effect which suggested that the inversion effect seen in our Coulomb staircases was due to the quantum noise of the SET is presented in figure 7.16. The series of Coulomb staircases

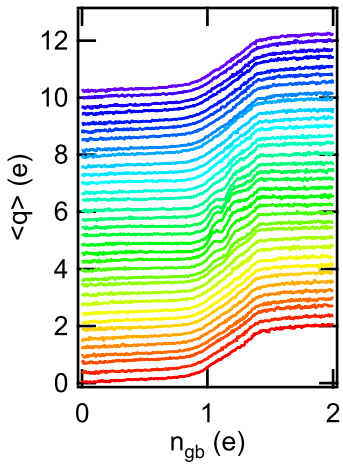

Figure 7.16: Coulomb staircases measured as the magnetic field was swept through one flux quantum, offset for clarity. The Coulomb staircases where E_J was at a minimum show a small kink thought to be a population inversion induced by SET backaction. Staircases measured where E_J was larger show no such disturbance.

presented there was measured as the applied magnetic field was swept by an amount corresponding to one flux quantum through the SQUID loop created by the box junctions (described in detail in section 3.3.2). As the magnetic field varies, the effective Josephson coupling of the Cooper pair box junctions varies, and so, too, does the energy splitting between the ground and the excited state of the Cooper pair box at $n_{gb} = 1$. When the SQUID loop is adjusted so that E_J is at a minimum, therefore, the Cooper pair box is sensitive to SET quantum noise at lower frequencies than it is when E_J is tuned to a maximum. In figure 7.16, we see Coulomb staircases that demonstrate inversion effects only when the magnetic field is tuned so that E_J is small; when it is tuned to be large, the effects disappear. Still, however, careful consideration of the Cooper pair box band diagram with quasiparticle states (figure 7.11a) suggests that modulation of the Josephson energy of the Cooper pair box may have subtle effects on the presence or absence of quasiparticle poisoning, and may cause effects that appear or disappear with magnetic field in a manner similar to the effects in figure 7.16.

7.7 SET Effects on the T1 of the Cooper Pair Box

In section 3.6 we described how the quantum noise of the SET was also predicted to vary the T1 of the Cooper pair box. While our initial observations, in 2003, suggested that we were able to observe this variation, subsequent examination of our results has led us to believe that the variation that we saw

may have been an experimental artifact. Measurements of later samples, where the environmental impedance of the Cooper pair box was well controlled to eliminate confounding environmental effects on our measured T1s, were neither able to confirm or refute our initial results: all Yale-fabricated samples showed quasiparticle poisoning, and T1 measurements of these samples were therefore not even attempted.

In this section, I will present the methodology used to study the relaxation of the Cooper pair box, and I will discuss our theoretical predictions for the variation in Cooper pair box relaxation time with operating point. I will then present the data that suggested to us that the SET may have been modulating the relaxation time of the Cooper pair box, and will discuss our reasons for believing that we may have instead been measuring other unintended and poorly understood effects.

The procedure by which we acquired and reduced T1 data from the Cooper pair box is summarized in figure 7.17. Briefly, an array of data was acquired where the gate of the box (x-axis) was swept through an array of points. For each such n_{gb} point the response of the box was measured continuously for $10\mu s$ (y axis). During the first half of that $10\,\mu s$ a spectroscopic microwave pulse was applied to the box gate; during the second $5\,\mu s$ the pulse was turned off (this scheme is described in more detail in section 5.8.2). One array measured in this way is displayed as a density plot in figure 7.17a. When flattened vertically, this array yields a Coulomb sawtooth (shown in figure 7.17b), where the peaks caused by spectroscopy are readily apparent. Measurements of T1 are made by selecting a range in n_{gb} (shown by the blue lines in figure 7.17a), and averaging together the box response in that region for each time step throughout the $10\mu s$. This averaging produces a T1 curve; a typical such curve is shown in figure 7.17c.

T1 data such as these were measured for many operating points near the DJQP feature of the SSET. These data were measured with the ultimate goal of comparison with the theoretical prediction for variation in SET T1 with operating point, which is summarized in figure 7.18. Our preliminary measurements of these curves seemed promising: T1 curves such as that shown in figure 7.17c were measured with very fast ($< 100ns$ and very slow ($> 1\mu s$) relaxations.

However, several problems with our data ultimately led us to discredit it. First among these was the fact that, when the relaxation time of our system seemed to vary, it did not do so in any way that agreed with the predictions of figure 7.18. This was most clearly demonstrated by the Coulomb sawtooths (like the one in figure 7.17b) that could be reduced from the T1 data. In every such sawtooth, without exception, the spectroscopy peaks that were observed were unequal in size. Each

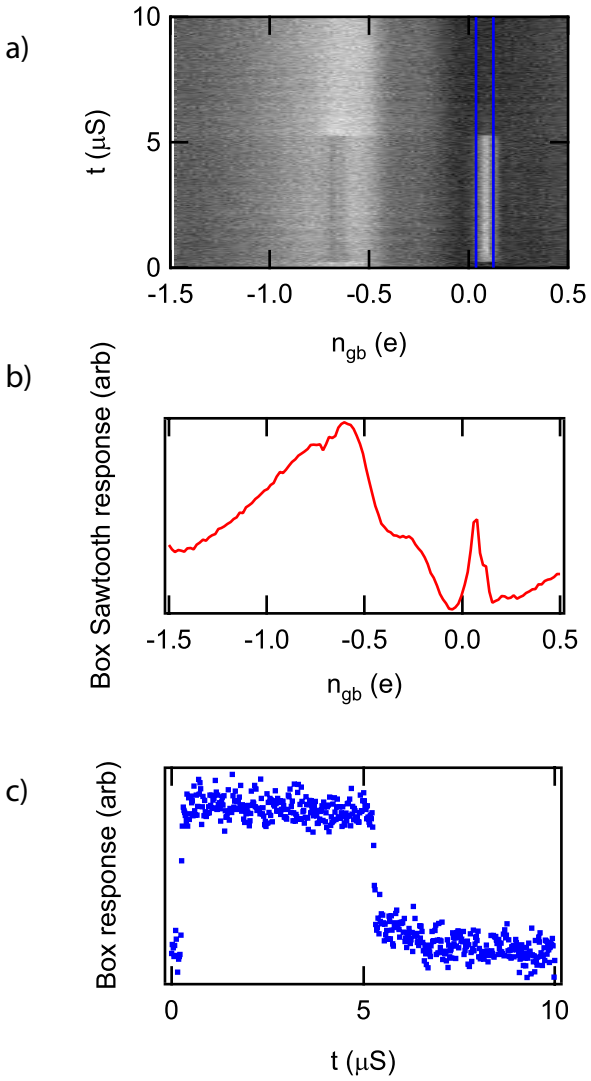

Figure 7.17: Measurement data and analysis for determination of Cooper pair box T1 Time. a) Raw data were measured as arrays, where at each box gate voltage (x-coordinate), the response of the box (z-coordinate) was measured continuously for 10 μs (y-coordinate), with a microwave signal on for the first half of the measurement, and off for the second half. b) By averaging together the data in each column of this array, the sawtooth response of the Cooper pair box may be recovered; in this plot, peaks from the spectroscopic response of the box are clearly visible (at $n_{gb} = 0.1$ and -0.6, as is a small "short step" feature (at $n_{gb} = -0.4$. c) A range of n_{gb} is selected (indicated as the area between the blue lines in part a) and averaged SET response, and the averaged box response in this region is plotted as a function of time. This yields a plot, shown in part c, that shows the relaxation of the Cooper pair box, from the mixture produced by the spectroscopic irradiation into the box's ground state.

time, the spectroscopic peak that was nearest to the center of the DJQP feature was very small, while the spectroscopic peak that was further from the center of the DJQP feature was much larger.

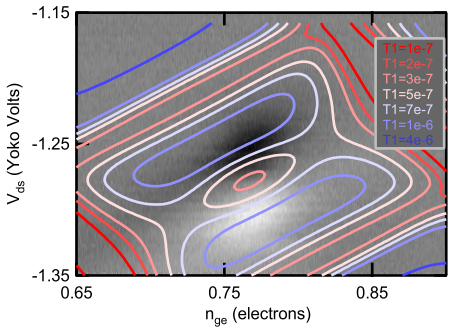

Figure 7.18: Contour Plot of Predicted Cooper pair box T1 vs SET operating point. Contours where the quantum noise effects of the SET predicts constant box relaxation time are overlaid on an image plot of the DJQP feature. Theoretical parameters are extracted as described above. The trends in relaxation time with operating point were not reproduced in our experimental measurements.

Figure 7.17b demonstrates this effect quite well: the down-going spectroscopy peak at $n_{gb} = -0.6$, which was closer to the center of the DJQP feature, is several times smaller than the up-going spectroscopy peak at $n_{gb} = 0.1$.

This was initially thought to be due to the backaction of the SET. According to our (since-discredited) thinking, the size of a spectroscopic peak was determined by the rate at which the applied microwave pulse excited population in the box, relative to the rate at which the SET relaxed the box. Spectroscopic peaks at operating points where the SET forced a short T1 should, therefore, be smaller in magnitude than spectroscopic peaks at points where the SET permitted a longer T1. Furthermore, as a Coulomb staircase was swept, the operating point of the SET was changing slightly; this change in the SET response is what permitted SET measurement. We therefore hypothesized that the spectroscopic peaks that were further from the center of the DJQP feature were larger precisely because, at such operating points, the quantum noise of the DJQP was less than at the operating points near the center of the DJQP. At points near the center of the DJQP, this logic suggests, the classical fluctuating potential of the SET island creates a large symmetrized quantum noise that strongly relaxes the Cooper pair box (see section 3.6).

Unfortunately, however, the modeled effects of the quantum noise of the SET island, which did take into account the symmetrized noise of current flowing in the SET, did not reproduce these effects in the way that our model did. In figure 7.18 it is apparent that the longest T1 – indicated by the bluest contour – is not always furthest from the center of the DJQP feature, and that for certain values of V_{ds} we expect the spectroscopic peak near the center of the DJQP feature to be relaxed less strongly than the one further out. This was never observed.

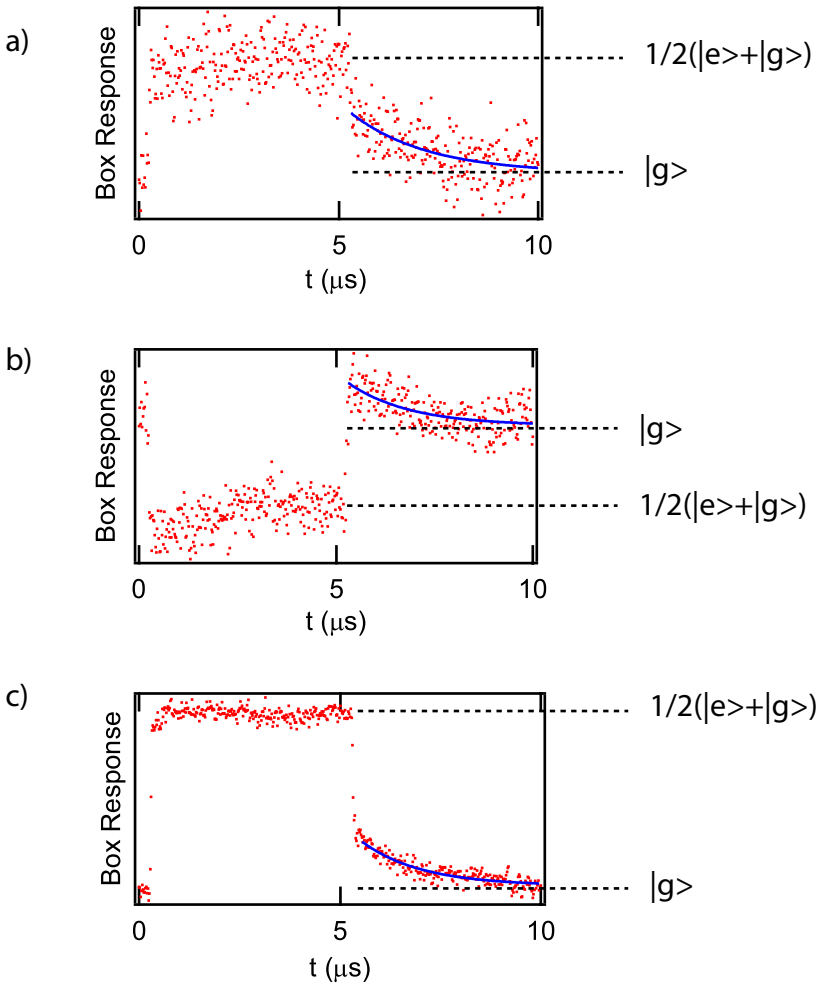

Figure 7.19: Demonstration of variation observed in Cooper pair box relaxation curves. Between $t = 0$ and $5\mu s$ the Cooper pair box is excited into a mixture of its ground and excited state by a spectroscopic pulse, and then it is observed as this mixture relaxes. Dots show the measured response of the SET measuring the box (in units of RF reflected power) as a function of time, while blue lines are an exponential fit to the relaxation. The mixture of ground and excited state measures a higher response in part a) and part c) and a lower response in part b; this is an artifact of the gain of the SET, and the particular charge states excited to and from. While some curves (a) show what appears to be an exponential relaxation from the spectroscopic mixture, other curves relax past the ground state, and relax back to it (b). Typically, a relaxation response would appear as in (c), with a rapid decay, followed by a slow exponential tail.

The most serious problem with our measured T1 data, however, lay in the nature of the relaxations that were observed. In various measurements, the relaxation that we measured was seen to be as large as $1 - 2\mu s$, and was occasionally also seen to be very short ($< 100ns$). However, it was never seen to have any intermediate values, when the theoretical prediction of figure 7.18 clearly suggests that there are regions of operating points where it should. Because of this, we believe

that the measured variation in the relaxation curves was due to different linear combinations of two separate relaxations in our system, one on a timescale faster than we could measure, and one at approximately $1.5\mu s$. Observations of the sort that led us to believe this are summarized in figure 7.19, where different curves are shown which may generally be described by a very quick jump followed by a slow exponential decay to an equilibrium state. In each of these an exponential is fit to the final decay, and is seen to have approximately the same time constant; the curves differ mainly in the relative magnitudes of these two effects.

In curves where the initial jump is small (shown in figure 7.19a), these data appear to reproduce the expected exponential decay of a spectroscopic peak, but it should be emphasized that curves such as this are far more the exception than the rule (it was generally noted that curves that "appeared exponential" – with a small initial jump – were usually found in data that was not on the center of a measured spectroscopy peak. We do not know why this would be the case).

The sources of these two different relaxations are unknown to us, and could not be probed experimentally as they were only discovered long after they had been measured. At times, we have thought that they may be due to slow thermal relaxation in the sample, or slow equilibration of the SET tank circuit, but no experiments had been done to seek their actual source.

7.8 Superconducting SET Backaction: Conclusions and Future Work

From the measurements described in this chapter, several conclusions about SET backaction on the Cooper pair box may be drawn with, we believe, differing levels of certainty. We believe that the SET can be instrumental in causing quasiparticle poisoning in measurements of the Cooper pair box, and that judicious choice of operating point may be able to lessen or eliminate quasiparticle poisoning effects in SET measurements. We think, but do not claim to have conclusively proven, that the SET produces backaction that may be understood within the formalism of quantum noise, and may cause population inversions in a Cooper pair box. Finally, while theory predicts that the SET is able to vary the relaxation time of a Cooper pair box understood as a quantum two-level system, our attempted observations of variations in Cooper pair box relaxation time were most likely due to some systematic effect in our measurement, and we do not claim to have conclusively observed any of these effects.

These combined observations suggest several directions for future research to be conducted in this

field. Attempted observations of population inversion in the Cooper pair box should be performed in a way that they are unambiguously differentiated from the effects of quasiparticle poisoning. One such experiment to do this would involve the spectroscopic probing of an ostensibly inverted Cooper pair box state. A true inversion would, under the influence of an external spectroscopic RF pulse, be driven towards equilibrium, creating a spectroscopy peak that would be qualitatively different (downwards, instead of upwards, or vice versa) from the spectroscopic peaks one would expect in a quasiparticle step.

Attempted observations of variability in Cooper pair box relaxation times with SET operating point would be well advised to heed the lessons of our experiment. A subsequent experiment attempting to recreate our results should perform checks to ensure that the observed difference in relaxation times was due to variations in the relaxation of the Cooper pair box, and not of any other element in the setup. Our experiment also suffered because the measured T1 data was not compared to theoretical predictions until long after the experimental run. A future experimenter should therefore be aware of the precise trends in Cooper pair box T1 expected with SET operating point during his measurements, and should perform experiments designed to directly test these trends.

Chapter 8

Other Measurements in the Superconducting State

In the process of completing this thesis, several investigations were undertaken that were related to the material at hand, but different enough to merit separate consideration. These measurements – involving quantitative measurement of the environmental impedance of the Cooper pair box qubit, and the 1/f noise affecting our devices – were not a direct consequence of the theoretical understanding of backaction developed in chapters 2 and 3, but they use the ideas developed therein to build and support our understanding of our system. In this chapter, I will describe these measurements and how they furthered our understanding of the SET as a measurement device and the Cooper pair box as a quantum bit.

8.1 Environmental Impedance Measurements

The environmental impedance of the SET was presumed to matter in the measurements made for this thesis for a variety of reasons. On the simplest level, good RF engineering was required to bring signals to a sample without introducing attenuation that might vary with frequency. More importantly, however, the quantum noise which determines the spontaneous emission of the qubit is directly proportional to the impedance of the environment at a given frequency. In an attempt to control this potential systematic effect on the T_1 of our qubits, we worked hard to engineer the impedance of our environment to be 50 Ω at all relevant frequencies. That the environmental impedance of our qubits was designed to be 50 Ω, however, does not mean that it empirically was always 50 Ω. The following experiments were motivated by a desire to measure the success of our attempts to control this environment.

The measurements described in the following section use the AC Josephson effect to self-induce Shapiro steps to probe this environmental impedance. This method was originally demonstrated in a paper by Holst(Holst et al., 1994) in 1994. The application of this technique to our problem, however, was a novel idea. It yielded a measurement of the actual environmental impedance seen by the Cooper-pair box. It is notable that our attempts to engineer the impedance of the CPB were successful – that the impedance, as measured with this "Josephson network analyzer," was surprisingly well controlled – but perhaps more notable is that the deviations from the expected behavior can be well explained with a simple electromagnetic model of the environment as we engineered it.

8.1.1 Theory: Shapiro Steps and the AC Josephson Effect

The mechanism of self-induced Shapiro steps may be quite easily understood within the context of the two simple equations governing the IV characteristic of a Josephson junction. In this section, I will build a theoretical understanding of our environmental impedance measurements, using the Josephson equations to first explain two well-known effects (the AC Josephson effect and Shapiro steps), and then to show how a combination of these effects produces the self-induced Shapiro steps that we used for our environmental impedance measurement.

All of the behavior described in the following section is derived from the Josephson equations(Josephson, 1962), which relate I, the current in a Josephson junction, to the voltage V across the Josephson junction and ϕ, the gauge invariant difference in the superconducting phase across the junction. The Josephson equations are usually expressed as:

$$I = I_c \ \sin(\phi) \tag{8.1}$$

$$\frac{d\phi}{dt} = \frac{2eV}{\hbar} \tag{8.2}$$

The first of these equations, often called the "current-phase relation," gives the current through a Josephson junction as proportional to the sine of the difference in the superconducting phase across the junction. The second of these equations describes the evolution of the phase, which increases at a rate proportional to the voltage applied across a junction. Together, these equations may be used to describe all behavior relevant to the measurements performed in this section.

The simplest behavior predicted by this model, which plays an important role in the Josephson network analyzer, is the AC Josephson effect. Phenomenologically, it may be described quite simply:

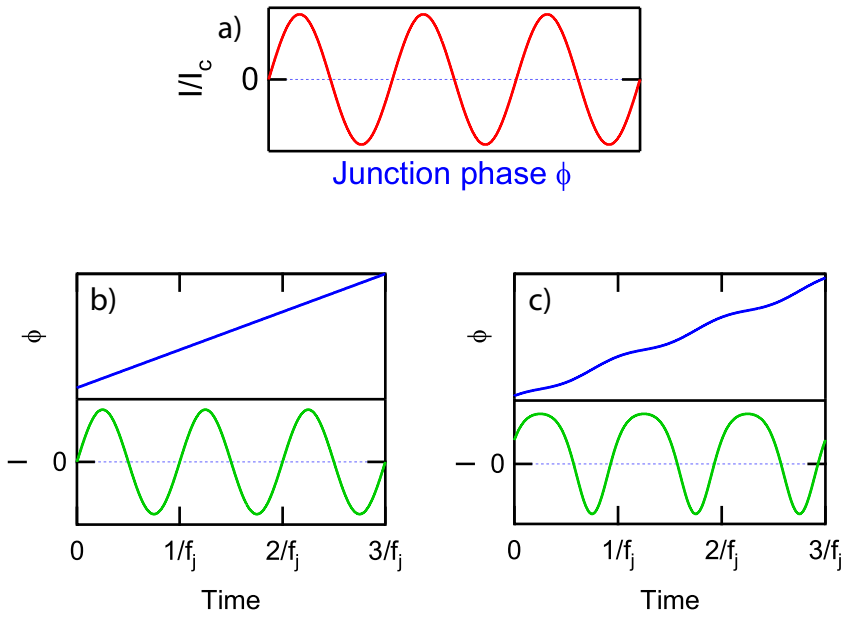

Figure 8.1: Phase and Current vs time in an AC Josephson effect measurement and a Shapiro step measurement. a) Plot of current vs junction phase ϕ for a Josephson junction. b) Plot of phase and current vs time for a constant applied DC Voltage. The phase increments linearly with time, and induces a sinusoidal current at the Josephson frequency. Time is expressed in units of the AC Josephson frequency, $f_J = \hbar/2eV$. c) Plot of phase and current vs time in a Shapiro step measurement. The combination of a DC+AC voltage applied to a Josephson junction gives rise to a nonzero average DC current.

a DC voltage applied to a Josephson junction produces an AC current across the junction at a frequency proportional to the applied voltage. Practically, this may be seen by integrating the second Josephson equation (8.2) when the voltage applied is constant in time:

$$\phi(t) = \frac{2eV}{\hbar}t + C \tag{8.3}$$

When inserted into the first Josephson equation, this gives an AC supercurrent that is purely sinusoidal in time:

$$I(t) = I_C \ \sin\left(\frac{2eV}{\hbar}t\right) \tag{8.4}$$

We may intuitively understand this behavior by considering the change in junction phase difference with time. The second Josephson equation (8.2) tells us that the rate of change of this phase difference is proportional to the voltage difference across the junction. If the phase difference across the junction is represented as a point on the x-axis of Figure 8.1a, then the applied voltage will determine the velocity of that point. A constant voltage will correspond to motion at constant

velocity; from the current-phase relation (figure 8.1a), we then infer that the resulting current is purely sinusoidal. The frequency of this sinusoidal current is typically referred to as the Josephson frequency, defined as:

$$f_J = \frac{2eV}{h} \tag{8.5}$$

Note that typical AC Josephson effect frequencies are very high: the constant of proportionality relating frequency and voltage, $2e/h$, causes the AC Josephson frequency to increase by 3 GHz for each μV of applied DC bias. In our experiment, therefore, we cannot directly measure this AC supercurrent. Note, also, that in this picture, a DC voltage applied to a junction produces only an AC current. It predicts, therefore, that there should be no measurable DC current when a pure DC bias is applied across a Josephson junction.

A different effect, known as "Shapiro steps," may be used to create DC current through a Josephson junction with a finite bias voltage. First noticed in 1963 by Shapiro(Shapiro, 1963), this effect is in some sense the opposite of the AC Josephson effect: where the AC Josephson effect converts a DC voltage into an AC current, the effect discovered by Shapiro converts an AC excitation into a DC current.

In a measurement of Shapiro steps, a voltage is applied to a junction that is a combination of a DC voltage and a high frequency AC excitation. The resulting current can be found in the same manner as above: we use the second Josephson equation [equation (8.2)] to find the phase of the junction as a function of time, and then we use the first Josephson equation to find the corresponding current. This is illustrated in figure 8.1c. The phase in figure 8.1c, increases with a slight sinusoidal variation added to its linear rise. If the frequency of this sinusoidal variation corresponds to the Josephson frequency of the DC component of the bias, then the IV curve will exhibit Shapiro steps. These may be understood, as before, by considering the motion of a phase particle along the axis of the current-phase relation (figure 8.1a). The combined DC and AC voltage applied to the Josephson junction cause the particle to always move to the right, but at a speed that increases and then decreases because of the small sinusoidal voltage added to the junction. The phase particle will therefore alternately move fast, and then hesitate, during its motion along the phase axis. If the Josephson frequency is at the same frequency as the applied RF, this hesitation will occur at the same relative phase in the sinusoidal current-phase relation (figure 8.1c). This will produce a current through the Josephson junction that is periodic, but is no longer purely sinusoidal, and, crucially, no

longer has a zero average. This DC current produced when a junction is biased with a DC voltage and an AC voltage at the corresponding Josephson frequency is called "Shapiro Steps", where the word "step" refers to the sharp features that are measured in the IV curve of an irradiated junction.

Shapiro steps may therefore be said to arise because the externally imposed RF voltage is oscillating in phase with the oscillation from the AC Josephson effect. This explanation, however, does not account for the value of the (fixed) difference in phase between these two oscillations, which will determine the magnitude of the measured DC current. The dynamics of this matching of the two signals – termed "phase locking" – will not be treated in our mathematical analysis of the Shapiro steps used in our experiment. Phenomenologically, it may be understood as a feedback loop, effected by the load line of the junction bias, that adjusts the phase of the Josephson oscillation to create a Shapiro step at a current consistent with the external bias.

The use of our junction as a Josephson network analyzer is simply a combination of these two effects: A DC voltage is applied to a Josephson Junction. The resulting AC Josephson current encounters an impedance – in our sample, the characteristic impedance of the transmission lines coupling the junction to our room temperature electronics. This generates an AC voltage – at exactly the Josephson frequency corresponding to our applied DC bias. An AC voltage, though, will induce Shapiro steps; the magnitude of the Shapiro steps may then be used as a measure of the impedance of the environment.

We will solve for this result analytically, using the Josephson equations, but to do so, we must make two simple assumptions. First, we will assume that the voltage applied across the Josephson junction consists only of components at DC, and at frequencies that are integer multiples of the Josephson frequency corresponding to the applied DC voltage. This is a very reasonable assumption to make: the DC voltage on the junction will create an oscillation at the Josephson frequency, and this may be mixed (by nonlinear elements) into integer multiples of that frequency, but it cannot be used to create components at unrelated frequencies. The practical consequence of this assumption is that the current across the Josephson junction (for example, as plotted in figure 8.1) is periodic in f_J, and does not have Fourier components at frequencies that are not a multiple of f_J.

We must also assume that the Fourier series for $I(t)$ converges rapidly. It will become apparent soon that the condition for this convergence is that

$$\frac{I_C \; Z(\omega_J)}{V_{DC}} < 1 \tag{8.6}$$

Where I_C is the critical current of the Josephson junction, and $Z(\omega_J)$ is the impedance of the environment at the Josephson frequency. This constraint may be interpreted as saying that the magnitude of the AC voltage self-inducing the Shapiro steps must be smaller than the magnitude of the external DC voltage applied; alternately, this expression states that the external voltage applied must be greater than the quantity $E_J/2e$. However it is expressed, this condition is found to be true for all relevant regimes of our measurement.

To understand the self-induced Shapiro steps analytically, we begin with the second Josephson equation:

$$\dot{\phi} = \frac{2\pi V}{\Phi_0} \tag{8.7}$$

Where we have used $\Phi_0 = \frac{h}{2e}$ to simplify equation (8.2). When the voltage bias applied is a pure DC voltage, then this equations become even simpler: the phase increases at a constant rate, related to the Josephson Frequency:

$$\dot{\phi} = 2\pi f_j = \omega_J \tag{8.8}$$

We will solve by progressive iterations: we will impose a DC voltage, solve for the resulting current, and the DC + AC voltage that it produces. Iteratively repeating this, we can build up the entire fourier series for the current as a function of time; we will find, however, that this series converges rapidly and only the first few terms are important. Integrating equation 8.8 gives:

$$\phi^{(0)}(t) = \omega_J t \tag{8.9}$$

Which, inserted into the first Josephson equation 8.1, gives

$$I^{(0)}(t) = I_C \sin(\omega_J t) \tag{8.10}$$

This current across a frequency-dependent environmental impedance will induce an additional voltage proportional to the environmental impedance at the Josephson frequency:

$$V(t) = I_C \ \sin(\omega_J t) Z(\omega_J) \tag{8.11}$$

To find the first-order approximation to the behavior of the junction we add this to V_{DC}, insert this into equation (8.2), and integrate:

$$\phi^{(1)}(t) = \omega_J t - \frac{I_C \ Z(\omega_J)}{V_{DC}} \cos(\omega_J t) \tag{8.12}$$

We define $\alpha = \frac{I_C\ Z(\omega_J)}{V_{DC}}$, the small parameter discussed above, which gives the relative magnitudes of successive terms in our fourier series. Thus:

$$I = I_C\ \sin\left[\omega_J t - \alpha\ \cos(\omega_J t)\right] \tag{8.13}$$

This is expanded using the usual sum identity for the sin function:

$$I = I_C\left\{\sin(\omega_J t)\ \cos\left[\alpha\ \cos(\omega_J t)\right] - \cos(\omega_J t)\ \sin\left[\alpha\ \cos(\omega_J t)\right]\right\} \tag{8.14}$$

Note that $Z(\omega)$, and therefore α can be complex. The complex portion of α, however, does not affect the net result, as the expansion of $\sin\left[\alpha\ cos(\omega_J t)\right]$ has no DC component. We therefore ignore the imaginary component of $Z(\omega)$. The sine of a sine in (8.14) can then be expanded in Bessel functions; see, for example, (Arfken and Weber, 1995), p. 632. This gives:

$$\begin{aligned} e^{ix\cos(\theta)} &= J_0(x) \\ &\quad + 2\left[J_2(x)\cos(2\theta) - J_4(x)\cos(4\theta) + ...\right] \\ &\quad + 2i\left[J_1(x)\cos(\theta) - J_3(x)\cos(3\theta) + ...\right] \end{aligned}$$

To lowest order, then, equation (8.14) becomes:

$$I(t) = I_C\left[\sin(\omega_J t) - 2\ J_1(\alpha)\ \cos^2(\omega_J t)\right] \tag{8.15}$$

The first term, here, reproduces the AC Josephson effect, and the second term contains both a higher frequency component (at $2f_J$) and a DC component. Ignoring the higher frequency component, and using a lowest-order expansion of $J_1(\alpha)$ for small α, we find:

$$I(t) = I_C \sin(\omega_J t) + \frac{I_C^2\ Z(\omega_J)}{2\ V_{DC}} \tag{8.16}$$

This is the result we desired: it shows that an externally applied DC voltage will produce a DC current proportional to the environmental impedance at the Josephson frequency of the DC bias. This equation is also referred to as the "power balance" equation, as it could be naively guessed by forcing the DC power supplied by the voltage bias ($= I_{DC}V_{DC}$) to be equal to the AC power dissipated in the resistive environment $\left[= \frac{1}{2}\ I_C^2\ Z(\omega)\right]$. Note that this equation only holds in a

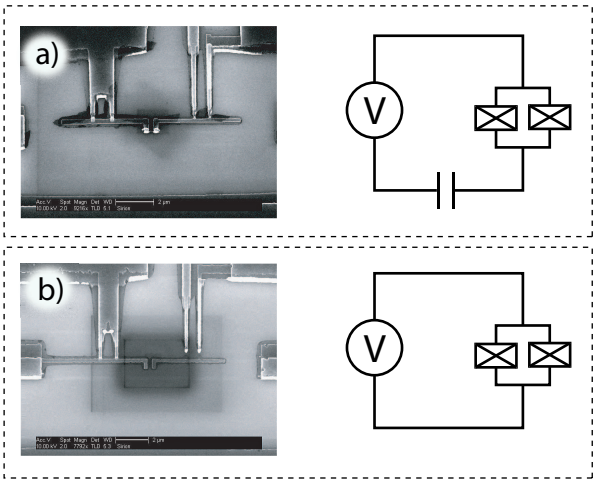

Figure 8.2: a) SEM of a typical Box-SET sample. A physical gap isolates the box island from the box gate. Circuit diagram of the box only is shown to the right. b) SEM of SQUID sample used for environmental impedance measurements. An aluminum trace provides electrical contact between the gate and the island. The rest of the fabrication is unchanged.

region where equation (8.6) is true. For the samples measured for this thesis, however, any DC bias larger than $3\mu V$ in magnitude satisfied this condition.

8.1.2 Measurements

Samples were fabricated quite simply, with a single small modification to the existing process. In the usual box-SET samples (figure 8.2a) an isolated superconducting island is created by a gap between the box gate lead and the box island. If this gap is shorted out with an aluminum trace (figure 8.2b), then the box becomes a DC Superconducting Quantum Interference Device (SQUID). This DC SQUID consists of two Josephson junctions, in parallel; for the purposes of our experiment, it can be considered to be a single Josephson junction with a Josephson energy that can be modulated with a magnetic field. It is important to note that this SQUID is fabricated in the same place, using the same fabrication, as the usual box-SET sample – and that, presumably, the SQUID will be exposed to the exact same environmental impedance as a Cooper-pair box.

Measurements were performed in both a pumped Helium-3 system at 250 mK and in a dilution refrigerator at 10 mK; the results were not substantially different. The wiring used was the same as that used for typical box-SET measurements (see figure 5.1), except that the high-frequency lines to room temperature were replaced with 50 Ω terminations. The environment close to the SQUID sample was designed to be as similar to the corresponding Box-SET measurements as possible (see

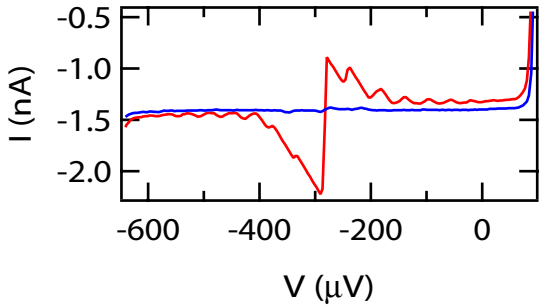

Figure 8.3: Modulation of the subgap structure in a SQUID sample used for environmental impedance measurement.

figure 5.5). The coplanar waveguide on the silicon chip was wirebonded to the coplanar waveguide on the jellyhog board (see figure 5.5), which was loosely matched in dielectric constant to the silicon. High performance SMP connectors were used to bring this signal onto coaxial lines. The unused coplanar waveguide traces on the Arlon board were, in different runs, either left open, or wirebonded to ground to suppress any parasitic modes; no difference was seen in the measured response. Similarly, no difference in the measured response was noted when the four CPW ground planes on chip were wirebonded together, in an attempt to suppress parasitic slotline modes.

Measurements of the IV curves were made with the usual bias electronics (see figure 5.7); a 10 kΩ bias resistor was found to provide reasonably precise measurements of the current while not obscuring the measurement with a very flat load line.

IV curves of the SQUID were first measured at an array of different magnetic fields. The modulation observed demonstrated that the fabrication was successful – by showing that there were two junctions, and that, combined, they operated effectively as a SQUID. The modulation of our IV curve also confirmed that the effects seen in the junction subgap were due to self-induced Shapiro steps, which are predicted to diminish with the magnitude of the junction supercurrent; possible confounding effects, such as photon-assisted quasiparticle tunneling, would not disappear in the same way. Finally, the SQUID current at minimum I_C (see figure 8.3) was used to provide an estimate of the background quasiparticle tunneling rate through the junction. From these IV curves, the superconducting gap of the aluminum was measured to be $186\mu V$. The Ambegaokar-Baratoff relation(Ambegaokar and Baratoff, 1963), with the junction normal state resistance, could then be used to estimate the junction critical current, which was typically 15 nA.

The measured currents and voltages across the junction showed sizable offsets (see figure 8.3).

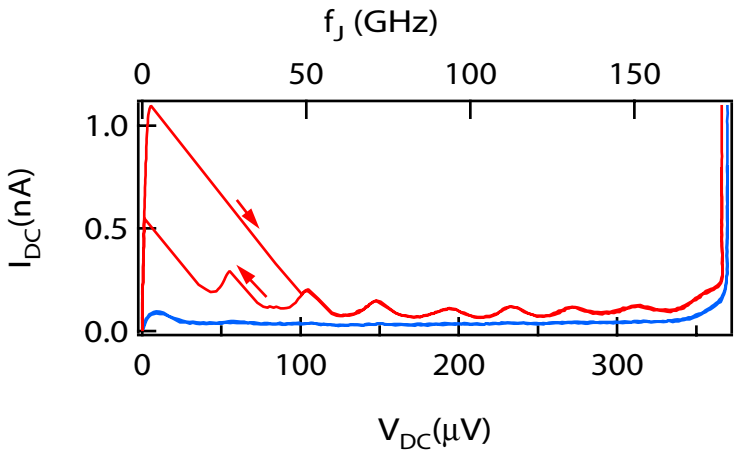

Figure 8.4: By reflecting the IV curve onto itself, offsets in the measured current-voltage curve are removed, and a measurement of absolute current vs. absolute voltage is reported. The blue curve shows the current through the junction when a magnetic field was used to adjust I_c to a minimum; current at this point was presumed to be entirely due to quasiparticles. The red curve shows the measured current-voltage characteristic when I_C was adjusted to a maximum. Their difference was reported as a measure of the self-induced Shapiro step current.

This was largely due to DC offsets of the amplifiers, but was nevertheless a confounding effect: to know frequency of the AC Josephson effect, we needed to know the the absolute magnitude of the voltage applied to the junction. Obtaining a good estimate of these offsets proved nontrivial, as load line-distortions of the IV curves were hysteretic (see figure 8.3), and the IV curves were therefore not symmetric in current or voltage. A good estimate of the offsets was nevertheless obtained by point reflecting the negative-current/negative voltage portion of each IV curve to overlay the positive current/positive voltage portion (see figure 8.4). The point of reflection that gave the optimal overlay was then considered to the true zero-current/zero-voltage point.

The power balance equation was then used to transform IV curves into impedance vs. frequency curves:

$$I_{DC}\ V_{DC} = \frac{1}{2} I_C^2\ Z(\omega_J)$$

$$Z(\omega_J) = \frac{2\ I_{DC}\ V_{DC}}{I_C^2} \tag{8.17}$$

An accurate measurement of the DC supercurrent flowing through the junction was obtained by subtracting the quasiparticle tunneling background (subgap current at minimum I_C) from the

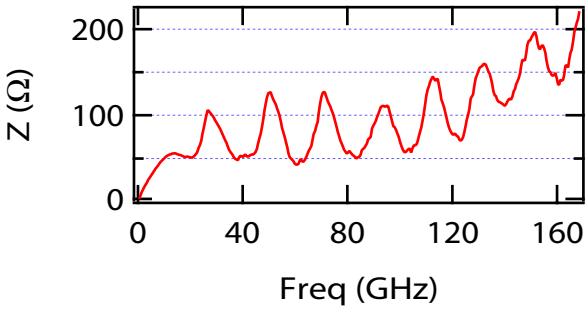

Figure 8.5: Impedance vs. frequency, calculated from the SQUID IV curves shown in Figure 8.4

(DC current at maximum I_C). The x axis, similarly, was converted from voltage to corresponding Josephson frequency, to yield a true plot of impedance vs frequency (figure 8.5).

The resulting plot of impedance vs frequency shows a resonance in the impedance recurring approximately every 20 GHz, which is immediately suggestive of a cavity resonance in the environment seen by the junction. In the following section we report on attempts to computationally model the junction environment to identify the source of these effects.

8.1.3 Modeling

Modeling was completed using Applied Wave Research Microwave Office, which was able to produce impedance vs frequency curves that could be directly compared to figure 8.5. We attempted to create a model using the minimum number of elements necessary to faithfully reproduce the physical layout of the chip and the phenomenological behavior of our system.

A circuit schematic of our best-guess model is shown in Figure 8.6. The impedance of the model is measured from the right side, where the junction is considered by Microwave Office as an input port. The junction capacitance, known approximately from the charging energy of the corresponding Cooper-pair boxes, was inserted as a 3.2 fF shunt capacitance local to the junction. The on-chip CPW transmission lines were inserted as a CPW transmission line in Microwave Office; the transmission line length that gave the best fit to the observed data, 2.6 mm, was in good agreement with the designed physical length of the on-chip transmission line, 2.5 mm. The wirebond was modeled by a series inductance, adjusted to 0.12 nH to give a best fit to the data; the environment beyond the wirebonds was modeled as a 50Ω termination.

Agreement between the model and the data was remarkable at frequencies above DC, and below 90 GHz. In both cases, however, these deviations may be, at least phenomenologically, understood.

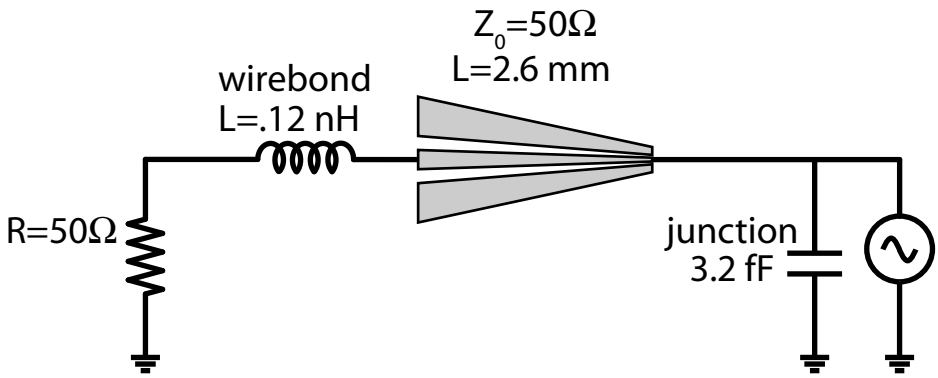

Figure 8.6: Best guess circuit model for environmental impedance measurements. The junction (right side of diagram), with a local capacitance from the physical capacitance of the junction, launches onto a 50 Ω transmission line, corresponding to the on-chip coplanar waveguide taper that can be seen in figure 5.5b. This coplanar waveguide linearly tapers from the $\sim \mu$m scale of our device to the mm scale used to match the on-board coplanar bias lines, but can be theoretically treated as a simple 50 Ω transmission line throughout its length (see section 4.2.2). At the end of the transmission line, wirebonds connect the junction to the environment external to our sample mount, which is presumed to have a characteristic impedance of 50 Ω.

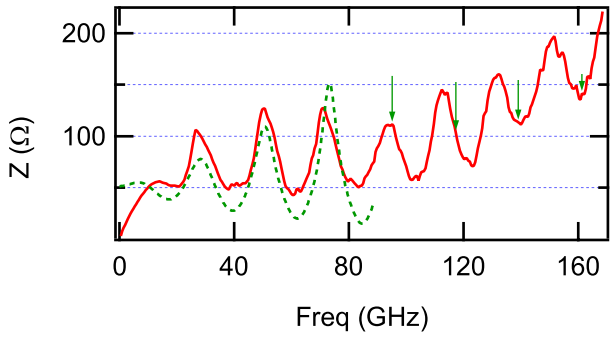

Figure 8.7: Environmental impedance vs. frequency calculated from measured data (red) and from the circuit schematic shown in figure 8.6 (dashed green curve). Agreement between these two curves is good until 90 GHz. Green arrows above 90 GHz show the location of the theoretically predicted resonance peaks, which shows an increasing mismatch with the measured data.

At DC, the power balance equation leads us to infer an impedance of zero for any measured current (see equation 8.17, with $V_{DC} \rightarrow 0$). This is clearly in error, but it is easily explained: the power balance equation was derived in the limit where V_{DC} is large [see equation (8.6)]. For small V_{DC}, it clearly does not hold. Note, also, that load line artifacts in the IV curve data (see, for example, figure 8.3) are transformed into parabolas when converting current into impedance with equation (8.17). Therefore, we must not only disregard the data near DC, but also the data parabolically extending away from it.

At higher frequencies, the disagreement is more subtle. It appears that he peak spacing (in

frequency) changes at higher harmonics of the fundamental resonance. Green arrows in figure 8.7 show the theoretically predicted location of higher harmonics of the fundamental resonance, which clearly do not match the measured data. In fitting these these effects, we generally found it difficult to contrive any model that would match the impedance oscillations at higher frequencies. Modeled results showed a resonance in the impedance at linear multiples of a fundamental frequency, whereas the higher frequency harmonics observed experimentally did not appear to extrapolate linearly back to zero frequency.

We believe that these effects are due to the superconducting gap of aluminum. Above 90 GHz, photons created by the AC Josephson effect have more than the 2Δ of energy required to break Cooper pairs in Aluminum. Photons propagating in our sample at this frequency will therefore experience a loss that is fundamentally different from that at low frequencies. No attempts have been made, however, to model these effects, and our explanation therefore remains only phenomenological.

8.2 1/f Noise Measurements

A recurrent theme throughout much of this thesis has been the charge noise in the substrate or oxide barrier of the SET samples measured, which I've frequently referred to as "1/f noise." As discussed in 1.4.5, this noise is thought to be a product of imperfect stoichiometry of Aluminum Oxide somewhere in our samples. Section 6.4 describes the techniques that were used to observe and eliminate the effects of charge noise in the normal state; section 7.2.1 describes the attempts to meliorate its effects in the superconducting state.

In the following section, I will describe studies of this charge noise for its own sake. I will begin with an overview of the current theoretical understanding of this noise, and then move on to an explanation of the experiments that we performed to measure this noise. Finally, I will include a brief description of the conclusions that we reached as a consequence of this investigation.

8.2.1 Theoretical Background

1/f fluctuations in nanoelectronic systems have been observed and studied extensively, particularly as the source of resistance fluctuations in thin metal films. The charge noise fluctuations in our own systems are thought to stem from the same source, and reviews on the subject (Weissman, 1988; Yu, 2004; Dutta and Horn, 1981) will frequently note such applicability. These reviews typically consider the 1/f noise in systems such as ours to be the product of many discrete charged two-level

systems.

The power spectrum of a signal that consists of Poisson-distributed switching between two possible states with a characteristic time of $\tau_0 = 1/f_0$ is Lorentzian, typically expressed as:

$$S(f) \propto \left[1 + (f/f_0)^2\right]^{-1} \tag{8.18}$$

This alone does not immediately suggest such fluctuators are the source of the 1/f noise observed in our junctions, as it falls off as f^{-2} instead of the expected 1/f. However, theorists were quick to realize that the superimposed effects of an ensemble of such fluctuators could provide the necessary 1/f spectrum.

The problem of understanding this 1/f noise then developed into the problem of finding a physically motivated model for a distribution of fluctuators, with varying tunneling times τ_0 and couplings, that would produce the required spectrum. A frequently cited early success in this effort is that of McWhorter (McWhorter, 1957), who suggested that the noise was due to quantum tunneling in to and out of charge traps at the semiconductor-oxide interface. This model was initially attractive, as a very plausible uniform distribution of charge traps could provide the required 1/f characteristic. This model has been generally discredited, however, because the mechanism proposed does not extrapolate to certain systems where 1/f noise has been observed – and also because its predictions about 1/f noise variation with temperature have not been born out in experiment(Weissman, 1988; Dutta and Horn, 1981). Another popular early model, described by Dutta and Horn (Dutta et al., 1979), presumes an ensemble of such bistable fluctuators which are thermally activated.

More recent theoretical efforts, summarized in (Yu, 2004), are focused on the possibility of correlations between the fluctuators. These reviews typically prescribe a measurement of the "second spectrum" of the noise as a test of various theoretical notions of fluctuator correlation. The second spectrum of a noise signal is constructed through a two-step process(Restle et al., 1985; Seidler and Solin, 1996): a large data set is first divided into multiple time traces, each of which is individually fourier transformed to yield a power spectral density. The power within a predetermined band of each of these spectra is then calculated, and its variability in time recorded . This variability may be fourier transformed to yield the noise in a measurement of the power in the selected frequency bin; the spectra of these fluctuations is termed the second spectrum. This second spectrum, in turn, may be used to distinguish between various models describing the interaction of the two-level

fluctuators(Nguyen and Girvin, 2001; Weissman, 1993). A measurement of the second spectrum of the noise affecting our qubit is therefore an important imperative for the understanding of the source and mechanism of this noise.

Almost independent of these theoretical treatments, the superconducting community itself has devoted considerable time and effort to the study of sources of 1/f noise, which is thought to be the largest impediment to maintaining quantum coherence in a potential qubit system. Nakamura has made measurements of the variation in 1/f noise with temperature, and claims that its magnitude varies as T^2 (Astafiev et al., 2006); the group of John Martinis claims to see signatures of coupling between individual fluctuators and their qubit (Simmonds et al., 2004), and believes that materials engineering of their junctions may eliminate these effects(Martinis et al., 2005). The Delft group has seen results similar to those that we will present in measurements of the noise of their junction resistances (Eroms et al., 2006). Observations of SET 1/f noise have both suggested that the source of 1/f fluctuators is in the device substrates (Furlan and Lotkhov, 2003), and that etching away this substrate has no effect on the 1/f noise (Hakonen et al., 1999).

Whatever the reason for the study of these effects, however, it is universally agreed upon that this is an important topic for the subject of superconducting quantum computing and for the study of mesoscopic systems in general. With this in mind, we endeavored systematize measurements of the 1/f noise in our system.

8.2.2 Measurement Techniques

The first measurements of 1/f noise made in this lab were almost incidental. 1/f noise had been found to be a problem in our measurement, and software was designed to remove its effects. This software maintained a detailed record of the charge noise effects that it had compensated, and a cursory inspection of that record showed that it seemed to be varying.

This did not come as a particular surprise; charge noise is widely known to vary. Theoretical predictions discussed above suggest that this noise varies with temperature, and it is empirically known that this charge noise will vary when the same sample is cooled down different times. It is widely known that this charge noise will settle after a few weeks of operation at dilution refrigerator base temperature, and experiments in our group have shown that an individual charged fluctuator may be "pinned" with the application of a strong DC voltage to a SET gate. Nevertheless, inspection of the record of the charge noise suggested another interesting thought: that the charge noise of the

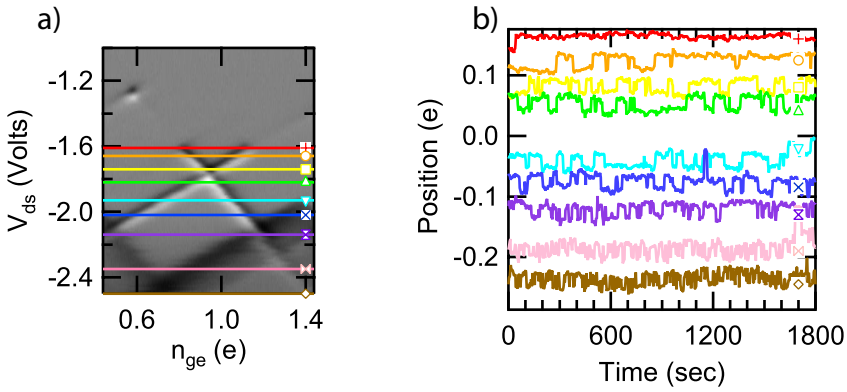

Figure 8.8: a) Different V_{ds} settings of the SET where transfer function shifts were measured. b) Plot of transfer function shift vs time for the SET V_{ds} settings of the corresponding color in part a).

SET varied with the SET operating point.

To demonstrate this assertion, a simple measurement was devised: The SET drain-source voltage was fixed to a constant value, and the SET gate voltage was swept repeatedly over a range corresponding to 1 electron of polarization charge. An SET transfer function was thus repeatedly measured, and the shifts of subsequent transfer functions were calculated relative to the initial measurement. The 1/f charge noise manifests itself as an offset in the apparent n_{ge} in a measured transfer function, and so, by tracking the position of the transfer function we were able to follow the 1/f noise of the SET for many hours.

The results are reproduced in Figure 8.8 for an array of SET operating points on the JQP feature and gaprise. At SET operating points where there is more current flowing, it would seem, the charge noise coupled to the SET appears to increase. Curiously, however, it does not appear that there is a large ensemble of fluctuators coupled to the SET, all of which are activated by the operation of the SET. Instead, it appears that there is a single fluctuator, coupling approximately .03 e of polarization charge to the SET island, which is activated by SET operation. At the operating point where the highest current flows – indicated by the brown line in Figure 8.8 – it appears that there is a drift in the transfer position, in addition to the two-state charge fluctuation. However, for all other operating points it seems that we measure the effects of SET activation on a single fluctuating charge.

Similar data were measured with the SET biased on the DJQP feature, but they are not reproduced here. That data, however, shows essentially the same behavior: at operating points where there is more current in the SET, it appears that the effects of charge noise are more severe. Fur-

thermore, as in this data, the data measured on the DJQP feature seem to show predominantly the effects of the activation of a single fluctuator.

From these measurements, we hypothesized that current flowing in the SET activated charged fluctuators in the oxide surrounding the SET. Our experiment as described above, however, was not a particularly well-controlled test of this idea. As each transfer function was measured, the polarization charge on the SET gate capacitor was swept through a full electron. During that sweep, current was not continually flowing in the SET, and the fraction of the time when current was flowing was a very sensitive function of V_{ds}. Measurements performed above the gaprise, for example, were measured with SET current continuously flowing; when the SET was measuring transfer functions in the vicinity of the DJQP feature, current would only flow for approximately 5% of the sweep. Each time trace in figure 8.8, then, combines the charge noise activation effects of a number of different operating points, and may have magnified the effects seen at higher V_{ds} values where the SET was "on" a larger fraction of the time.

A new charge noise measurement scheme was implemented in 2006, when Box-SET samples fabricated at Yale were measured, to resolve this problem. Instead of making repeated sweeps of the transfer function, the SET was fixed at a single operating point. A small sinusoidal voltage of known magnitude was applied to the SET gate. The output of the SET therefore consisted of a measurement of the SET output modulated by both the small sinusoidal input and the effects of the charge noise on the SET.

The spectral density was then calculated from this measurement and converted (via the known magnitude of the "calibration tone") to units of charge noise e^2/Hz. It is worth noting that this scheme produces only an approximate measurement of the SET charge noise: it presumes that the SET output is linearly related to the charge coupled to the SET island. As discussed previously, this is an approximation, and may be only true for across a very limited range near certain SET operating points. Nevertheless, measurement in this fashion was able to discern systematic differences in charge noise as a function of SET operating point, and so the measurement, if not perfectly accurate, was considered to be precise.

Figure 8.9 shows a characteristic measurement made using this methodology. This plot has been loosely divided into four regions, where we believe the dominant contribution to the noise to come from four different sources. In region I the noise appears to resemble the $1/f^2$ Lorentzian noise of a single charged fluctuator. Region II contains $1/f$ noise that does not show dramatic systematic

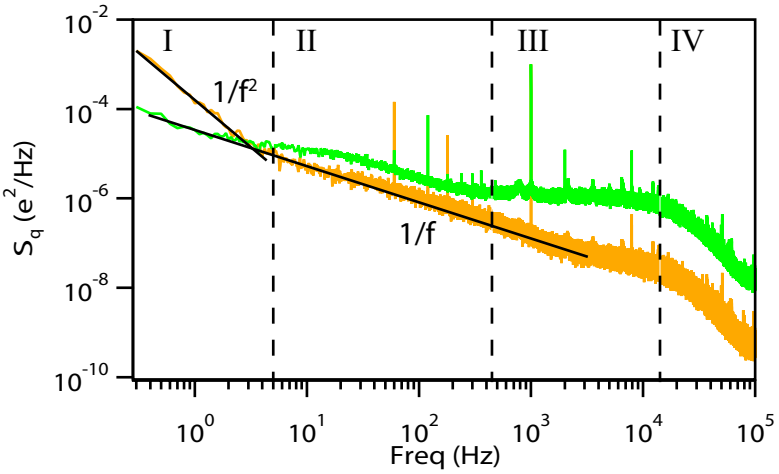

Figure 8.9: Measurements of Charge noise vs. frequency when the SET is biased on the edge of the JQP (green) and on the gaprise (orange). Each spectrum may be decomposed into four regions. In region I, a single charged fluctuator with a low characteristic frequency appears to dominate the orange spectrum, but does not seem evident in the green spectrum. In region II, both spectra show approximately 1/f noise. In region III, the noise appears white with frequency, and is likely due to the amplifiers in the system; the different levels appear because the amplifier noise, referenced to the SET input, depends on the gain of the SET. In region IV, the noise rolls off with frequency because of filtering imposed on the signal.

variation with operating point. The amplitude of this $1/f$ part of the spectrum, $7 \times 10^{-5} e^2/Hz$ at 1 Hz, agrees with similar published observations (Kenyon et al., 2000). In region III, we see the white noise of the following amplifiers, which, when referenced to the input of the SET will have an amplitude determined by the effective SET gain. Finally, in region IV, we see a rolloff in the noise caused by filtering imposed on our signal.

Repeated measurements with the SET biased at these two operating points yield the same spectra; the variation between these spectra is real. Nevertheless, further investigation of this data suggests that, as in the previous measurements, the most significant variability of these spectra – in region I of figure 8.9 – comes form the activation of a single two-level fluctuator by the SET, and not of a large ensemble of fluctuators.

In an attempt to confirm this hypothesis, spectra such as those in 8.9 were recorded over a much longer time, to probe much lower frequencies. The corresponding time traces were then analyzed, and the duty cycle and magnitude of the dominant fluctuator was estimated. From these data, a Monte Carlo simulation of the expected charge noise spectrum for the observed fluctuator was generated. This spectrum is compared to the observed spectrum in figure 8.10. While this does not

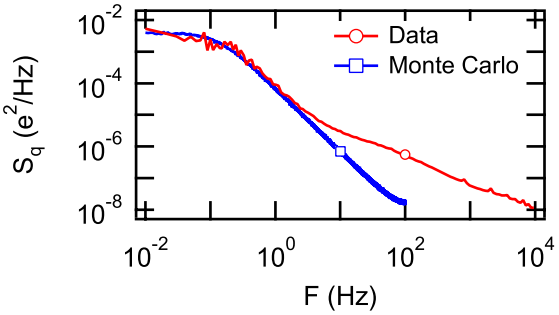

Figure 8.10: Comparison of measure 1/f charge noise spectrum (red) to Monte Carlo simulation inferred from observation of a single switcher. This suggests, but does not prove that the low frequency charge noise variations were due to a single two-level switcher activated by SET operation. The fluctuator at low frequency was simulated to have an amplitude of .05 e, a characteristic switching time of 1.5 s to switch to its high state, and 6 s to switch to its low state.

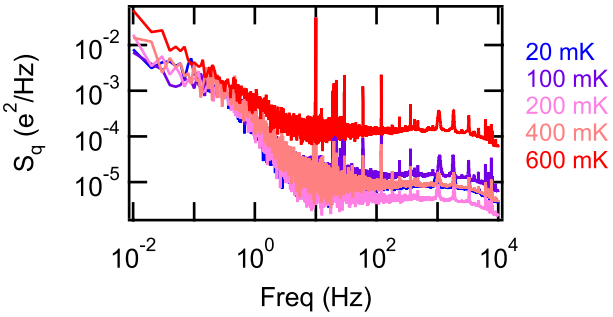

Figure 8.11: 1/f noise measured in the normal state at a variety of temperatures. Care was taken to operate the SET at the same operating point for all shown traces. Because of these data, we do not believe that the SET 1/f noise varies with temperature. The noise grows smaller near the right side of each plot because the data were decimated by a factor that increases with frequency, to eliminate the extensive redundancy of data points measured at high frequency.

prove that the charge noise variations that we observed were due to a single two-level fluctuator, it does strongly suggest that this is the case.

Our 1/f noise measurement software was then used in an attempt to observe variations in the charge noise of the SET in the normal state as the temperature of the sample was varied; this measurement attempted to confirm the results of (Astafiev et al., 2006). Unfortunately, however, our measured results, (see figure 8.11) do not seem to conclusively suggest any variation in 1/f noise with temperature.

It also should be mentioned that occasionally, and not in any rigorous fashion, the charge offset noise affecting the single electron box/Cooper-pair box was investigated in conjunction with the noise affecting the SET. In each such case, it was see that charge noise that affected the SET did not

seem to affect the box, and that the activation of charge noise on the SET was not accompanied by a corresponding activation of charge noise on the box. As previously noted, this was quite fortuitous for the measurements we performed, as charge noise on the SET could be observed and rejected on a reasonable timescale, while the signal-to-noise ratio inherent to measurements of the box rendered it impossible to to reject charge noise offsets on a similarly fast timescale.

8.2.3 1/f Noise Conclusions

The measurements of 1/f noise on the SET, while inconclusive in their attempts to prove or disprove any particular model of charge noise activation, nevertheless seem to suggest at least one important point: Charge noise in the SET may be affected by SET operation. We do not understand the mechanism of this coupling, which may be any of a variety of things: perhaps the SET is heating the substrate, which is activating two-level fluctuators (this may be unlikely, as temperature variations that we imposed did not seem to have a comparable effect). Alternately, perhaps the electromagnetic noise of the voltage fluctuations of the island served as a radiation bath to excite the switchers via their electromagnetic coupling to the island. Perhaps the electrons tunneling on and off of the SET island physically collided with impurities, and caused dislocations; I do not know how any of these models may be tested.

We do conclusively report that several individual charged fluctuators in our sample were activated by SET operation. Furthermore, it appears that the degree to which these fluctuators are activated is related to the current flowing in the SET; however, our attempts to rigorously quantify this claim were ultimately unsuccessful.

Because we believe that the effects that we observed were isolated to individual charged impurities coupled to our SET, we do not believe that this result is so general as to merit publication; the reported behavior of two individual charged fluctuators on two measured samples may not demonstrate a general maxim that can be applied to all such measurements. Nevertheless, the effects described here are reported in hopes that future groups may be wary of their consequence.

Finally, it should be noted that these effects, although not a consequence of the modeled backaction described in Chapters 2 and 3, are an excellent demonstration of yet another sort of noise (or backaction) effect in the SET. As a function of its operating point, the SET appears to activate systems in the surrounding oxide barrier. Although these two-level fluctuators are not the carefully designed quantum bits that our experiment is designed to measure, they nevertheless fill the same

role: they are systems which are both measured and disturbed by the operation of the SET. This, in turn, serves to support the central tenet of this thesis, that SET measurement is capable of disturbing and activating systems that it measures in a way that varies with SET operating point.

Chapter 9

Conclusions

9.1 Summary of Results

This thesis presents measurements made with unprecedented accuracy using the RF-SET. These measurements are novel for their use of slow charge noise rejection techniques to make charge measurements with unprecedented accuracy. Our measurements used this high accuracy to observed a variety of effects, generally related to different types of SET noise, in both the normal and the superconducting state.

In the normal state, we describe work done towards the end of observing the backaction of the SET. SET backaction was modeled using a sequential tunneling model for the full coupled SET-box system. This model predicted subtle variations in the Coulomb staircase of the single electron box that were confirmed by detailed measurements where the SET operating point was systematically varied. The high precision of our measurement techniques also permitted observations of subtle effects of quantum fluctuations of charge on the single electron box.

We also describe work done towards the end of observing SET backaction in the superconducting state. As motivation for our backaction measurement efforts, we presented a formalism for the modeling and measurement of quantum noise in coherent two level systems. We describe the theoretical underpinnings for the measurement and calculation of quantum noise, and show how our understanding motivated careful design of the environmental impedance seen by our devices. We then report on two different measurements developed to test these ideas. We talk, first, about searches for the effects of SET backaction on the Cooper pair box, which showed suggestive effects that we could not conclusively attribute to SET backaction. A second set of measurements that we describe uses the AC Josephson effect and self-induced Shapiro steps to measure the environmental

impedance that we engineered for our qubits.

9.2 Impact

The work described in this thesis is notable both for the results it presents and for the techniques that were employed to find them. Our most central results describe the theoretical treatment and experimental observation of backaction effects arising when a mesoscopic amplifier, the SET, measures a nanoscale system. Other groups concerned with SET measurement will find these results immediately useful for their description of the nature, the magnitude, and the variation of backaction in SET systems. The general framework in which backaction was theoretically considered – by modeling the collective evolution of strongly coupled systems – will also be of more general use to groups studying other mesoscopic amplification systems.

The experimental techniques used for data acquisition in this thesis are also notable. Our measurements were based on algorithms that, concurrent with our data acquisition, observed and rejected the effects of charge offset noise coupled to our devices. Rejecting this noise effectively eliminated slow gain drifts in the SET, and allowed us to average the output of our experiment almost indefinitely. This permitted SET measurement with unprecedented precision, and facilitated many of the measurements in this thesis. Any future groups interested in high-precision SET electrometry are well advised to employ similar methods.

9.3 Future Work

While the normal state measurements presented in this thesis were conclusive and complete, the superconducting state measurements made in this thesis call for more research. The formalism of quantum noise that we used to model our system in the superconducting state predicted effects that are consistent with the results of some of our measurements, but do not fully explain our results. Further SET-Cooper pair box work could use the formalisms discussed in this thesis and the techniques that we developed to search for these same effects. Such work would serve as a valuable proof of the effects of noise on a quantum mechanical system.

Such measurements were not completed in our lab because the samples that we fabricated all experienced serious problems with quasiparticle poisoning. Our observation of trends in poisoning with SET operation suggest that it is another form of SET backaction, but the microscopic details

of this assertion are poorly understood. Further work would examine the mechanisms and seek to eliminate the consequences of these effects in the SET. Such an effort, ideally combined with materials or design revisions to the samples described in this thesis, would hopefully eliminate parity effects and allow quantifiable measurements of SET backaction.

Appendix A

Derivation of The Quantum Noise of a Resistor

This section contains an explicit calculation of the quantum noise from a simple resistor. This discussion is useful as an example of the calculation of a quantum noise spectrum, but also as a foundation for the consideration of the effects of a qubit's environment on its relaxation. Implications of these calculations are discussed in section 3.5.2.

To quantum mechanically treat the noise of a resistor, we use the fact that an a physical resistor with a real impedance R_0 is mathematically equivalent to a semi-infinite electromagnetic transmission line with the same characteristic impedance. Following (Caldeira and Leggett, 1983), we can calculate the effects of coupling to a resistor by considering a qubit's interaction with a bath of harmonic oscillators, each corresponding to a normal electromagnetic mode of the line. This model reproduces the effects of dissipation by allowing signals to propagate infinitely far away, while preserving the energy conservation that our quantum mechanical calculations require. This section reproduces a derivation that was initially presented in (Schoelkopf et al., 2002), and I am indebted to the authors for the understanding I present here.

In a quantum mechanical treatment of an infinite transmission line, the voltage at the end of the line is, expressed as a sum of harmonic oscillator ladder operators (a and $a^\dagger$) for each of the normal modes (n) of the line:

$$V = \sum_{n=1}^{\infty} \sqrt{\frac{\hbar\Omega_n}{Lc}} \left(a_n^\dagger + a_n\right) \tag{A.1}$$

In this expression, c and ℓ are the capacitance and inductance per unit length of our transmission line. For now, we consider a length of transmission line L; we will soon extend this derivation into a semi-infinite line. On our finite line, however, $k_n \equiv \frac{\pi n}{L}$ is the wavevector of the nth electromagnetic mode.

By analogy with classical transmission line theory (Pozar, 2005), we can calculate the corresponding frequency of that mode as $\Omega_n = (k_n/\sqrt{\ell c})$. We wish to calculate the spectral density of this voltage, from equation (3.48):

$$S_V(\omega) = \int_{-\infty}^{\infty} d\tau\, e^{i\omega\tau} \langle V(0)V(\tau)\rangle \tag{A.2}$$

Treating only the autocorrelation term in the integrand, we find:

$$\langle V(0)V(\tau)\rangle = \frac{\hbar}{Lc} \sum_{n,m=1}^{\infty} \sqrt{\Omega_m \Omega_n} \left\langle \left(a_n^\dagger + a_n\right) e^{-iH_b t/\hbar} \left(a_m^\dagger + a_m\right) e^{iH_b t/\hbar} \right\rangle \tag{A.3}$$

Where $\hat{H}_b = \sum_n \hbar\Omega_n a_n^\dagger a_n$ is the Hamiltonian for the transmission line.

The angled brackets $\langle \ldots \rangle$ now represent the expectation value of the quantum mechanical operator $V(0)V(\tau)$. Because we are considering an ensemble of quantum mechanical measurements, this expectation value is the trace of the quantity in brackets multiplied by the density matrix:

$$\langle V(0)V(t)\rangle = \mathrm{tr}\left(\rho_{\mathrm{eq}} \mathrm{V(0)V(t)}\right) \tag{A.4}$$

In thermal equilibrium, the density matrix of the oscillator modes in the lines is expressed as:

$$\rho_{eq} = \frac{e^{-\beta H_b}}{Z} \tag{A.5}$$

We will consider this calculation in the basis denoted by combinations of harmonic oscillator modes, enumerated $|n_0, n_1 \ldots n_i\rangle$, or simply, $|\mathbf{n_i}\rangle$. Returning to the autocorrelation term (A.3), we find:

$$\begin{aligned}\langle V(0)V(\tau)\rangle = \frac{\hbar}{ZLc} \sum_{n,m=1}^{\infty} \sqrt{\Omega_m \Omega_n} \sum_{\mathbf{n_i}} &\langle \mathbf{n_i}| e^{-\beta H_b} a_m^\dagger e^{iH_b t/\hbar} a_n e^{-iH_b t/\hbar} |\mathbf{n_i}\rangle \\ &+ \langle \mathbf{n_i}| e^{-\beta H_b} a_m e^{iH_b t/\hbar} a_n^\dagger e^{-iH_b t/\hbar} |\mathbf{n_i}\rangle \end{aligned} \tag{A.6}$$

Where the fact that all of the exponential terms have only diagonal elements has been used to discard the $a_m a_n$ and $a_m^\dagger a_n^\dagger$ terms. We proceed to reduce this equation, first by acting the exponentials to the left and the right

$$\begin{aligned}\langle V(0)V(\tau)\rangle = \frac{\hbar}{ZLc} \sum_{n,m=1}^{\infty} \sqrt{\Omega_m \Omega_n} \sum_{\mathbf{n_i}} e^{-\beta E_{\mathbf{n_i}} - iE_{\mathbf{n_i}} t/\hbar} \Big(&\langle \mathbf{n_i}| a_m^\dagger e^{iH_b t/\hbar} a_n |\mathbf{n_i}\rangle \\ &+ \langle \mathbf{n_i}| a_m e^{iH_b t/\hbar} a_n^\dagger |\mathbf{n_i}\rangle \Big) \end{aligned} \tag{A.7}$$

The ladder operators then act on the many particle states $|\mathbf{n_i}\rangle$ to add or remove a quanta from the n or mth state, giving modified many-particle states that we label with the shorthand $|\mathbf{n_i} - n\rangle$:

$$\begin{aligned} = \frac{\hbar}{ZLc} \sum_{n,m=1}^{\infty} \sqrt{\Omega_m \Omega_n} \sum_{\mathbf{n_i}} e^{-\beta E_{\mathbf{n_i}} - iE_{\mathbf{n_i}} t/\hbar} \Big(&\langle \mathbf{n_i} - m| e^{iH_b t/\hbar} |\mathbf{n_i} - n\rangle \\ &+ \langle \mathbf{n_i} + m| e^{iH_b t/\hbar} |\mathbf{n_i} + n\rangle \Big) \end{aligned} \tag{A.8}$$

The final exponential may now act on these modified many particle states, and produces a c-number exponential of the many-particle state energy, with a missing (or extra) quanta of energy in the state n:

$$= \frac{\hbar}{ZLc} \sum_{n,m=1}^{\infty} \sqrt{\Omega_m \Omega_n} \sum_{\mathbf{n_i}} \Big(e^{-\beta E_{\mathbf{n_i}}} e^{-iE_{\mathbf{n_i}} t/\hbar} \langle \mathbf{n_i} - m | \, e^{i(E_{\mathbf{n_i}} - E_n)t/\hbar} \, | \mathbf{n_i} - n \rangle + e^{-\beta E_{\mathbf{n_i}}} e^{-iE_{\mathbf{n_i}} t/\hbar} \langle \mathbf{n_i} + m | \, e^{i(E_{\mathbf{n_i}} + E_n)t/\hbar} \, | \mathbf{n_i} + n \rangle \Big) \tag{A.9}$$

We now can rearrange terms; in particular, the two oscillating exponentials may be combined, leaving a factor of $e^{\pm iE_n t/\hbar} \equiv e^{i\Omega_n t}$. We also move the Boltzmann factor into the matrix element, and bring the ladder operators out of the modified many-particle states, in anticipation of the next step:

$$= \frac{\hbar}{Lc} \sum_{n,m=1}^{\infty} \sqrt{\Omega_m \Omega_n} \sum_{\mathbf{n_i}} \frac{1}{Z} \left(e^{-i\Omega_n t} \langle \mathbf{n_i} | \, a_m^\dagger a_n e^{-\beta E_{\mathbf{n_i}}} \, | \mathbf{n_i} \rangle + e^{i\Omega_n t} \langle \mathbf{n_i} | \, a_m a_n^\dagger e^{-\beta E_{\mathbf{n_i}}} \, | \mathbf{n_i} \rangle \right) \tag{A.10}$$

The sum over the many-particle states $\mathbf{n_i}$ can now be performed, and trivially yields Bose occupancy factors $n_\gamma(\Omega_n)$:

$$= \frac{\hbar}{Lc} \sum_{n,m=1}^{\infty} \delta_{m,n} \sqrt{\Omega_m \Omega_n} \left[e^{-i\Omega_n t} n_\gamma(\Omega_n) + e^{i\Omega_n t} \left[n_\gamma(\Omega_n) + 1 \right] \right] \tag{A.11}$$

This term may now be Fourier transformed, per equation (A.2), to yield the spectral density. We note that the only factors that vary with time are the oscillating exponentials, and so the Fourier transform trivially yields two Dirac delta functions:

$$S_V(\omega) = \frac{2\pi\hbar}{Lc} \sum_{n=1}^{\infty} \Omega_n \left\{ \delta(\omega + \Omega_n) n_\gamma(\Omega_n) + \delta(\omega - \Omega_n) \left[n_\gamma(\Omega_n) + 1 \right] \right\} \tag{A.12}$$

To simplify this expression, we will convert the sum in n to an integral:

$$S_V(\omega) = \frac{2\pi\hbar}{Lc} \int_{n=0}^{\infty} dn \, \Omega_n \left\{ \delta(\omega + \Omega_n) n_\gamma(\Omega_n) + \delta(\omega - \Omega_n) \left[n_\gamma(\Omega_n) + 1 \right] \right\} \tag{A.13}$$

We shift the variable of integration to $\Omega_n = n\pi/(L\sqrt{\ell c})$:

$$S_V(\omega) = 2\hbar \sqrt{\frac{\ell}{c}} \int_{\Omega_n=0}^{\infty} d\Omega_n \, \Omega_n \left\{ \delta(\Omega_n + \omega) n_\gamma(\Omega_n) - \delta(\Omega_n - \omega) \left[n_\gamma(\Omega_n) + 1 \right] \right\} \tag{A.14}$$

The term $\sqrt{\ell/c}$ may now be identified as the characteristic impedance R_0 of the transmission line. The Dirac delta functions now allow us to calculate the integral in $d\Omega_n$. We must be careful, however, as the first term will only be nonzero if ω is negative, and the second term will only be nonzero if ω is positive. We enforce this with Θ (step) functions preceding each of these terms:

$$S_V(\omega) = 2\hbar R_0 \left\{ (-\omega)\Theta(-\omega) n_\gamma(-\omega) + \omega\Theta(\omega) \left[n_\gamma(\omega) + 1 \right] \right\} \tag{A.15}$$

Or, more concisely:

$$S_V(\omega) = 2\hbar R_0 \left|\omega\right| \left\{\Theta(-\omega) n_\gamma(\left|\omega\right|) + \Theta(\omega) \left[n_\gamma(\left|\omega\right|) + 1\right]\right\} \tag{A.16}$$

By explicitly inserting the Bose-Einstein occupation factor for the harmonic oscillator states $[n_\gamma(\omega) = 1/(e^{-\beta\hbar\omega} - 1)]$, we may finally reduce this expression to its most concise form:

$$S_V(\omega) = \frac{2R_0\hbar\omega}{1 - e^{-\hbar\omega/k_B T}} \tag{A.17}$$

References

Aassime, A., Johansson, G., Wendin, G., Schoelkopf, R. J., and Delsing, P. Radio-frequency single-electron transistor as readout device for qubits: Charge sensitivity and backaction. *Physical Review Letters*, 86(15):3376–, 2001. URL: http://link.aps.org/abstract/PRL/v86/p3376.

Abragam, A. *The Principles of Nuclear Magnetism*, volume 32 of *The International Series of Monographs on Physics*. Oxford University Press, Oxford, England, 1983.

Allen, L. and Eberly, J. *Optical Resonance and Two Level Atoms*. Dover Publications, Inc., 1987.

Ambegaokar, V. and Baratoff, A. Tunneling between superconductors. *Physical Review Letters*, 10(11):456–459, 1963. URL: http://prola.aps.org/abstract/PRL/v10/i11/p486_1.

Arfken, G. B. and Weber, H. J. *Mathematical Methods for Physicists*. Academic Press, 4th ed. edition, 1995.

Astafiev, O., Pashkin, Y., Nakamura, Y., Yamamoto, T., and Tsai, J. Temperature square dependence of the low frequency 1/f charge noise in the josephson junction qubits. *Physical Review Letters*, 96(13):137001–1, 2006. ISSN 0031-9007. URL: http://scitation.aip.org/getabs/servlet/GetabsServlet?prog=normal&id=PRLTAO000096000013137001000001&idtype=cvips&gifs=yes.

Aumentado, J., Keller, M., Martinis, J., and Devoret, M. Nonequilibrium quasiparticles and 2e periodicity in single-cooper-pair transistors. *Physical Review Letters*, 92(6):066802–1, 2004. ISSN 0031-9007. URL: http://scitation.aip.org/getabs/servlet/GetabsServlet?prog=normal&id=PRLTAO000092000006066802000001&idtype=cvips&gifs=yes.

Averin, D. and Odintsov, A. Macroscopic quantum tunneling of the electric charge in small tunnel junctions. *Physics Letters A*, 140(5):251–7, 1989. ISSN 0375-9601. URL: http://linkinghub.elsevier.com/retrieve/pii/0375960189909341.

Bladh, K. *Quantum Coherence in the Single Cooper Pair Box*. Ph.D. thesis, Chalmers University of Technology, 2005.

Bladh, K., Gunnarsson, D., Hurfeld, E., Devi, S., Kristoffersson, C., Smalander, B., Pehrson, S., Claeson, T., Delsing, P., and Taslakov, M. Comparison of cryogenic filters for use in single electronics experiments. *Review of Scientific Instruments*, 74(3):1323–7, 2003. ISSN 0034-6748. URL: `http://scitation.aip.org/getabs/servlet/GetabsServlet?prog=normal&id=RSINAK000074000003001323000001&idtype=cvips&gifs=yes`.

Blum, K. *Density Matrix Theory and Applications*. Plenum Press, 2 edition, 1996.

Bouchiat, V. *Quantum fluctuations of the charge in single electron and single Cooper pair devices*. Ph.D. thesis, Universite Paris 6, 1997.

Buettiker, M. Zero-current persistent potential drop across small-capacitance josephson junctions. *Physical Review B*, 36(7):3548–, 1987. URL: `http://link.aps.org/abstract/PRB/v36/p3548`.

Caldeira, A. and Leggett, A. Quantum tunnelling in a dissipative system. *Annals of Physics*, 149(2):374–456, 1983. ISSN 0003-4916.

Carmichael, H. *Statistical Methods in Quantum Optics 1: Master Equations and Fokker-Planck Equations*. Springer, 1999.

Caves, C. M. Quantum limits on noise in linear amplifiers. *Physical Review D*, 26(8):1817–, 1982. URL: `http://link.aps.org/abstract/PRD/v26/p1817`.

Cerna, M. and Harvey, A. F. National instruments application note 041: The fundamentals of fft-based signal analysis and measurement. 2000. URL: `http://zone.ni.com/devzone/cda/tut/p/id/4278`.

Clerk, A., Girvin, S., Nguyen, A., and Stone, A. Resonant cooper-pair tunneling: quantum noise and measurement characteristics. *Physical Review Letters*, 89(17):176804–1, 2002. ISSN 0031-9007. URL: `http://prola.aps.org/abstract/PRL/v89/i17/e176804`.

Clerk, A. A. Resonant cooper-pair tunneling: Counting statistics and frequency-dependent current noise. *cond-mat/0301277*, 2003. URL: `http://arxiv.org/abs/cond-mat/0301277`.

Clerk, A. A. and Bennett, S. Quantum nanoelectromechanics with electrons, quasi-particles and cooper pairs: effective bath descriptions and strong feedback effects. *New Journal of Physics*, 7:238–238, 2005. ISSN 1367-2630. URL: http://www.iop.org/EJ/article/1367-2630/7/1/238/njp5_1_238.html.

Cooper, K., Steffen, M., McDermott, R., Simmonds, R., Oh, S., Hite, D., Pappas, D., and Martinis, J. Observation of quantum oscillations between a josephson phase qubit and a microscopic resonator using fast readout. *Physical Review Letters*, 93(18):180401–1, 2004. ISSN 0031-9007. URL: http://scitation.aip.org/getabs/servlet/GetabsServlet?prog=normal&id=PRLTAO000093000018180401000001&idtype=cvips&gifs=yes.

Cottet, A. *Implementation of a Quantum Bit in a Superconducting Circuit*. Ph.D. thesis, Universite Paris VI, 2002. URL: http://www.lps.u-psud.fr/Utilisateurs/cottet/ACottetThesis.pdf.

Davenport, W. B. and Root, W. L. *An Introduction to the theory of Random Signals And Noise*. McGraw Hill Book Co., Inc, 1958.

Devoret, M. *Quantum Fluctuations (Les Houches Session LXIII)*, chapter 10, pages 351–386. Elsevier, 1997.

Devoret, M. and Schoelkopf, R. Amplifying quantum signals with the single-electron transistor. *Nature*, 406(6799):1039–46, 2000. ISSN 0028-0836. URL: http://www.eng.yale.edu/rslab/papers/Nature_SET_amplifier.pdf.

Devoret, M. H., Wallraff, A., and Martinis, J. M. Superconducting qubits: A short review. *cond-mat/0411174*, 2004. URL: http://www.citebase.org/abstract?id=oai:arXiv.org:cond-mat/0411174.

Dutta, P., Dimon, P., and Horn, P. Energy scales for noise processes in metals. *Physical Review Letters*, 43(9):646–9, 1979. ISSN 0031-9007. URL: http://prola.aps.org/abstract/PRL/v43/i9/p646_1.

Dutta, P. and Horn, P. Low-frequency fluctuations in solids: 1/f noise. *Reviews of Modern Physics*, 53(3):497–516, 1981. ISSN 0034-6861. URL: http://prola.aps.org/abstract/RMP/v53/i3/p497_1.

Eroms, J., van Schaarenburg, L., Driessen, E., Plantenberg, J., Huizinga, C., Schouten, R., Verbruggen, A., Harmans, C., and Mooij, J. Low-frequency noise in josephson junctions for superconducting qubits. *Applied Physics Letters*, 89(12):122516–1, 2006. ISSN 0003-6951. URL: http://scitation.aip.org/getabs/servlet/GetabsServlet?prog=normal&id=APPLAB000089000012122516000001&idtype=cvips&gifs=yes.

Fulton, T. A. and Dolan, G. J. Observation of single-electron charging effects in small tunnel junctions. *Physical Review Letters*, 59(1):109–, 1987. URL: http://link.aps.org/abstract/PRL/v59/p109.

Furlan, M. and Lotkhov, S. Electrometry on charge traps with a single-electron transistor. *Physical Review B*, 67(20):205313–1, 2003. ISSN 0163-1829. URL: http://prola.aps.org/abstract/PRB/v67/i20/e205313.

Geerligs, L. J., Averin, D. V., and Mooij, J. E. Observation of macroscopic quantum tunneling through the coulomb energy barrier. *Physical Review Letters*, 65(24):3037–3040, 1990. doi: 10.1103/PhysRevLett.65.3037.

Goppert, G. and Grabert, H. Charge fluctuations in the single-electron box. *Physical Review B*, 63(12):125307–1, 2001. ISSN 0163-1829. URL: http://prola.aps.org/abstract/PRB/v63/i12/e125307.

Goppert, G., Grabert, H., Prokof'ev, N., and Svistunov, B. Effect of tunneling conductance on the coulomb staircase. *Physical Review Letters*, 81(11):2324–7, 1998. ISSN 0031-9007. URL: http://prola.aps.org/abstract/PRL/v81/i11/p2324_1.

Grabert, H. Charge fluctuations in the single-electron box: perturbation expansion in the tunneling conductance. *Physical Review B*, 50(23):17364–77, 1994. ISSN 0163-1829. URL: http://prola.aps.org/abstract/PRB/v50/i23/p17364_1.

Grabert, H. and Devoret, M. H., editors. *Single Charge Tunneling: Coulomb Blockade Phenomena in Nanostructures*, volume 294 of *NATO ASI Series*. Plenum Press, 1992. Proceedings of a NATO Advance Study Institute on Signle Charge Tunneling held March, 1991 in Les Houches, France.

Gunnarsson, D. *The Single Cooper Pir Box – a Quantum-Mechanical Electronic Circuit*. Ph.D. thesis, Chalmers University of Technology, 2005.

Gunnarsson, D., Duty, T., Bladh, K., and Delsing, P. Tunability of a 2e periodic single cooper pair box. *Phys. Rev. B*, 70(22):224523–6, 2004. URL: `http://link.aps.org/abstract/PRB/v70/e224523`.

Hakonen, P., Ikonen, J., Parts, U., Penttila, J., Roschier, L., and Paalanen, M. Noise of a single electron transistor on a si3n4 membrane. *Journal of Applied Physics*, 86(5):2684–6, 1999. ISSN 0021-8979. URL: `http://scitation.aip.org/getabs/servlet/GetabsServlet?prog=normal&id=JAPIAU000086000005002684000001&idtype=cvips&gifs=yes`.

Holst, T., Esteve, D., Urbina, C., and Devoret, M. Effect of a transmission line resonator on a small capacitance tunnel junction. *Physical Review Letters*, 73(25):3455 – 8, 1994. ISSN 0031-9007. URL: `http://dx.doi.org/10.1103/PhysRevLett.73.3455`.

Horowitz, P. and Hill, W. *The Art of Electronics*. Cambridge University Press, second edition, 1989.

Imry, Y. *Introduction to Mesoscopic Physics*. Oxford University Press, 1997.

Josephson, B. Possible new effects in superconductive tunnelling. *Physics Letters*, 1(7):251 – 253, 1962. URL: `http://dx.doi.org/10.1016/0031-9163(62)91369-0`.

Kane, B. E., McAlpine, N. S., Dzurak, A. S., Clark, R. G., Milburn, G. J., Sun, H. B., and Wiseman, H. Single-spin measurement using single-electron transistors to probe two-electron systems. *Physical Review B*, 61(4):2961–, 2000. URL: `http://link.aps.org/abstract/PRB/v61/p2961`.

Kastner, M. A. The single-electron transistor. *Reviews of Modern Physics*, 64(3):849–, 1992. URL: `http://link.aps.org/abstract/RMP/v64/p849`.

K.C. Gupta, I. B., Ramesh Garg and Bhartia, P. *Microstrip Lines and Slotlines*. Artech House, 2nd ed. edition, 1996.

Kenyon, M., Lobb, C., and Wellstood, F. Temperature dependence of low-frequency noise in al-al2o3-al single-electron transistors. *Journal of Applied Physics*, 88(11):6536–40, 2000.

ISSN 0021-8979. URL: http://scitation.aip.org/getabs/servlet/GetabsServlet?prog=normal&id=JAPIAU000088000011006536000001&idtype=cvips&gifs=yes.

Knobel, R. and Cleland, A. Nanometre-scale displacement sensing using a single electron transistor. *Nature*, 424(6946):291–3, 2003. ISSN 0028-0836. URL: http://www.nature.com/nature/journal/v424/n6946/abs/nature01773.html.

Konig, J., Schoeller, H., and Schon, G. Cotunneling at resonance for the single-electron transistor. *Physical Review Letters*, 78(23):4482–5, 1997. ISSN 0031-9007. URL: http://prola.aps.org/abstract/PRL/v78/i23/p4482_1.

Kouwenhoven, L. and Marcus, C. Quantum dots. *Physics World*, 11(6):35–9, 1998. ISSN 0953-8585. URL: http://physicsweb.org/articles/world/11/6/9.

Lafarge, P. *Macroscopic Charge Quantizations in Metallic Nanostructures*. Ph.D. thesis, L'Universite Paris 6, 1993.

Lafarge, P., Joyez, P., Esteve, D., Urbina, C., and Devoret, M. Two-electron quantization of the charge on a superconductor. *Nature*, 365(6445):422–4, 1993. ISSN 0028-0836. URL: http://www.nature.com/nature/journal/v365/n6445/abs/365422a0.html.

Lehnert, K., Turek, B., Bladh, K., Spietz, L., Gunnarsson, D., Delsing, P., and Schoelkopf, R. Quantum charge fluctuations and the polarizability of the single-electron box. *Physical Review Letters*, 91(10):106801–1, 2003a. ISSN 0031-9007. URL: http://prola.aps.org/abstract/PRL/v91/i10/e106801.

Lehnert, K. W., Bladh, K., Spietz, L. F., Gunnarsson, D., Schuster, D. I., Delsing, P., and Schoelkopf, R. J. Measurement of the excited-state lifetime of a microelectronic circuit. *Physical Review Letters*, 90(2):027002–4, 2003b. URL: http://link.aps.org/abstract/PRL/v90/e027002.

Lutchyn, R. M., Glazman, L. I., and Larkin, A. I. Kinetics of the superconducting charge qubit in the presence of a quasiparticle. *Physical Review B*, 74(6):064515–12, 2006. URL: http://link.aps.org/abstract/PRB/v74/e064515.

Martinis, J., Cooper, K., McDermott, R., Steffen, M., Ansmann, M., Osborn, K., Cicak, K., Oh, S., Pappas, D., Simmonds, R., and Yu, C. Decoherence in josephson qubits from dielectric loss. *Physical Review Letters*, 95(21):210503–1, 2005.

ISSN 0031-9007. URL: http://scitation.aip.org/getabs/servlet/GetabsServlet?prog=normal&id=PRLTAO000095000021210503000001&idtype=cvips&gifs=yes.

Martinis, J., Devoret, M., and Clarke, J. Experimental tests for the quantum behavior of a macroscopic degree of freedom: the phase difference across a josephson junction. *Physical Review B*, 35(10):4682–98, 1987. ISSN 0163-1829. URL: http://prola.aps.org/abstract/PRB/v35/i10/p4682_1.

Martinis, J. M., Nam, S., Aumentado, J., and Urbina, C. Rabi oscillations in a large josephson-junction qubit. *Physical Review Letters*, 89(11):117901–, 2002. URL: http://link.aps.org/abstract/PRL/v89/e117901.

Matveev, K. Quantum fluctuations of the charge of a metal particle under the coulomb blockade conditions. *Soviet Physics - JETP*, 72(5):892–9, 1991. ISSN 0038-5646.

McWhorter. *Semiconductor Surface Physics*. University of Pennsylvania, 1957.

Nakamura, Y., Chen, C. D., and Tsai, J. S. Spectroscopy of energy-level splitting between two macroscopic quantum states of charge coherently superposed by josephson coupling. *Physical Review Letters*, 79(12):2328–, 1997. URL: http://link.aps.org/abstract/PRL/v79/p2328.

Nakamura, Y., Pashkin, Y. A., and Tsai, J. Coherent control of macroscopic quantum states in a single-cooper-pair box. *Nature*, 398:786–788, 1999. URL: http://www.nature.com/nature/journal/v398/n6730/abs/398786a0.html.

Nguyen, A. and Girvin, S. Non-gaussian noise in quantum spin glasses and interacting two-level systems. *Physical Review Letters*, 87(12):127205–1, 2001. ISSN 0031-9007. URL: http://prola.aps.org/abstract/PRL/v87/i12/e127205.

Nielsen, M. A. and Chuang, I. L. *Quantum Computation and Quantum Information*. Cambridge University Press, 2000.

Pohlen, S. L. *The Superconducting Single Electron Transistor*. Ph.D. thesis, Harvard University, 1999.

Pozar, D. M. *Microwave Engineering*. John Wiley & Sons, Inc., 3rd edition, 2005.

Redfield, A. On the theory of relaxation processes. *IBM Journal of Research and Development*, 1(1):19–31, 1957.

Restle, P., Hamilton, R., Weissman, M., and Love, M. Non-gaussian effects in 1/f noise in small silicon-on-sapphire resistors. *Physical Review B*, 31(4):2254–62, 1985. ISSN 0163-1829. URL: http://prola.aps.org/abstract/PRB/v31/i4/p2254_1.

Roschier, L., Hakonen, P., Bladh, K., Delsing, P., Lehnert, K., Spietz, L., and Schoelkopf, R. Noise performance of the radio-frequency single-electron transistor. *Journal of Applied Physics*, 95(3):1274–86, 2004. ISSN 0021-8979. URL: http://scitation.aip.org/getabs/servlet/GetabsServlet?prog=normal&id=JAPIAU000095000003001274000001&idtype=cvips&gifs=yes.

Sakurai, J. J. *Modern Quantum Mechanics Revised Edition*. Addison-Wesley Publishing Company, 1994.

Schneiderman, J. F., Delsing, P., Johansson, G., Shaw, M. D., Bozler, H. M., and Echternach, P. M. Quasiparticle poisoning in a single cooper-pair box. *AIP Conf. Proc.*, 850(1):931–932, 2006. URL: http://link.aip.org/link/?APC/850/931/1.

Schoelkopf, A. A., R. J. amd Clerk, Girvin, S., Lehnert, K., and Devoret, M. H. Qubits as spectrometers of quantum noise. *cond-mat/0210247*, 2002. URL: http://arxiv.org/abs/cond-mat/0210247.

Schoelkopf, R., Wahlgren, P., Kozhevnikov, A., Delsing, P., and Prober, D. The radio-frequency single-electron transistor (rf-set): a fast and ultrasensitive electrometer. *Science*, 280(5367):1238–42, 1998. ISSN 0036-8075. URL: http://www.eng.yale.edu/rslab/papers/RFSETScience.pdf.

Schuster, D. I. *Circuit Quantum Electrodynamics*. Ph.D. thesis, Yale University, 2007.

Seidler, G. and Solin, S. Non-gaussian 1/f noise: Experimental optimization and separation of high-order amplitude and phase correlations. *Physical Review B*, 53(15):9753–9, 1996. ISSN 0163-1829. URL: http://prola.aps.org/abstract/PRB/v53/i15/p9753_1.

Shapiro, S. Josephson currents in superconducting tunneling: The effect of microwaves and other observations. *Physical Review Letters*, 11(2):80–82, 1963. doi:10.1103/PhysRevLett.11.80. URL: http://prola.aps.org/abstract/PRL/v11/i2/p80_1.

Simmonds, R., Lang, K., Hite, D., Nam, S., Pappas, D., and Martinis, J. Decoherence in josephson phase qubits from junction resonators. *Physical Review Letters*, 93(7):077003–1, 2004. ISSN 0031-9007. URL: http://scitation.aip.org/getabs/servlet/GetabsServlet?prog=normal&id=PRLTAO000093000007077003000001&idtype=cvips&gifs=yes.

Simons, R. N. *Coplanar Waveguide Circuits, Components, and Systems*. Wiley-Interscience, 2001.

Slichter, C. P. *Principles of Magnetic Resonance*. Springer, 3rd. edition, 1990.

Teufel, J. D. Ph.D. thesis, Yale University, 2007.

Tinkham, M. *Introduction to Superconductivity*. Dover Publications, Inc., 1996.

Turek, B., Lehnert, K., Clerk, A., Gunnarsson, D., Bladh, K., Delsing, P., and Schoelkopf, R. Single-electron transistor backaction on the single-electron box. *Physical Review B*, 71(19):193304–1, 2005. ISSN 0163-1829. URL: http://scitation.aip.org/getabs/servlet/GetabsServlet?prog=normal&id=PRBMDO000071000019193304000001&idtype=cvips&gifs=yes.

van den Brink, A., Schon, G., and Geerligs, L. Combined single-electron and coherent-cooper-pair tunneling in voltage-biased josephson junctions. *Physical Review Letters*, 67(21):3030–3, 1991. ISSN 0031-9007. URL: http://prola.aps.org/abstract/PRL/v67/i21/p3030_1.

Van der Ziel, A. Flicker noise in electronic devices. *Advances in Electronics and Electron Physics*, 49:225, 1979.

Van Duzer, T. and Turner, C. *Principles of superfconductive devices and circuits*. Elsevier, 1981.

Vion, D., Aassime, A., Cottet, A., Joyez, P., Pothier, H., Urbina, C., Esteve, D., and Devorett, M. Manipulating the quantum state of an electrical circuit. *Science*, 296(5569):886–9, 2002. ISSN 0036-8075. URL: http://www.sciencemag.org/cgi/content/abstract/296/5569/886.

Wallraff, A., Schuster, D., Blais, A., Frunzio, L., Majer, J., Devoret, M., Girvin, S., and Schoelkopf, R. Approaching unit visibility for control of a superconducting qubit with dispersive readout. *Physical Review Letters*, 95(6):060501–1, 2005.

ISSN 0031-9007. URL: http://scitation.aip.org/getabs/servlet/GetabsServlet?prog=normal&id=PRLTAO000095000006060501000001&idtype=cvips&gifs=yes.

Wallraff, A., Schuster, D., Blais, A., Frunzlo, L., Huang, R., Majer, J., Kumar, S., Girvin, S., and Schoelkopf, R. Strong coupling of a single photon to a superconducting qubit using circuit quantum electrodynamics. *Nature*, 431(7005):162–7, 2004. ISSN 0028-0836. URL: http://www.nature.com/nature/journal/v431/n7005/abs/nature02851.html.

Weissman, M. What is a spin glass? a glimpse via mesoscopic noise. *Reviews of Modern Physics*, 65(3):829–39, 1993. ISSN 0034-6861. URL: http://prola.aps.org/abstract/RMP/v65/i3/p829_1.

Weissman, M. B. 1/f noise and other slow, nonexponential kinetics in condensed matter. *Reviews of Modern Physics*, 60(2):537–571, 1988. doi:10.1103/RevModPhys.60.537. URL: http://prola.aps.org/abstract/RMP/v60/i2/p537_1.

Yamamoto, T., Nakamura, Y., Pashkin, Y., Astafiev, O., and Tsai, J. Parity effect in superconducting aluminum single electron transistors with spatial gap profile controlled by film thickness. *Applied Physics Letters*, 88(21):212509–1, 2006. ISSN 0003-6951. URL: http://scitation.aip.org/getabs/servlet/GetabsServlet?prog=normal&id=APPLAB000088000021212509000001&idtype=cvips&gifs=yes.

Yu, C. Why study noise due to two level systems: a suggestion for experimentalists. *Journal of Low Temperature Physics*, 137(3-4):251–65, 2004. ISSN 0022-2291. URL: http://www.springerlink.com/content/u68t3hh017858050/.